UNIVERSITY OF LONDON

University College London

Department of Electronic and Electrical Engineering

Fast Waveform Metrology: Generation, Measurement and Application of Sub-picosecond Electrical Pulses

Andrew J A Smith

November 1995

Thesis submitted to the University of London

for the degree of *Doctor of Philosophy*

ABSTRACT

This thesis describes work performed at the National Physical Laboratory to improve the electrical risetime calibration of instruments such as fast sampling oscilloscopes. The majority of the work can be divided into four sections: development of an ultrafast optoelectronic pulse generator; measurement of fast electrical pulses with an electro-optic sampling system; de-embedding of transmission line and transition effects as measured at different calibration reference planes; and calibration of an oscilloscope.

The pulse generator is a photoconductive switch based on low-temperature Gallium Arsenide, which has a very fast carrier recombination time. Sub-picosecond electrical pulses are produced by illuminated a planar switch with 200 fs optical pulses from a Ti:sapphire laser system.

The pulses are measured using a sampling system with an external electro-optic probe in close proximity to the switch. The electro-optic sampling system, with a temporal resolution better than 500 fs, is used to measure the electrical pulse shape at various positions along the planar transmission line. The results are compared to a pulse propagation model for the line. The effects of different switch geometries are examined.

Although the pulse generator produces sub-picosecond pulses near to the point of generation, the pulse is shown to broaden to 7 ps after passing along a length of transmission line and a coplanar-coaxial transition. For a sampling oscilloscope with a coaxial input connector, this effect is significant. Frequency-domain measurements with a network analyser, further electro-optic sampling measurements, and the transmission line model are combined to find the network transfer function of the transition.

Using the pulse generator, the electro-optic sampling system and the transition knowledge, a 50 GHz sampling oscilloscope is calibrated. The determination of the instrument step response (nominal risetime 7 ps) is improved from an earlier value of 8.5 -3.5 / +2.9 ps to a new value of 7.4 -2.1 / +1.7 ps with the calibration techniques described.

To Mary

CONTENTS

ACKNOWLEDGEMENTS

ILLUSTRATIVE MATERIAL

Chapter 1

Chapter 2

Chapter 3

Chapter 4

Chapter 5

Chapter 6

Chapter 7

No tables or figures.

Appendix A

1 INTRODUCTION

1.1 The sampling oscilloscope

1.1.1 History

In the early 1960s, a major advance was made by Hewlett-Packard[Ref 1] and Tektronix in improving the measurement of repetitive time-domain pulses and transients by the development of the sampling oscilloscope. This provided short duration time measurements by a method known as equivalent time sampling, where a single sample from a successive repetition of a train of similar pulses is captured on an instrument display, with the next sample being acquired and displayed at a slightly different time relative to the starting pulse, so building up a picture or waveform of the pulses in the time-domain. The advantage of such an instrument readily became apparent - the measurement time to acquire and display a waveform was decoupled from the actual duration of the pulses (for example, a train of nanosecond pulses could be acquired over milliseconds, the time corresponding to multiples of the pulse repetition frequency) - and the temporal resolution limit of the real-time cathode-ray oscilloscope was surpassed.

1.1.2 Recent developments

Sampling oscilloscopes and electrical pulse generators are now commercially available with bandwidths greater than 50 GHz or risetimes less than 7 ps. The drive behind the development of such high-bandwidth systems has been rapid advances made in the fields of optoelectronics, computing and telecommunications. Traceability of such systems to national standards is important, supporting market sectors whose emerging technologies rely on such systems and encouraging growth by the provision of a sound metrological base.

Research to provide electrical risetime measurements traceable to national standards has been active at the National Physical Laboratory (NPL) in the United Kingdom, the National Institute for Standards and Technology (NIST) - formerly the National Bureau

of Standards (NBS) - in the United States and other world class standards laboratories.

It is worth emphasizing that the provision of a facility to calibrate sampling oscilloscopes and pulse generators *to specification* is not a trivial problem. If a 50 GHz oscilloscope has a specified risetime of less than 7 ps, then in theory one requires a risetime measurement capability of 5 ± 2 ps, 6 ± 1 ps or 6.5 ± 0.5 ps etc.

Table 1.1 shows some of the oscilloscopes available in recent years and contrasts their risetimes with the level of calibration NPL has been able to attain since starting a service in 1988. The author of this thesis has been closely involved with the research work at NPL since 1989. This text outlines the applied research which culminated in the improved 1994 facility, with NPL close to being able to calibrate a 50 GHz oscilloscope to specification.

Table 1.1 Recent history of oscilloscope risetimes and NPL calibration facilities.

Example of Oscilloscope	Typical Risetime / ps	NPL Calibration facility	
		Year	response / ps
Tektronix S4 HP 1430A	<28	1988	25 ± 4
HP 54120 Tektronix SD26	<16	1990	18 ± 3.5
HP 54121 Tektronix SD32	< 7	1992	10 ± 2
"	"	1994	8 ± 2

1.2 Introduction to waveform metrology

A waveform - defined fully in the thesis terminology - is a measured pulse or transient. Metrology is the science of measurement. The core theme of this text is waveform metrology, where measurements are described, typically shorter than 20 ps, of pulses or transients associated with the development of standards to calibrate sampling oscilloscopes.

1.2.1 Impulse response

The performance of an oscilloscope is usually described by its response to one of two mathematical concepts: an electrical impulse, with infinitesimal short pulse duration;[2] or a Heaviside step, with infinitesimal short risetime.[3]

In theory, if an infinitesimal short pulse generator were available and connected to an "ideal" oscilloscope - with perfect lossless and distortion-free connectors - then the oscilloscope would display such a function. A real oscilloscope would, however, not reproduce the function perfectly, due to the inherent limitations of the oscilloscope (and indeed any measuring instrument). The impulse response of the oscilloscope describes the extent to which the instrument does not behave in an idealized manner. In this hypothetical case, the oscilloscope measurement of the infinitesimal pulse would define the impulse response of the instrument.

In practice, a pulse generator capable of producing an infinitesimal pulse is not required. As long as the pulse generator has a duration significantly shorter than the nominal response time of the oscilloscope, then accurate characterisation of the oscilloscope is possible. However, the technology to make state-of-the-art electrical pulse generators has often been similar to that used to make state-of-the-art oscilloscopes. One example of such a pair of instruments, still much in use today, is the Tektronix S4 sampler and S52 pulse generator. Throughout most of the history of the sampling oscilloscope, the temporal resolution of the best commercial electrical pulse generators has not been

significantly faster than the response of oscilloscopes of the same era. The current situation is very similar. Although convolution techniques (addressed later) can compensate to a certain extent, alternative methods are needed to enable the accurate characterisation of sampling oscilloscopes to provide traceability.

1.2.2 Optoelectronic approach

The pulsed electrical measurement system developed at the NPL uses a picosecond optoelectronic technique to generate electrical pulses that are faster than can be generated by purely electrical means. The fast electrical pulses are generated by illuminating photodiodes or photoconductive switches with femtosecond lasers. The resultant waveform recorded on an oscilloscope (CRO) is the convolution of the oscilloscope impulse response with the pulse generator signal, together with the response of the interconnecting transmission lines. The pulse generator signal is measured, independently of the CRO, using electro-optic or photoconductive sampling techniques with sub-picosecond resolution. The oscilloscope response is obtained by deconvolution of the test signal from the recorded waveform, normally performed with associated windowing and filtering techniques.

The pulse generator used in the calibration system at the outset of this project was a commercially available 50 GHz Schottky barrier photodiode,[4] capable of producing 9 ps pulses. Using such a system, the NPL established facilities to calibrate sampling oscilloscopes and electrical pulse generators with risetimes down to below 10 ps or bandwidths of 35 GHz and above.[5] To improve the temporal resolution of the system and to reduce the uncertainties in the existing measurements, a faster pulse generator was required. It was to meet this, and other requirements, that the pulse generator project at the NPL was initiated, on which some of this thesis is based.

To achieve the stated aim, various options were considered, such as advanced photodiodes and non-linear transmission lines.[6] However, the photoconductive switch appeared to offer the simplest and most cost-effective route to achieve the target. This

switch works on the principle of changes in the conductance of a material, induced by the injection of a large number (>10^{17} cm^{-3}) of electron-hole pairs. If the electron-hole pairs are produced by illumination with photons from a femtosecond laser, and the carrier characteristics of the material are fast, then rapid changes in the conductance of the material may be produced which provide a mechanism for a fast pulse generator.

1.3 Organisation of thesis

This introductory chapter concludes in *section 1.4* by introducing and defining some of the terminology used in this thesis. The content and organisation of the rest of the thesis follows below.

Chapter 2

The principle of the photoconductive switch is investigated in *section 2.2* and a simple model developed *(section 2.3)*. The relative merits of semiconductor photoconductive materials are discussed in *section 2.4* and the growth and properties of the favoured material for waveform metrology, low-temperature GaAs, are described in *sections 2.5* and *2.6* respectively.

Chapter 3

In *section 3.2,* design equations for coplanar transmission lines are discussed and photoconductive devices using such lines are designed *(section 3.3)* and fabricated (*section 3.4*). The devices are electrically characterised in *section 3.5*.

Chapter 4

Photoconductive switch measurement configurations are described in *section 4.2*. The theory of electro-optic sampling (EOS) is summarised in *section 4.3*, and EOS systems with a dye laser (*section 4.4*) and a Ti:sapphire laser (*section 4.5*) are described. Measurements made with a sampling oscilloscope and the EOS systems are explored in *section 4.6* (dye laser) and *section 4.7* (Ti:sapphire laser). The chapter concludes by

describing the EOS system limitations and deriving the response of the photoconductor (*section 4.9*).

Chapter 5

Section 5.1 introduces the concept of de-embedding. A transmission line model is developed in *section 5.2*. In *section 5.3*, frequency-domain measurements of planar lines and transitions are performed with a network analyser, and the results compared with the model. Time-domain measurements of planar lines and transitions are also made with a sampling oscilloscope and the EOS system, and the results compared to the model (*section 5.4*). Using a two-transition measurement scheme and previous results in the chapter, the impulse response of a transition is derived and uncertainties are calculated (*section 5.5*).

Chapter 6

In *section 6.2,* a deconvolution technique and the uncertainties associated with it are described with the aid of an example. The measurement of jitter is described in *section 6.3*, again with the aid of an example. Using the previous sections and the results of *chapter 4* and *chapter 5*, the response of a sampling oscilloscope is determined (*section 6.4*). The uncertainties in the impulse and step response are calculated in *section 6.5*.

Chapter 7

The thesis concludes with closing comments and suggested future work

Appendix A

Some results and remarks on the measurement of bias tees and attenuators are summarised.

1.4 Thesis Terminology

A key issue in metrology is precision. Because of this, there is a need to be specific about

definitions and terminology.

1.4.1 Domains and FFT

This thesis uses the two domains most applicable in describing the electrical and optoelectronics work associated with the calibration of sampling oscilloscopes, namely the time and frequency-domains.

Time-varying changes in electrical voltages are represented by the electrical waveform V(t). The frequency spectrum, S(ω), of the time-domain waveform is defined as its Fourier transform[2]:

$$S(\omega) = \int_{-\infty}^{\infty} V(t)\, e^{-i\omega t}\, dt \quad , \tag{1.1}$$

and conversely, V(t) is defined as the Fourier transform of S(ω):

$$V(t) = \frac{1}{2\pi} \int_{-\infty}^{\infty} S(\omega)\, e^{i\omega t}\, d\omega \quad , \tag{1.2}$$

where ω is the frequency in radians.

In practice, measurements consist of discrete numbers of points defined within limited ranges. Therefore, discrete transforms, such as the Fast Fourier Transform (FFT), are used to approximate the above integrals.

1.4.2 BSI/ IEC standards

Further details of some of the following terms and definitions are found in the relevant standards publications.[7]

A wave is a modification of the physical state of a medium which propagates in that medium as a function of time as a result of one or more disturbances. Pulses and

transitions are included in the wave definition. A waveform is a manifestation, representation or visualization of a wave, pulse or transition. Put succinctly - the measurement process yields a waveform from a (physical) pulse.

A single pulse waveform (i.e. one that departs from, and then returns to, a nominal state) has a large number of terms associated with it. The pulse start time is defined as the instant specified by a magnitude referenced point, usually the mesial or 50 per cent point of the first transition. The pulse stop time is similarly defined for the last transition. The pulse duration is the duration between the pulse start and stop times. An alternative term for the pulse duration, used in this text, is the Full-Width-at-Half-Maximum (FWHM).

The proximal and distal points are usually specified to be at the 10 and 90 per cent reference magnitudes respectively. The first transition duration is the duration between the first proximal and distal points of the pulse transition. This thesis uses previous BSI notation, and defines the "risetime" to be the first transition duration, as defined above, and the "falltime" to be the last transition duration

It should be noted that for comparison purposes it is occasionally useful to quote the proximal and distal points defined at 20 and 80 per cent respectively, giving an alternative transition duration. These are clearly referred to as the 20%-80% risetime or falltime.

1.4.3 Definition of oscilloscope response

The expression "measurement of the response of an oscilloscope" is imprecisely defined and can include many possibilities. Descriptions such as "a 50 GHz oscilloscope" are frequently used. Whilst not incorrect, the use of single parameter definitions in either the time or frequency-domains can be misleading, and may not be helpful to the user. Such terminology can also encourage manufacturers to raise the published bandwidth. For example, higher frequency components can be tweaked to the detriment of lower frequencies, providing an instrument whose time-domain performance is less well-behaved than before the tweaking. National standards laboratories encourage good practice by

providing waveforms which describe more fully the performance or response of the sampling oscilloscope than can be provided by parametric definitions. However, parametric definitions can still be useful, providing the above is taken into account.

The risetime of an oscilloscope is the single parameter quoted by many to describe the step response of an oscilloscope to an Heaviside step function[3] input. The step response is the integral of the impulse response, as previously defined.

For a Gaussian impulse response, duration τ_{FWHM}, it can be shown[8] that

$$\frac{\tau_r}{\tau_{FWHM}} = 1.089 \quad , \tag{1.3}$$

where τ_r is the risetime (of the step response).

The bandwidth, or -3 dB frequency, of the oscilloscope is defined to be the frequency at which the power spectrum decreases by a factor of two from the d.c. value. The power bandwidth should not be confused with the frequency at which the voltage drops by a factor of two (sometimes loosely referred to as the voltage bandwidth); the frequency at the -3 dB power point is equivalent to the frequency at the -6 dB voltage point.

For a Gaussian impulse response,

$$f_{3dB} \approx \frac{0.34}{\tau_r} \approx \frac{0.31}{\tau_{FWHM}} \quad , \tag{1.4}$$

where f_{3dB} is the (power) bandwidth. It is worth noting that such a relation depends on the shape of the response. Although a practical oscilloscope response often has a similar shape to a Gaussian, an exponential decay (RC time constant) is frequently assumed. For an exponential decay,

$$f_{3dB} \approx \frac{0.35}{\tau_r} \quad , \tag{1.5}$$

where τ_n is the risetime of the integrated decay.

1.4.4 Convolution and deconvolution

Convolution is best described here in the context - fast waveform metrology - in which it is to be used. When an instrument such as a sampling oscilloscope is used to measure a time-domain pulse or transient, the recorded waveform, h(t), is not a true representation of the original pulse, f(t), but is affected by the non-perfect oscilloscope, represented by the system response. The signal f(t) is convolved with the oscilloscope system response g(t), to provide the measured waveform h(t) recorded on the oscilloscope - see equation (1.6); x is a dummy variable. Convolution is ubiquitous in measurement as all measuring instruments have a finite system response or resolving limitation.

$$h(t) = \int_{-\infty}^{\infty} f(x)\, g(t-x)\, dx \quad . \tag{1.6}$$

The symbol $\otimes$ is used to represent a convolution, such that equation (1.7) is equivalent to equation (1.6):

$$h(t) = f(t) \otimes g(t) \quad . \tag{1.7}$$

Deconvolution is the inverse of convolution. Deconvolution is required to recover the desired signal from an instrument-limited measurement process. In the example, a known oscilloscope system response may be deconvolved from the recorded data waveform to obtain the original signal. The result of jitter, noise and filtering on practical examples of deconvolution is addressed in *chapter 6*.

It is worth noting that in *chapter 6* the application is reversed - the oscilloscope system response is the desired quantity, which is found by deconvolving a known pulse generator signal from the recorded data waveform.

1.5 References to Chapter 1

1 Hewlett Packard Co, "Time Domain Reflectometry", Application Note 62, Palo Alto, CA, USA, 1964.

2 R.N.Bracewell, "The Fourier Transform and Its Applications", McGraw-Hill Inc, 1986.

3 P.E.Stuchert, "Pulse Standards: Basic Tools for Waveform Analysis", IEEE Trans. Instr. Meas. IM-31, 1982, pp 192-198.

4 D.G.Parker, "Indium Tin oxide/GaAs Photodetectors for Millimetric-wave Applications", Electr. Lett., Vol. 22, 1986, pp 1266-1267.

5 D.Henderson, A.G.Roddie and A.J.A.Smith, "Recent Developments in the Calibration of Fast Sampling Oscilloscopes", IEE Proc. A, Vol. 139, No.5, Sept 1992, pp 254-260.

6 M.J.Rodwell and M.Kamegana, "GaAs Nonlinear Transmission Lines for Picosecond Pulse Generation and Millimetre Wave Sampling", IEEE Trans. MTT-39, No.7, July 1991, pp 1194-1204.

7 British Standard guide to "Pulse Techniques and Apparatus", BS-5698 BSI, London, 1989 (identical to IEC 469-1).

8 D.Henderson, "Measurement of the Temporal Response of a Picosecond Oscilloscope by Optoelectronic Techniques", Ph.D. Thesis, University College London, July 1989.

2 BACKGROUND THEORY

2.1 Introduction

This chapter provides some theoretical and experimental background to the photoconductive switch. The principle of the photoconductive switch is first summarised and the principle further explored by the development of a simple model. Criteria to select a suitable photoconductive material - from which a pulse generator for metrology can be fabricated - are explored, and after considering the criteria a semiconductor material, low-temperature (LT) GaAs, is chosen. The published properties of the material are summarised. Finally, the growth of LT-GaAs is described.

2.2 Principle of the photoconductive switch

A photodetector or optoelectronic converter is defined here to be a rectifying device which converts a.c. light to d.c. current. Photodiodes and photoconductors are classes of photodetector. A photodiode consists of a semiconductor junction (p-n, p-i-n, etc.) operating under reverse bias. Details are provided in a wide range of literature.[1] A photoconductor usually consists of two contacts separated by a semiconductor region (Figure 2.1). Optical illumination of the semiconductor material results in the generation of electron-hole pairs, which increases the conductivity of the material.

The conductivity σ is given by:

$$\sigma = q\,(\mu_n n + \mu_p p) \quad , \tag{2.1}$$

where n and p are the number densities of free electrons and holes, μ_n and μ_p their respective mobilities, and q the electronic charge. A voltage source connected across the two contacts drives a current through a load resistor. Changes in optical illumination produce changes in the conductivity of the semiconductor, and thus change the electrical current generated in the load. The optical illumination for ultrafast photoconductive

switches is usually provided by a laser, as an intense source with ultrafast changes in illumination is required.

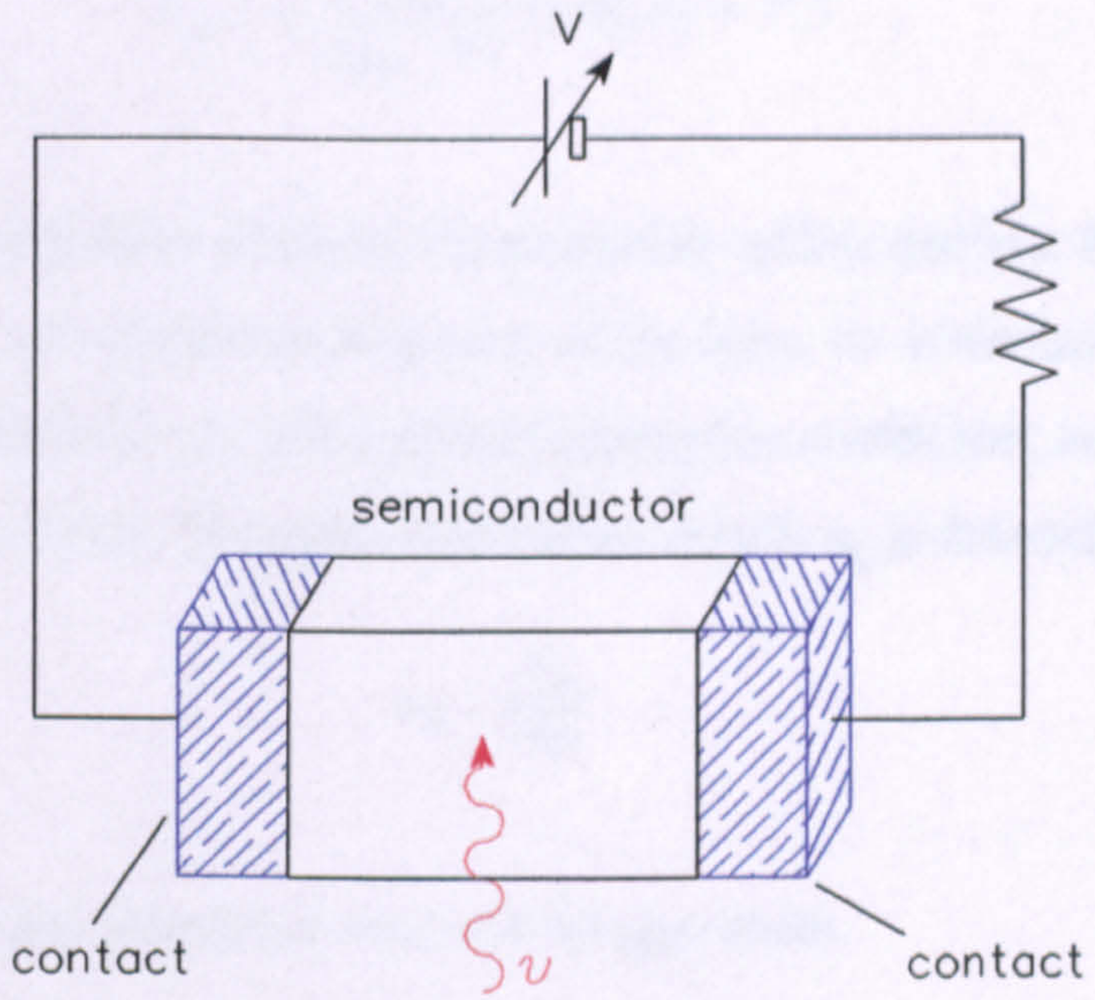

Figure 2.1 Simple photoconductor circuit.

A pulse generator suitable as a calibration source may have two alternative output shapes: a pulse, starting and returning to zero amplitude; or a step, consisting of a rising edge followed by a flat top. In practice, the output of a photoconductive step generator displays a slow exponential decay in signal after the initial step. The application of step generators to oscilloscope calibration has previously been addressed[2] and this thesis concentrates on developing a photoconductive impulse generator.

2.3 Modelling the photoconductive switch

2.3.1 Voltage considerations

A model for the voltage produced by a photoconductive switch can initially be obtained using a quasi-stationary treatment. The photons illuminating the semiconductor are all assumed to absorb uniformly within the thickness of the semiconductor active layer, except for the photons which are reflected.

Illumination of the semiconductor with a modelocked laser generates N_g free carriers (electron-hole pairs) per optical pulse:

$$N_g = \eta . \frac{P_{av}}{f_{laser}\ h\upsilon} . (1-R) . (1-e^{-\alpha_a d}) \quad , \tag{2.2}$$

where η is the quantum efficiency for production of free carriers, P_{av} is the average optical power, f_{laser} is the repetition frequency of the laser, hν is the energy of one photon, R is the optical reflectivity, α_a is the optical absorption coefficient, and d the thickness of the semiconductor layer. The generated carrier density n_g is determined from

$$n_g = \frac{N_g}{l d w} \quad , \tag{2.3}$$

where l is the gap separation and w is the gap width.

For example, assuming $\eta = 1$, an illumination of 5 mW at 800 nm and 80 MHz onto a 2 μm thick GaAs layer produces a value of $N_g = 1.5 \times 10^8$. If the optical beam diameter is 20 μm then $n_g = 2.4 \times 10^{17}$ cm^{-3}. This is quite a significant value, larger than typical doping levels, and so may be expected to alter the properties of the material.

The photo-induced change in conductivity in the semiconductor can be estimated by substituting equation (2.3) into equation (2.1), assuming $\mu_h << \mu_n$ and $N \approx P$ for excitation levels greater than the intrinsic doping. The resistance across the switch, R_g, is calculated from the conductivity:

$$R_g = \frac{1}{\sigma} . \frac{l}{dw} = \frac{l^2}{q\mu_n} . \frac{1}{\eta} . \frac{f_{laser}\ h\upsilon}{P_{av}\ (1-R)\ (1-e^{-ad})} \quad . \tag{2.4}$$

In the example, the above terms are known except the electron mobility μ_n. A simple equivalent circuit of the photoconductive switch is shown in Figure 2.2. Z_o is the impedance of the transmission line before and after the switch, R_c is the total metal-semiconductor contact resistance in the circuit, $R_g(t)$ is the gap or switch resistance (which will later be described as a function of time), and C_g is the capacitance of the gap. The

circuit acts as a potential divider such that the switched voltage V(t) is given by

$$V(t) = V_b \frac{Z_o}{2Z_o + R_c + R_g(t)} \quad , \tag{2.5}$$

where V_b is the d.c. bias voltage.

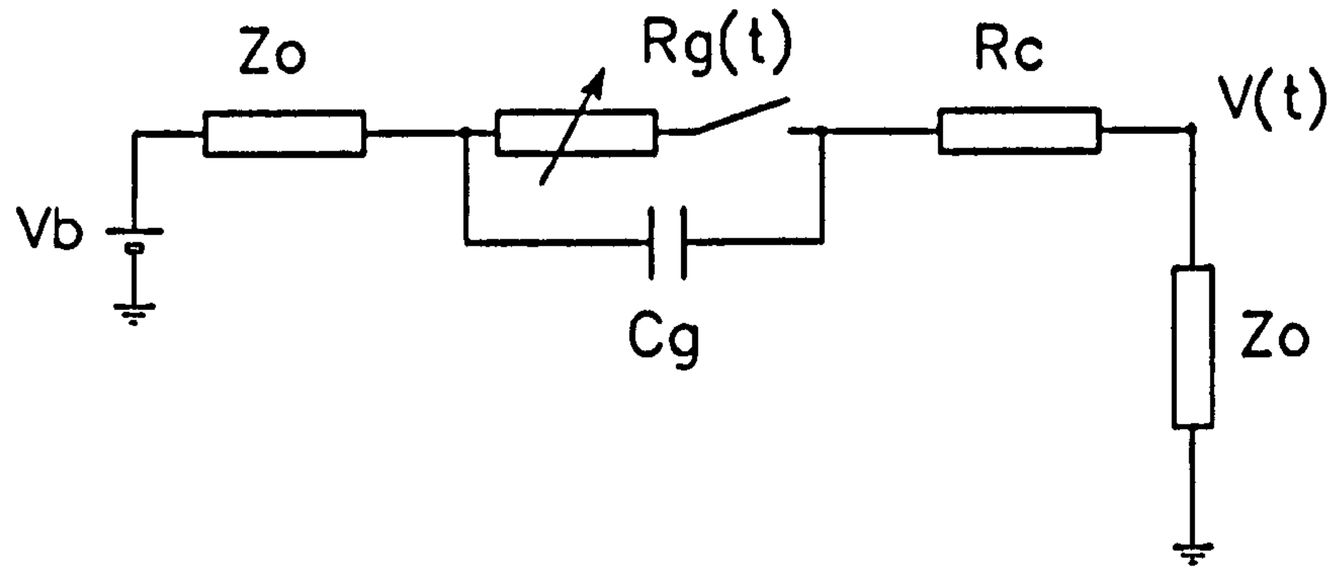

Figure 2.2 Equivalent circuit of photoconductive switch.

If it is assumed that a switching efficiency of 5% of the bias voltage enables accurate sampling oscilloscope and electro-optic sampling analysis (e.g. a 10 V bias produces a 20 mV photoconductively-generated peak), then for typical 50 Ω geometry, R_c and $R_g(t)$ must together be lower than approximately 900 Ω. Usually $R_c << R_g(t)$. To achieve such a gap resistance, a minimum intensity of optical illumination and gap length l are defined, given the material's mobility.

The above quasi-stationary treatment enables a change of switch resistance from a known number of incident photons to be estimated in the static case. The photoconductive switch is to be used to generate ultrafast electrical pulses from ultrafast optical pulses provided by the laser. Therefore, the factors which affect the speed of performance must also be discussed.

2.3.2 Speed considerations

The bulk photoconductor shown in the previous section (Figure 2.1) is ideal for low-speed, high-power applications. However, if ultrafast changes in photoconductivity are to be used to produce fast electrical pulses then an alternative faster geometry is required, such as the coplanar transmission lines introduced and described in *chapter* 3. Coplanar photoconductive devices can be fabricated from semiconductor substrates or substrates

with appropriate active semiconductor layers, usually on the substrate top. Suitable fast semiconductor materials are discussed in *section* 2.4.

The coplanar photoconductive switch consists a pattern of metallisation deposited on the top of the semiconductor. Various geometries are possible, including the coplanar waveguide sliding contact, coplanar waveguide series-gap, and the coplanar stripline sliding contact, referenced, discussed and measured in *chapter* 4. All the devices used in this thesis assume complete optical illumination across the gap in the metallisation defined on the semiconductor. Alternative photoconductive mechanisms such as the non-uniform illumination or covered-gap technique[3], where fast pulses are obtained from a partially-illuminated gap across a slow semiconductor, are not further discussed here.

Two properties which affect the temporal response of a photoconductor are the *dielectric relaxation time* and the *free carrier lifetime*. Given an infinitely short optical excitation, electron-hole pairs in the semiconductor are generated extremely quickly, in the short time it takes for particles to separate physically. The field distribution, and hence conductivity, do not simultaneously change since initially the space charge of the electrons and holes are neutralised. Drift in opposite directions to the applied field creates a space charge field. The dielectric relaxation time, τ_{dr}, is defined as the time taken for the space charge dependent field in the photoconductor to evolve and is a complicated function of the semiconductor, geometry and illumination.[4]

The photo-generated carriers recombine at a rate given by the free carrier lifetime, τ_{fc}, causing a corresponding decrease in photoconductivity. The free carrier lifetime of a semiconductor depends on the semiconductor and the recombination mechanism. For example, impurities can act as recombination centres by trapping free carriers and shortening the lifetime. The decay time depends on the type and cross-section of the impurity, but the decay is non-radiative. Such a recombination is frequently used when ultrafast photoconductive switches are required.

Two further recombination mechanisms are summarised below, but are not as important

for the operation of an ultrafast photoconductor. Radiative recombination, or luminescence, involves the excess energy being given up by emitting photons. Such a process is relatively slow, often in the order of tens of nanosecond.[5] Another non-radiative (but slow) carrier decay mechanism is three-particle Auger recombination. The excess energy raises other free carriers to higher states in their bands which subsequently relax by the emission of phonons.[5]

Other factors which affect the temporal response of the photoconductor include the parasitics associated with the switch geometry (estimated in *chapter* 4) and the ability of the transmission line to propagate fast pulses (estimated in *chapter* 5).

Returning to equations (2.4) and (2.5), the quasi-stationary approximation to the switched voltage can be extended to apply to the fast photoconductor. The switch resistance was calculated from the energy of one optical pulse. As a first approximation, this resistance can be multiplied by the ratio of the optical pulse duration to the free carrier lifetime, providing a value for the average switch resistance over the duration the switch is "closed". (In effect this adds τ_{fc} to the denominator of equation (2.4) and replaces P_{sv} and f_{laser} with the peak power of the optical pulse.)

A useful figure of merit for photoconductors is the lifetime-mobility product,[5] which describes the sensitivity of the photoconductor to photoexcitation. In the above paragraph, the estimated switch resistance is inversely proportional to this product.

In summary, the risetime of a pulse generated by a photoconductor depends mainly on the rising edge of the optical excitation and τ_{dr}, and the falltime depends mainly on the falling edge of the optical pulse and τ_{fc}.

2.4 Photoconductive material selection

The following properties are important in the selection of a semiconductor material

suitable for use in a metrological photoconductive switch: band-gap; wavelength; free carrier lifetime; mobility, responsivity, contacting and ageing.

The *band-gap*, E_g, of a semiconductor is the energy separating the bottom of the conduction band and top of the valence band. The optically-induced generation of electron-hole pairs in an intrinsic semiconductor requires incident photons to have sufficient energy to transfer an electron or hole between the two bands. The availability of a laser with suitable wavelength is therefore an important consideration in the design

Table 2.1 Some typical photoconductive semiconductors.

Semiconductor	Band-gap E_g (eV)	Equivalent Wavelength λ (nm)	Free Carrier Lifetime τ_{fc} (ps)	Estimated Mobility (cm^2/Vs)
Cr-doped GaAs	1.42	870	50 - 200	1000
MBE LT-GaAs	1.42	870	< 1	200
Amorphous Si	1.12	1110	1 - 10	1
Ion-damaged SOS	1.12	1110	< 1	20
MOVPE CdTe	1.56	800	< 1	150

of photoconductive switches. Table 2.1 shows examples of some semiconductors previously utilised for fast photoconductive switches along with various properties. The equivalent wavelength defines the cut-off wavelength above which the photons have insufficient energy for absorption in the semiconductor. Below the wavelength, the number of photons absorbed is estimated in the previous section.

Many materials, included those in Table 2.1, have sub-picosecond dielectric relaxation times. However, specialised semiconductor growth techniques are needed to achieve sub-picosecond recombination lifetimes, τ_{fc}. Such techniques introduce recombination centres or traps into the semiconductor by various methods, including: doping (Cr-doped GaAs);[6] the use of grain boundary defects (amorphous Si);[7] ion-implantation damage (silicon-on-sapphire);[8] epitaxial growth (CdTe);[9] or by low-temperature epitaxial growth (LT-GaAs). Properties of LT-GaAs are described in *section 2.5.*

In addition to time-resolved carrier dynamics, the responsivity of a photoconductive device is an important consideration. The pulse amplitude needs to be sufficient to provide adequate signal-to-noise in the metrological application. Factors which affect the responsivity include the semiconductor mobility, resistivity, and contact resistance, as shown in the previous section.

Mobility is an important consideration for charge transport because it describes the effect an applied electric field has on the motion of an electron or hole. A material with a higher mobility will, given similar device conditions, produce pulses of larger amplitude. An unfortunate consequence of the introduction of traps/recombination centres in many materials is the subsequent decrease in mobility. Materials which maintain a relatively high mobility and short free carrier lifetime are therefore ideal.

The interface, or contact between a semiconductor and metal has been the subject of much research.[10] The ohmic contact can be defined as a contact with a linear I-V characteristic, that is stable in time and temperature, and contributes as little parasitic resistance as possible. This ideal contact is not always possible to fabricate. Placing a metal on a wide band-gap semiconductor, such as GaAs, depletes a region of the semiconductor (beneath the metal) of carriers, producing a rectifying junction known as a blocking or Schottky contact. The I-V characteristic of such a junction is non-linear, as the applied voltage can alter the depth of the depletion region.

Most semiconductor devices require an ohmic contact for effective operation unless non-

ohmic behaviour is particularly advantageous. For a photoconductive device which is transit-time-limited - i.e. when the free carrier lifetime is much longer than the time of travel between the two contacts or electrodes - then ohmic contacts will decrease the series resistance, R_c, of the device, and in the external circuit produce higher-amplitude pulses.

For devices in this thesis, where the free carrier lifetime is shorter than the transit-time, some carriers will reach one electrode and must be replaced by carrier injection from the other electrode. An ohmic contact is more efficient at carrier replacement[5] and therefore increases the device responsivity, although careful consideration is required further to define the relative merits of the ohmic contact. This is not further discussed here.

One further property to consider is ageing. It has been found with some silicon-on-sapphire devices that ion-induced damage can vary significantly over time-periods of months. There is no evidence to suggest LT-GaAs suffers similar ageing problems. In addition to this, some contact metallurgies have been found to be unstable over similar time scales. Clearly such factors require consideration in choosing a suitable photoconductor for metrological application.

Considering all the above factors, and referring back to Table 2.1, it was decided to grow LT-GaAs as a photoconductive material, due to its published fast carrier recombination time, relatively high mobility and expected long-term performance stability in a switch.

2.5 Properties of LT-GaAs

MBE growth of GaAs is usually performed at a substrate temperature of around 600 °C. It has been found, however, that GaAs grown at lower temperatures (LT-GaAs) has some useful properties. LT-GaAs was first grown as a buffer layer to eliminate side-gating and back-gating effects in GaAs MESFET devices, taking advantage of the high resistivity of the annealed material.[11] When initially used as the photoconductive material in a

transmission line, 1.6 ps electrical pulses were generated.[12] Subsequent investigations of the ultrafast carrier dynamics by time-resolved reflectivity[13] and transient absorption spectroscopy[14] have shown the free carrier lifetime of the LT-GaAs to be sub-picosecond. More recently, sub-picosecond electrical pulses have been generated by LT-GaAs photoconductive devices.[15]

Studies performed on LT-GaAs[16] indicate the importance of excess As for the structural, optical and transport properties of the material. Reports describing these properties suggest knowledge of some of the mechanisms is still speculative. Growth at 200 ^{o}C produces a non-stoichiometric material with up to 1.5% (>10^{21} cm^{-3}) excess As as measured by Auger Electron Spectroscopy. This can be in the form of interstitials $(As)_i$, As-microclusters, gallium vacancies $(V)_{Ga}$, or antisite defects $(As)_{Ga}$. A large concentration of deep traps is measured (>10^{19} cm^{-3}), thought to comprise mainly of $(As)_{Ga}$ defects. The number of traps can be compared with an approximate value of 10^{16} cm^{-3} for Cr-doped GaAs. X-ray rocking curves show the presence of two distinct peaks, indicating differences in lattice parameter between the LT-GaAs epilayer and GaAs substrate. The resistivity of the layer is small (around 10^2 Ωcm), with the dominant conductivity thought to be due to hopping within the arsenic antisite defect band.

Thermally annealing a LT-GaAs layer at temperatures greater than 450 ^{o}C causes the concentration of As antisite defects to decrease, with As-precipitate densities in the order of 10^{17} to 10^{18} cm^{-3} observed by transmission electron microscopy (TEM)[16]. The LT-GaAs becomes stoichiometric with the lattice parameter similar to that of bulk GaAs. The resistivity of the material increases, from 10^2 Ωcm to greater than 10^6 Ωcm. This high value of resistivity, comparable with that of semi-insulating GaAs, is attributed to conduction by free carriers, excited from mid-gap levels with a low mobility due to the presence of some defects. The LT-GaAs mobility (200 cm^2/Vs), although relatively small compared with Cr-doped GaAs (1000 cm^2/Vs), is found to be larger than typical alternative photoconductive materials, such as silicon-on-sapphire (20 cm^2/Vs).

The substrate temperature during the LT-GaAs growth has been shown to be a very

important parameter.[11,13,14,16] Deviations by as little as 20 °C from the optimal temperature can produce significantly different properties. For example, the free carrier lifetime can increase to beyond 10 ps. Most MBE machines enable reproducibility of the substrate growth temperature. However the typical accuracy of absolute measurements is not usually better than ±20 °C.[17] The anneal temperature is found to be less critical than the initial LT-GaAs growth temperature, with a range of 450-600 °C producing similar results.

2.6 Wafer growth

LT-GaAs has ideal properties from which to fabricate sub-picosecond photoconductive switches. The material needs to be incorporated into wafers or substrates before yielding such devices. Bulk gallium arsenide is traditionally grown in crystal ingots using either the horizontal Bridgman (HB) or the liquid encapsulated Czochralski (LEC) method.[18] However, the growth of a whole wafer of LT-GaAs is not feasible using either method. Thinner, epitaxial layers can be grown using two commonly-available techniques: molecular beam epitaxy (MBE); and metal-organic vapour phase epitaxy (MOVPE).[18] The reaction rates for an MOVPE process are not sufficient to enable specialised growth of GaAs at low temperatures. Although in principle LT-GaAs can be grown by an MBE process onto any semiconductor substrate, in practice the strains induced by lattice mismatches limit the useful possibilities. It has, however, recently been shown that these strains can be advantageously used to reduce carrier recombination times by creating further trapping centres under carefully controlled conditions.[19]

For this project, it was decided to grow LT-GaAs layers onto bulk GaAs wafers. As well as the possibility of using the electro-optic coefficient of GaAs to enable direct electro-optic sampling of the substrate, the future direction of other work supported this decision, in particular: the possibility of incorporating LT-GaAs photoconductive switch technology into the UCL's existing GaAs device work; and the possibility of incorporating this technology into the NPL's existing GaAs work (for impedance and network analysis

standards) and into future electro-optic probing of MMICs. It is recognised that LT-GaAs grown onto silicon wafers, could, potentially, be invaluable in the future to the huge silicon technological base.

Three LT-GaAs layers were grown to an NPL specification using an MBE process at the SERC III-V Semiconductor Facility (now the Commercial and Industrial Development Bureau) at the University of Sheffield[1]. All three wafers were grown using similar conditions outlined below, with only minor changes to the procedure.

Each bulk substrate, 450 μm thick, was a commercially available semi-insulating LEC GaAs wafer, optically polished on both sides, orientated 2^{o} off the [100] plane. The combination of the last two properties allows the option of direct electro-optic sampling. The GaAs substrate was heated to 630 ^{o}C, using a slow ramp of 12-15 minutes duration, in order to decompose the oxide surface. During this process the substrate was exposed to a low flux of As_2. Reflection high-energy electron-diffraction (RHEED) techniques[20] indicated GaAs clean-up by a strong (2x4) GaAs reconstruction pattern. The substrate temperature was decreased to around 570 ^{o}C before commencing growth. The As_2 flux was then increased to give an As/Ga beam-equivalent (ion-gauge) pressure ratio of fifteen, before a 30 nm buffer layer of GaAs was deposited at the higher temperature of 580 ^{o}C. The higher arsenic flux was needed to prevent desorption; GaAs dissociates if there is no arsenic overpressure. The arsenic source was carefully chosen; the solid As_4 source was first cracked before evaporation to the dimeric As_2, to facilitate incorporation of arsenic precipitates into the wafer. The arsenic precipitates provide an important contribution to the special properties of the LT-GaAs layer. The prevalent conditions described are not significantly different to those used for normal GaAs growth.

The substrate was then cooled down to 200 ^{o}C over a period of six minutes, keeping the arsenic over-pressure. In total about 100 nm of GaAs was deposited before the temperature reached this target condition. A LT-GaAs layer, thickness 1900 nm, was then deposited over a two-hour period. The observation of a clear (but relatively weak) (2x4)

---

[1] Actual growth of samples was carried out by Mark Hopkinson.

RHEED pattern indicated relatively smooth two-dimensional growth was occurring, even at this low temperature. On completion of the 2 μm layer, the gallium source was shuttered and the substrate temperature was increased to 600 ^{O}C over a period of 6 minutes. There was then a post-growth anneal at this temperature and pressure for 10 minutes.

The first wafer had a 5 nm silicon-doped ($Si^{28} = 10^{18}$ cm^{-3}) GaAs layer deposited at 600 ^{O}C, before the substrate was cooled to room temperature over a period of about 10 minutes. The structure of the first wafer is shown in Figure 2.3. The second and third wafers were grown using similar conditions except the second wafer had a 10 nm thick, $Si^{28} = 5 \times 10^{18}$ cm^{-3}, GaAs cap layer and the third wafer had no cap. The thin n+ cap layers was grown to aid contacting purposes.

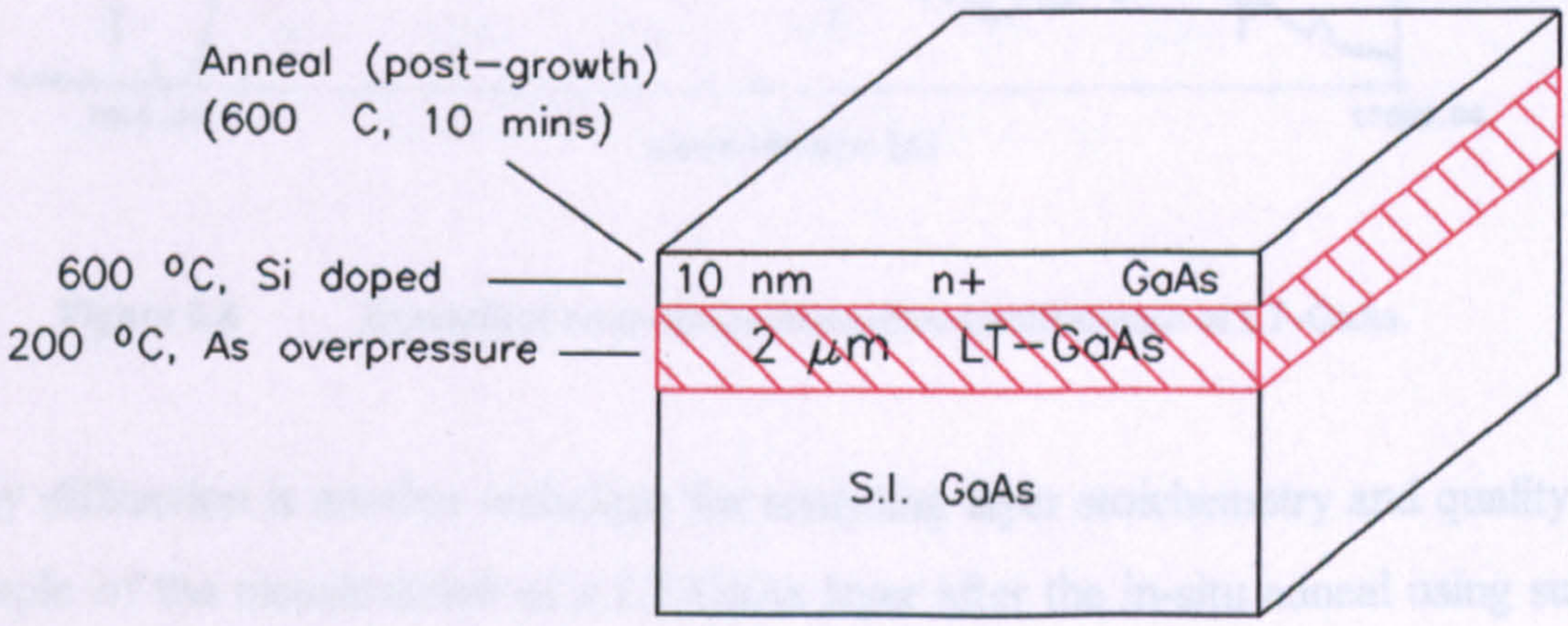

Figure 2.3 Structure of LT-GaAs wafer.

X-ray and room-temperature photoluminescence (PL) analysis were performed on the LT-GaAs wafers at the University of Sheffield. The results for each wafer were slightly different, but the general trends were similar.

An example of one of the PL measurements is displayed in Figure 2.4. This does not have the sharp peak typical of normal-temperature growth, but instead has a long tail with

relatively low intensity. The broad emission, below the GaAs band gap (E_g), suggests the presence of lots of extrinsic energy states, probably due to antisite defects formed at low temperature. The low intensity implies the presence of fast non-radiative recombination centres in the sample. PL measurements of the other two wafers showed similar behaviour, with lower intensities.

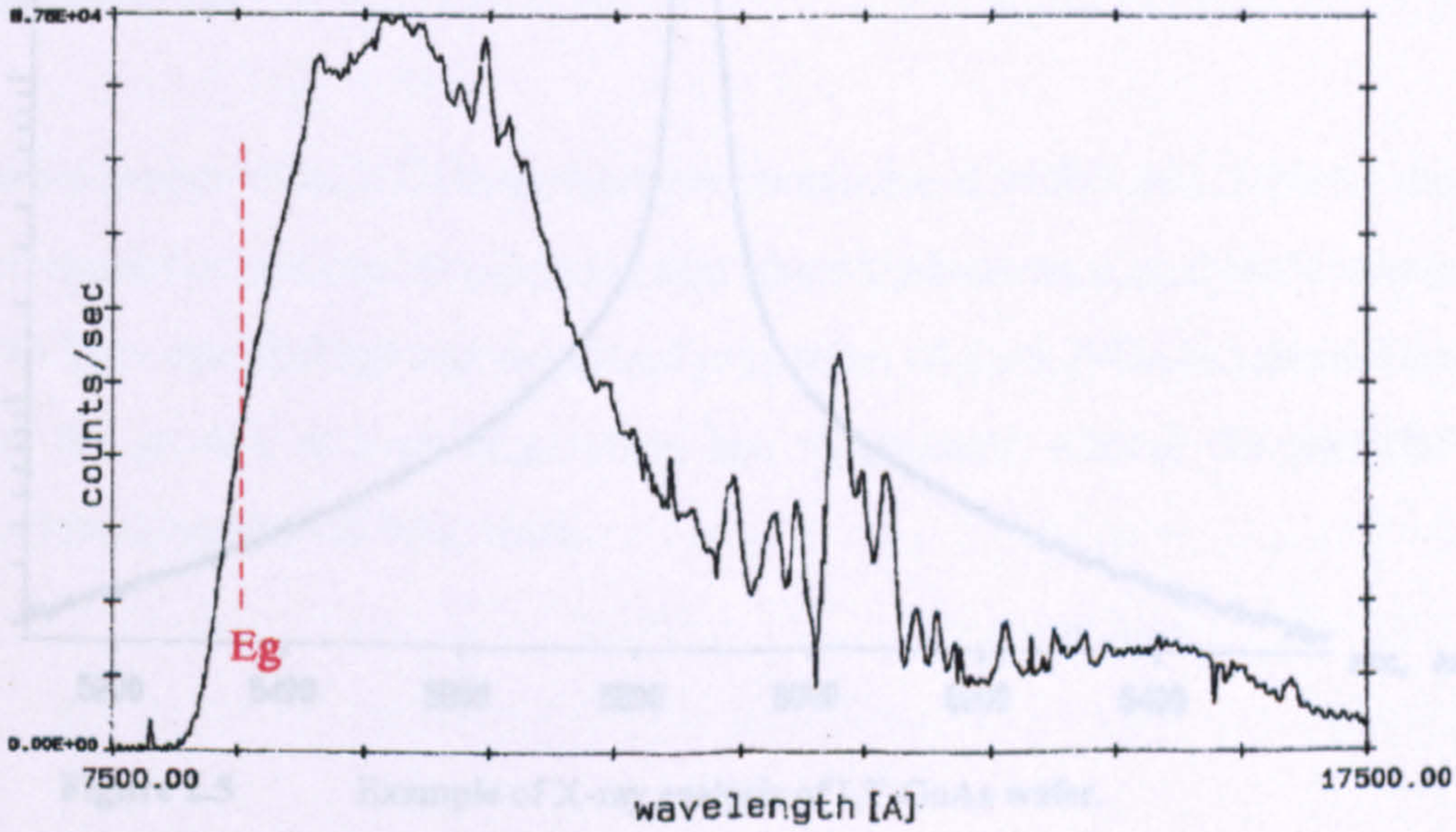

Figure 2.4 Example of room-temperature photoluminescence of LT-GaAs.

X-ray diffraction is another technique for analysing layer stoichemetry and quality. An example of the measurement of a LT-GaAs layer after the in-situ anneal using such a technique is shown in Figure 2.5. The peak of 15.8 sec (FWHM) indicates a good quality layer and compares well with values typically obtained with high-temperature growth. For comparison, a value of 12 sec was obtained with the semi-insulating GaAs substrate, shown in Figure 2.6. Values of 16.1 and 17.7 sec were obtained with the two other LT-GaAs wafers.

The single peak in Figure 2.5 also implies a successful anneal, with the lattice parameter shifted back to that of bulk GaAs. The peak shape differs somewhat from layers grown at higher temperature, such as Figure 2.6, in that the pedestals are more pronounced. The tails can be associated with dislocations, inhomogeneities, or a high defect density in the

layer. The slight asymmetry is believed to be due to As precipitates.[17]

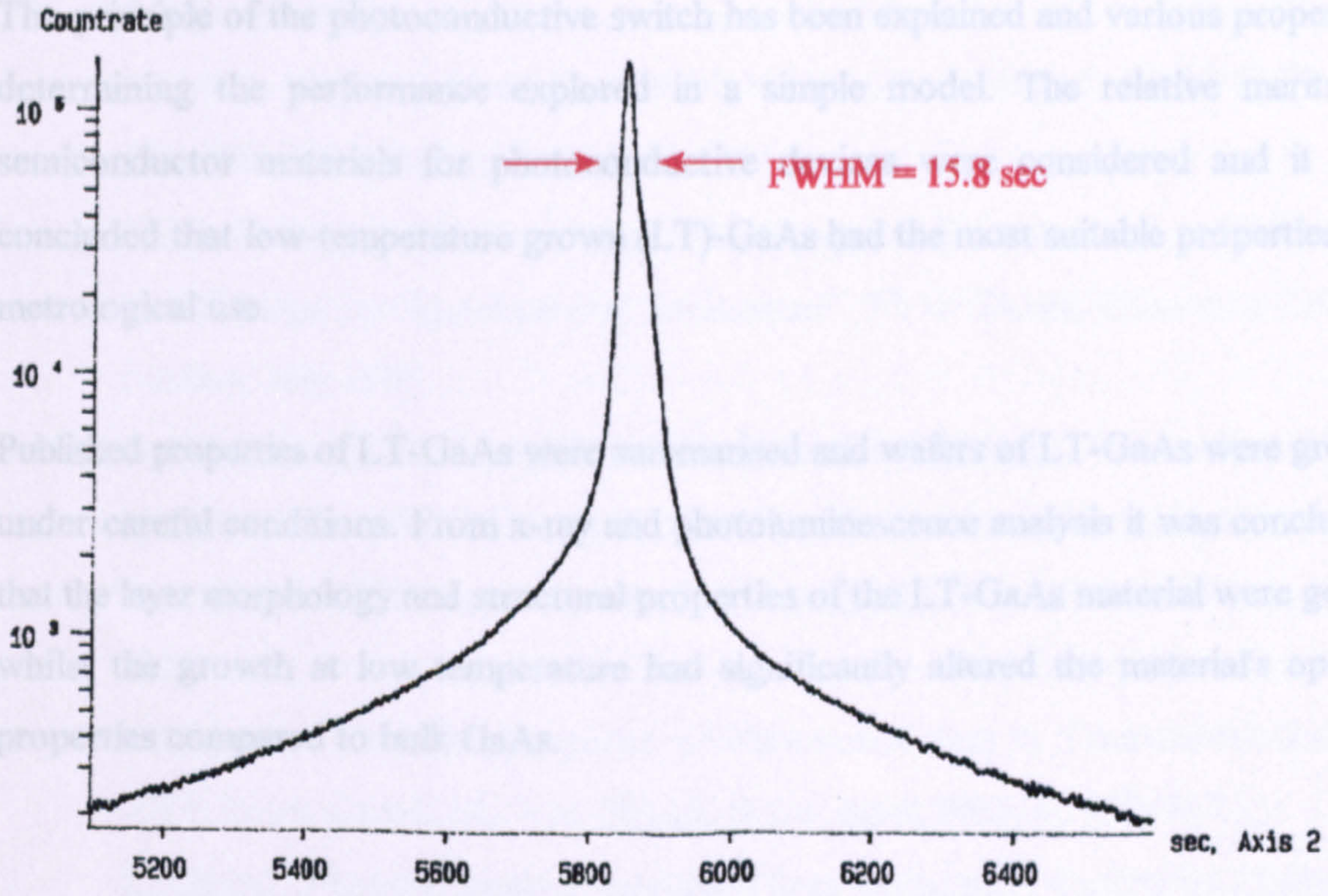

Figure 2.5 Example of X-ray analysis of LT-GaAs wafer.

Figure 2.6 X-ray analysis of SI-GaAs wafer.

2.7 Conclusions

The principle of the photoconductive switch has been explained and various properties determining the performance explored in a simple model. The relative merits of semiconductor materials for photoconductive devices were considered and it was concluded that low-temperature grown (LT)-GaAs had the most suitable properties for metrological use.

Published properties of LT-GaAs were summarised and wafers of LT-GaAs were grown under careful conditions. From x-ray and photoluminescence analysis it was concluded that the layer morphology and structural properties of the LT-GaAs material were good, whilst the growth at low temperature had significantly altered the material's optical properties compared to bulk GaAs.

2.8 References to Chapter 2

1 See for example:
S.M.Sze, "Semiconductor Devices Physics and Technology", AT&T Bell Labs, John Wiley & Sons Inc. Publishing, 1985.

2 D.Henderson, "Measurement of the Temporal Response of a Picosecond Oscilloscope by Optoelectronic Techniques", Ph.D. Thesis, University College London, July 1989.

3 S.Alexandrou, C-C.Wang, R.Sobolewski and T.Y.Hsiang, "Generation of Sub-picosecond Electrical Pulses by Nonunifrom Illumination of GaAs Transmission-Line Gaps", IEEE Journ. Quant. El., Vol. QE-30, No. 5, May 1994, pp1332-1338.

4 D.H.Auston, "Impulse Response of Photoconductors in Transmission Lines", IEEE Journ. Quant. El., Vol. QE-19, No. 4, April 1983, pp 639-647.

5 R.H.Bube, "Photoelectronic Properties of Semiconductors", Cambridge University Press, 1992.

6 C.H.Lee, A.Antonetti and G.Mourou, "Measurements on the Photoconductive Lifetimes of Carriers in GaAs by Optoelectronic Gating Techniques", Optical Comm., Vol. 21, April 1977, pp 158-161.

7 D.H Auston, A.M.Johnson, P.R.Smith and J.C.Bean, "Picosecond Optoelectronic Detection, Sampling, and Correlation Experiments in Amorphous Silicon", Appl. Phys. Lett, Vol. 37, August 1980, pp 371-372.

8 F.E.Doany, "Carrier Lifetime Versus Ion-Implantation Dose in Silicon on Sapphire", Appl. Phys. Lett., Vol. 50, 1987, pp 460-462.

9 M.C.Nuss, D.Whisker, P.R.Smith and T.E.Harvey, "Efficient Generation of 480 fs Electrical Pulses on Transmission Lines by Photoconductive Switching in Metalorganic Vapour Deposited CdTe", Appl. Phys. Lett., Vol. 54 (1), 2 Jan. 1989, pp 57-59.

10 R.E Williams, "Gallium Arsenide Processing Techniques", Artech House Publishing, chapter 11, 1984.

11 F.W.Smith, A.R.Calawa, C.L.Chen, M.J.Mantra and L.J.Mahoney, "New MBE

buffer used to eliminate backgating in GaAs MESFETs", IEEE Elect. Dev. Lett., Vol. 9, No. 77, 1988.

12 F.W.Smith, H.Q.Le, V.Diodiuk, M.A.Hollis, A.R.Calawa, S.Gupta, M.Frankel, D.R.Dykaar, G.A.Mourou and T.Y.Hsiang, "Picosecond GaAs-based Photoconductive Optoelectronic Detectors", Appl. Phys. Lett., Vol. 54, No. 10, March 1989, pp 890-892.

13 S.L.Williamson, J.F.Whitaker, Y.Chen and F.W.Smith, "Epitaxial Methods Produce Robust Ultrafast Detectors", Laser Focus World, June 1992, pp 97-104.

14 T.B.Norris, W.Sha, W.Schaff and X.J.Song, "Absorption of Low-Temperature MBE-Grown GaAs", Proceedings, Picosecond Electronics and Optoelectronics Topical Meeting, paper FC4, OSA, 1989, pp 200-203.

15 S.Gupta, J.F.Whitaker & G.A.Mourou, "Ultrafast Carrier Dynamics in III-V Semiconductors Grown by Molecular-Beam Epitaxy at Very Low Substrate Temperatures", IEEE Journ. Quant El., Vol. QE-28, No. 10, 1992, pp 2464-2472.

16 M.Kaminska, E.R.Weber, Kin Man Yu, R.Leon, T.George, F.W.Smith and A.R.Calawa, "High Resistivity of Low-temperature GaAs", Proceedings 6th Conference on Semi-Insulating III-V Materials, Toronto, IOP 1990, pp 111-115.

17 Private communication with Mark Hopkinson, University of Sheffield.

18 R.E.Williams, "Gallium Arsenide Processing Techniques", Artech House Publishing Inc., chapters 2, 6, & 11, 1984.

19 M.Y.Frankel, B.Tudayon and T.F Carruthers, "Integration of Low-temperature GaAs on Si Substrates", Appl. Phys. Lett., Vol. 62 (3), 18 June 1993, pp 255-257.

20 R.Ludeke, R.M.King and E.H.C.Parker, "Use of Electron Diffraction Techniques to Determine Surface Structure", chapter 1.2 in "MBE Surface and Interface Studies".

3 DESIGN, FABRICATION AND ELECTRICAL CHARACTERISATION

3.1 Introduction

The previous chapter provides some background to photoconductive switches and details the growth of a suitable semiconductor material. This chapter explores the design, fabrication and electrical testing of photoconductive switches. Design equations for coplanar transmission lines are first summarised. From these equations, dimensions of transmission lines are calculated and masks are designed. The fabrication of photoconductive devices, using photolithographical patterns obtained with the masks, is described. Initial electrical testing of the devices is achieved by measuring line conductivities and current-voltage contact characteristics.

3.2 Coplanar waveguide and stripline transmission lines

The term "coplanar line" refers to the set of transmission lines for which all the conductors are in the same plane; namely, on the top surface of the dielectric substrate. This differentiates them from other types of planar line such as microstrip, where conductors are present on both planes of the substrate. Most of the work in this thesis uses coplanar waveguide (CPW), first proposed by Wen.[1] The CPW line in Figure 3.1

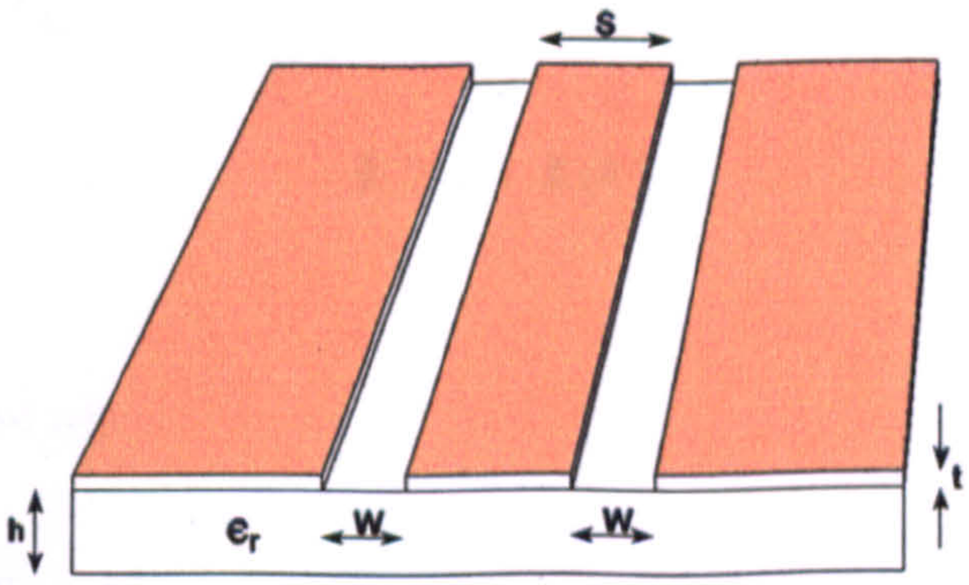

Figure 3.1 Geometry of coplanar waveguide (CPW).

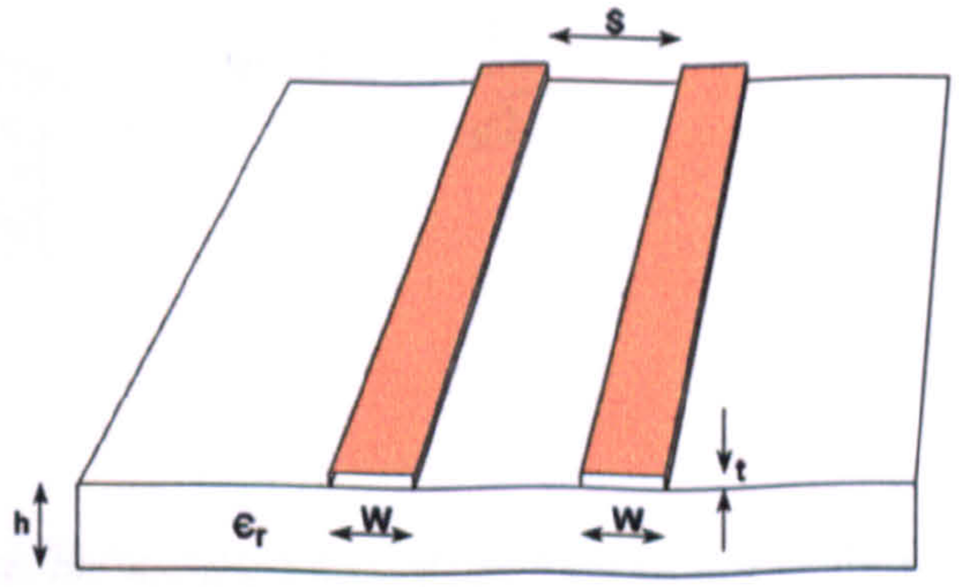

Figure 3.2 Geometry of coplanar stripline (CPS).

consists of a central conductor strip of width S and two ground planes located parallel to the central strip. The CPW shown is symmetrical, with both conductor-ground plane gaps or slots having equal width W. The substrate thickness is h. A line complimentary to the coplanar waveguide is coplanar stripline (CPS), also used in this project. This consists of two strips, typically of equal width, running parallel on the same plane of the dielectric substrate (Figure 3.2). Design equations for CPW and CPS lines are discussed below.

3.2.1 Design equations for CPW

Design equations for the characteristic impedance and effective dielectric constant of CPW have previously been calculated.[2] The characteristic impedance Z_{cpw} for CPW may be modified using frequency-independent or quasi-static analysis[3] to give

$$Z_{cpw} = \frac{30\pi}{\sqrt{\epsilon_{re}}} \frac{K'(k)}{K(k)} \quad , \tag{3.1}$$

where K(k) and K'(k) are the complete elliptical integrals of the first kind, with modulus k and complementary modulus k' such that:

$$k = \frac{S}{S+2W} ; \qquad k' = \sqrt{(1-k^2)} ; \qquad K'(k) = K(k') \tag{3.2}$$

and the integrals may be approximated as

$$\frac{K(k)}{K'(k)} = \frac{1}{\pi} \ln\left[2\,\frac{(1+\sqrt{k})}{(1-\sqrt{k})}\right] \qquad for\ \frac{1}{\sqrt{2}} \le k \le 1 \tag{3.3}$$

$$\frac{K(k)}{K'(k)} = \frac{\pi}{\ln\left[2\,\frac{(1+\sqrt{k'})}{(1-\sqrt{k'})}\right]} \qquad for\ 0 \le k \le \frac{1}{\sqrt{2}} . \tag{3.4}$$

These equations have been calculated to be accurate to within 3 parts per million and are

sufficiently accurate for the purposes in this text. An approximation for the effective dielectric constant ϵ_{re} in equation (3.1), derived from the quasi-static approximation[2] is:

$$\epsilon_{re} = \frac{\epsilon_r+1}{2}\left[\tanh\{1.785\ln(\frac{h}{W})+1.75\} + \frac{kW}{h}\{.04-.7k+.01(1-.1\epsilon_r)(.25+k)\}\right] \quad . \tag{3.5}$$

This expression is accurate to better than 1.5 percent providing the following conditions apply:

$$\frac{h}{W} \gg 1 \ ; \qquad \epsilon_r \geq 9 \ ; \qquad 0 \leq k \leq 0.7 \quad . \tag{3.6}$$

Equations (3.3) and (3.4) assume infinitesimally thin metallisation conductor and ground planes. For a finite metallisation thickness, t, the above results are modified due to the change in field distributions above and within the dielectric. Firstly an effective strip spacing S_t and strip width W_t can be calculated,

$$S_t = S+d \quad , \qquad W_t = W-d \tag{3.7}$$

where

$$d = \frac{1.25t}{\pi}\left[1+\ln\left(\frac{4\pi S}{t}\right)\right] \quad . \tag{3.8}$$

Secondly, the quasi-static effective dielectric constant is modified by adding a term attributed to the metallisation thickness. This term is, in effect, caused by the change in the capacitance of the CPW.[2]

$$\epsilon_{re}^{t} = \epsilon_{re} - \frac{0.7\ (\epsilon_{re}-1)\ \frac{t}{W}}{\left[\frac{K(k)}{K'(k)} + 0.7\frac{t}{W}\right]} \tag{3.9}$$

Equation (3.1) is modified to give the quasi-static characteristic impedance Z_{cpw}^{t} of the CPW with finite metallisation thickness:

$$Z_{cpw}^{t} = \frac{30\pi}{\sqrt{\epsilon_{re}^{t}}} \frac{K'(k_e)}{K(k_e)} \quad , \tag{3.10}$$

where

$$k_e = \frac{S_t}{S_t + 2W_t} \quad . \tag{3.11}$$

The above quasi-static approximations are valid for calculating the effective dielectric and impedance of the CPW at frequencies less than a few GHz. However, full-wave analysis needs to be performed to consider the situation at higher frequencies. For this researchers have used the spectral domain technique.[3] Empirical formulae curves have been fitted to the results,[4] giving the approximation to the frequency-dependent effective dielectric constant as

$$\sqrt{\epsilon_{re}(f)} = \sqrt{\epsilon_{re}(0)} + \frac{\left[\sqrt{\epsilon_{re}(f)} - \sqrt{\epsilon_{re}(0)}\right]}{\left[1 + a\left(\frac{f}{f_{TE}}\right)^{-b}\right]} \quad , \tag{3.12}$$

where $\epsilon_{re}(0)$ is the quasi-static value (which may be corrected for metallisation thickness), f_{TE} is the cut-off frequency for the lowest order TE mode given by

$$f_{TE} = \frac{c}{4h}\sqrt{\epsilon_r - 1} \quad , \tag{3.13}$$

b = 1.8 for CPW, and a is a constant derived from

$$\ln(a) \approx v + u \ln\left(\frac{S}{W}\right) \quad . \tag{3.14}$$

The constants u and v depend on the substrate thickness h and are given by:

$$u \approx 0.54 - 0.64q + 0.015q^2 \tag{3.15}$$

and

$$v \approx 0.43 - 0.86q + 0.54q^2 \tag{3.16}$$

where

$$q = \ln\left(\frac{S}{h}\right) . \tag{3.17}$$

The closed-form approximation in equation (3.12) has been verified to be accurate to within 5 percent of the full-wave analysis values,[4] over the following range of parameters:

$$0.1 < \frac{S}{W} < 5 , \quad 0.1 < \frac{S}{h} < 5 , \quad 1.5 < \epsilon_r < 50 , \quad 0 < \frac{f}{f_{TE}} < 10 . \tag{3.18}$$

The frequency-dependent effective dielectric constant given in equation (3.12) can be substituted into equation (3.9) to give the frequency-dependent characteristic impedance.

The above equations, used in this chapter for the mask design, are further developed in *chapter 5* for modelling purposes.

3.2.2 Design equations for CPS

CPS line is complementary to CPW line; many derived terms are the same and only terms which are different are noted here. The characteristic impedance, Z_{cps}, may be written[2] as

$$Z_{cps} = \frac{120\pi}{\sqrt{\epsilon_{re}}} \frac{K(k)}{K'(k)} , \tag{3.19}$$

where ϵ_{re} and the elliptical integral terms are as previously defined (noting that W is the strip width and S the spacing between strips).

For coplanar strips, the effect of strip thickness, t, on Z_{cps} and ϵ_{re} is similar to that in

CPW, with d and k_e being given by the formulae previously stated. A modified effective dielectric constant term[2] is substituted into equation (3.19), given by

$$\epsilon'_{re} = \epsilon_{re} - \frac{1.4\ (\epsilon_{re}-1)\ \frac{t}{S}}{\left[\frac{K'(k)}{K(k)} + 1.4\frac{t}{S}\right]} \qquad (3.20)$$

The frequency-dependence of ϵ_{re} for CPS follows the equations given for CPW.

3.3 Mask design

The growth of a semiconductor wafer is described in *chapter 2*. A mask is required to fabricate a semiconductor device from a wafer by a photolithographical process. A good mask design makes efficient and effective use of available space, and typically accommodates a variety of useful features.

3.3.1 Packaging issues

Several of the device designs on the masks incorporate two sizes of CPW, large and small, with various artifacts such as tapers interlinking them. Some designs use CPS. The rationale behind some of these design features is explained.

Most microwave, millimetre-wave, and high-speed optoelectronic devices are packaged with coaxial transmission lines, the main advantages of which are ruggedness combined with flexibility, repeatability of connection, and low insertion loss. Examples of these connectors include (with maximum working frequencies in brackets): Wiltron "K" (46 GHz) and "V" (64 GHz); and Hewlett-Packard "3.5 mm" (32 GHz) and "2.4 mm" (50 GHz). The larger dimension CPW is designed to interface with the Wiltron "V" connector.

Test fixtures are commercially available to connect planar lines (microstrip and CPW) with coaxial lines by means of appropriate transitions. Most current GaAs devices at NPL are connected to coax by a test-fixture (UTF),[1] with jaws weakened to decrease chance of device damage. The characteristic impedance of the CPW is designed to be 50 Ω, reducing the reflections from the interface with the 50 Ω coaxial lines. Ideally the ratio of central-line-width to ground-plane-gap should be maintained across the coax-planar transition, to minimize the excitation of spurious modes. This is not possible with GaAs CPW line and air-spaced "V" coax connector. It was decided to match the inner dimensions, i.e. the central line width of the CPW and the diameter of the V connector step contact pin. Such a design defines the dimensions of the large GaAs CPW for mounting in the UTF.

A smaller dimension GaAs CPW is better for fast pulse generation, propagation and measurement. The illumination of a photoconductive gap has a constant average optical power independent of the gap size, and therefore the same number of photons and hence excited electron-hole pairs are generated independent of that size. A larger gap would reduce the electric field, resulting in smaller velocities for constant mobilities. Therefore, not only the responsivity of the photoconductor device, but the speed of response of the switch is reduced with a larger gap.

Usually there is a length of CPW between the excitation and measurement points, and therefore the temporal response of the photoconductive switch as measured by electro-optic or photoconductive sampling also depends on the CPW. The cut-off frequency of the TE_1 surface mode increases with smaller dimension transmission lines and therefore smaller lines have less effect on the propagation of fast pulses. A smaller line also increases the electric field and therefore increases the signal-to-noise of electro-optic measurements across a gap.

Therefore, to maintain the temporal resolution of such a system and improve the signal-to-noise ratio the CPW line devised for the pulse generation had a smaller design width

---

[1] Wiltron Universal Test Fixture UTF 3680V

than the CPW required to provide a good match to coax.

Equations (3.1)-(3.5) in *section 3.2.1* were used to calculate the quasi-static design impedance for the small and large CPW lines. The correction due to a metallisation thickness of 0.6 μm was calculated from equation (3.9) to be small. The drop in impedance of the lines with increasing frequency was also assessed according to equation (3.12), and the size of the change found to be strongly dependent on the line dimensions, with the impedance of the large CPW decreasing significantly at higher frequencies. Table 3.1 summarizes the information.

Table 3.1 Frequency-dependent effect of line size and metal thickness on impedance.

	Characteristic Design Impedance [Ω]				
	Quasi-static (no metallisation correction)	Quasi-static (metallisation correction)	30 GHz	120 GHz	500 GHz
Large CPW	49.67	49.72	47.88	40.31	36.09
Small CPW	50.18	50.58	50.57	50.52	49.94

3.3.2 Taper

Tapers were used to join the larger and smaller CPW lines. Well documented techniques exist to match two different impedance microstrip lines by tapering.[7] However, little prior work has been performed to optimise the transition between two similar-impedance CPW lines with differing dimensions. Some analysis has been performed in the context of coplanar probes.[8] A simple intuitive approach was employed to solve the problem. It is

recognised that a full-wave solution to the problem may be of greater benefit, but time has prevented the attempt of such a solution.

Several possibilities exist to alter the CPW dimensions whilst maintaining constant impedance. The simplest technique is to introduce linear changes of slot and central line width. At any point within such a taper the impedance is constant. A more refined approach was, however, developed. The rate of change of slot and central line width (with propagation distance) was maintained along the length of the taper, by employing an exponential fit. To avoid sharp edges at the taper extremities, rounded edges were included. It is believed the reflection given by a fast pulse propagating along such a taper is reduced. Figure 3.3 shows the central line section of the taper, from the small CPW to the large CPW line (not to scale).

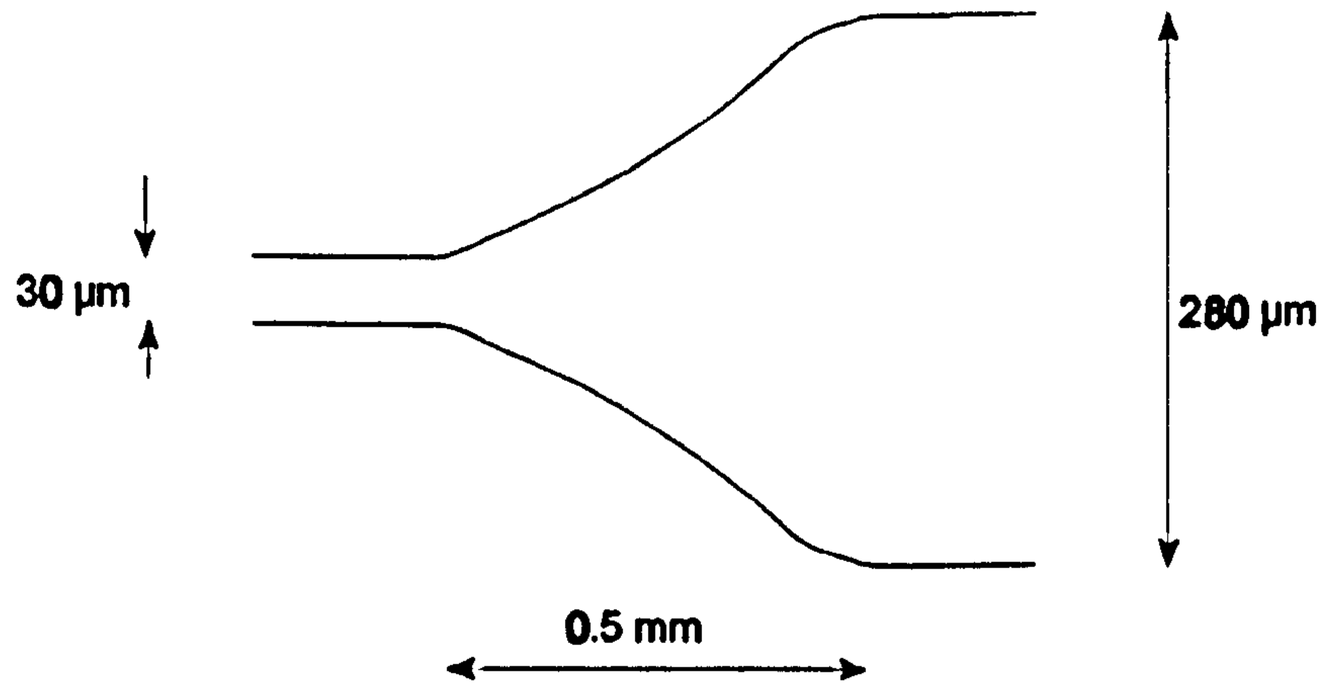

Figure 3.3 Central line taper from small to large CPW.

3.3.3 Example of devices - design A

An example of the design of a device - denoted as device "A" - is shown in Figure 3.4. This shows more clearly the tapers between the differing size CPW lines (large-small-large). The small CPW has central conductor width W=30 µm and slot width S=21 µm, with 3 mm wide ground planes. The large CPW has W=280 µm and S=175 µm, with outer dimensions of the ground plane continuous with those of the small CPW.

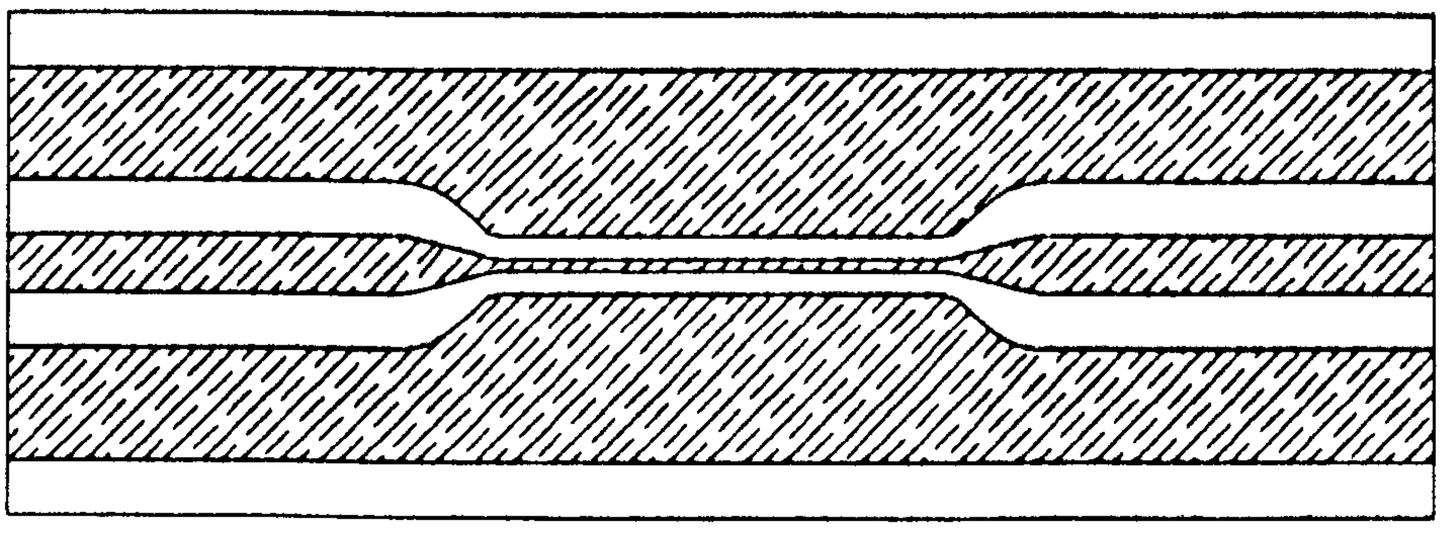

Figure 3.4 Device A with tapers.

3.3.4 Features on a mask

An example of a mask is shown in Figure 3.5. The mask has been split into nine squares of equal size, labelled A to I. On the scale shown, some of the mask details, such as the small CPW lines, are not visible. The dark represents area where device metallisation is required. The squares and triangles are reference marks for alignment.

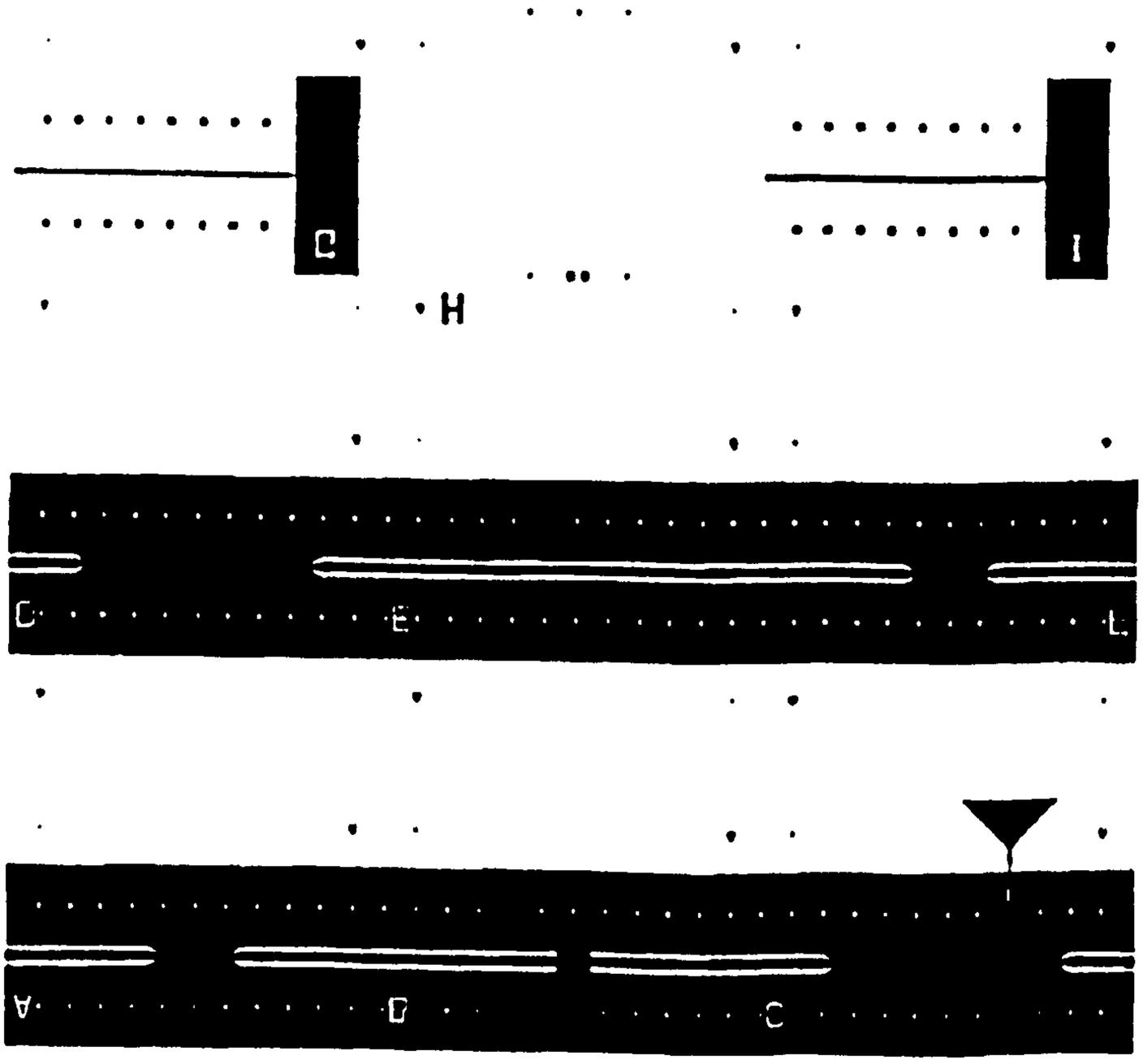

Figure 3.5 Example of features on NPL-designed mask.

Device design A has been previously discussed. (The resolution of the figure is insufficient to show the small CPW detail. The reader is referred back to Figure 3.4 for a clearer diagram of design A.) Design D is similar, but with a longer length (7 mm) of small CPW between the large CPW than device A (2 mm). Both A and D are through-line designs to enable sliding contact devices[5] to be fabricated. Design F is similar to that of A, but with the addition of a 20 μm gap in the central line, allowing Auston switch devices[6] to be produced. Designs B (short) and E (large CPW through-line) are to enable the fabrication of devices for network analysis calibration artifacts. Design C is similar to D, but with the addition of a finger interrupting one of the ground planes. This design was included to enable the fabrication of photoconductive sampling devices. Finally designs G and I consist of CPS lines, with contacting pads on one end, and design H allows resistor/shorts to be incorporated into the previously discussed designs.

3.4 Device fabrication

Devices were fabricated in class 100 or better clean rooms, using photolithographical techniques. Initial devices were fabricated at UCL with later devices made at a new NPL facility. There were slight differences between the systems used in each clean room, and, to a certain extent, processing techniques generally evolved, but the differences are minor and are generally not recorded here. To aid device development and characterisation, some semi-insulating (S.I.) GaAs and n+ doped GaAs were processed alongside the LT-GaAs substrates.

Care was taken to ensure the dimensions of the metallisation lines were close to the design, as deviations affect the impedance of the devices. Errors resulting from incorrect dimensions are discussed in *chapter 5*.

Each wafer was first inscribed with a diamond blade and cleaved into suitable sizes. The substrate was heated in trichloroethylene for five minutes, followed by a clean in acetone and methanol. Filtered Shipley Microposit S1400/31 photoresist was spun onto the

substrates at a speed of 4500 rpm for one minute[2], and the resist soft-baked for 20 minutes (85 ^{o}C), removing the majority of solvent and resulting in typical resist thicknesses of 0.6 μm. The required feature on the mask, cleaned in acetone, isopropanol and water, was aligned over the substrate and contacted with a vacuum seal.

Areas not covered by the mask were exposed to UV light for 8 seconds. The high energy photons cause chemical changes to the photo-active component of the positive resist, forming molecules which are soluble in developer. The substrate was then soaked in chlorobenzene for 10 minutes, to desensitize the top layer of resist. This facilitates good lift-off by the formation of an undercut. After a five minute soft-bake, the substrate was developed for 35 seconds in a 1:2 mix of "351" developer:deionised water, and then soaked in hydrochloric acid for 30 seconds to aid adhesion of the metallisation, by removing oxide formations on the top surface. At this stage each substrate was examined under a microscope to ensure that the pattern developed on the resist was well-defined and well-resolved.

The substrate was then loaded into an evaporator, and the chamber pumped with a diffusion pump down to pressures typically less than 2 x 10^{-6} mbar. Boats containing different pure metals were then heated to several hundred degrees, in order of deposition, to evaporate multi-layers of thin-film metallisation onto the substrate. The thickness of each metal deposit was measured *in situ* with a thin-film monitor, which had been previously calibrated. Two structures of metallisation layers were used: tin /gold (Sn/Au) and nickel-gold-germanium /gold /silver /gold (NiAuGe/Au/Ag/Au).

After cooling, the substrate was soaked in acetone. The areas of metallisation deposited on top of unexposed resist were not affected. The rest of the metallisation lifted off, with careful agitation, as the exposed (softened) resist underneath dissolved in the solvent. The formation of the undercut edge profile aided this process by producing breaks between the metal required to lift-off and that required to adhere. The need for forceful lift-off, with the subsequent risk of tearing and damaging the device metallisation, was therefore

---

[2] These conditions were varied slightly for optimum lift-off.

reduced. If successful, the resultant device consisted of a well-defined and adhered metallisation pattern on the substrate with similar line dimensions to those designed on the mask.

Two further fabrication processes were used for some of the devices: wet etching and annealing. The wafers had thin n+ GaAs layers grown on top of the LT-GaAs layers. The thin layers absorb photons with energy near to the GaAs band-gap, reducing device efficiency. More importantly, the very low resistivity of the n+ layer, compared with both the LT-GaAs region and the bulk substrate, increases the background current of a device and decreases device responsivity. Therefore a wet etch was used to remove the n+ layer from those areas of the device not covered by metallisation.

The etch consisted of a weak solution of ammonium hydroxide (NH_3OH) and hydrogen peroxide (H_2O_2). Initially the etch was applied after a second photolithographical process, with resist covering the metal definition before etching. It was, however, later found that metal alone acted as an excellent barrier to the etchant, easing considerably the processing stages. A mixture of 3:1:996 of NH_3OH:H_2O_2:H_2O was sufficient to etch through 100 nm of GaAs in 30 seconds. This thickness, larger than the n+ layer (5-10 nm), was chosen to allow a generous margin of error in the process without significantly reducing the available LT-GaAs absorption depth.

Annealing is a process of heating, usually in an inert atmosphere, to temperatures of typically a few hundred degrees for a given period of time. For this application, the annealing of a semiconductor device can increase the hardness of the metallisation, and, more importantly, can reduce the electrical contact resistance between the top metallisation layer and the semiconductor, forming a contact less rectifying and more ohmic. The ideal anneal is one where the temperature is raised as quickly as possible to the maximum. UCL are developing rapid thermal anneal apparatus to meet this requirement, but it was not available for use during the period of this thesis. Some initial devices were, however, annealed at UCL using their existing facility. Typically this consisted of a slow ramp up to 450 ^{o}C, and an anneal of two minutes under a nitrogen

atmosphere, although the effect of decreasing both parameters was investigated. The effect of the anneal is discussed in *section 3.5*.

Two additional stages were found to be necessary to complete the device fabrication. Uneven photoresist thicknesses were produced at the extremities of square substrates during the spinning, affecting the adhesion and metallisation lift-off at the edges of devices, and sometimes producing broken metal. In some cases, imperfections in the cleaving of the substrates were also present. Therefore the edges of devices were trimmed to facilitate contacting to the UTF. A straight GaAs edge was produced using a wafer saw[3]. The saw blade type and cutting parameters were optimised to cut the GaAs without tearing the metallisation.

Devices were mounted on a fused quartz carrier, as otherwise the GaAs was prone to break in the jaws of the UTF. Fused quartz has a dielectric constant considerably lower than GaAs. It is, therefore, recognised that electrical reflections, from the LT-GaAs generation surface to the carrier-GaAs interface and returning to the metallisation, might be present. Reflections can be reduced if the difference in dielectric constants between the carrier and GaAs is reduced. A higher dielectric material, such as sapphire, is preferable to maintain the optical properties if bottom illumination of the device is required. Electrical reflections from the bottom of the carrier-air interface (or indeed from the GaAs-air interface with no carrier) can be suppressed with microwave absorbing material.

Table 3.2 lists the main devices fabricated to date, in chronological order. Each device has been assigned an identification (I.D.) code, which is referred to throughout the rest of this text. (I.D. prefixes "TL" are short for transmission lines (SI-GaAs) and prefixes "PG" short for pulse generators (LT-GaAs)). The resulting electrical characteristics of these devices are described in the next section.

---

[3] Loadpoint wafer saw fitted with blade 1245.

Table 3.2 Summary of important devices.

Device I.D.	Device Type	Substrate	Metallisation (top layer down)		Length mm	Etch	Anneal
PG1,2	D,F	LT - GaAs	Au Sn	200 nm 20 nm	10.2	Yes	450 °C 2 mins
TL1	D	n+ GaAs	Au Ag Au NiAuGe	130 nm 100 nm 40 nm 30 nm	11.8	No	No
TL2	D	n+ GaAs	Au Ag Au NiAuGe	130 nm 100 nm 40 nm 30 nm	11.8	No	450 °C 2 mins
TL3	D	S.I. GaAs	Au Ag Au NiAuGe	200 nm 100 nm 40 nm 30 nm	12.1	No	450 °C 2 mins
TL4	D	S.I. GaAs	Au Ag Au NiAuGe	200 nm 100 nm 40 nm 30 nm	12.5	No	No
PG3	D	LT - GaAs	Au Ag Au NiAuGe	230 nm 100 nm 40 nm 30 nm	12.0	Yes	450 °C 2 mins
TL5	D	S.I. GaAs	Au Ag Au NiAuGe	120 nm 200 nm 40 nm 30 nm	12.0	No	360 °C 1 min
TL6	A	S.I. GaAs	Au Ag Au NiAuGe	120 nm 200 nm 40 nm 30 nm	12.1	No	400 °C 1 min
TL7	A	S.I. GaAs	Au Ag Au NiAuGe	150 nm 150 nm 40 nm 30 nm	11.8	No	No
PG4	A	LT - GaAs	Au Ag Au NiAuGe	50 nm 150 nm 40 nm 30 nm	11.0	Yes	No
PG5	A	LT - GaAs	Au Ag Au NiAuGe	330 nm 140 nm 70 nm 60 nm	8.2	No	No
PG6	F	I.T - GaAs	Au Ag Au NiAuGe	360 nm 120 nm 60 nm 60 nm	11.2	No	No
PG7	F	LT - GaAs	Au Ag Au NiAuGe	330 nm 140 nm 40 nm 60 nm	6.2	No	No
PG8	G	LT - GaAs	Au Ag Au NiAuGe	330 nm 140 nm 40 nm 60 nm	7.0	No	No

3.5 D.C. and low frequency measurements

The surface conductivity of the metallisation and the metal-semiconductor contact resistance are two parameters important for good photoconductive device performance. The conductivity was measured with a d.c. digital volt meter (DVM) by two methods. The first method, which involved contacting the metallisation surface with probes,[4] was found to be imprecise due to the lack of repeatability of the connections, especially as the sharp probes degraded the surface finish of the conductor. The method did, however, enable the measurement of both central line and ground planes of CPWs, and was more suitable for non-continuous lines ("F" type devices). The second method involved using the UTF V pins for contacting the CPW. This method depended on good positioning of the contact pins - which was found to be quite repeatable. The disadvantage was that only continuous central lines of the CPW could be measured.

Table 3.3 Measured device resistances and derived metallisation resistivities.

Device I.D.	Measured d.c. resistance [Ω]	Calculated resistivity ρ [10^{-8} Ωm]
PG1	420	36
TL1	43 *	-
TL2	< 1 *	-
TL3	128	16.9
TL4	25	3.5
PG3	80	12.8
TL5	80	12.3
TL6	40	14.9
TL7	11	3.7
PG4	14	3.4
PG5	8	4.9

[4] Wiltron UTF model 36803 bias probes

Table 3.3 shows the measured d.c. central line resistance for some of the devices specified in the previous table. From these resistances, using the measured line lengths, widths and evaporation thicknesses, the resistivity values were calculated. For this purpose the exponential tapers were approximated by assuming linear changes in line dimension. The resistivity values and the significance of the n+ GaAs measurements (marked *) are discussed after the metallurgical structures are explained.

The first device, PG1, used the Sn/Au metallisation structure. Au is the ideal metal to use as a transmission line, due to its high electrical conductivity and relative chemical inertness. However, Au does not adhere directly to GaAs (or indeed any substrate) very readily, but does adhere well to previously-deposited metals, such as Sn and Cr, if a good vacuum is maintained during the evaporation process. Sn also adheres well to GaAs and, for thin layers, does not have electrical characteristics too detrimental to overall device performance. Sn is, therefore, ideal to deposit prior to thicker layers of Au. Annealed Sn/Au is also expected to result in an adequate ohmic contact.

It was, however, found that annealed device PG1, containing 10 % Sn, had a measured resistance 12 times higher than that of Au. This agrees with Williams[9], who showed that a mere 1 % of Sn impurity, when annealed with Au, increases the conductor resistivity by 2.5 times. Such a high central line resistance of 420 Ω, when compared with the transmission line design impedance of 50 Ω, affects the ability of the line to propagate short electrical pulses. This can be seen in *chapter 4*. To attempt to overcome this severe loss of conductivity and improve the ohmic contact, a NiAuGe/Au/Ag/Au structure was deposited for further devices. The reasoning behind the fabrication of this, at first sight complex, structure is described.

When a group IV donor impurity is allowed to diffuse into n+ type GaAs by annealing, the heavily doped region created under the metal allows electrons to tunnel through the metal-semiconductor barrier, producing a good ohmic contact on GaAs. For example, both Ge and Si act as donors only when occupying Ga sites. A method of creating the

proper Ga vacancies in the underlying GaAs substrate is to include in the contact metallurgy an element highly reactive with Ga, e.g. Au. Ni is further added to the AuGe alloy to act as a wetting agent, as well as facilitating the diffusivity of Ge into the GaAs.[10] Hence the first metal deposited is the eutectic alloy NiAuGe.

When a NiAuGe alloy is annealed to n+ GaAs, an ohmic contact is usually formed. However, the conductivity of the metallisation is very poor. Depositing a much thicker layer of Au onto the NiAuGe improves the conductivity, but the deposition must be done before the anneal. As with the Sn/Au system, the anneal causes impurity levels of only a few percent to diffuse into the top Au layer, and vice-versa, causing the overall conductivity to be many times lower than that of pure Au. Researchers have found[11] that the presence of Ag, acting as a diffusion barrier between the NiAuGe and Au, results in improved conductivity. The Ag maintains a low contact resistance by minimising the diffusion. Adhesion of the Ag directly onto the NiAuGe is poor, and hence a further thin layer of Au is added, resulting in the overall metallurgy system of NiAuGe/Au/Ag/Au. This system has produced reliable devices with adequate yield.

In light of the above, four points are concluded from the resistivity values in Table 3.3:

i) The line resistivity for the NiAuGe-based structure (PG3) has improved by almost a factor of three compared to the Sn/Au structure (PG1).

ii) The effect of annealing, even at lower temperatures than usual, on the resistivity of SI-GaAs lines is significant:

450 °C anneal (TL3), $\rho = 16.9 \times 10^{-8}$ Ωm

400 °C anneal (TL6), $\rho = 14.9 \times 10^{-8}$ Ωm

360 °C anneal (TL5), $\rho = 12.3 \times 10^{-8}$ Ωm

no anneal (TL4), $\rho = 3.5 \times 10^{-8}$ Ωm.

iii) Annealed LT-GaAs (PG3) has a lower resistivity than annealed SI-GaAs (TL3).

iv) The resistivity of the unannealed devices range between $\rho = 3.4 \times 10^{-8}$ Ωm and 4.9×10^{-8} Ωm.

It should be noted that whilst the above values were derived from the measured

resistances, the effect of different metallisation layers was not taken into account. Further measurements also showed that the product of the line resistance and the metallisation thickness was not constant.

The second parameter of interest is the contact resistance. A mask with standard patterns[9] - enabling test devices to be processed and the contact resistance of the metal-semiconductor interface to be measured directly - was not designed and procured. Instead a transistor-curve tracer[5], operating at 50 Hz, was used to assess the relative contact characteristics of each device by measuring the current-voltage (I-V) curves. Each measurement was performed across the ground-plane to central pin UTF coax connection, with the CPW test device held in the UTF. Figure 3.6 shows a schematic of the arrangement, with dotted lines representing the contacts. Because the bias across the two metal-semiconductor junctions was opposite, the two contacts were measured back-to-back. Some of the measurements displayed two curves slightly offset from each other. This was thought to be due to capacitive and inductive parasitics at 50 Hz and the average value can be assumed.

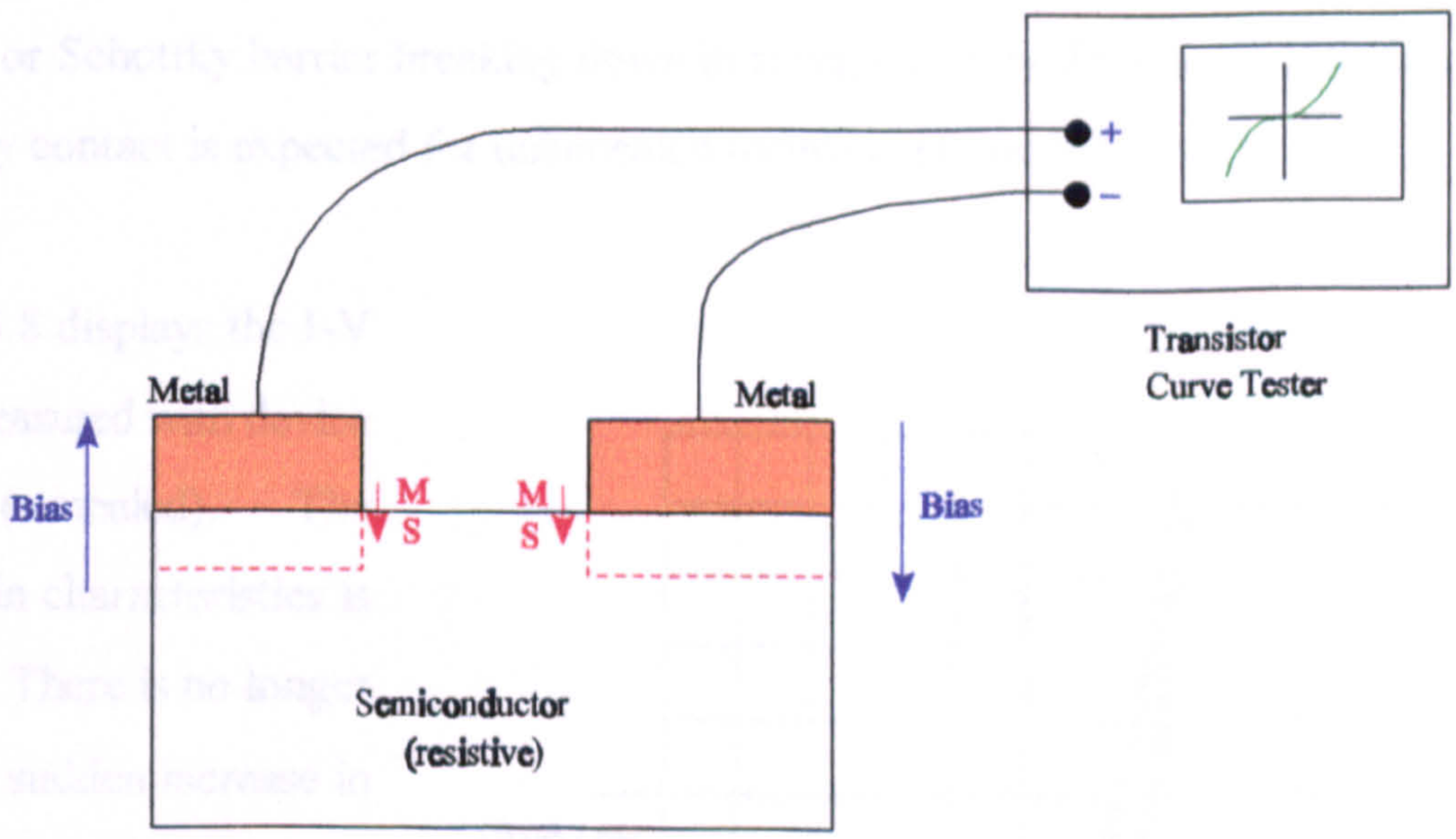

Figure 3.6 Schematic of I-V contact measurements.

The interpretation of the following results is not conclusive. The origin for the three

[5] Tektronix type 575 Transistor Curve Tracer.

curves that follow is at the bottom left of the figures. All three devices showed similar I-V behaviour with the polarity reversed. The Sn/Au system is not here investigated.

The NiAuGe alloy was first deposited on S.I. GaAs. Figure 3.7 shows the I-V curve measured for device TL4 (not annealed). It can be seen that a small current, less than 5 μA, is initially recorded until a point around 50 V is reached, after which the current suddenly increases at a very rapid rate. Since the curve shows the measurement of two contacts back-to-back, the result can be interpreted as typical behaviour of a blocking contact or Schottky barrier breaking down in reverse bias by thermionic emission.[12] A Schottky contact is expected for unannealed metallisation on S.I. GaAs.

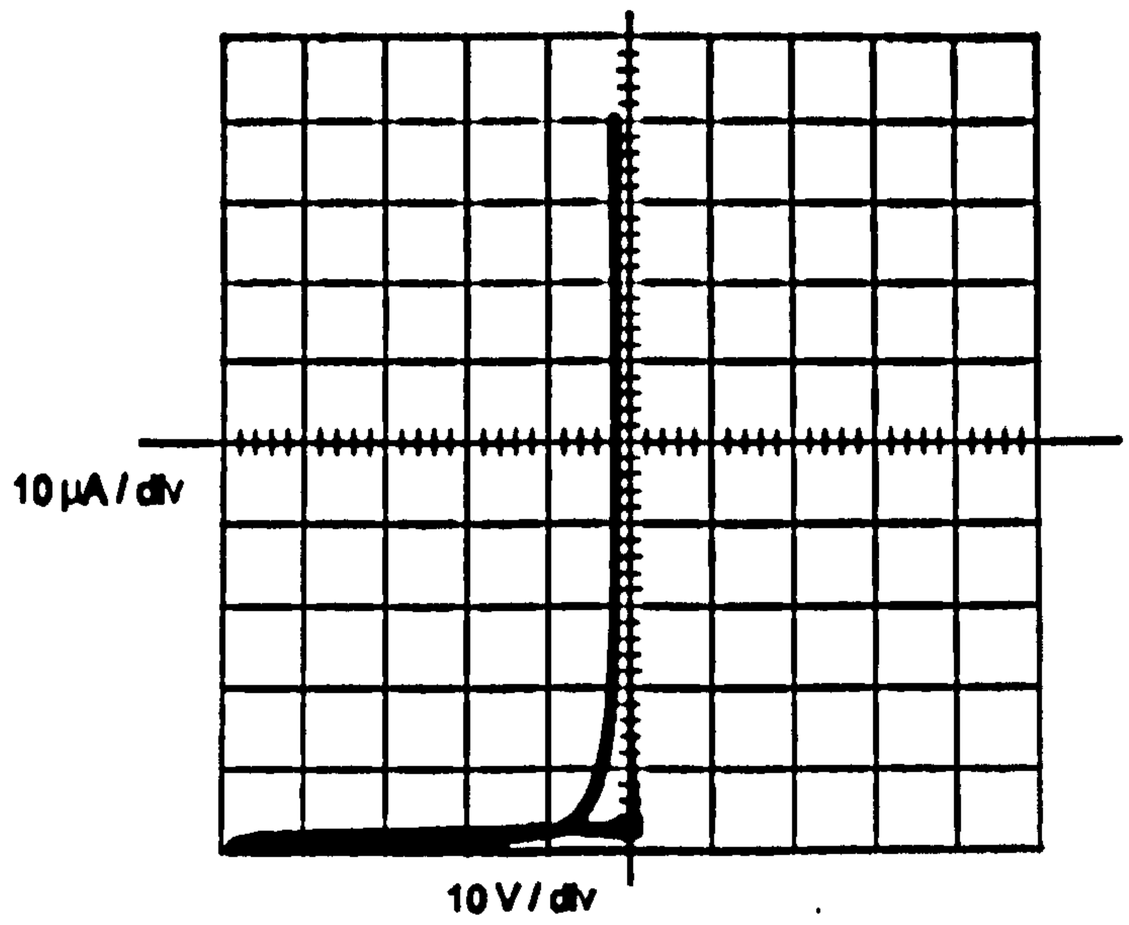

Figure 3.7 I-V curve of unannealed S.I. GaAs device TL4.

Figure 3.8 displays the I-V curve measured with device TL5 (annealed). The change in characteristics is marked. There is no longer a sharp, sudden increase in current with voltage. Instead the rate of change of current (with voltage) increases steadily with increasing voltage. At

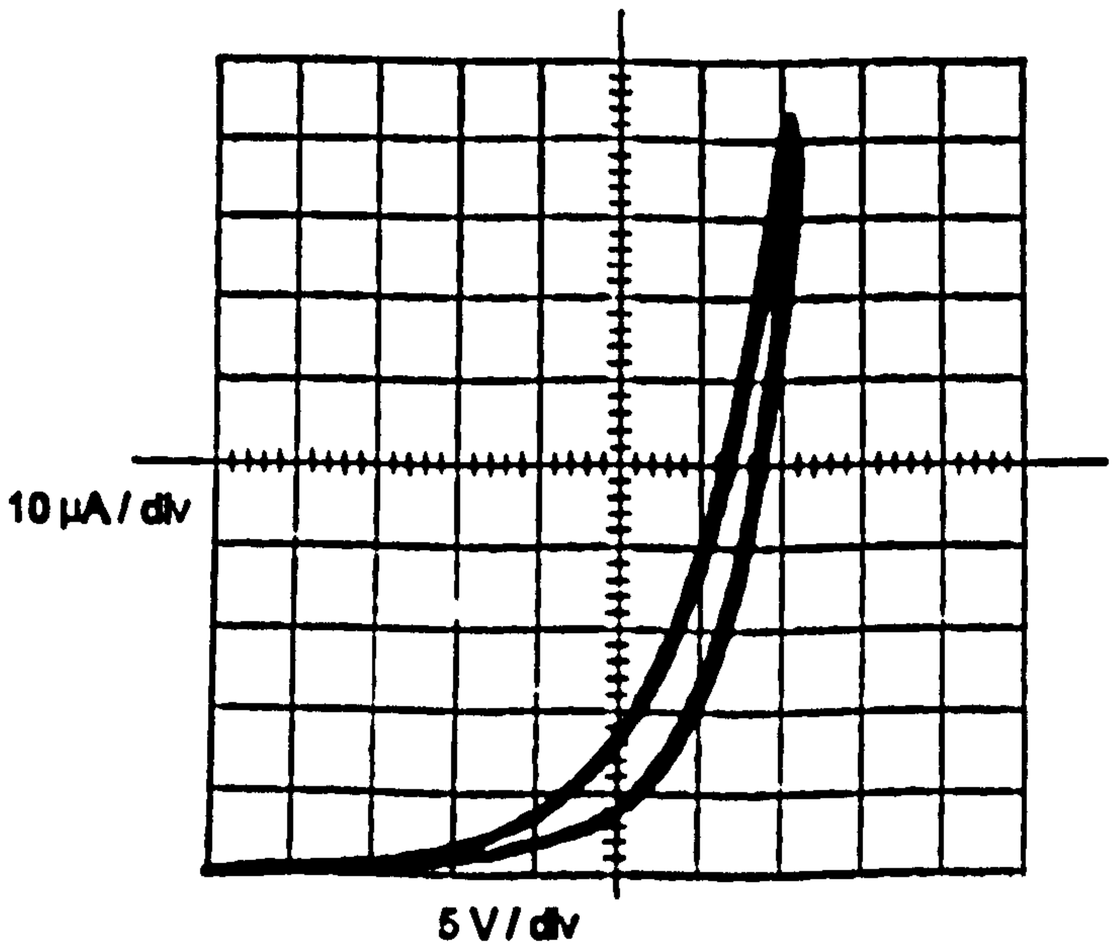

Figure 3.8 I-V curve of annealed S.I. GaAs device TL5.

around 35 V, the increase is very steep. The ideal ohmic contact would be one where the rate of change were constant. Therefore this contact can be interpreted as being closer to ohmic than the unannealed device, but far from ideal, as this would require significant doping of the surface GaAs.

The results so far indicate that annealing affects the contact interface, as well as affecting the line conductivity. Figure 3.9 shows the I-V curve measured for LT-GaAs device PG4 (not annealed). The rate of change of current (with voltage) increases slowly with increasing voltage up to the displayed value of 35 V.

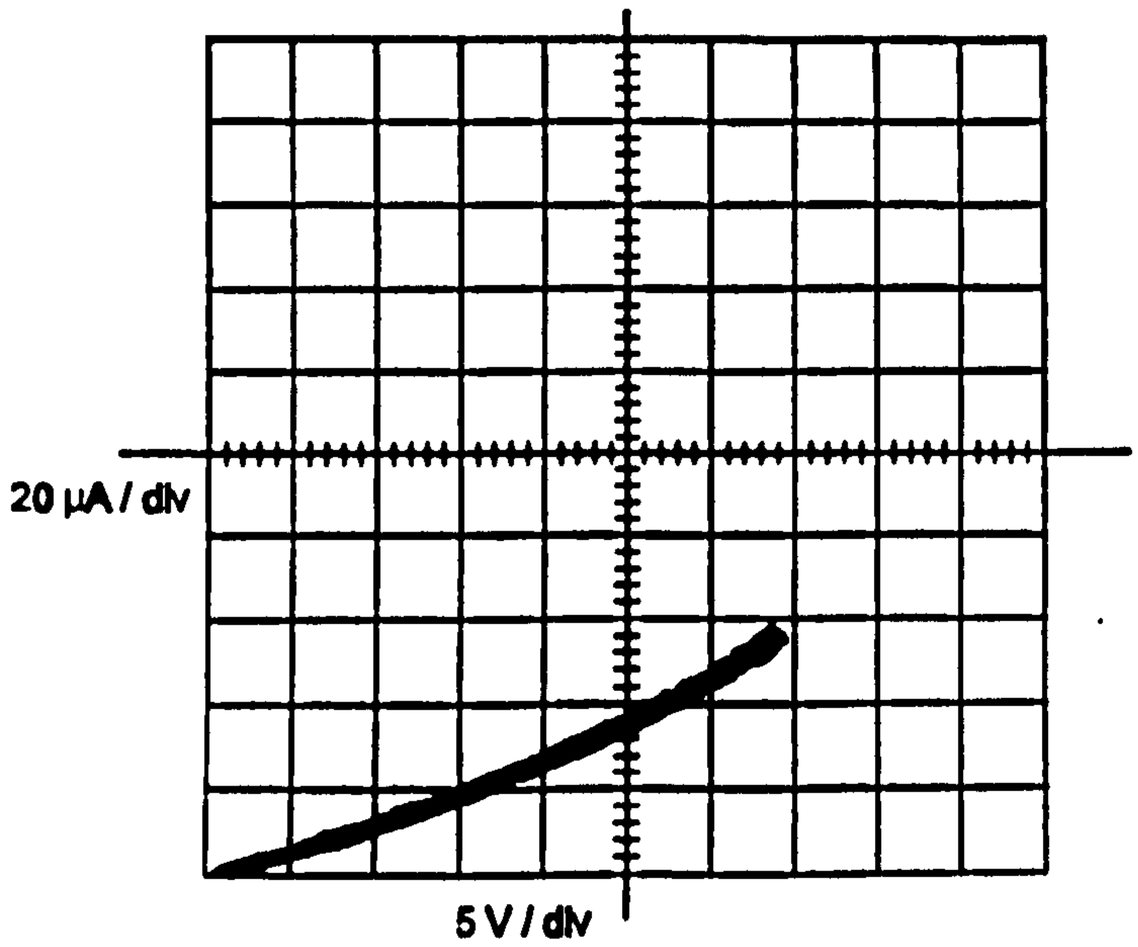

Figure 3.9 I-V curve of unannealed LT-GaAs device PG4.

Although not shown, the rate of change maintained a steady increase above this value, resulting in a current of around 150 µA at 50 V. The I-V characteristic of this device is not too dissimilar to that of TL5, with the current higher in general, and showing a slower rate of change than for TL5. It is suggested that this contact is closer to being ohmic and that the higher current compared to the S.I. GaAs is due to the lower resistivity of the LT-GaAs compared to the S.I. GaAs.

As the I-V curves of the annealed S.I. GaAs and unannealed LT-GaAs are not drastically different, it was concluded that an anneal of LT-GaAs was not essential to produce a reasonable contact. The detrimental effect of annealing on line conductivity is therefore avoided with devices such as PG4 and PG5.

Some LT-GaAs devices were, however, annealed (e.g. PG3). The resulting I-V curves are not shown, but did, in general, display further progress towards the ideal ohmic contact.

A further insight into the effect of the anneal on the metallisation-semiconductor contact can be obtained from the measurement of n+ GaAs devices. The resistances of devices TL1 (unannealed) and TL2 (annealed) were measured using both the probe and UTF contact pin methods. The values obtained along the full length of the central line are those quoted in Table 3.3 (see *). By positioning the probes at locations along the line, it was ascertained that the resistance of the contacts measured through the substrate was less than the resistance along the central line conductor.

As the bulk substrate is highly conductive, then d.c. resistance measurements across any two points of metallisation can provide the resistance of two back-to-back contacts. The probes were contacted across the CPW slots, between the central line conductor and ground planes. Similar values for the two contacts were obtained in this geometry as they were along the line, with the resistance decreasing from 43 Ω to less than 1 Ω with an anneal.

3.6 Conclusions

The theory of coplanar lines has been discussed and the design equations for CPW and CPS lines summarised. Criteria were described which enabled dimensions of transmission lines for photoconductive switches mounted in commercial test-fixtures to be chosen. A photolithographical mask was procured, with CPW-based designs, consisting of small and large CPW lines interlinked by tapers, and CPS-based designs.

The fabrication of GaAs devices in a clean-room was described and a summary given of the important devices made to date. Current-voltage characteristics of different devices was explored and it was concluded that an adequate ohmic contact was produced with unannealed metallisation on LT-GaAs.

3.7 References to Chapter 3

1 C.P.Wen, "Coplanar Waveguide: A Surface Strip Transmission Line suitable for Non-Reciprocal Gyromagnetic Device Application", IEEE Trans. Vol. MTT-17, Dec 1969, pp 1087-1090.

2 K.C.Gupta, R.Garg and I.J.Bahl, "Microstrip Lines and Slotlines", Artech House Inc. Publishing, chapter 7, 1979.

3 J.B.Knorr and K.D.Kuchler, "Analysis of Coupled Slots and Coplanar Strips on Dielectric Substrate", IEEE Trans. Vol. MTT-23, 1975, pp 74-80.

4 G.Hasnain, A.Dienes and J.R.Whinnery, "Dispersion of Picosecond Pulses in Coplanar Transmission Lines", IEEE Trans. Vol. MTT-34, No.6, June 1986, pp 738-741.

5 D.Grischkowsky, I.N.Duling, J.C.Chen and C.C.Chi, "Electromagnetic Shock Waves from Transmission Lines", Phy. Review Lett., APS Vol.59, No.15, 1987, pp 1663-1666.

6 C.H.Lee, A.Antonetti and G.A.Mourou,"Measurements on the Photoconductive Lifetimes of Carriers in GaAs by Optoelectronic Gating Techniques", Optic Comm., Vol. 21, 1977, pp 158-161.

7 K.N.S.Rao and S.P.Kosta, "On Tapered Microstrip Transmission lines", A.E.U., Vol. 1, 1974, pp 34-36.

8 N.Mathukrishnan and S.M.Riad, "A Thick-film Coplanar Probe for Time Domain Measurements", IEEE Transactions Vol. CHMT-12, No.2, June 1989, pp 297-302.

9 R.E.Williams, "Gallium Arsenide Processing Techniques", Artech House Publishing Inc., chapters 2, 6, & 11, 1984.

10 W.T.Anderson, A.Christou and J.Davey, "Development of Ohmic Contacts for GaAs Devices using Ge Epitaxial Ge Films", IEEE J.Solid State Circuits, SC-13, No.4, Aug 1978, pp 430-435.

11 C.S.Wu, K.K.Yu and H.Kanber, "Optimisation of Ohmic Contacts for Reliable Heterostructure GaAs Materials", J. Elect. Materials, Vol. 19, No. 11, 1990, pp 1265-1271.

12 S.M.Sze, "Semiconductor Devices: Physics and Technology", John Wiley & Son, chapter 5, 1985.

4 SAMPLING OSCILLOSCOPE AND ELECTRO-OPTIC SAMPLING MEASUREMENTS

4.1 Introduction

The previous chapter describes the design, fabrication and initial electrical testing of photoconductive switches. This chapter describes optoelectronic measurements of photoconductive switches. The key issue in this chapter is to explore whether the response of a LT-GaAs pulse generator is short enough for the metrological application.

Three photoconductive excitation configurations are first described. The theory of electro-optic sampling (EOS)[1] is discussed. The first batch of LT-GaAs devices (Sn/Au metallurgy) were excited with a dye laser system and measured using a sampling oscilloscope. The results indicated a short response time. The EOS scheme was therefore used to measure the devices, as the temporal resolution of the EOS is better than that of the sampling oscilloscope.

The laser system was upgraded to a titanium-sapphire (Ti:sapphire) laser and measurements were made on later photoconductive devices (AuGeNi/Au/Ag/Au metallurgy). The results obtained with each laser are described separately for CRO and EOS measurements. As the Ti:sapphire system superseded the dye system (the latter only being used for initial measurements), the Ti:sapphire results are explored in more detail. The discussion at the end of the chapter concentrates on the limitations and uncertainties in the EOS measurements and what can be ascertained about the LT-GaAs response. Uncertainties in CRO measurements are addressed in *chapter 6*.

4.2 Photoconductive switch configurations

Three photoconductive switch configurations are described: the Coplanar Waveguide (CPW) sliding contact; the CPW Auston switch; and the Coplanar Stripline (CPS) sliding

contact. The two CPW configurations enable a sampling oscilloscope to be connected via a CPW-coax transition, and are therefore important if the switch is to be used as a pulse generator test source for an oscilloscope. The CPS enables better characterisation of the LT-GaAs. All three configurations show the EOS measurement system with an external probe (discussed in the EOS theory).

4.2.1 CPW sliding contact

The CPW sliding contact configuration[2] is shown in Figure 4.1. The sliding contact is a distributed detector - the position of optical illumination (the excitation beam) can be moved along the line.

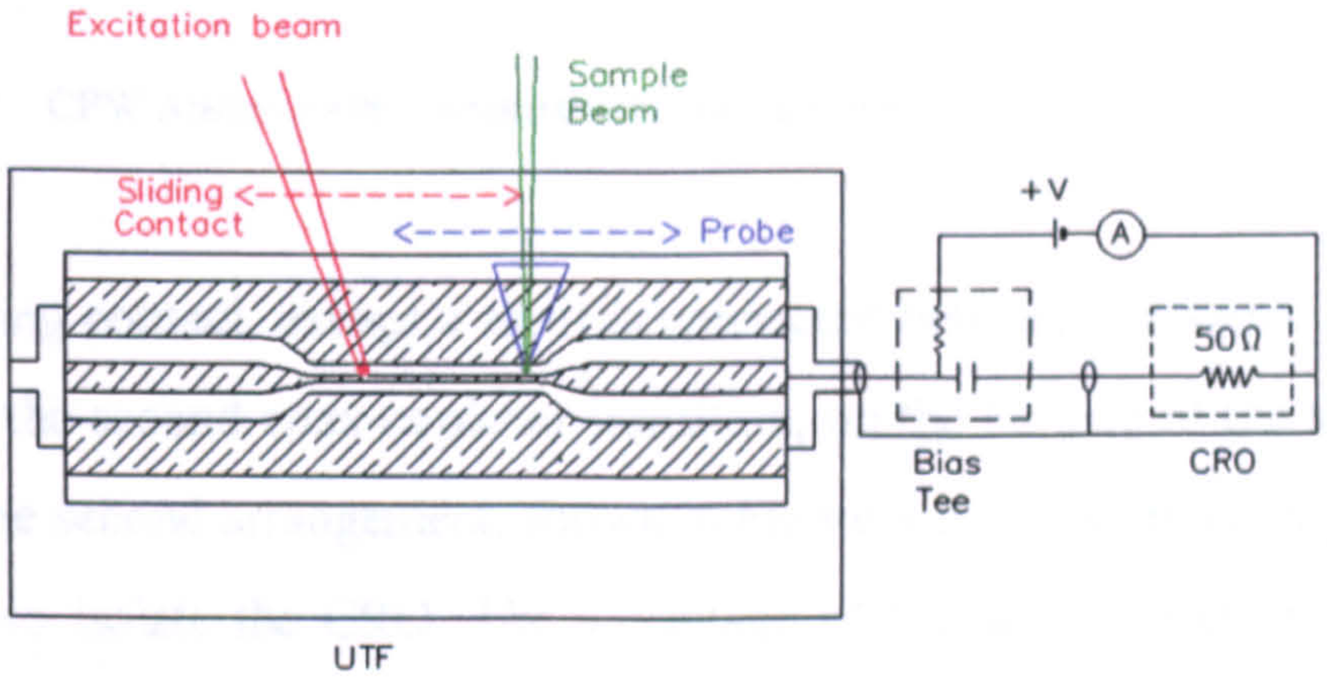

Figure 4.1 CPW sliding contact measurement configuration.

For EOS measurements the sampling position can also be varied with an external probe. The electrical biasing arrangement is also shown. The capacitor in the bias tee provides a fast path for current to the CRO whilst maintaining d.c. isolation to the CRO.

4.2.2 CPW Auston switch

The CPW Auston switch configuration[3] is presented in Figure 4.2. The addition of a gap in the central line of the CPW is analogous to the original Auston gap in a microstrip line. The gap defines the point to be illuminated by the excitation beam, and is fixed.
Two possible biasing arrangements may be used. The first arrangement is similar to that

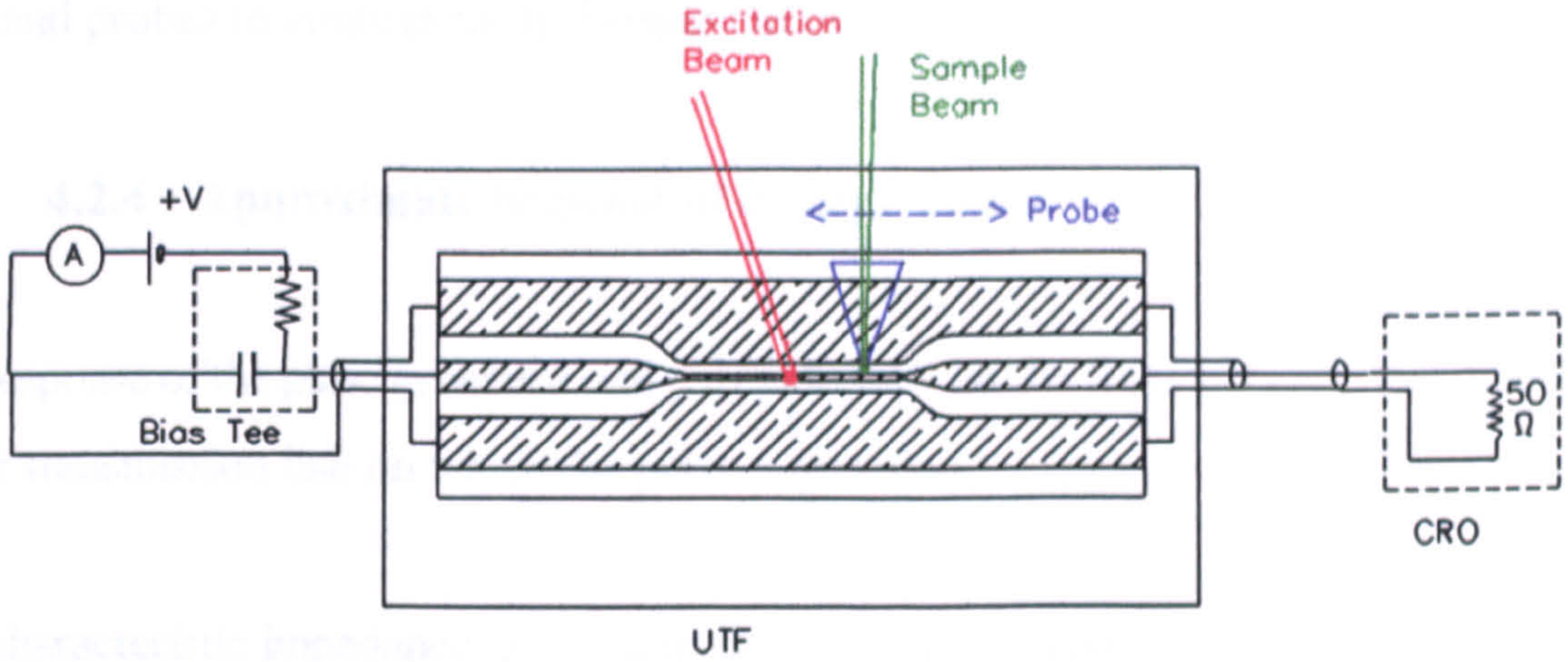

Figure 4.2 CPW Auston switch measurement configuration.

used for the CPW sliding contact, except a short is connected between the signal and ground contacts after the second coax-coplanar transition, on the far side of the test-fixture to the CRO. The second arrangement, shown in Figure 4.2, relies on the gap in the CPW central line to isolate the CRO. The advantage of the latter system is the removal of the bias tee between the pulse generator and the CRO, enabling CRO measurements of the photoconductive switch which exclude the response of the bias tee.

4.2.3 CPS sliding contact

The principle of the sliding contact switch for a CPS device (Figure 4.3) is similar to that for a CPW device. The generating beam may be slid

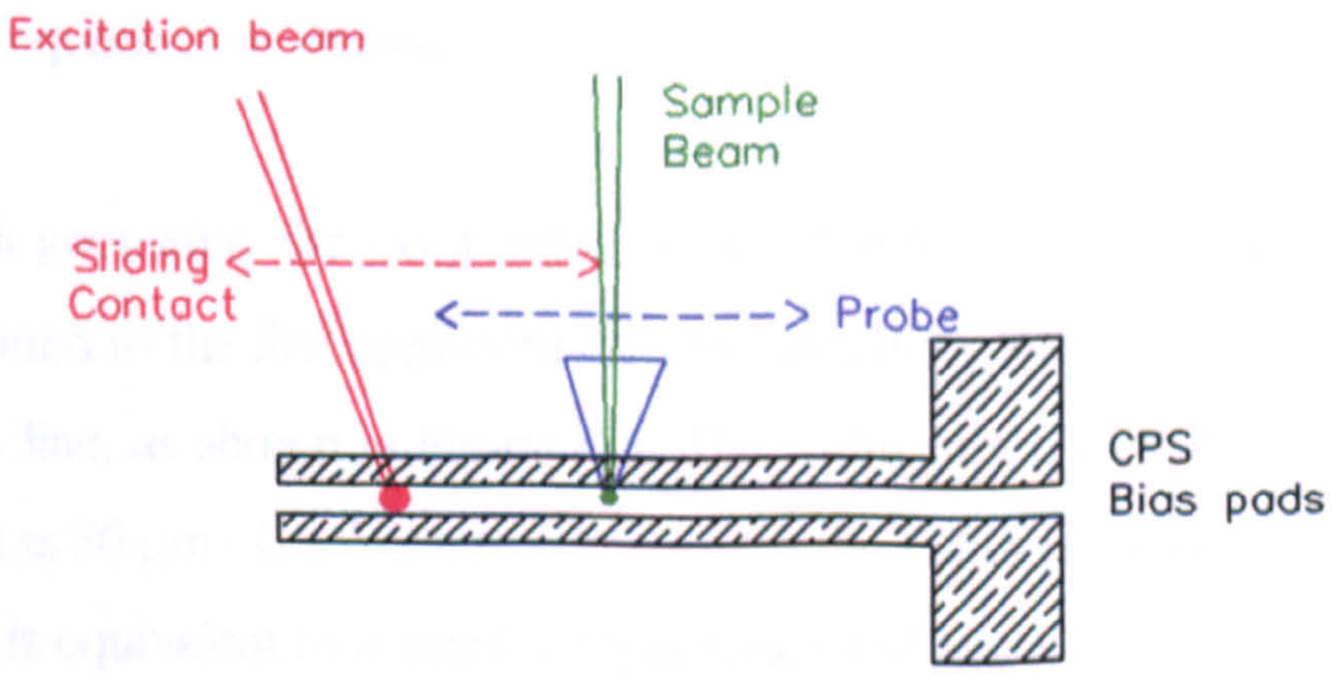

Figure 4.3 CPS sliding contact measurement configuration.

along the line, varying the point of excitation. Whereas the previous CPW lines are mounted in a test-fixture (UTF) using coaxial-coplanar transitions, the CPS line uses bias pads and probes to connect to the biasing circuit.

4.2.4 Approximate response of configurations

The response of the pulse generator will partly depend on the finite parasitic capacitance of the transmission line on which the pulse is generated.

The characteristic impedance, $Z_{O,}$ of a transmission line is given by

$$Z_O = \frac{1}{C_l v_p} \quad , \tag{4.1}$$

where C_l is the capacitance per unit length, calculable from conformal mapping,[4] and the phase velocity, v_p, is defined from *chapter 3* as

$$v_p = \frac{c}{\sqrt{\epsilon_{re}}} \quad . \tag{4.2}$$

A simple RC exponential decay is assumed to approximate the parasitic response of the transmission line (where the impedance Z_0 defines R). For a sliding contact geometry, the diameter of the laser beam illuminating the photoconductive switch defines the length of the transmission line from which the capacitance is approximated, using the value per unit length found from the equations in *chapter 3*.

For an Auston switch geometry, the extra capacitance - due to the gap in the CPW central line - may be found to the first approximation by calculating the capacitance for a small length of CPS line, as shown in Figure 4.4. The width of the CPS line in this approximation - shown as 30 μm - is arbitrary, as increasing the width produces a larger impedance line which is equivalent to a smaller capacitance and hence the RC product remains constant. The extra capacitance is parallel to, and is therefore added to, the CPW

sliding contact capacitance as calculated from the generation spot size. Note the effect of the two ground planes is not included in this approximation.

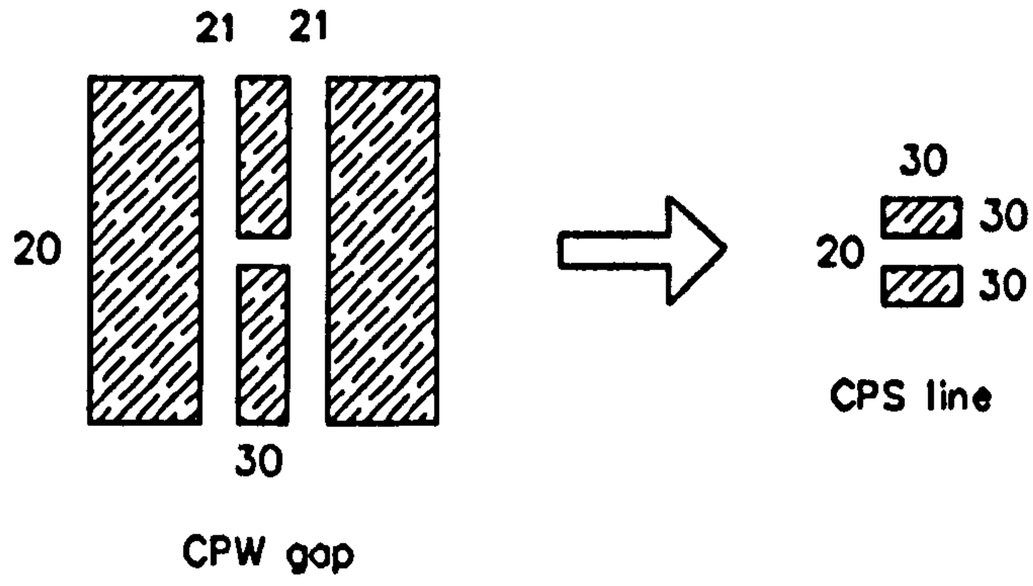

Figure 4.4 Approximating the capacitance of the CPW gap by a CPS line. Dimensions are in μm.

For the three configurations, the following single exponential RC time-constants are obtained: 90 fs for the 10 μm CPS sliding-contact switch; 170 fs for the 21 μm CPW sliding-contact switch; and 300 fs for the 21 μm CPW Auston switch with the 20 μm gap. The Gaussian impulse response is approximately equal to three times the RC time-constant.

4.3 Theory of EOS

4.3.1 Pockels effect

In general, given a direction of propagation of electromagnetic waves in a crystal, two possible linearly polarised modes exist, named the *ordinary* and *extraordinary* rays. The linear electromagnetic effect, or Pockel's effect, describes the change in refractive indices of the ordinary and extraordinary rays that is caused by, and is proportional to, an applied electric field. The existence of two rays with different indices of refraction is called *birefringence*.

Electro-optic sampling utilises the Pockels effect[5] as displayed by certain materials. A field applied across the material causes a phase difference, called *a retardation*, between two mutually orthogonal polarisation components ϕ_y and ϕ_z. such that the retardation Γ is given by:

$$\Gamma = \phi_y - \phi_z = \pi \frac{V}{V_\pi} \quad , \tag{4.3}$$

where V_π is the voltage which gives a retardation of π. V_π is known as the half-wave voltage as it causes a spatial displacement of $\lambda/2$ for the two polarisation components.

A phase retardation changes the state of polarisation of the two orthogonal components. A circular polarisation state (the magnitude of the two orthogonal components is equal) would change to an elliptical state (one component has a larger magnitude). This is called polarisation rotation.[5]

An electro-optic (EO) amplitude modulator can be constructed from an electro-optic crystal placed between crossed polarisers (Figure 4.5). With no applied voltage, light is polarised by the input polariser and travels through the crystal and compensator before being analysed by the output polariser.

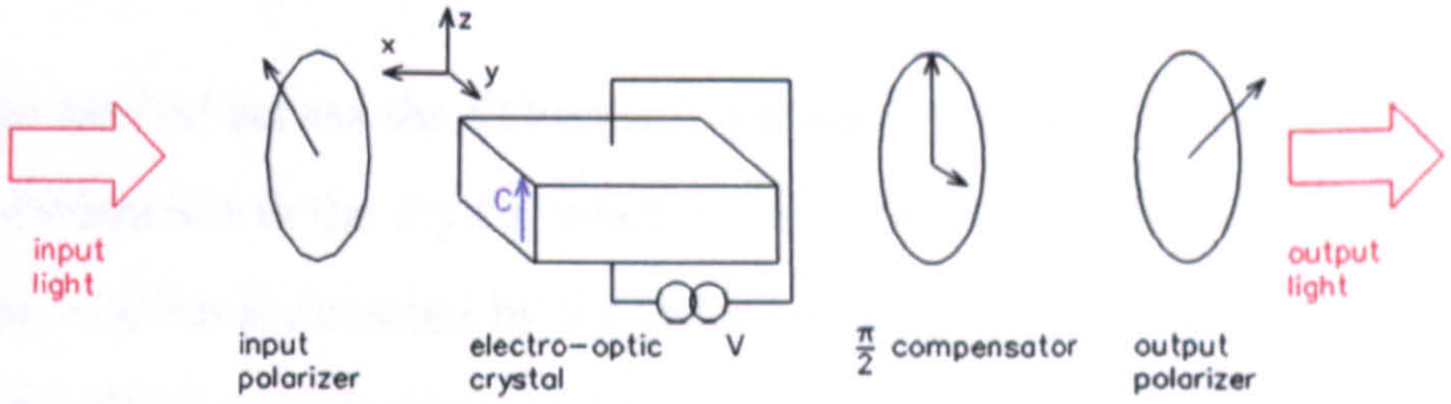

Figure 4.5 Schematic of electro-optic modulator.

The transmission I/I_o of an EO modulator[1], is given by

$$\frac{I}{I_o} = \sin^2 \frac{\pi}{2} \frac{V}{V_\pi} \quad , \tag{4.4}$$

where I_o is the 100 % transmission level and V the modulation voltage. The transmission curve is displayed in Figure 4.6.

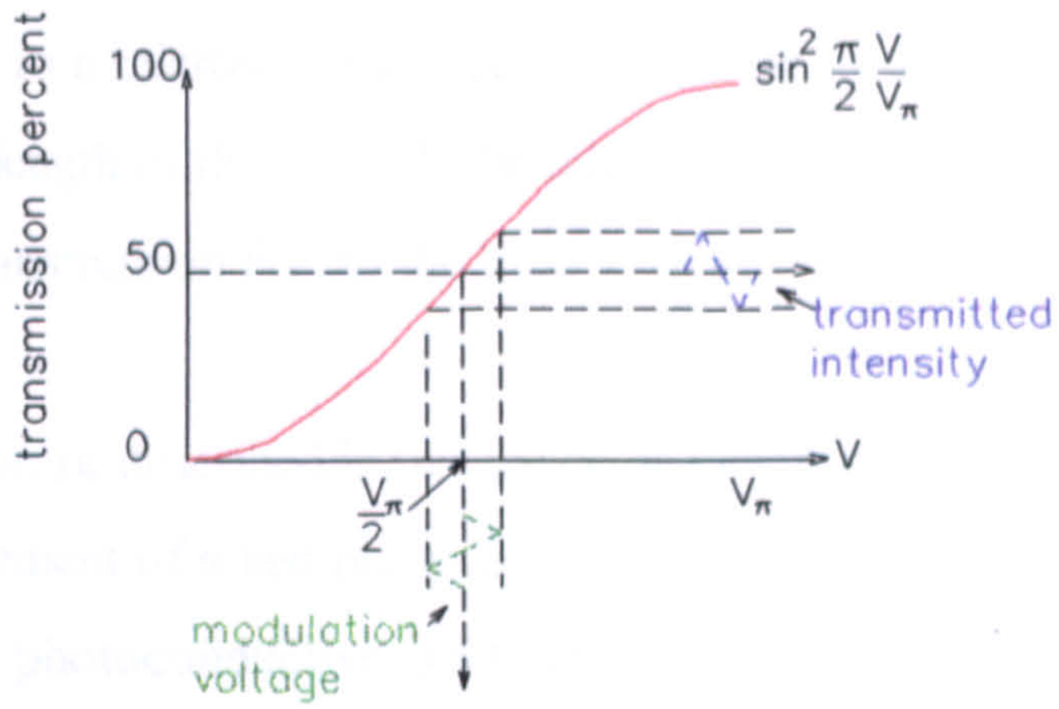

Figure 4.6 Transmission of an electro-optic modulator.

The compensator biases the EO modulator at the linear part of the transmission curve, midway between zero and the half-wave voltage V_π. A quarter-wave retardation plate may be used instead of a compensator, but a compensator allows the retardation to be adjusted to compensate for the naturally-occurring birefringence of the crystal (called *static* birefringence).

A voltage applied across the EO crystal, parallel to the axis marked "c", induces (non-static) birefringence in the crystal which rotates the polarisation state of the transmitted light. The rotation is detected by the polariser-analyser pair and converted to a change in intensity. Thus a small sinusoidal modulation voltage around $V_\pi/2$ produces a small sinusoidal modulation in transmitted intensity. Further details of the Pockels effect are found in a wide range of literature.[5,6]

4.3.2 Sampling and detection

Electro-optic sampling is, as the name suggests, a combination of the EO effect and sampling. An electro-optic sampling system measures an electrical field across an electro-optic material. Systems are optical and usually involve either a CW or modelocked laser source. The CW system is not discussed here.[7] With a modelocked laser, two schemes are possible. The laser can be used to illuminate an optoelectronic pulse generator, which

generates fast electrical pulses and produces fields along a transmission line which are measured by the electro-optic crystal. The optical pulses from the modelocked laser can also be phase-locked to a microwave source, for example by using a phase-locked loop to control the cavity length of the laser.[8] The microwave field from the source can then be measured on a transmission line by the EOS system.

At the outset of the work described in this thesis, the calibration facilities at NPL relied on the EOS measurement of a fast photodiode. The EOS system is used in this text to measure LT-GaAs photoconductive switches. Illumination of a switch generates electrical pulses which propagate along a CPW or CPS transmission line. The sampling beam - a train of optical pulses synchronous with the electrical pulses - passes through a polariser and a compensator onto the EO material.

Two possible schemes are *direct* EOS, and *indirect* EOS[9]. Direct EOS use the substrate of the planar line, for example GaAs or lithium tantalate ($LiTaO_3$), as the EO material. The sampling beam may be transmitted through the substrate or reflected off the transmission line metallisation. Indirect sampling involves the use of a probe, external but close to the transmission line, as the EO material. With some materials, for example GaAs, the *transverse* effect is used - the field being measured is parallel to the incident light. Other materials such as $LiTaO_3$ and $LiNbO_3$ make use of the *longitudinal* effect, which occurs when the field being measured is perpendicular to the incident light. The use of indirect longitudinal sampling with $LiTaO_3$ is explored in this thesis.

One implementation of indirect sampling uses a Glan-Taylor (GT) polarising prism as both a polariser and analyser (in double-pass). When the probe is brought into close proximity to the transmission line, electric fields due to the electrical pulses cause the EO material to rotate the polarisation of the optical sampling beam. The beam is reflected back through the GT-prism. For measurements typical at the NPL, the change in polarisation, equivalent to about 0.1% of V_π, is approximately linear with the detected change in intensity. The delay between the generating and sampling beams is altered using an optical delay line, for example a stepper motor and retro-reflecting prism, creating a

sampled waveform of the electrical pulse by measuring the change of intensity at each sampling point.

Various schemes may be used to detect the EOS signal. The choice of scheme depends on factors such as the sensitivity of the EO material (e.g. electro-optic coefficient and geometry), the amplitude of the photodetector pulse being sampled, and the noise performance of the laser. Detection can be broadly classified into either high or low-bandwidth schemes. A high-bandwidth detection scheme acquires several complete waveforms, each quickly, and then averages them together to improve the signal-to-noise (S/N). An example is a fast scanning optical delay line and signal averager. A low-bandwidth scheme acquires individual points more slowly, building up complete waveforms over a longer time and so does not require averaging at the end. An example is a chopper and phase sensitive detector (PSD). The second type of scheme is described in more detail below.

The optical beam with which the photoconductor is illuminated is first transmitted through a chopper or acousto-optic (A/O) modulator driven by a signal generator at an r.f. frequency, before exciting the LT-GaAs switch and generating electrical pulses. The optical beam is hence modulated, and therefore the generated electrical pulses are also modulated. The r.f. frequency is determined by the noise performance of the laser. After the sampling beam has been reflected from the probe, an r.f. diode is used to detect the intensity change and drive the input to the PSD. The PSD increases the S/N of the system by the use of a time-constant; each point is acquired over a longer period and the effective measurement bandwidth, and hence noise, is decreased. A personal computer acquires waveforms by controlling a stepper motor, changing the relative delay between the generating and sampling beams, and reading the PSD signal.

4.4 The dye laser EOS system

The laser system consists of a modelocked[10] argon ion laser[1], producing 70 ps FWHM

[1] Coherent CR12 HD

pulses which are used to synchronously pump a dye laser[2]. The dye laser has twin rhodamine 6G gain and DODCI saturable absorber jets. The output consists of a train of 600 nm optical pulses, spaced with 13 ns period and with pulse durations of 1.5 ps FWHM.

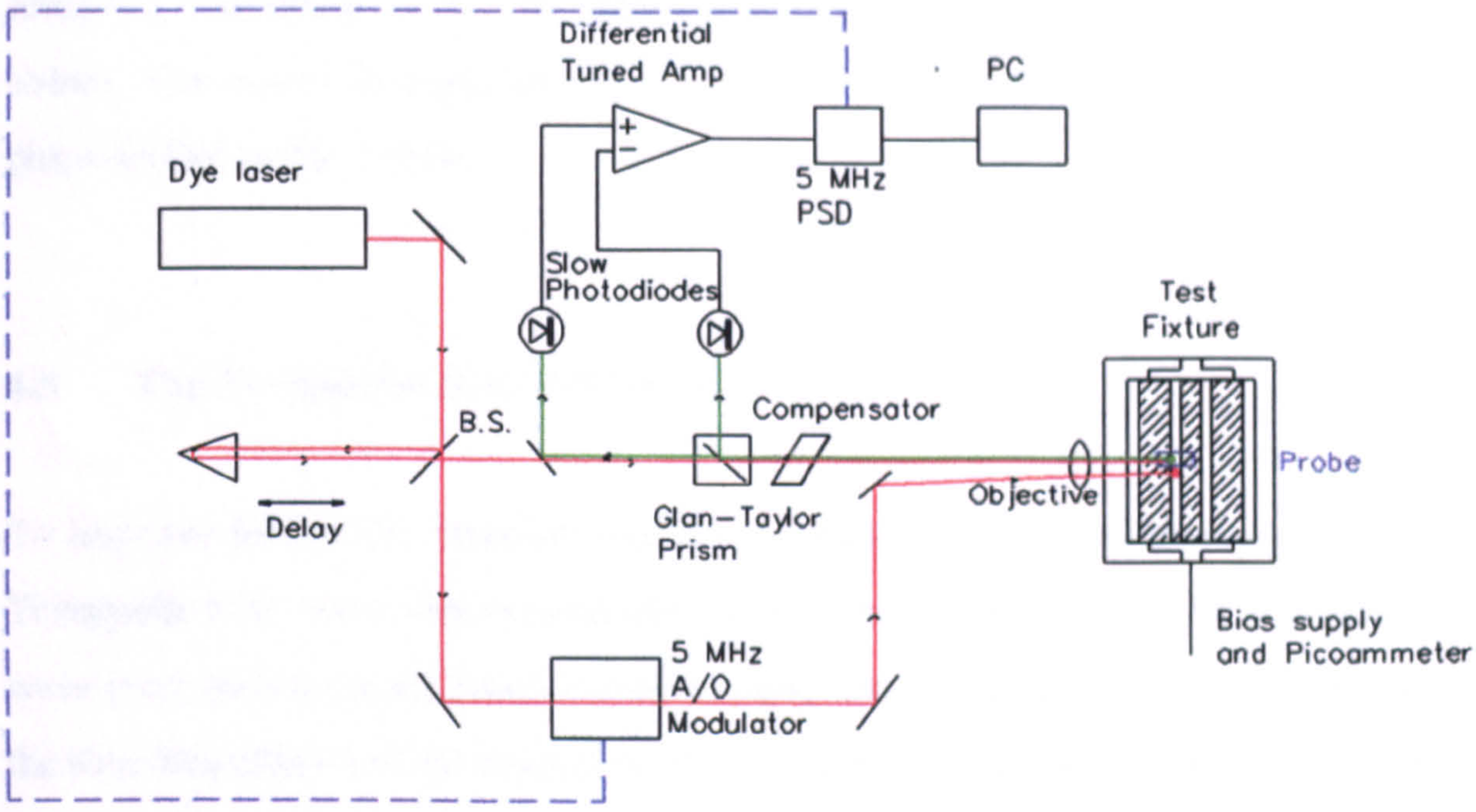

Figure 4.7 Dye laser electro-optic sampling system.

The EOS system, based on the above laser, is used to generate and measure fast electrical pulses from a LT-GaAs photoconductive switch (Figure 4.7). The excitation beam is focused onto a LT-GaAs region using a 10x microscope objective. The probe for the measurements described here is a piece of 100 μm thick $LiTaO_3$, with a hard dielectric reflective coating peaked at 600 nm. The $LiTaO_3$ is stuck onto the CPW of interest. This arrangement has the advantage that the sampling beam can be passed through the same objective as the beam used for pulse generation. By illuminating the edge of the $LiTaO_3$, the distance between the excitation and sampling beams can be minimised. The position of the various beams in relation to the circuit and probe is determined from CCD imaging systems located at strategic points.

---

[2] Coherent 701

The A/O modulation frequency was chosen to be 5 MHz after analysis of the noise characteristics of the dye laser. At frequencies above 4 MHz the excess laser noise reached the noise floor of a spectrum analyser measurement system (see *section* 4.9.1.1). After reflecting from the probe, the sampling beam is split into two paths by the GT-prism and the signal is differentially detected. A common-mode rejection ratio of 10 is achieved, improving the S/N by cancelling coherent noise (for example, laser excess noise). The output is amplified with an active tuned circuit before driving the PSD, phase-locked to the 5 MHz.

4.5 The Ti:sapphire laser EOS system

To improve further the temporal resolution, a second system, based on a commercial Ti:sapphire laser and a new external electro-optic probe, was assembled. A continuous wave (cw) all-lines argon laser[3] is used to pump the Ti:sapphire laser[4], modelocked by the Kerr lens effect and the integral cavity aperture, together functioning as a saturable absorber system.[11] The resulting train of optical pulses, tuneable in wavelength between 800 - 900 nm, has pulse durations shorter than 200 fs FWHM. In addition to providing shorter pulse durations than the dye laser and a larger average optical power (typically 800 mW compared to 100 mW), the Ti:sapphire laser system was chosen for reliability (long-term stability), convenience (useable after 5 minutes warm-up time, no dyes to maintain) and a relatively large tunability range (without the need to change dyes).

4.5.1 Prism probe

A prism probe, external to the transmission line, has the advantage of allowing flexibility in the probing geometry. A small size does not impart a large impedance discontinuity above the CPW or CPS.

---

[3] Coherent Innova 400

[4] Coherent Mira 900

Three methods exist to return the sampling beam from such a probe to the measurement system: using the metallisation of the device being probed for reflection; using a probe with sides arranged to totally internally reflect; and depositing a reflective coating on the outside of the probe. The first method is convenient to use with microstrip lines, due to the field emanating from the central conductor. However, with a CPW the longitudinal field is maximum at the gaps between the central conductor and ground planes, and hence the S/N is reduced by probing over CPW metallisation. Probes using the second method have recently become commercially available[5], but the temporal resolution of the probing system may vary due to an effect known as velocity matching. The light (or rather the effective resolved part of the light vector) can travel parallel to, or anti-parallel to, the electrical pulse being measured, changing the effective interaction time and producing different results. At the NPL, a prism probe with the last (coating) method was used.

The structure of the probe, specially made[6] for the NPL, is shown in Figure 4.8. $LiTaO_3$ pieces, of the order of 1 mm thick, were glued to fused-quartz substrates with optical cement. The cement thickness was measured and the $LiTaO_3$ polished down to the target thickness of 20 μm. This thickness was chosen so that the double-pass transit time through the probe was not large enough to significantly decrease the temporal resolution of the measurement system and the invasiveness of the probe was minimised[12] A prism shape, chosen to minimise the stress imparted during manufacture, was created by careful grinding and polishing, with the target 50 μm top achieved. The probe is considered adequately small to allow flexible use and minimise the perturbation of the measured CPW field.

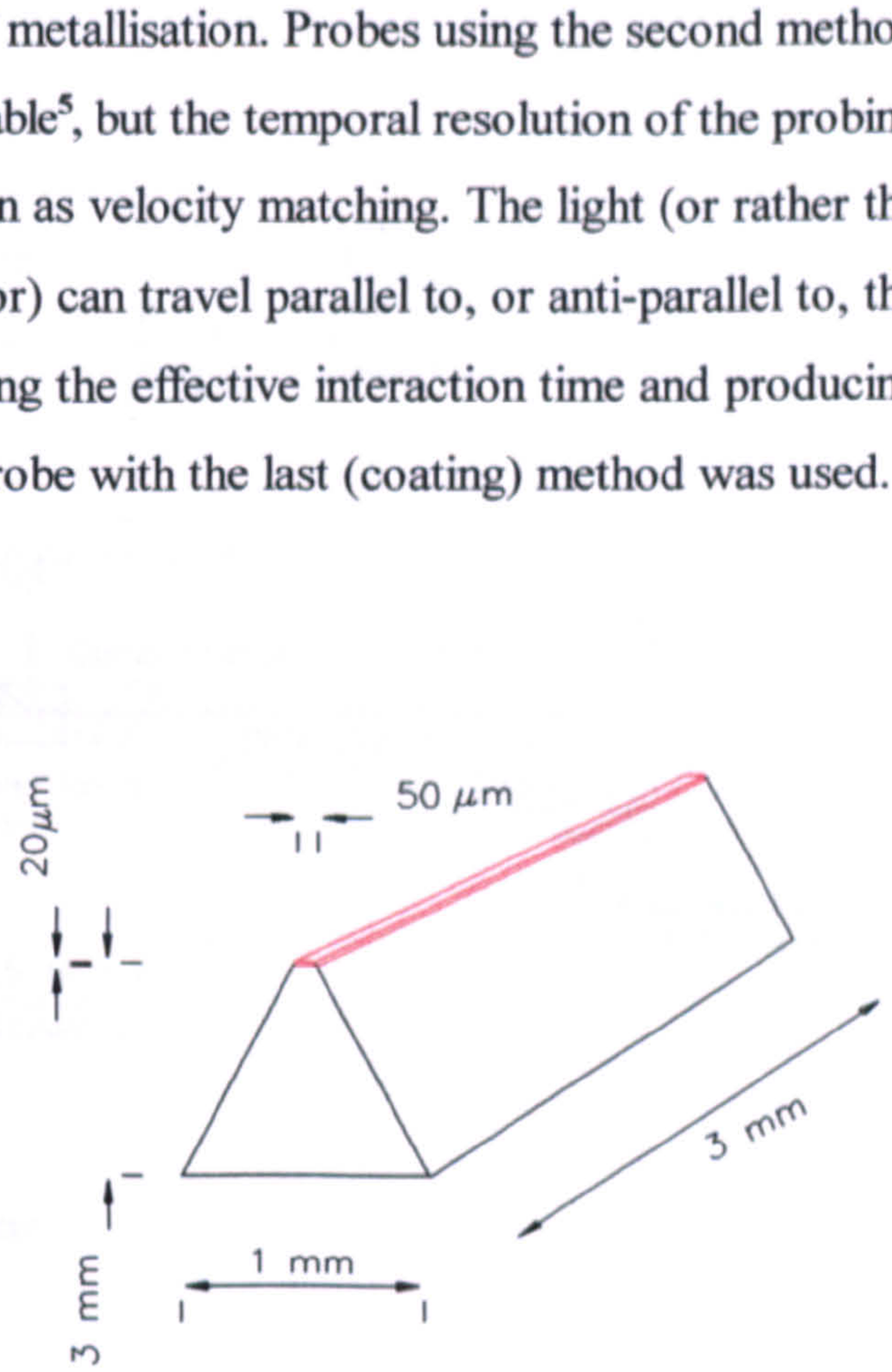

Figure 4.8 Structure of $LiTaO_3$ probe.

[5] Terametrics Inc.

[6] Gooch and Housego Ltd

The NPL prism probe was coated for reflection on the top surface, after the grinding and polishing stages. This was achieved by soft-coating an 8-layer dielectric stack, consisting of alternate layers of titanium dioxide and magnesium fluoride, onto the prism. The risk of inadvertently damaging the adhesion of the optical cement, higher with more widely used high temperature hard-coatings, was therefore reduced, at the expense of a decrease in reflectivity and coating stability. The resulting stack produced a measured reflection of 85 % peaking at 830 nm.

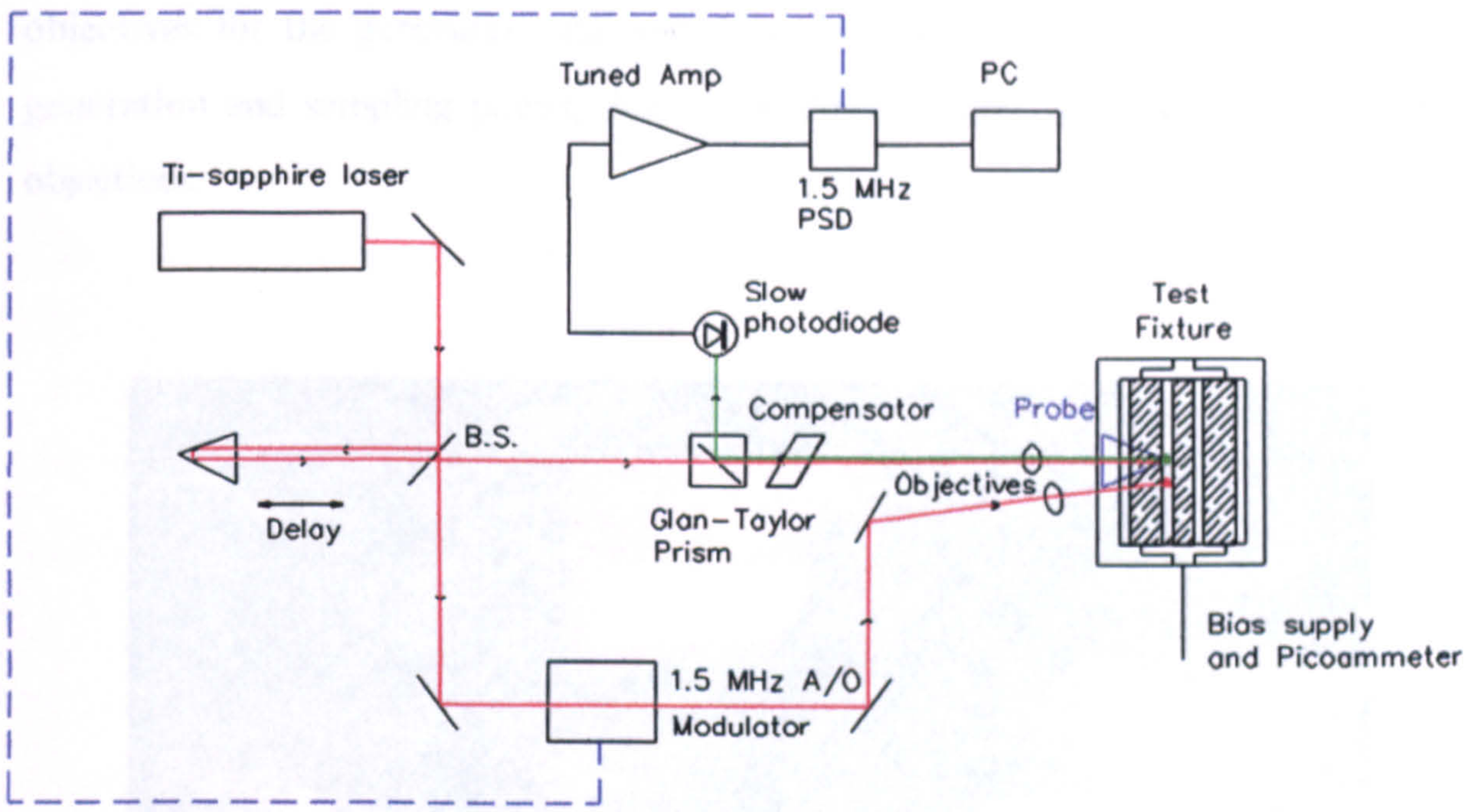

Figure 4.9 Ti:sapphire EOS system.

Figure 4.9 shows a diagram of the Ti:sapphire EOS system. The EOS system is similar to the previous dye-based system, but with some changes. The noise performance of the laser is improved, enabling non-differential, phase sensitive detection at the lower frequency of 1.5 MHz. It was hoped to move the detection frequency down to 100 KHz, further simplifying the detection electronics. However the noise spectrum of the NPL laser, as measured with a spectrum analyzer, was found to extend out to beyond 1.2 MHz. The noise performance of the NPL laser was worse than at least one other example.[13]

4.5.2 Probe station

A different method was needed to illuminate the LT-GaAs pulse generator close to the sampling point with the new probe arrangement. A single microscope objective was not sufficient, as the focal planes for the excitation beam (direct) and sampling beam (through a 3 mm thick probe) are different, and the optical arrangement also necessitates being able to steer the excitation beam clear of the 1 mm wide probe substrate and still illuminate near to the sampling point. The use of two separate commercial microscope objectives for the generation and sampling does not allow close proximity of the generation and sampling points, due to the diameter and working distance of such objectives.

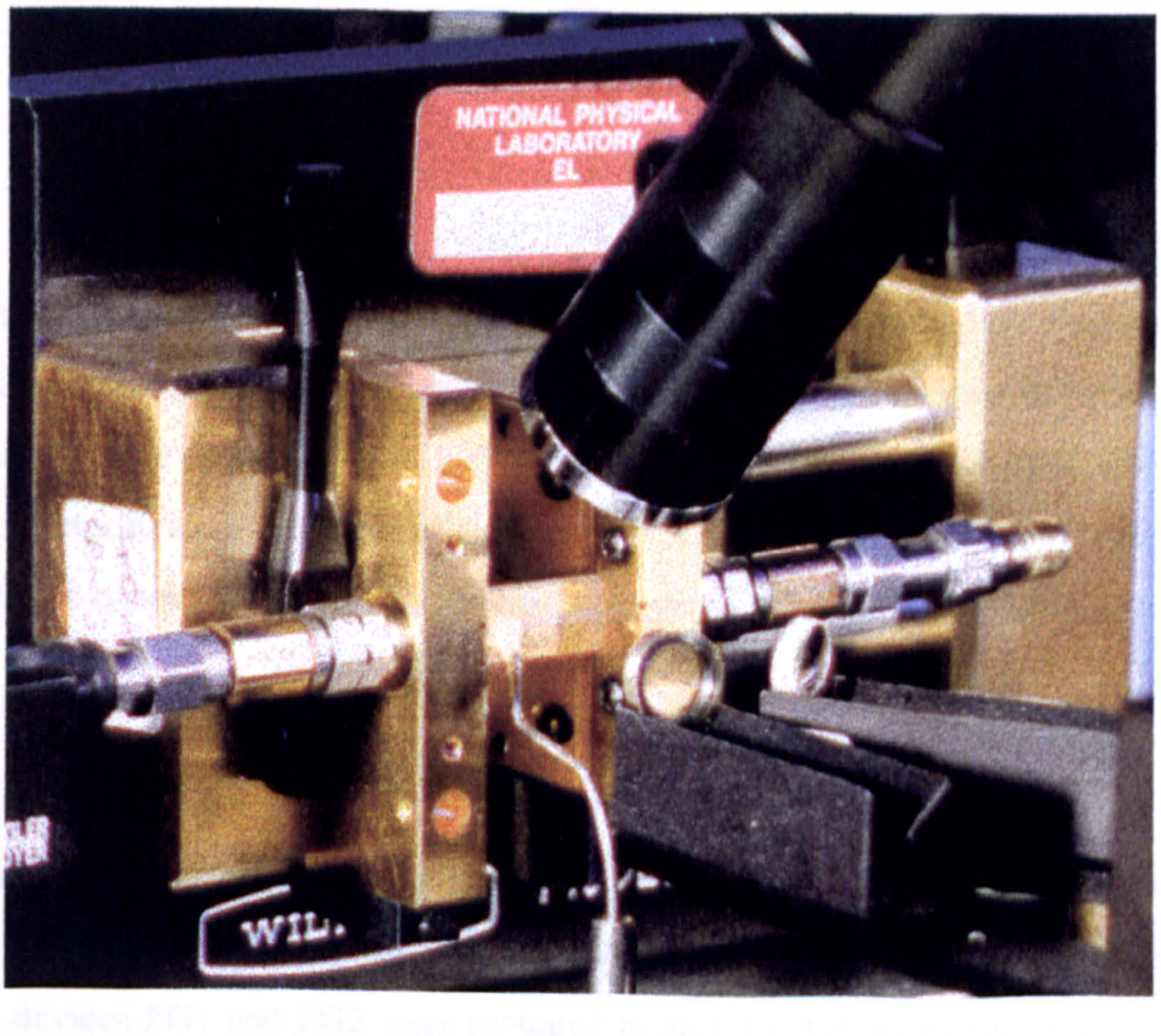

Figure 4.10 Photograph of probing station, showing optical arms for the generation, sampling and CCD imaging systems around a device mounted in a UTF.

Therefore the diameter (and structure) of some microscope objectives was reduced by careful dismantling and use of a lathe. A probing station was assembled, consisting of NPL-made vee-groves (to hold the small diameter objectives) and machined physical and optical mounting arrangements, together with commercial high precision xyz controllers. A photograph showing these features is presented in Figure 4.10

4.5.3 Calibration of voltage

To measure the absolute peak voltage using the EOS system, the probe is first aligned on the transmission line. An r.f. signal (e.g. 1.5 MHz) of known amplitude (e.g. TTL) is launched onto the line via the test-fixture coaxial connector. By adjusting the phase of the PSD to give the peak signal, a calibration factor is obtained, converting the measured PSD signal to the voltage at the EOS reference plane.

4.6 Dye laser measurements

Having explored the systems and background, the results are now described. The dye laser CRO measurements were initial experiments with early LT-GaAs devices, to test photoconductive operation. The EOS measurements of the same devices produced the fastest electrical pulses measured at the time at NPL, and demonstrated the requirement for a faster system, based around an updated laser, to improve measurement accuracy.

4.6.1 CRO results

The measurement of a photoconductive switch with a sampling oscilloscope was initially performed with Sn/Au metallurgy devices available at early stages of the project. LT-GaAs devices PG1 and PG2 were mounted in an UTF and connected to a sampling oscilloscope[7] with a high speed module[8]. The oscilloscope trigger was optimised using

---

[7] Tektronix Communication Signal Analyzer CSA803

[8] Tektronix 50 GHz (nominal) sampler module SD32

a 5 GHz photodiode[9] illuminated by pulses from the same laser, minimising the jitter between the laser and the oscilloscope sampling gate to less than 2 ps rms. The measurement of jitter is explored in *chapter 6*. The dark current and photocurrent were measured using a picoammeter.

Device PG2 was used in the Auston switch type configuration, but initial measurements produced unsatisfactory results. The dark current was larger than the photocurrent and problems were encountered in illuminating the central-line gap without apparently exciting regions across the width of the transmission line. This was in part due to poor device metallisation and imprecise etching of the LT-GaAs region. Measurements on better versions of these devices are investigated in later sections.

The sliding contact configuration was used with device PG1, with a bias tee[10]. The experimental arrangement is displayed in Figure 4.11.

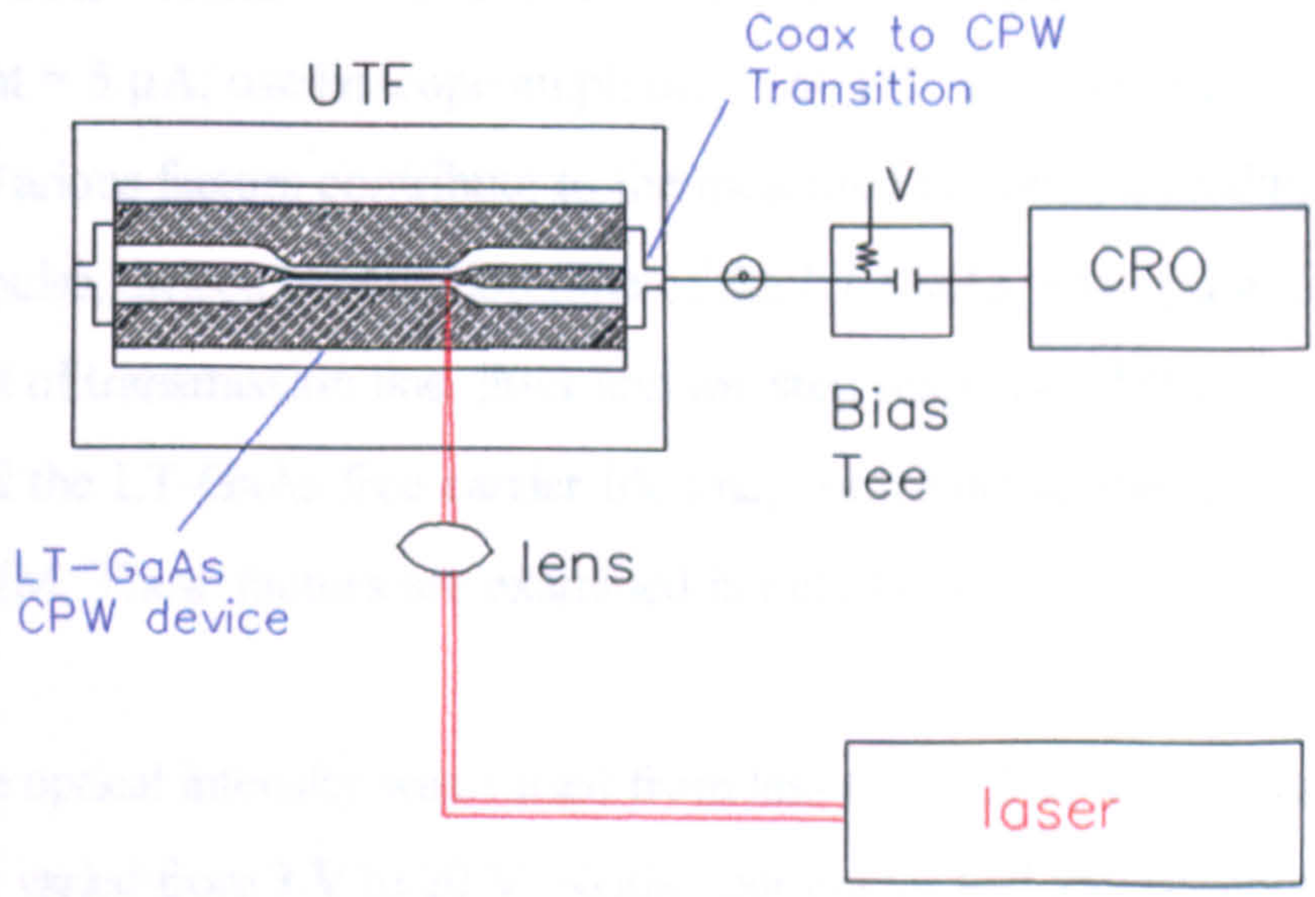

Figure 4.11 Schematic of sampling oscilloscope measurement system.

Using this system, the linearity of device PG1 with respect to optical intensity and bias voltage was investigated, and the effect of exciting the sliding contact gap at various positions along the transmission line was assessed.

---

9 Plessey Research special 50 μm device CX.L082

10 Wiltron K250 Bias Tee

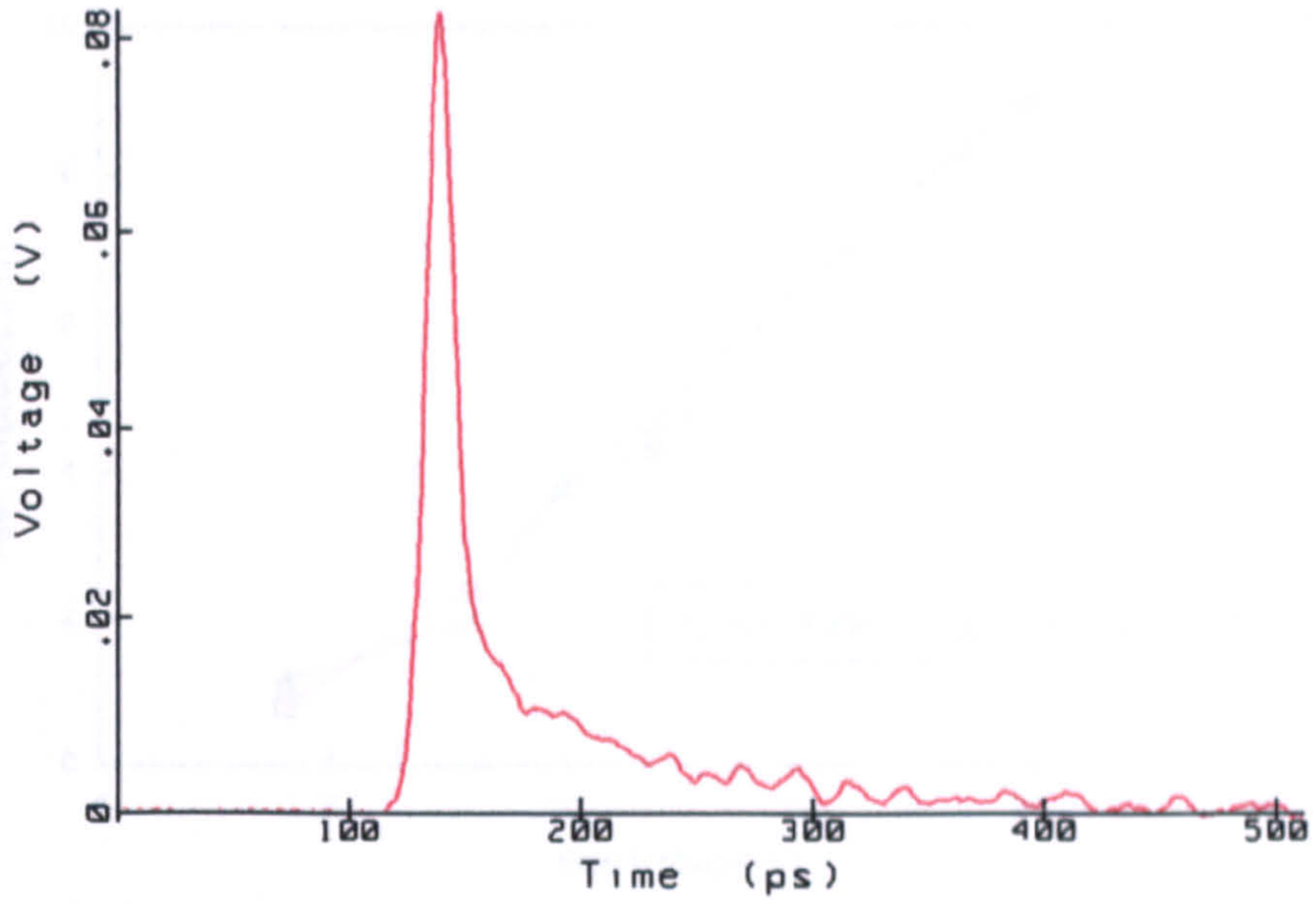

Figure 4.12 Oscilloscope measurement of PG1.

Figure 4.12 shows a waveform obtained with the following conditions: d.c. bias voltage = 30 V ; dark current = 0.2 μA; average optical illumination = 8 mW; average photocurrent = 5 μA; oscilloscope amplitude = 60 mV; risetime = 11.1 ps; and FWHM = 16.0 ps. Various factors contribute to the measured risetime, including the risetime of the optical pulse, dielectric relaxation time of the LT-GaAs, absorption depth of the LT-GaAs, effect of transmission line, jitter and the step response of the oscilloscope. These effects, and the LT-GaAs free carrier lifetime, contribute to the recorded falltime and hence FWHM. These factors are examined in detail in the next two chapters.

The average optical intensity was varied from less than 0.5 mW to 10 mW, and the bias voltage was varied from 3 V to 20 V. Neither parameter had any significant effect on the pulse shape. Reversing the polarity of the biasing voltage produced an inverted, but otherwise similar, waveform. The average photocurrent and the peak amplitude of the oscilloscope waveforms varied linearly with respect to the bias voltage (Figure 4.13) and intensity.

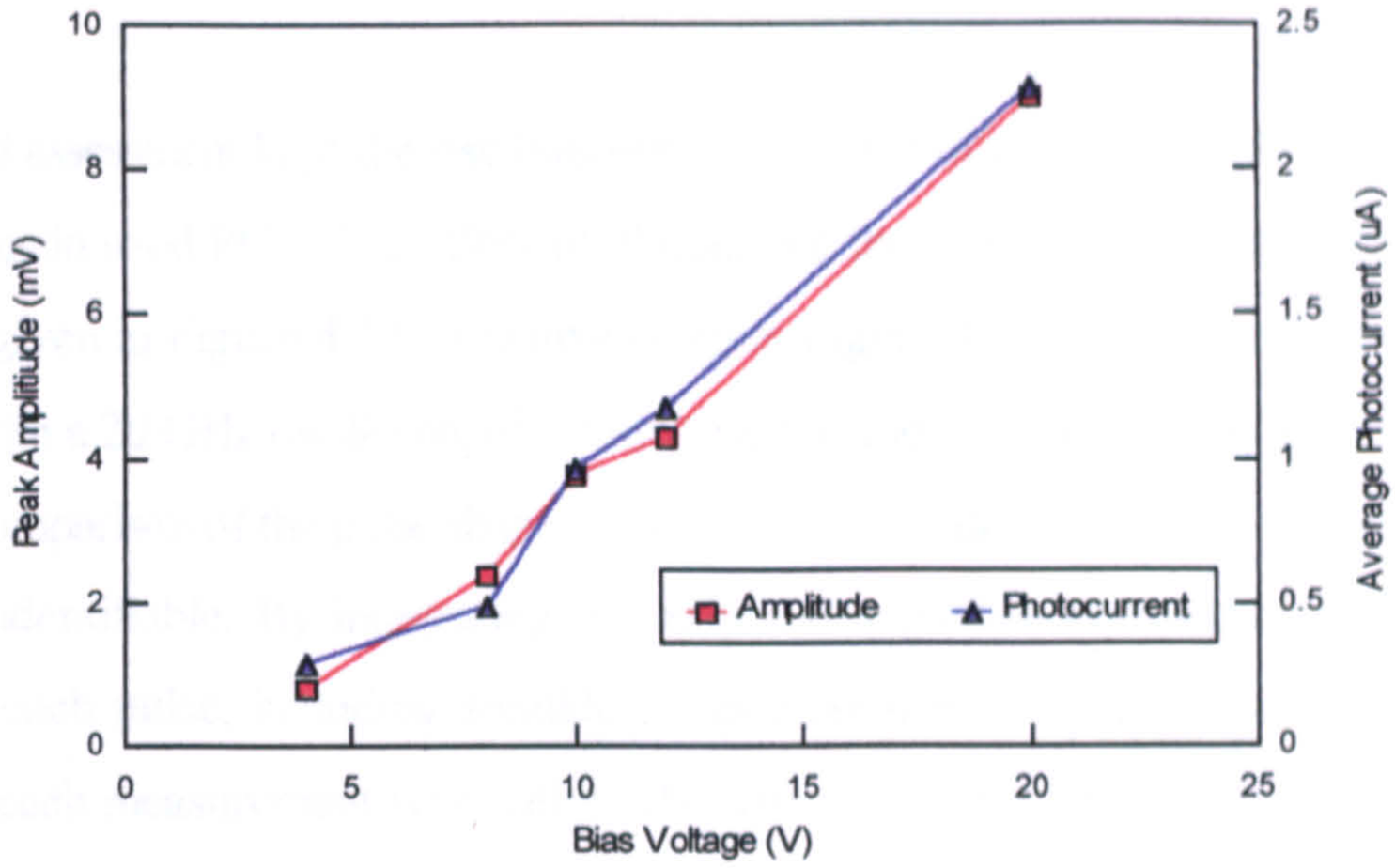

Figure 4.13 Linearity of photoconductive switch with respect to bias voltage.

The effect of illuminating different regions of the sliding contact was investigated in two ways. The first method involved exciting the device across opposite gaps of the small CPW in turn, at points 1 and 2 in Figure 4.14, and measuring on the oscilloscope the pulse obtained at the end of the UTF. The photocurrent was adjusted to 10 μA in each case. There was no significant difference in shape or speed between the resulting waveforms. The waveform from excitation at point 1 had the opposite polarity to that excited at point 2, due to the inverted excitation condition. Points 4 and 5 were also excited, with the oscilloscope moved to the other side of the UTF, producing similar pairs of inverted waveforms. The disagreement in width (< 1 ps) and amplitude (< 10%) between all four measurements is not considered significant; small differences between waveform pairs 1 and 2, and 3 and 4, were expected due to the slight difference in length of the large CPW,

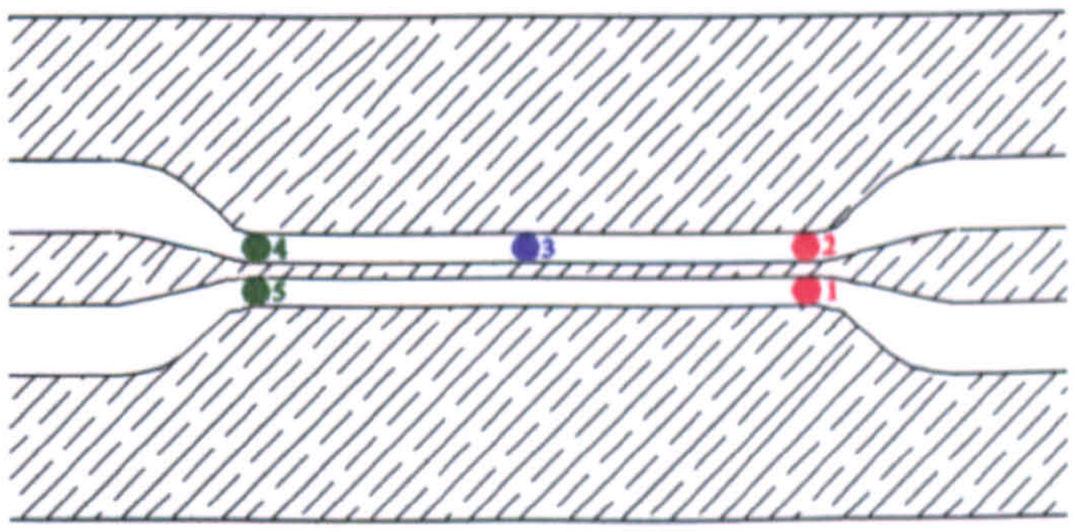

Figure 4.14 Location of excitation points.

produced during trimming of the device lines for test fixture mounting.

The second assessment kept the oscilloscope on the side of the UTF as shown in Figure 4.11, and again used PG1. The effect of illuminated the sliding contact at positions 2, 3 and 4 (as given in Figure 4.14) was investigated. Figure 4.15 shows the measurements acquired with a 20 GHz oscilloscope[11], normalised to the peak amplitude in each case to facilitate comparison of the pulse shape. A significant shoulder, drastic in the worse case, is readily identifiable. By integrating the amplitudes (before normalisation), the total charge in each pulse, including shoulder, was quantified. The agreement in the total charge of each measurement was within 8%. The waveform with the device excited at point 2 had a risetime of 16.3 ps and a FWHM of 26 ps, that excited at point 3 had values of 18.5 ps and 66 ps respectively, and that excited at point 4 values of 19.2 ps and 93 ps respectively. These measurements on the highly resistive LT-GaAs device (420 Ω central line) suggest that high resistance transmission lines may degrade the propagation of fast pulses.

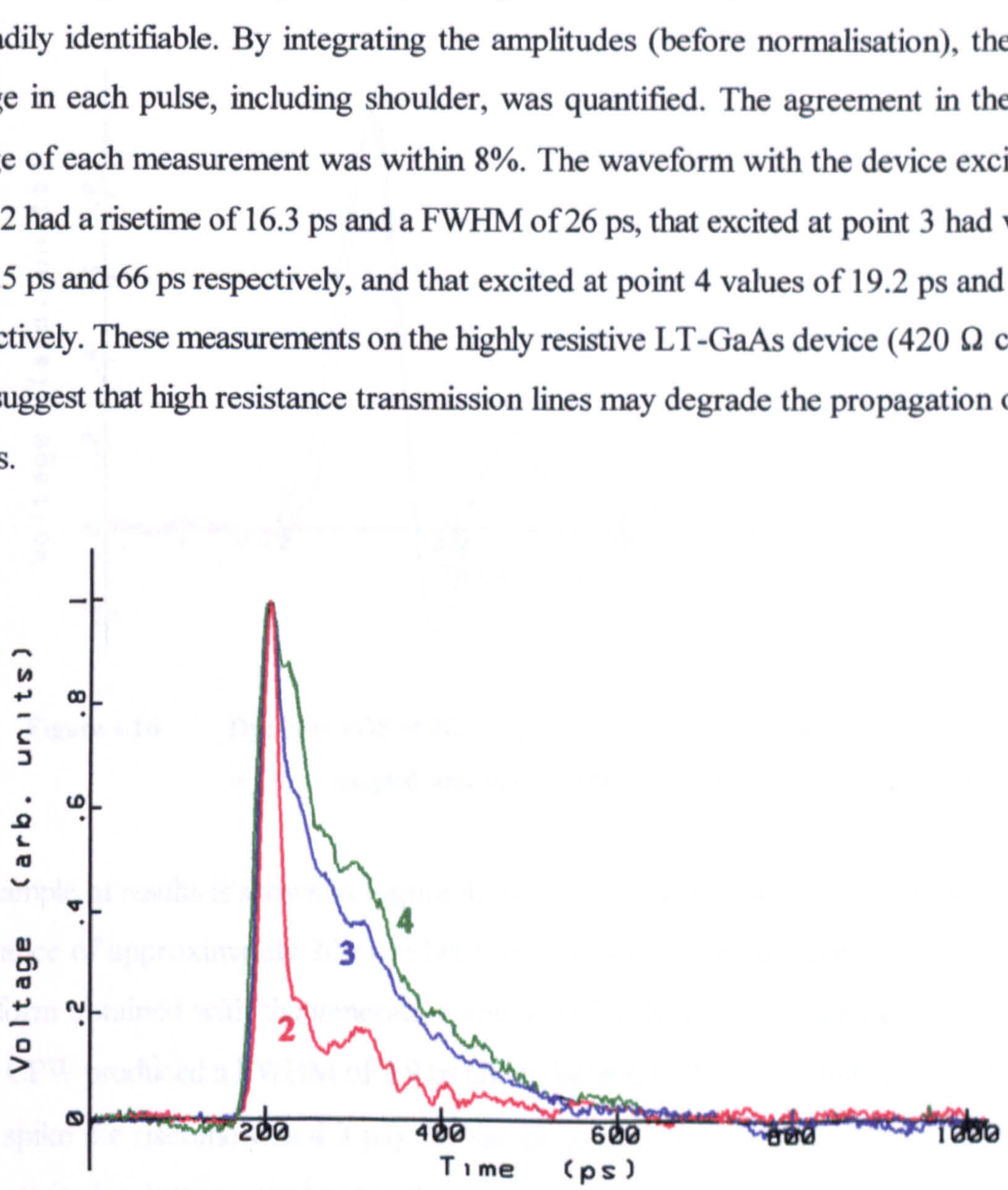

Figure 4.15 Oscilloscope measurement of pulse generator at various excitation locations. Points 2, 3, and 4 correspond to Figure 4.14.

[11] Tektronix SD26 sampler module

4.6.2 EOS results

The dye laser EOS system was used to investigate early devices, such as PG1, under sliding contact conditions, with better resolution than that attainable with the CRO. The photoconductive switch was illuminated with similar optical power to the dye laser CRO measurements. The EOS signal was sufficient to provide adequate S/N with which to compare the shapes of the waveforms.

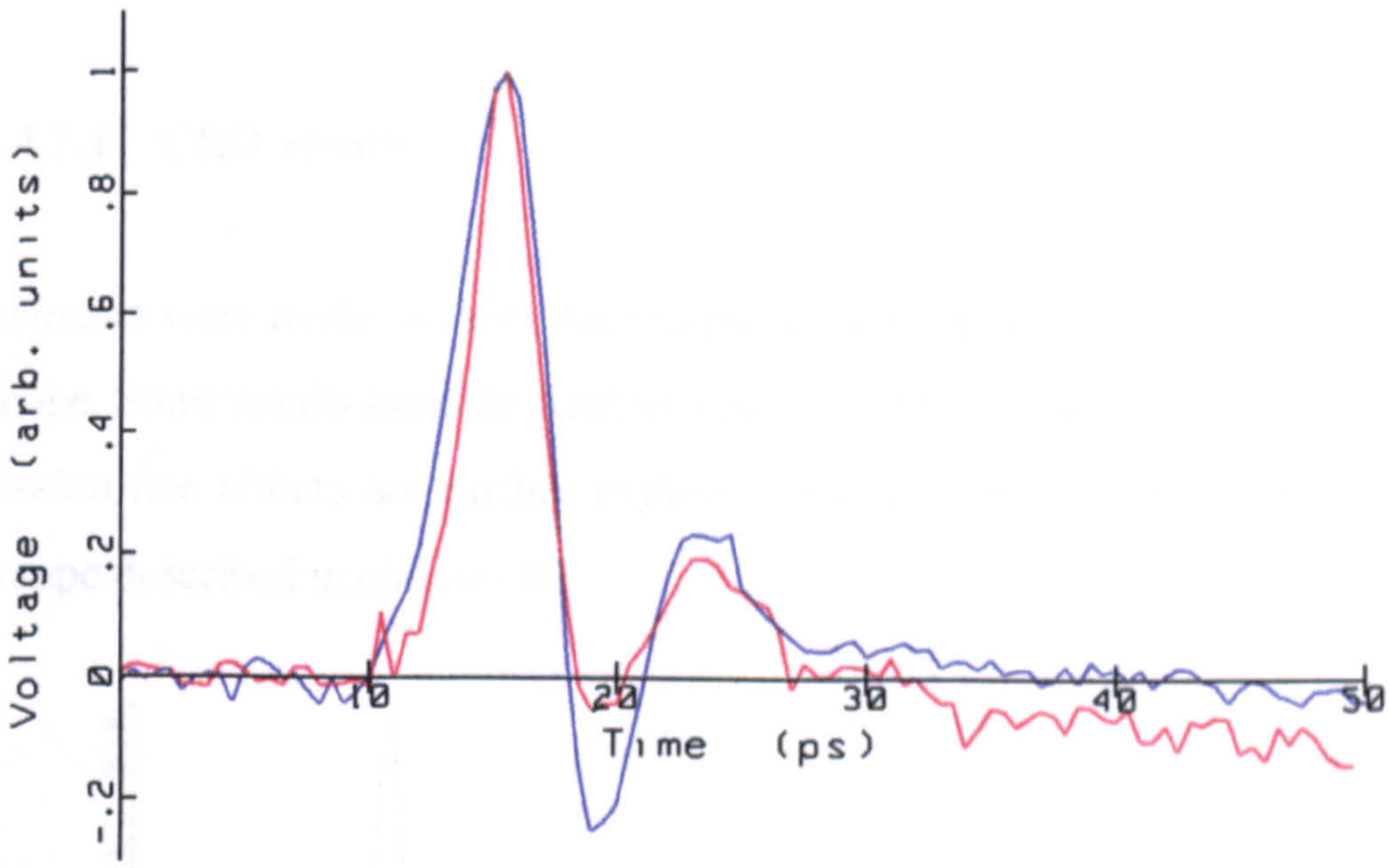

Figure 4.16 Dye laser EOS of PG1 with 200 μm generate-sample separation:
—— sampled same side of CPW as excited; —— sampled opposite side.

An example of results is shown in Figure 4.16. The two waveforms were measured with a distance of approximately 200 μm between the generation and sampling points. The waveform obtained with the generation and sampling beams illuminating the same side of the CPW produced a FWHM of 2.9 ps and a risetime of 2.6 ps (including the pre-pulse noise spike the risetime was 4.3 ps). By sampling the opposite slot of the CPW to that being excited, a larger overshoot and ringing was produced, with an increased FWHM of 4.0 ps and a risetime of 3.6 ps. The waveforms are shown normalised to enable the comparison of shape. It is worth noting that the amplitude of the same slot waveform is actually three times that of the opposite slot waveform and that neither waveform is shown inverted, i.e. the polarity of the pulses are the same despite being measured on

opposite sides of the CPW. More work is required to investigate the difference, but the distribution of energy between CPW modes is likely to be a relevant factor.

4.7 Ti:sapphire laser measurements

The Ti:sapphire laser measurements are described in more detail than the initial dye laser measurements. The upgraded system is used to measure all but the first batch of devices.

4.7.1 CRO results

Measurements were made on both Auston switch and sliding contact devices using an oscilloscope. Some results from the Auston switch devices are shown in *chapter 5,* where transmission line effects are further explored, and are used in the calibration of the oscilloscope described in *chapter 6*.

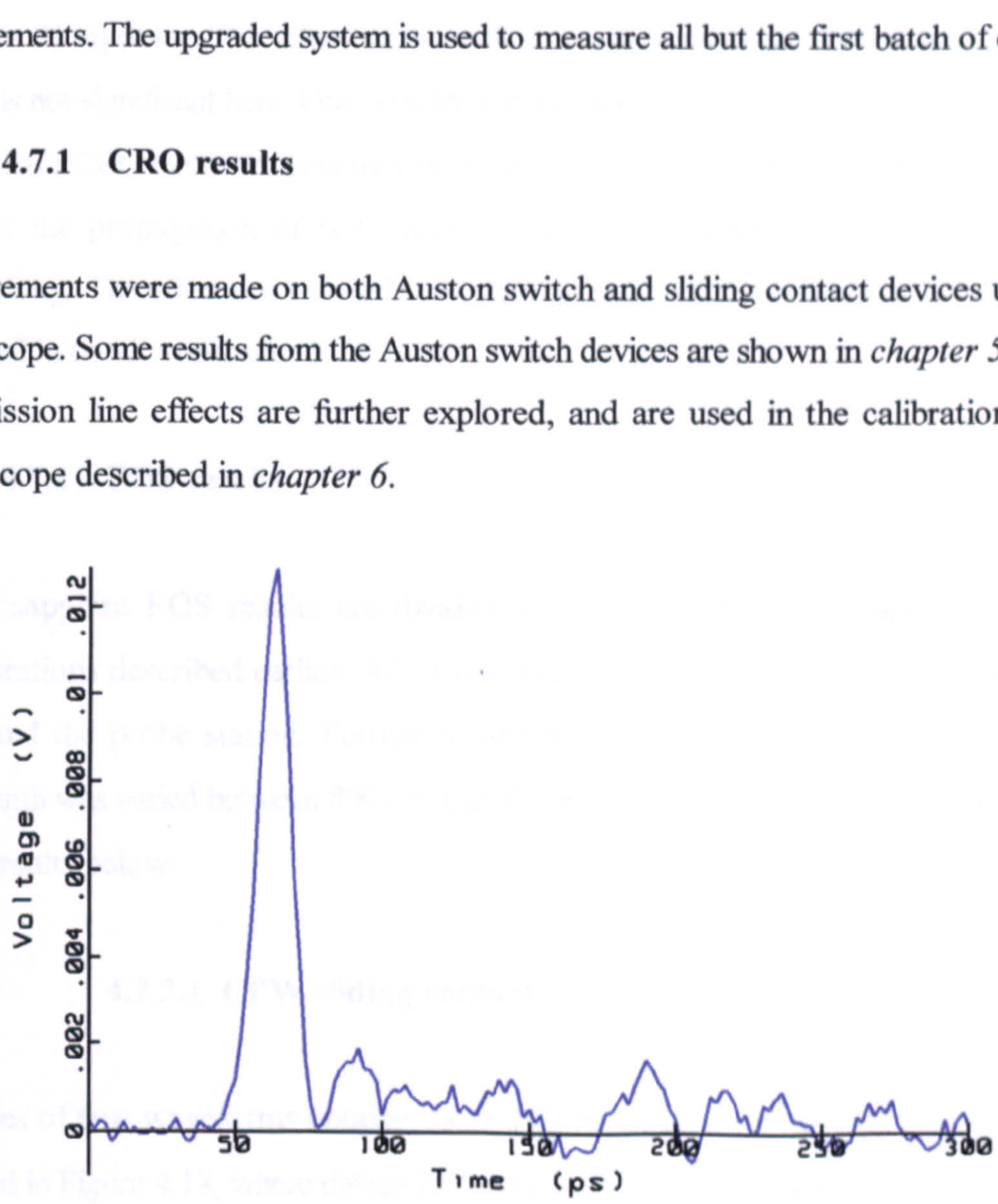

Figure 4.17 Oscilloscope measurement of PG4.

Figure 4.17 shows the SD32 oscilloscope waveform obtained with device PG4 (14 Ω central line resistance) illuminated at sliding contact point 1 (Figure 4.14) with the

following conditions: bias voltage = 15 V; dark-current = 0.8 μA; photocurrent = 3 μA; and pulse amplitude = 13 mV. The risetime of 11.0 ps is similar to that obtained with device PG1 with the dye laser system, but it can be seen that the structure of the waveform is improved, with no large trailing shoulder and a shorter FWHM of 12.8 ps.

Although the Ti:sapphire laser pulses are shorter than those of the dye laser, the difference is not large enough to explain the improvement in measured electrical FWHM using the Ti:sapphire. The effect of the different laser wavelength is investigated later; again it is not significant here. One possible explanation is that the shoulder obtained with the dye-laser CRO measurements may be attributable to high resistive transmission lines, and that the propagation of fast pulses improves on transmission lines with higher conductivity. The effects of transmission lines on pulse propagation is investigated and discussed in detail in *chapter 5*.

4.7.2 EOS results

The Ti:sapphire EOS results are divided into three sections corresponding to the configurations described earlier. All of the results have been obtained using the prism probe and the probe station. Further results are also shown in *chapter 5*. The laser wavelength was varied between 800 nm and 850 nm with no significant difference to any of the results below.

4.7.2.1 CPW sliding contact

Examples of two waveforms obtained with a CPW sliding contact photoconductor are displayed in Figure 4.18, where device PG5 was sampled approximately 200 μm from the sliding contact generation point. The device was biased with a voltage of 15 V, and 5.1 mW of 810 nm light was incident on the LT-GaAs region, producing an average photocurrent of 5.2 μA. One waveform was obtained with the sampling point the same side of the CPW as the excited photoconductor (FWHM = 1.1 ps, shown in red), the other waveform was sampled the opposite side (FWHM = 0.7 ps, in blue). (In fact the

sampling point was not changed, but the generation point swopped. This is equivalent and is more convenient to do as the system is less easily misaligned.) It is observed that the waveform recorded on the same side of the CPW has an amplitude approximately three times that recorded on the opposite side of the CPW and that the polarity of both waveforms is the same. Reversing the bias polarity inverted the results.

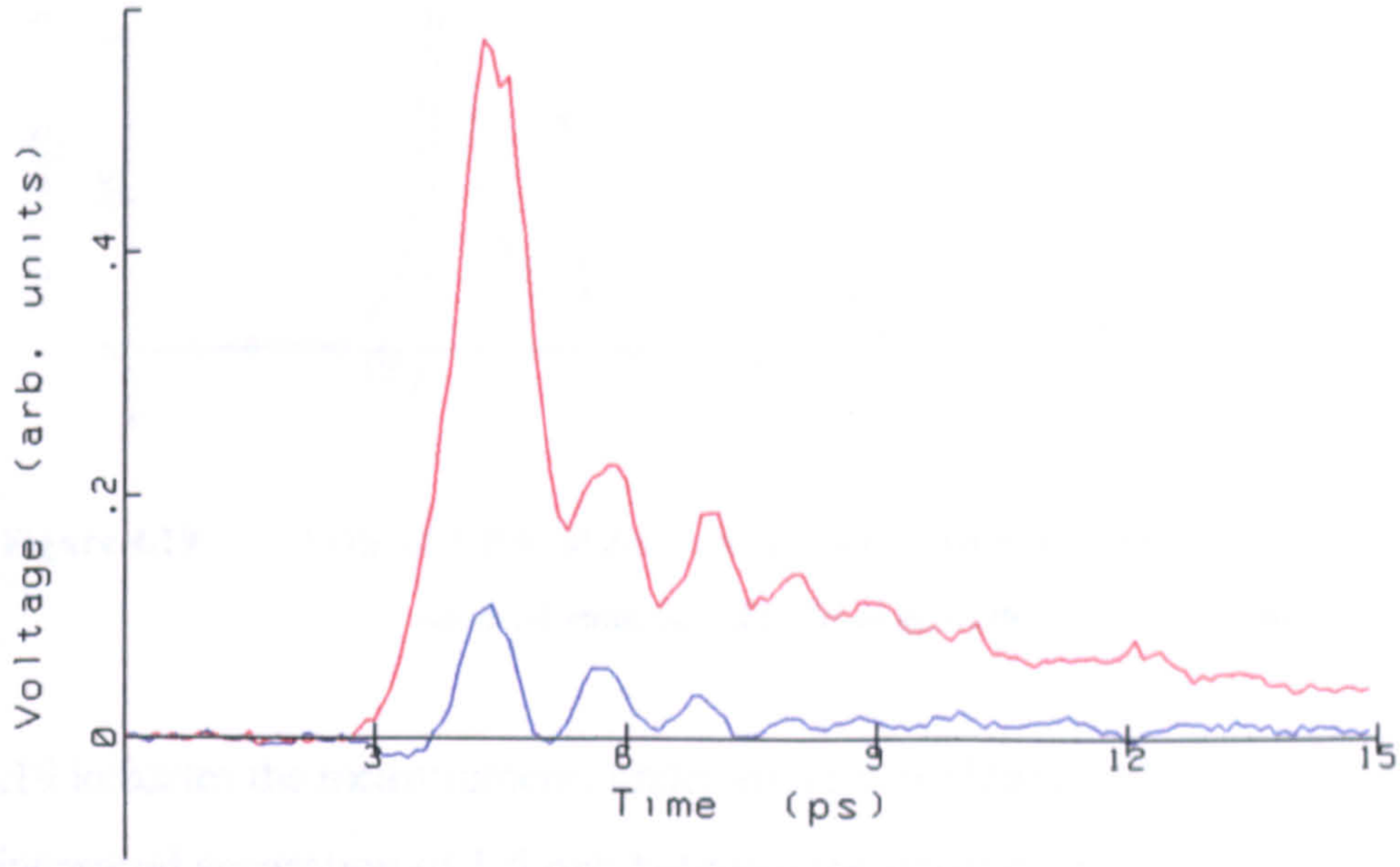

Figure 4.18 EOS of CPW sliding contact with generate-sample spacing of 200 μm: —— sampled same side of CPW as generated; —— sampled opposite side.

At the peak of the first waveform, the detected PSD signal was 14 mV. The input of a TTL signal along the line returned a value of 200 mV on the PSD. Using the voltage calibration technique, the calibrated EOS peak signal of the photoconductor is calculated to be 350 mV.

A peak amplitude of 20 mV was measured using a SD26 sampling oscilloscope connected at the end of the UTF. The temporal resolution of the instrument is approximately 20 ps. The peak therefore corresponds to 400 mV at a time-resolution of 1 ps - the approximate speed of the pulse as measured by EOS. The agreement with the calibrated EOS peak amplitude is reasonable and demonstrates the validity of the voltage calibration technique.

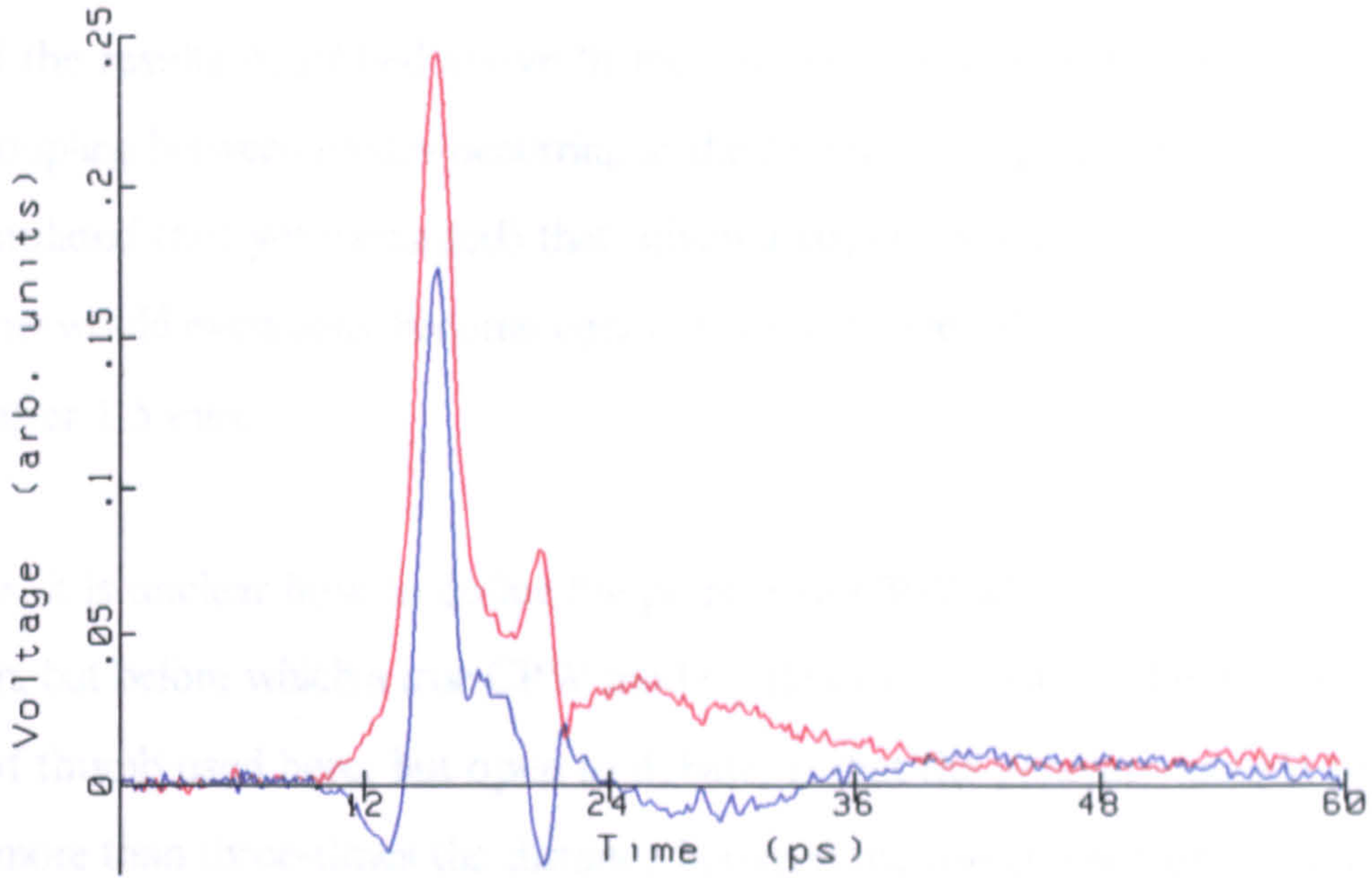

Figure 4.19 EOS of CPW sliding contact with generate-sample spacing of 1.5 mm: —— sampled same side of CPW as generated; —— sampled opposite side.

Figure 4.19 indicates the measurement, under similar conditions, of a pair of waveforms with an increased separation of 1.5 mm between the generation and sampling points. It can be seen that the amplitudes of the red waveform (FWHM = 2.1 ps) and the blue waveform (FWHM=1.6 ps) are closer to each other than was achieved with the smaller generate-sample spacing. The polarity of both waveforms is still the same.

The broadening effect of a length of CPW is explored in *chapter 5*. It is, however, worth commenting on the above results. The CPW has an odd and even mode (the even mode sometime being referred to as the slotline mode).[14] The odd mode is such that, at a given temporal location, the field between the central line and top ground plane is equal in magnitude, but opposite in direction, to the field between the central line and the bottom of the CPW line. The odd mode is excited under symmetrical conditions, such as the transition from a coaxial connector to a CPW, or a central gap Auston switch. The even mode is such that the magnitude and field direction is the same on both sides of the CPW - this is only likely to occur with asymmetrical excitation of the CPW.

Coupling between modes can occur, and therefore a mixture of modes is possible on a

CPW which change in relative proportions as a pulse propagates along a line. It is believed the results described above fit the category of asymmetrical excitation, with further coupling between modes occurring as the generate-sampling separation increases. It is postulated (not yet measured) that, given a larger separation, the top and bottom waveforms would eventually become equal in shape and amplitude. This is beginning to happen after 1.5 mm.

However, it is unclear how to define the point on a CPW where a mode exists after an excitation, but before which a true CPW mode (odd or even) cannot be deemed to exist. A rule of thumb used here, but open to debate, is that the generate-sample separation must be more than three-times the distance between the top and bottom ground planes, for the CPW modes to exist in the form described above. This is around 150 μm for the NPL CPW line.

4.7.2.2 CPW Auston switch

Auston switch device PG6 was measured with EOS conditions similar to those above. It was found that, provided the centre of the gap was illuminated, sampled waveforms with the same shape and opposite polarity were measured on the top and bottom of the CPW, the symmetry being irrespective of the generation-sampling separation. This implies the CPW odd mode only was being excited. Figure 4.20 displays examples of waveforms obtained with a spacing of 200 μm between the points of generation and sampling; both waveforms have a FWHM of 1.5 ps.

If the illumination were not in the middle of the central gap but was closer to the top or bottom slots of the CPW, then for generate-sample separations less than about 0.5 mm the structure of the measured pulse at the top was found to be different from that at the bottom. Such a result from asymmetrical excitation supports the results found with the CPW sliding contact.

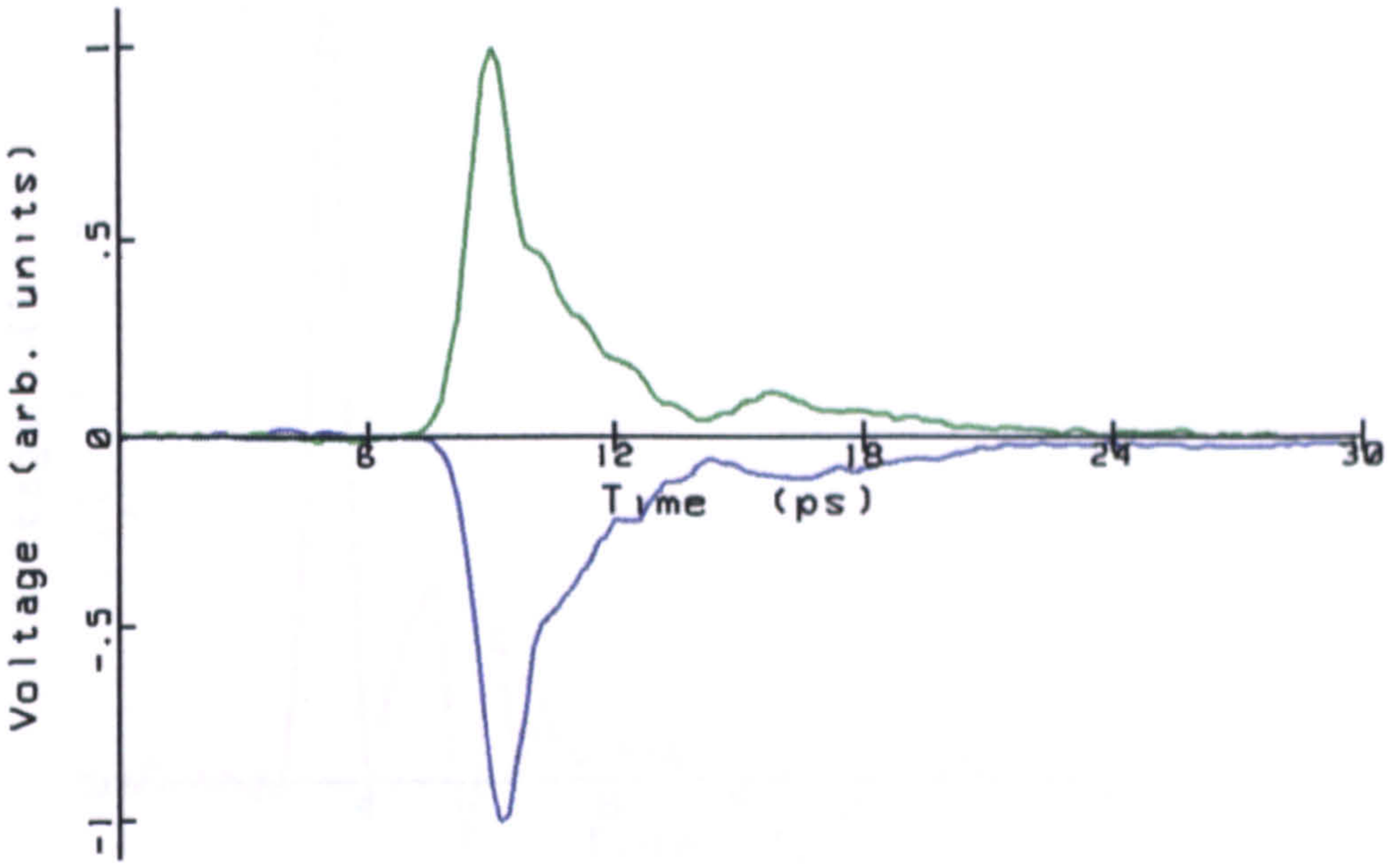

Figure 4.20 EOS of Auston switch with 200 µm generate-sample spacing: —— measurement of top CPW slot; —— measurement of bottom slot.

4.7.2.3 CPS sliding contact

In order to explore further the LT-GaAs response and to support understanding of the CPW mode issues raised above, CPS device PG8 was electro-optically sampled with the Ti:sapphire system. The arrangement is similar to before, except the UTF and coax connectors were replaced with bias probes, used to contact to the CPS pads. Care was needed to avoid over-damaging the device metallisation with such probes.

An example of a result with a 50 µm generation-sampling separation is given in Figure 4.21. The bias voltage was 12 V with a dark current of 0.8 µA and a 10 µA photocurrent. The duration was 650 fs FWHM, the fastest electrical pulse measured at the NPL.

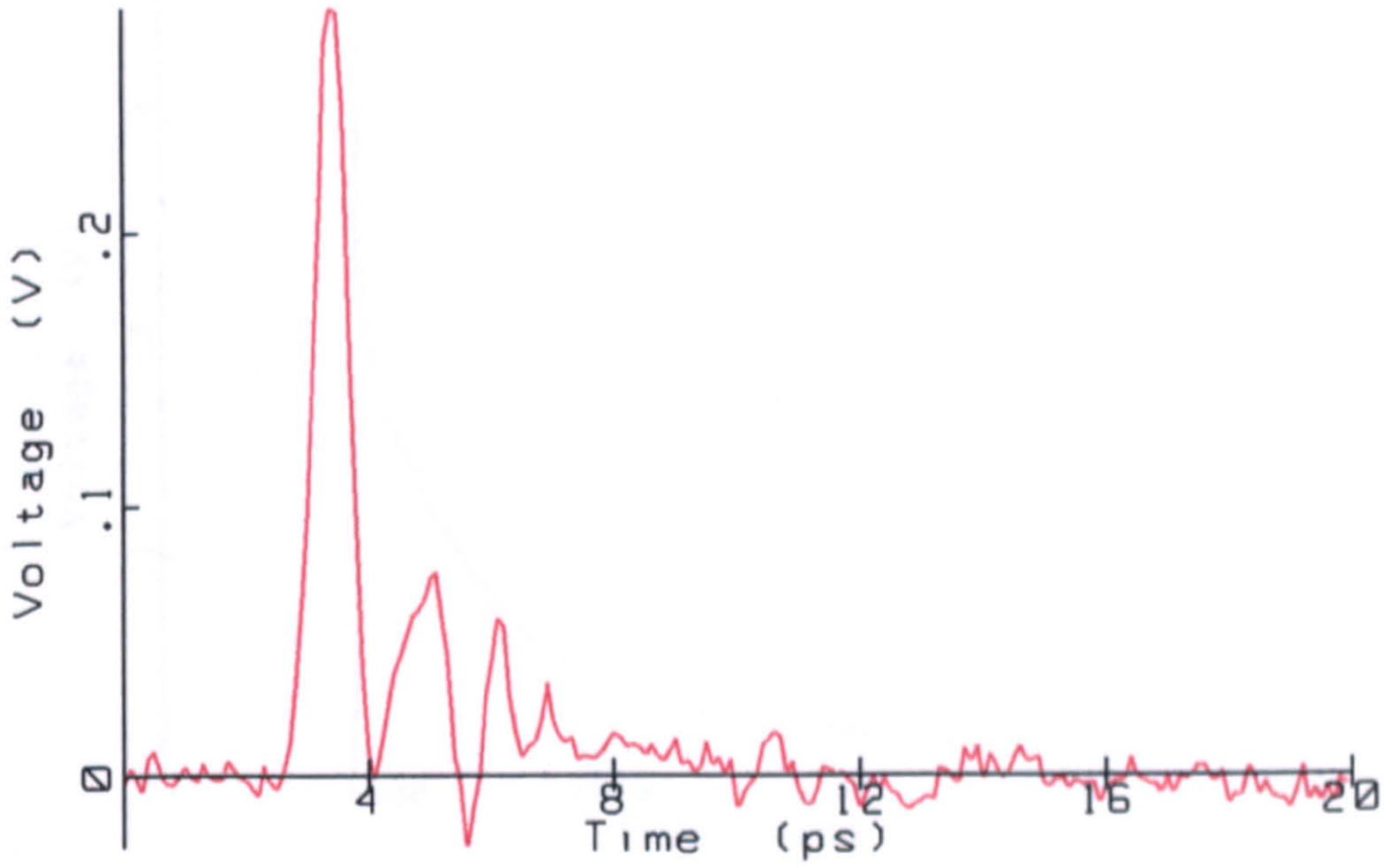

Figure 4.21 Ti:sapphire EOS measurement of CPS sliding contact.

4.8 CRO measurements of SI-GaAs

The Ti:sapphire system was used with the SD26 oscilloscope to measure a semi-insulating GaAs photoconductive switch, for comparison purposes. Figure 4.22 indicates a typical response of device TL7. The risetime is 16 ps, limited by the 20 GHz CRO, and comparable with that obtained with LT-GaAs. The FWHM is 90 ps, but the waveform shape does not make the parameter very meaningful, and the falltime is 1.3 ns.

Assuming a single exponential decay, a decay constant of 1.4 ns is estimated from a logarithmic plot. It is documented that the free carrier lifetime for GaAs typically varies between 300 ps and 2 ns, dependent on the wafer - this is verified by experiment. The peak voltage is similar to that obtained with LT-GaAs, but over a longer time window or epoch. This implies that the responsivity of GaAs is much larger than LT-GaAs, again as expected.

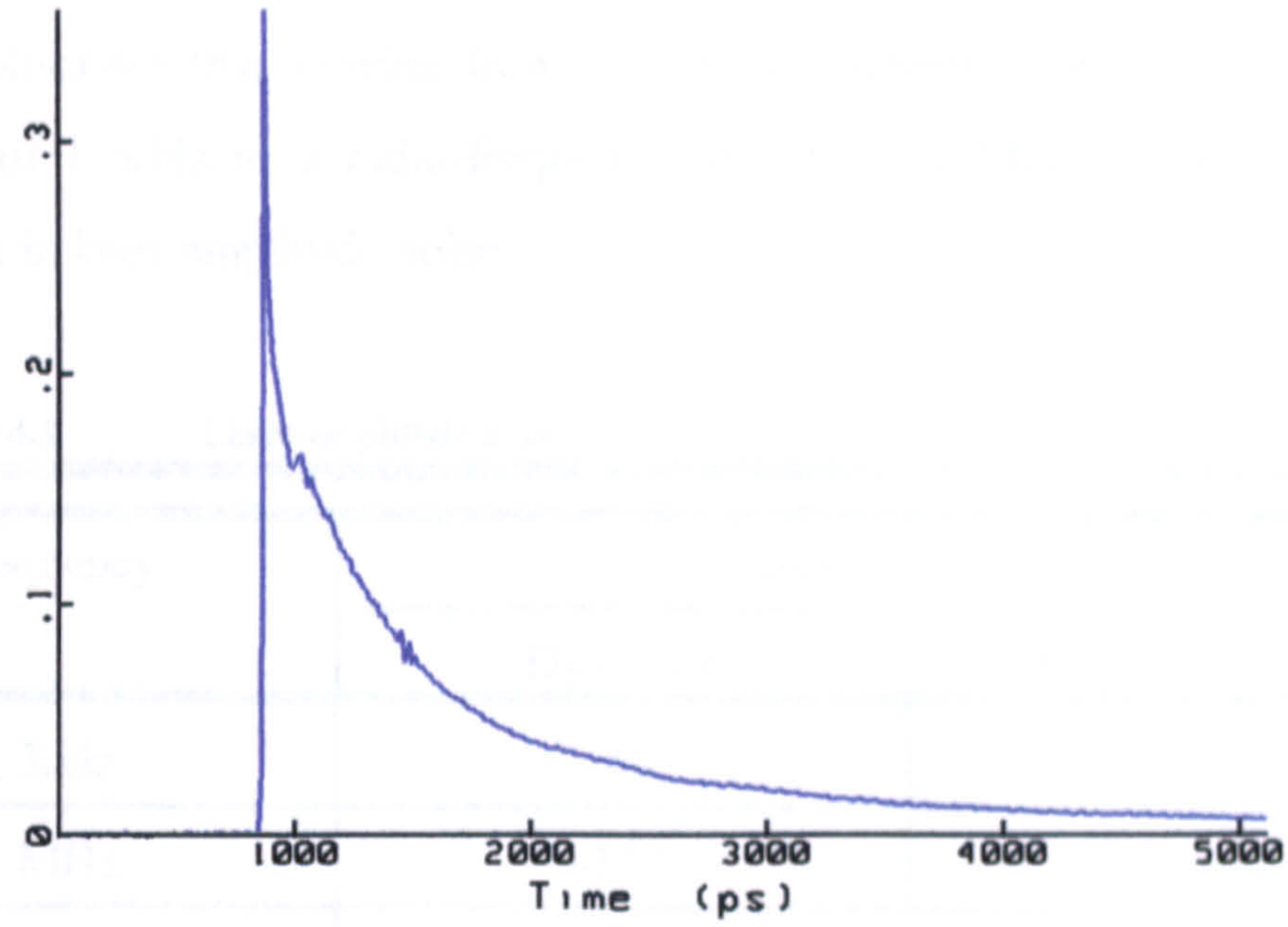

Figure 4.22 CRO measurement of SI-GaAs.

4.9 EOS system limitations and response of LT-GaAs

The signal-to-noise ratio and minimum detectable voltage of the Ti:sapphire EOS system is described. Contributions to the temporal resolution of the EOS systems with both the dye and Ti:sapphire lasers are also examined in this section and a summary provided (Table 4.2). The temporal response of the LT-GaAs photoconductive switches is then explored. Uncertainties are expressed at 95% confidence levels (2σ).

4.9.1 Noise and voltage limitations

4.9.1.1 Laser noise

Numerous measurements on different aspects of laser and EOS noise have been performed at NPL over the last few years,[12] the details of which are not recorded here. The choice of frequency at which each EOS system operates was primarily determined

[12] Many of these measurements were performed by Dr A.G.Roddie and Dr D.Henderson.

from measurements of laser amplitude noise, shown in Table 4.1. With the Ti:sapphire laser, it is observed that moving from a detection scheme that operates at audio-frequencies of 1 KHz to a radio-frequency scheme at 1 MHz results in a 36 dB improvement in laser amplitude noise.

Table 4.1 Laser amplitude noise.

Frequency	Noise dBc /Hz	
	Dye laser	Ti:sapphire laser
1 KHz	-88	-91
1 MHz	-110	-127
5 MHz	-122	-130

4.9.1.2 EOS S/N

The Ti:sapphire laser EOS signal-to-noise ratio (S/N) was found from a typical measurement of a LT-GaAs switch. A S/N of 150 (-43 dB) was obtained using a PSD time-constant of 1s per point at a phase-locked frequency of 1.5 MHz. From knowledge of the peak voltage - using the voltage calibration method described earlier - a minimum detectable voltage of 0.5 mV/$\sqrt{Hz}$ was calculated for the system, sampling across a 20 μm gap. As the EOS system measures electric field strength, the figure can be improved to 100 μV/$\sqrt{Hz}$ by sampling across a 4 μm gap - the optical limit of the microscope objective.

Differential detection produced a 10 dB S/N improvement with the dye laser system. A similar system could be employed with the Ti:sapphire-based system to provide better sensitivity, if the application required it.

4.9.1.3 Dynamic range

The dynamic range of a system is also an important parameter. The minimum detectable voltage has already been found. To estimate the maximum voltage before which the system would overload, or produce significant non-linearities, a phase change equivalent to 1% of V_π was initially assumed. If such a voltage, around 10 V, were applied to the transmission line and the EOS system could detect the voltage, the dynamic range would be 86 dB.

To measure the dynamic range, a system comprising a 20 GHz microwave source phase-locked to the Ti:sapphire laser was used.[13] The microwave signal was launched onto an alumina CPW line and the power was varied. The EOS system was used to probe the standing wave signals on the CPW. The variation in input power enabled a dynamic range of at least 60 dB to be measured.

4.9.1.4 Probe height sensitivity

It is known that the height an EOS probe is positioned above a circuit of interest can be a critical parameter.[9] The field strength and hence EOS signal decrease with distance from the circuit. Also if the probe is invasive, i.e. perturbs the transmission line being measured, then a variation in height can vary the shape of the measured response.

To investigate the first effect, a TTL signal at the system detection frequency of 1.5 MHz was launched onto a 10 μm CPS device (PG8). The probe was varied from a position where it was virtually touching the circuit to a height of 80 μm and the EOS signal was measured. Figure 4.23 shows the signal plotted in dB (relative to the first measurement) against height. It is seen that each successive doubling in spacing between the probe and transmission line causes approximately 8 dB loss in signal, and therefore in signal-to-noise. Further work is required to investigate the effect more thoroughly with different

---

[13] The system was built at the NPL by Dr D.Henderson as part of a EU contract and has a measured optical-electrical jitter of < 3 ps rms.

transmission line and probe geometries.

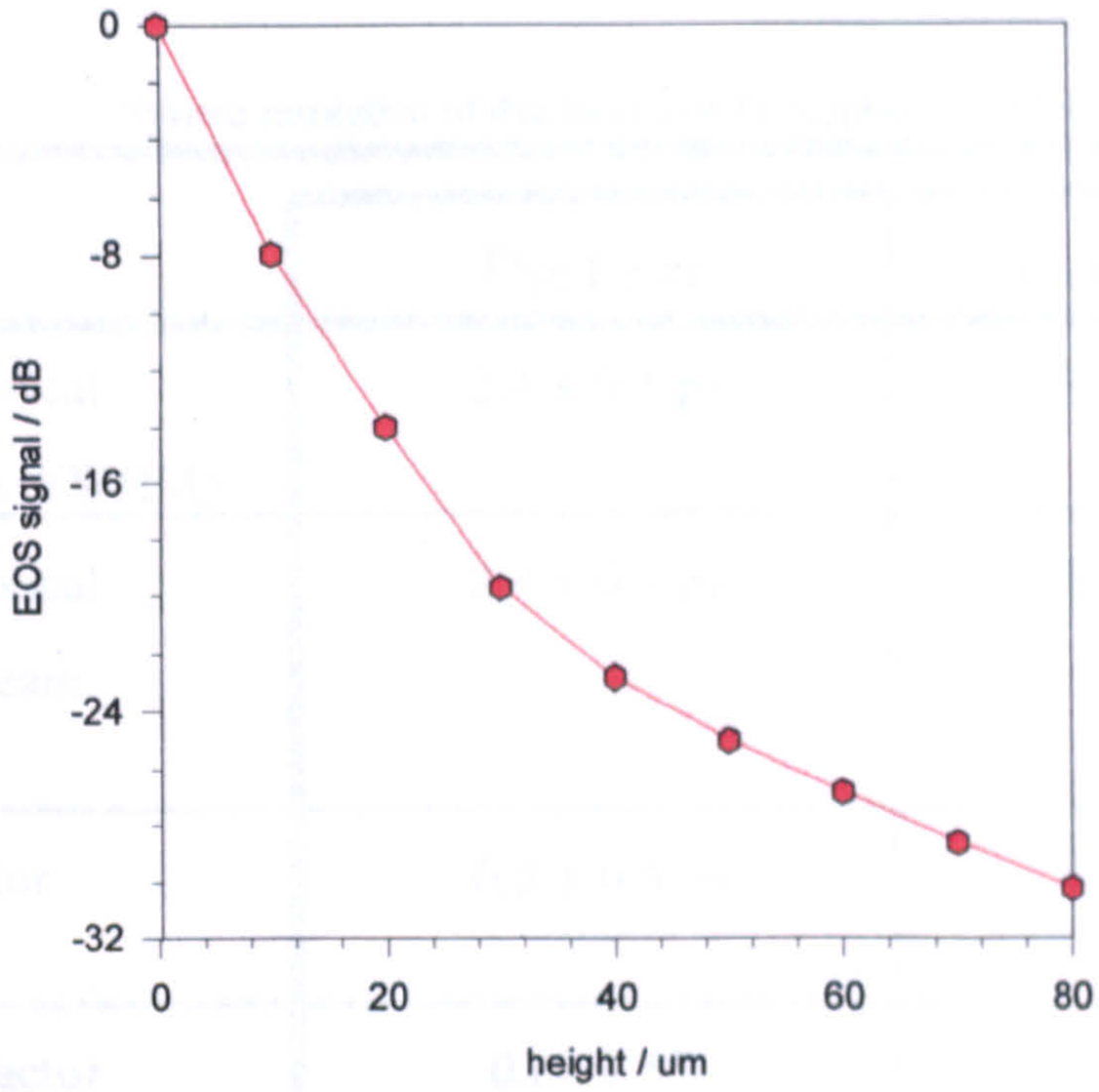

Figure 4.23 Variation of EOS signal with probe height.

The experiment was repeated with PG8 functioning as a pulse generator and a generation-sampling separation of 500 μm. Similar changes in peak EOS signal with height were measured. Small changes in shape were also apparent, but these was hard to quantify due to structure caused by other effects and, again, more work is required to investigate the invasiveness of the probe.

It is concluded that providing the probe was positioned no further than 20 μm away from the circuit, the S/N was adequate for the application.

4.9.2 Dye laser system resolution

The optical pulse duration for the dye laser EOS system, measured by an autocorrelator[14], was the same for the generation and sampling beams. The temporal resolution of the autocorrelator, quoted as < 1 ps, was assumed to be 0.5 ± 0.5 ps after

[14] Spectra-Physics Model 409.

a correction factor for the pulse shape was calculated (see later). The optical transit-time was calculated for light travelling through the 100 μm thick $LiTaO_3$ in double pass.

Table 4.2 System resolution of dye laser and Ti:sapphire laser EOS.

	Dye Laser	Ti:sapphire Laser
Measured optical sample beam (FWHM)	2.4 ± 0.1 ps	260 ± 10 fs
Measured optical generation beam (FWHM)	2.4 ± 0.1 ps	520 ± 20 fs
Autocorrelator resolution	0.5 ± 0.5 ps	80 ± 30 fs
Correction factor (shape dependant)	0.68 ± 5%	0.68 ± 5%
Corrected sample beam (FWHM)	1.5 ± 0.3 ps	170 ± 30 fs
Corrected generation beam (FWHM)	1.5 ± 0.3 ps	350 ± 40 fs
Optical transit time through $LiTaO_3$ probe	1.4 ± 0.1 ps (thickness 100 μm)	290 ± 30 fs (thickness 20 μm)
Electrical transit time across Gaussian beam waist (1/e spot diameter)	-	90 ± 20 fs
Overall system impulse response (FWHM)	2.6 ± 0.3 ps	490 ± 40 fs
Overall system electrical bandwidth (-3 dB)	120 ± 15 GHz	630 ± 50 GHz

Approximating the optical pulses to Gaussian shapes, and assigning an equivalent Gaussian to the transit-time value, the contributions were added in quadrature (equivalent to full convolution for Gaussian waveforms) to obtain an approximate value of 2.6 ± 0.4 ps FWHM for the system response (Table 4.2). This response corresponds to an electrical measurement bandwidth (-3 dB) of 120 ± 20 GHz, again assuming a Gaussian.

4.9.3 Ti:sapphire laser system resolution

With the Ti:sapphire system, the optical pulse measurements made with an autocorrelator[15] approached the temporal resolution limit of the instrument. This resolution is primarily determined by the optical delay block and doubling crystal. The Inrad manual states that the "resolution is better than 200 fs with the 35 mm glass block, and better than 50 fs with the 2.9 mm block". At the NPL the large block is used to give a broader temporal range.

Using the refractive indices given in the manual, the resolution was calculated for a wavelength of 800 nm. To do this it was assumed that the Mira output was not transform-limited. A time-bandwidth product of unity was taken, corresponding to a 10 nm optical bandwidth for 200 fs FWHM pulses. This gives an equivalent optical block resolution of 60 fs. The block resolution was added in quadrature to the quoted 50 fs (assumed to be a minimum due to contributions such as the thickness of the doubling crystal and photomultiplier tube response), giving a total resolution of 80 ± 30 fs.

An example of a Ti:sapphire sampling beam autocorrelation trace is presented in Figure 4.24 (the time scale has not been corrected for the scan rate). The autocorrelation of two theoretical pulse shapes, a Gaussian and the square of a hyperbolic secant ($sech^2$), are also displayed for comparison. It is seen that the measured Ti:sapphire pulse shape appears to match the Gaussian more closely, although differences between all three plots

---

[15] Inrad Model 5-14.

are small. (It should be stated here that the Mira manual[11] suggests that a typical Mira laser shape, before autocorrelation, is $sech^2$.) The correction factor, to convert a measured autocorrelation width to the width of the initial function, is dependent on the shape of the function. A value of 0.68 (between the Gaussian value of 0.707 and the $sech^2$ value of 0.648) is used here.

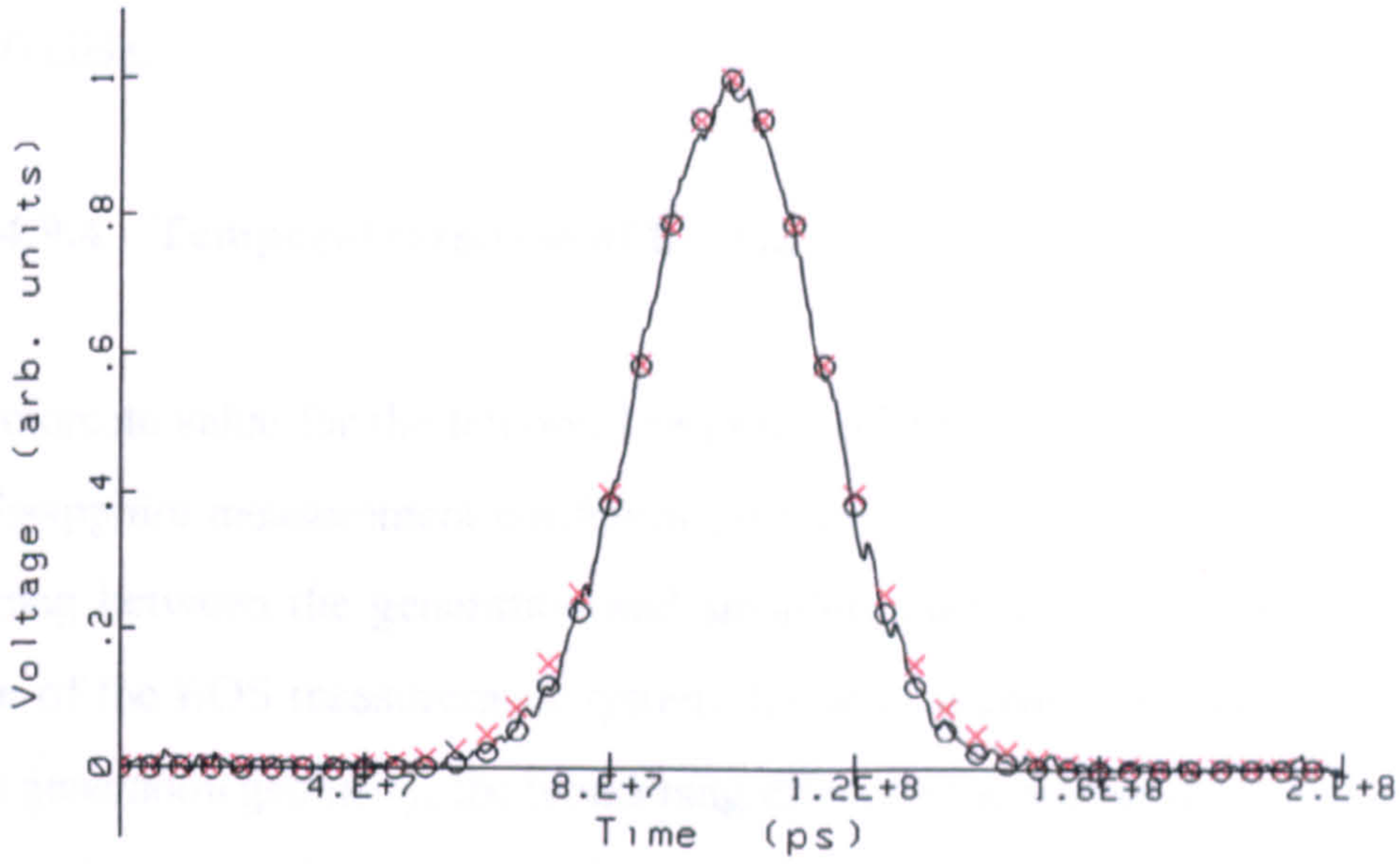

Figure 4.24 Background-free autocorrelations: —— measured Ti:sapphire trace; × Gaussian model; o $sech^2$ model.

It is observed that the measured (and corrected) Ti:sapphire excitation pulses in Table 4.2 are longer than the sampling pulses. The difference may be due to the material dispersion (group velocity dispersion) of the acousto-optic modulator, through which the excitation pulse is transmitted. A similar calculation to that for the optical block is performed. The theoretical propagation of 200 fs optical pulses, at 800 nm, along an 18 mm-long lead molybdate ($PbMoO_4$) modulator is found to account, within a factor of three, for the broadening of the excitation beam. Such broadened pulses are not well-defined shapes and therefore the difference may be due to the Gaussian approximation.

An additional contribution is needed for completeness, before calculating the EOS system response. The degradation in the EOS response due to the electrical pulse propagating across the sampling beam radial profile has been considered elsewhere,[6,15] and an

approximate value is included in the table.

Assuming Gaussian shapes for all the system contributions (as previously), and adding them in quadrature, an overall response of 490 ± 60 fs (FWHM) is obtained for the Ti:sapphire EOS system (Table 4.2). This is approximately five times faster than the dye laser EOS system. The equivalent electrical -3 dB bandwidth is increased to 630 ± 80 GHz.

4.9.4 Temporal response of LT-GaAs

An approximate value for the temporal response of the LT-GaAs is calculated here. All three Ti:sapphire measurement configurations are used. In each of the three examples, the spacing between the generation and sampling points was 100 μm. The temporal response of the EOS measurement system, the approximate RC parasitic contribution from the generation geometry, the broadening effect of the transmission line and the LT-GaAs response were all assumed to be Gaussian.

The EOS system response was convolved with the parasitic RC contribution of the geometry and the transmission line transfer function. (The value of the transfer functions are derived in *chapter 5*, where broadening effects of transmission lines are investigated.) The combined result was then deconvolved from the EOS measurement of the LT-GaAs to give a calculated LT-GaAs response. A summary of results from the three measurement configurations is shown in Table 4.3. The results illuminating the top and bottom slots of the CPW sliding contact are included, although the FWHM parameter does not provide sufficient information about the pulse shape and hence effect of the even CPW mode under such circumstances - therefore these results should be discarded and are not further discussed here.

The uncertainties in the calculation appear at first sight quite large. An uncertainty of 20% was estimated for the RC parasitic time-constant. The other uncertainties in the table are those quoted in this chapter and *chapter 5*. The effect of approximating all the

contributions to be Gaussians has not been included here, but it is believed that this would also be significant. The weighted mean of the CPW Auston switch and CPS results gives a LT-GaAs response of 430 fs.

Table 4.3 Deconvolved response of LT-GaAs.

	CPW sliding contact	CPW Auston switch	CPS sliding contact
3 × RC time-constant	510 ± 100 fs	900 ± 180 fs	270 ± 55 fs
Broadening effect of 100 μm line (FWHM)	600 ± 60 fs	600 ± 60 fs	380 ± 40 fs
EOS system response (FWHM)	490 ± 40 fs	490 ± 40 fs	490 ± 40 fs
EOS Measurement (FWHM)	1090 ± 55 fs (top slot) 800 ± 40 fs (bottom slot)	1330 ± 70 fs	770 ± 40 fs
Deconvolved LT-GaAs response (FWHM)	570 ± 155 fs (top slot) >0 fs (bottom slot)	530 ± 350 fs	370 ± 110 fs

4.10 Conclusions

It has been shown that electro-optic sampling provides an effective method of measuring very fast electrical pulses propagating along planar transmission lines. LT-GaAs photoconductive switches have been tested by EOS. Various geometries were appraised,

with the fastest pulse of 650 fs FWHM measured on a 10 μm coplanar stripline at a distance of 50 μm from the point of generation. Contributions to the resolution of the EOS system were considered and an uncertainty budget was calculated, resulting in an impulse response of 490 ± 40 fs, equivalent to a -3 dB bandwidth of 630 ± 50 GHz, for the Ti:sapphire-based system.

Using the EOS response, an RC parasitic contribution estimated from the geometry, and a value for the broadening effect of the transmission line derived in *chapter 5*, the response of the LT-GaAs was found by deconvolution to be approximately 400 fs FWHM. The results indicate that the transmission line and coax-planar transition need to be characterised before a LT-GaAs photoconductive switch can be used to calibrate a CRO, but the speed of the material is sufficiently fast for the application.

4.11 References to Chapter 4

1 J.A.Valdmanis and G.Mourou, "Sub-picosecond Electro-optic Sampling: Principles and Applications", IEEE J. Quant Elect, QE-22 , 1986, p 69-78.

2 D.Grischkowsky, I.N.Duling, J.C.Chen and C.C.Chi, "Electromagnetic Shock Waves from Transmission Lines", Phy. Review Lett., APS Vol.59, No.15, 1987, pp 1663-1666.

3 D.H.Auston, A.M.Johnson, P.R.Smith and J.C.Bean, "Picosecond Optoelectronic Detection, Sampling, and Correlation Experiments in Amorphous Silicon", Appl. Phys. Lett, Vol. 37, August 1980, pp 371-372.

4 K.C.Gupta, R.Garg and I.J.Bahl, "Microstrip Lines and Slotlines", Artech House Inc. Publishing, chapters 1 and 7, 1979.

5 See for example:
E.Hecht, "Optics", Addison-Wesley Publishing, reprint 1989, pp 318-320.

6 D.Henderson, "Measurement of the Temporal Response of a Picosecond Sampling Oscilloscope by Optoelectronic Techniques", Ph.D. Thesis, University of London, July 1989.

7 D.Le.Quang, D.Erasme and B.Huyart, "Calibrated Electro-optic Measurements of a MMIC", IEEE MTT-S Digest, paper TH3C-2, pp 1593-1596.

8 M.J.Rodwell, D.M.Bloom and K.J.Weingarten, "Subpicosecond Laser Timing Stabilization", IEEE Journ. Quant. Elect., Vol. 25, No.4, April 1989, pp 817-827.

9 W.Mertin, C.Roths, F.Taenzler and E.Kubalek, "Probe Tip Invasiveness at Indirect Electro-optic Sampling of MMIC", IEEE Microwave Theory and Techniques Symposium Digest, 1993, pp 1351-1354.

10 J.G.Edwards and D.Henderson, "Temperature Control of an Acousto-optic Modulator in an Argon Ion Laser using an R.F. Servo Loop", NPL Internal Report DES 78, 1983.

11 "Mira Model 900 Operator Manual", Coherent Inc., Pam Alto, 1992, Chapter 7.

12 M.Y.Frankel, J.F.Whitaker, G.A.Mourou and J.A.Valdmanis, "Experimental Characterisation of External Electro-optic Probes", IEEE Microwave & Guided

Lett., Vol. 1, No. 3, March 1991, pp 60-62.

13 J.Son, J.V.Rudd and J.F.Whitaker, "Noise Characteristics of a Self-mode-locked Ti:sapphire Laser", Optics Lett., Vol. 17, No. 10, May 1992, pp 733-735.

14 M.Riaziat, R.M.Ahy and I.J.Feng, "Propagation Modes and Dispersion Characteristics of CPW", IEEE Trans. Microw. Theory & Tech., MTT-38, No. 3, March 1989, pp 245-251.

15 B.H.Kolner and D.M.Bloom, "Electro-optic Sampling in GaAs Integrated Circuits", IEEE Journal Quant. Elect., Vol. QE-22, No. 1, Jan 1986, pp 79-93.

5 DE-EMBEDDING THE TRANSMISSION LINE AND TRANSITION

5.1 Introduction

The previous chapter demonstrates that low-temperature (LT)-GaAs photoconductive switches can produce very short electrical pulses - sub-picosecond when measured by electro-optic sampling close to the generation point. However, the fidelity degrades as the pulses propagate along lengths of planar transmission line (Coplanar Waveguide (CPW) or Coplanar Stripline (CPS)) and/or across CPW-coaxial transitions. For example, dispersion and losses broaden the pulse width and decrease the pulse amplitude. To be a practical calibration source for an oscilloscope, the pulse generator needs to be well characterised. The pulse shape needs to be known at the coaxial reference plane - where an oscilloscope would be connected and calibrated. Measuring the pulse generator close to the generation point and at points between the coaxial plane and generation point characterises the generator more fully.

Knowledge of the effect of the transmission line and transition is particularly important if the speed of the pulse generator is significantly slower at the coaxial reference plane than at, or close to, the generation point, and also if the pulse generator at the coax reference plane is comparable to, or slower, than the speed of the oscilloscope to be calibrated. Both of these conditions are found to apply in *chapter 6*. A known effect can be removed from the result by deconvolution - this technique is known as de-embedding - and can improve the uncertainties in a calibration of an oscilloscope. The subject of deconvolution is addressed in *chapter 6*.

This chapter describes how knowledge of transmission line and transition effects can be built up by comparing results from different time and frequency-domain measurement techniques, and by the application of transmission line modelling. A single-transition transfer function is derived which is used in the next chapter.

5.1.1 Approach to de-embedding - organisation of chapter

Although the pulse generator has a GaAs substrate, some measurements and modelling are also performed on CPW lines with alumina substrates. The purpose of these measurements is to help validate some of the time and frequency-domain comparisons and techniques.

A transmission line model is described which calculates the losses and phase changes on planar lines. Alumina CPW and small, large and tapered sections of GaAs CPW are accommodated. An attempt is made to explore the uncertainties in the model.

The section on frequency-domain measurements begins by summarising the functionality and calibration of an automatic network analyser (ANA). The ANA measurement of a test-fixture (comprising two coaxial-coplanar transitions and an insertable length of CPW, such as GaAs or alumina) is then described. The direct measurement of a complete test-fixture (two transitions and line) is compared to a method which combines reference planes to obtain a transfer-function of one transition and line. ANA results with different lines are compared to the frequency-domain model results.

The time-domain section starts by comparing sampling oscilloscope measurements of the test-fixture with measurements in the frequency-domain section. The results from the transmission line model are examined in the time-domain and compared to electro-optic sampling (EOS) measurements.

Using an EOS back-to-back transition technique and a combination of previous results from the chapter, the impulse response (time-domain transfer-function) of a single coax-coplanar transition is derived.

5.1.2 Transmission line components of the pulse generator

An LT-GaAs device is shown in Figure 5.1, with the individual components of the

photoconductive switch, between the generation point and oscilloscope reference plane, labelled for ease of discussion. An Auston switch device (series-gap) is shown although the diagram is equally applicable to a sliding contact device (through line).

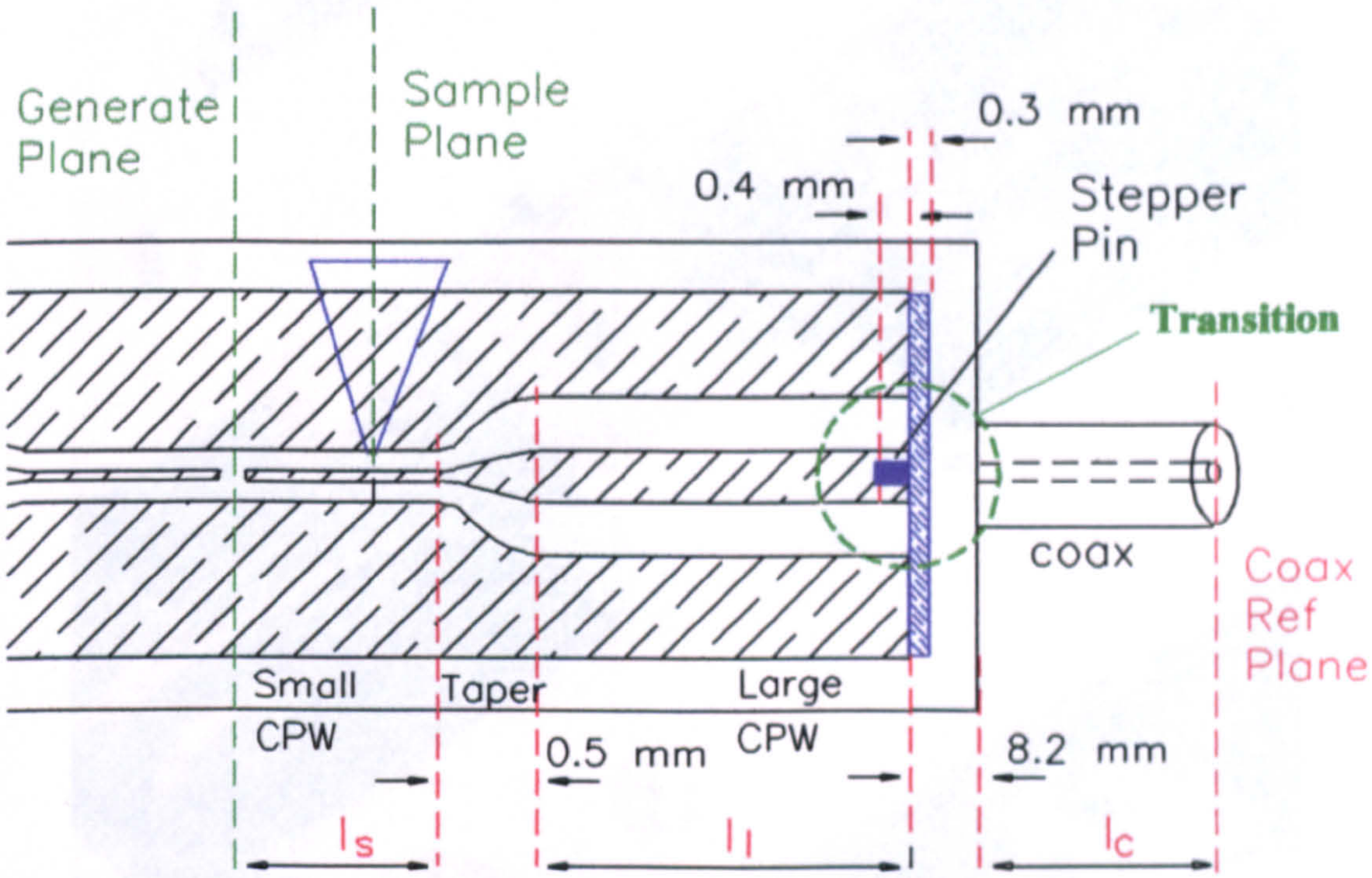

Figure 5.1 Transmission line components of the photoconductive switch.

The components along which the pulses propagate can be summarised as: a length l_s of small CPW; a 0.5 mm long taper; a length l_l of large CPW; a CPW-coaxial transition; and a length l_c of coaxial transmission line. A bias tee may also be present between the coaxial transmission line and the oscilloscope reference plane.

The transition consists of three main items: spring-loaded jaws of the test-fixture (hatched blue area), which hold the circuit in place by clamping approximately 0.3 mm of the substrate end and the ground planes; a stepper pin (solid blue area), which contacts to the central line of the CPW and which intrudes past the ground plane clamps by about 0.4 mm; and a dielectric bead inside the metal flange, whose inner connects the stepper pin to the central coax connector and whose outer is soldered to the flange, connecting the coax outer to the CPW ground planes. The total thickness of the flange is 7.9 mm. A

photograph of a UTF, detailing a transition and GaAs circuit is shown in Figure 5.2.

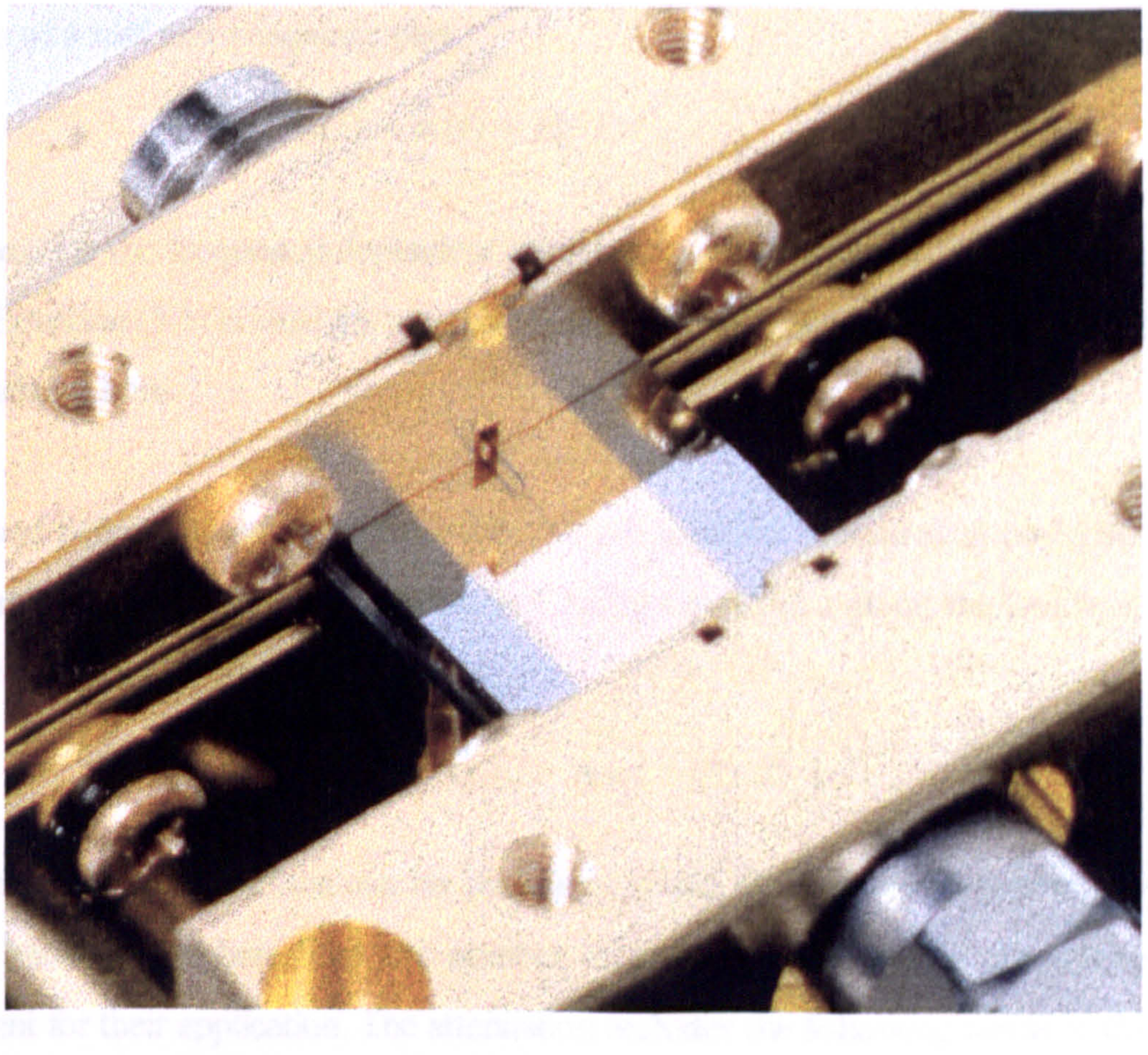

Figure 5.2 Picture of UTF showing coax-CPW transition.

To model the transition to the required frequency requires a full 3D simulator. Commercial packages, such as Hewlett Packard's High-Frequency Structure Software, require processing time on workstations of approximately one half a day per frequency point. This was not considered within the scope of the project.

5.2 Transmission line modelling

The propagation of a pulse along a transmission line can be described[1] by

$$V(t,z) = V(t,0) \exp(-\gamma(f).\ z) \quad , \tag{5.1}$$

where V(t,0) is a pulse initially at position z = 0 (z is the direction of propagation on the transmission line), and V(t,z) is the pulse after propagating along distance z. Term $\gamma(f)$ consists of a real and imaginary part,

$$\gamma(f) = \alpha(f) + j\beta(f) \quad , \tag{5.2}$$

where $\alpha(f)$ is the frequency-dependent attenuation and $\beta(f)$ is the frequency-dependent phase. Equation (5.1) is valid for any transmission line geometry, but only the planar case is considered here.

If $\alpha(f)$ and $\beta(f)$ are known, then the evolution of the pulse, measured at position z = 0 on a transmission line, can be calculated at a further position z along the line by using the Fourier transform (FT):

$$V(t,z) = FT^{-1}\left[FT(V(t,0)) \cdot \exp(-\gamma(f) \cdot z) \right] \quad . \tag{5.3}$$

Many physical contributions can be contained within the general terms attenuation and phase. Most researchers limit the number of contributions used in a model to those significant for their application. The attenuation includes the following terms in this thesis:

$$\alpha(f) = \alpha_d(f) + \alpha_c(f) + \alpha_r(f) \quad , \tag{5.4}$$

where α_d is the dielectric loss, α_c is the conduction loss, and α_r is the radiation loss. The phase includes the following terms:

$$\beta(f) = \beta_m(f) + \beta_c(f) \quad , \tag{5.5}$$

where β_m is the modal dispersion and β_c is the conductor phase shift.

The physical manifestation of each term above is briefly explored and the functional dependence of all the terms summarised. Some of the equations follow on from those defined in *chapter 3*. Where possible, known errors or limitations are stated for each of the three types of CPW line investigated: alumina, small GaAs and large GaAs. Stated systematic uncertainties are assumed to be at the 95% confidence level, and stated random uncertainties are assumed to be equal to one standard deviation, and are doubled to give

equivalent 95% confidence levels. Uncertainties are added in quadrature. The latest procedure in applying uncertainties is adhered to.[2]

5.2.1 Modal dispersion β_m

Coplanar transmission lines are inherently dispersive and cannot support pure TEM waves. A term for the frequency-dependent effective dielectric constant $\epsilon_{re}(f)$ was noted in *chapter 3*. The frequency dependence is due to the fringing electric fields of the line experiencing an inhomogeneous dielectric. At low frequencies $\epsilon_{re}(f)$ is approximately equal to the average of the dielectric constants for the substrate and air. As the frequency increases, the lower wavelength confines more of the CPW guided wave energy into the substrate. Therefore, the effective dielectric constant increases, with a subsequent decrease in the phase velocity. Such a frequency-dependent phase velocity is known as modal dispersion.

The phase velocity can be defined as

$$v_p = \frac{2\pi f}{\beta(f)} \quad . \tag{5.6}$$

An alternative definition is

$$v = \frac{c}{\sqrt{\epsilon_{re}(f)}} \quad . \tag{5.7}$$

Combining these two definitions gives an expression for the modal dispersion as

$$\beta_m(f) = \frac{2\pi f}{c}\sqrt{\epsilon_{re}(f)} \quad . \tag{5.8}$$

Over a similar frequency range, modal dispersion is more apparent in larger CPW lines than smaller lines. This is because changes in frequency affect the modal energy confinement, and therefore the frequency-dependent dielectric constant, more in larger lines than smaller lines. Smaller lines can support smaller wavelengths, corresponding to

higher frequencies. A guide to the effect is the ratio of wavelength to size of line.

The uncertainties in β_m include four contributions which are discussed:

(i) The knowledge of the dielectric constant ϵ.

For GaAs assume 13.1 ± 0.2, for alumina assume 9.98 ± 0.02.

(ii) The error in the quasi-static effective dielectric constant ϵ_{re} expression.

Chapter 3 (and the references therein) state this to be ± 1.5% provided three conditions apply, namely that h/W >>1, $\epsilon_r \geq 9$, and $0 \leq k$ 0.7. For the GaAs and alumina CPW lines in this chapter, all three conditions apply.

(iii) The error in the square-root of the frequency-dependent effective dielectric constant ($\sqrt{\epsilon_{re}}$) expression.

The references in *Chapter 3* give the error in the closed-form equations as within ± 5% of the full-wave solution, provided that four conditions apply. The first two conditions, that $0.1 < S/W < 3$ and $1.5 < \epsilon < 50$, are valid for the lines considered here. The third condition, that $0 < f/f_{TE} < 10$, limits the range of validity to be 400 GHz or less. Lastly, $0.1 < S/h < 5$ applies to the alumina and large GaAs CPW, but the small GaAs CPW has a S/h ratio of 0.06. The condition in not quite met, but the extra error is assumed to be small at ± 1%. No attempt has been made to quantify the error in the full-wave solution referenced.

(iv) The error introduced in the calculation of $\sqrt{\epsilon_{re}}$ by the uncertainty in the line dimensions W and S. (The effect of changes in substrate thickness h of ± 10 μm is negligible).

The uncertainty in W and S is estimated to be ± 2 μm for the small GaAs and alumina lines, and ± 5 μm for the large GaAs line. Although the effect of the uncertainty limits can change the characteristic impedance by ± 6% in the case of the small GaAs, this only changes the $\sqrt{\epsilon_{re}}$ expression by ± 1.6%.

Applying the above uncertainties gives the total error in $\beta_m(f)$ for frequencies below

400 GHz as: ± 5.2% for the alumina line; ± 5.3% for the large GaAs line; and ± 6.3% for the small GaAs line.

5.2.2 Conductor loss α_c and conductor phase β_c

Changes in the conductivity of materials with frequency are well documented.[3] The skin-effect arises in a conducting material when high frequencies propagate in the cross-section of a conductor smaller than that available, effectively limited by short-wavelength components. Coplanar lines experience conduction loss and phase changes due to the frequency dependence of the transmission line metallisation. The characteristic impedance Z_{cpw} of the line and the complex surface impedance Z_s of the conductor affect both α_c and β_c, and can be expressed[1] as:

$$\alpha_c(f) = g_2(f) . Z_{cpw}(f) . Re\left[Z_s(f)\right] \quad , \tag{5.9}$$

and

$$\beta_c(f) = g_2(f) . Z_{cpw}(f) . Im\left[Z_s(f)\right] \quad , \tag{5.10}$$

where Z_{cpw} is described in *chapter 3*, the geometric factor g_2 is given by[1]

$$g_2 = 4.88\times10^{-4}\,\epsilon_{re} . \frac{P}{\pi W} . \left(1 + \frac{S}{W}\right) . \frac{\frac{1.25}{\pi}\log\frac{4\pi S}{t} + 1 + \frac{1.25\,t}{\pi s}}{\left[2 + \frac{S}{W} - \frac{1.25\,t}{\pi W}\left(1 + \log\frac{4\pi S}{t}\right)\right]^2} \quad , \tag{5.11}$$

where P is defined by

$$P = \frac{1}{(1-k)\sqrt{k}} \qquad for\ \frac{1}{\sqrt{2}} \le k \le 1 \tag{5.12}$$

$$P = \frac{k}{(1-k^2)^{\frac{3}{4}}\,(1-\sqrt{1-k^2})} \cdot \frac{K(k)^2}{K'(k)^2} \qquad for\ 0 \le k \le \frac{1}{\sqrt{2}}\ , \tag{5.13}$$

and Z_s is given by[1]

$$Z_s(f) = \sqrt{\frac{i2\,\pi f \mu_0}{\sigma}} \cdot \coth\left[t\sqrt{i2\,\pi f \mu_0 \sigma}\right]\ , \tag{5.14}$$

where μ_o is the vacuum permeability, σ is the metallisation conductivity (real) and t is the metallisation thickness.

The uncertainties in α_c and β_c include contributions from Z_{cpw}, Z_s and g_2:

(i) The uncertainty in Z_{cpw} includes the error in $\sqrt{\epsilon_{re}}$ and in the elliptical integral terms given in *chapter 3*.

The $\sqrt{\epsilon_{re}}$ term is the same term used in the modal dispersion calculation and hence the error is the same. The error in the elliptical integral can be split into two parts: the error in calculating k = S/(S+2W) from the uncertainties in the line dimensions (see 5.2.1 modal dispersion); and the error in approximating the elliptical integrals. The latter calculation has been found to be accurate to three parts per million and is ignored here.

(ii) The uncertainty in Z_s depends on the error in σ and t.

For a GaAs line, the total thickness t is measured during the vacuum deposition with a calibrated thin-film monitor, giving a typical value of $0.60 \pm 0.05\ \mu m$. The conductivity is not constant for multi-layered metallisation structures as it depends on the "quality" of the deposition, which varies with the vacuum pressure and evaporation boat current. An average resistivity value of $(4 \pm 1) \times 10^{-8}\ \Omega m$ is assumed, experimentally derived from resistance measurements in *chapter 3*.

The thickness of the alumina lines has not been independently measured. Wiltron quote the thickness of their lines as $t = 4.0 \pm 0.5 \mu m$. The resistivity of the Au is assumed to be $2.2 \pm 0.3 \times 10^{-8}\ \Omega m$.

(iii) The uncertainty in the geometric constant g_2.

The main uncertainty in g_2 is given by the uncertainties in the line dimensions already discussed. The error in the accuracy of the expression is not known and is assumed relatively small.

The total uncertainties in $\alpha_c(f)$ and $\beta_c(f)$ have been calculated for frequencies below 400 GHz and are defined here as percentages: ± 18% for the alumina line; ± 16% for the large GaAs line; and ± 18% for the small GaAs line.

5.2.3 Dielectric loss α_d

Dielectric loss, sometimes referred to as substrate loss, arises from the substrate not being a perfect insulator. Conduction occurs which results in some energy absorption in the substrate and hence a small loss.[4] For coplanar lines, the dielectric loss is given[5] by

$$\alpha_d(f) = 27.3 \frac{\epsilon_r}{\sqrt{\epsilon_{re}(f)}} \cdot \frac{\epsilon_{re}(f) - 1}{\epsilon_r - 1} \cdot \frac{\tan\delta(f)}{\lambda_0} \quad , \tag{5.15}$$

where $\tan\delta$ is the dielectric loss tangent and λ_0 is the free-space wavelength. The loss is much smaller with semi-insulating substrates than for conducting substrates, but must still be included in the model.

The total uncertainty in α_d arises from the uncertainty in the terms comprising ϵ_r and $\epsilon_{re}(f)$, and the uncertainty in the loss tangent:

(i) Uncertainty in ϵ_r and $\epsilon_{re}(f)$.

The uncertainty in the terms preceding the loss tangent are calculated assuming the errors defined in the modal dispersion section. The accuracy of the expression is unknown.

(ii) Loss tangent.

The loss tangents of GaAs and alumina are dependent on the exact type of substrate and the frequency of interest. For GaAs, a value of $8 \pm 3 \times 10^{-4}$ up to frequencies of 100 GHz

is typical[6]. With most substrates, the loss tangent slowly decreases with frequency, up to about 300 GHz, but different substrates can give atypical results. The loss tangent of alumina is highly dependent on the amount and type of impurities, and can vary[7] between 2×10^{-4} and 10×10^{-4}. A value of $4.0 \pm 2 \times 10^{-4}$ is used here. The loss tangent of alumina varies more slowly over frequency and the effect is small compared to the other uncertainties.

The uncertainties in $\alpha_d(f)$ are estimated to be: ± 50% for the alumina line; ± 38% for the large GaAs line; and ± 39% for the small GaAs line.

5.2.4 Radiation loss α_r

The origin of radiation loss lies in the propagating guided-mode signal travelling with a faster velocity than the electromagnetic propagation velocity of the substrate. Because of this, the guided mode loses energy through an electromagnetic shock wave, which is emitted into the substrate at an angle ψ, determined by the velocity mismatch between the guided and radiated modes, as

$$\cos\varphi = \sqrt{\frac{\epsilon_{re}(f)}{\epsilon_r}} \quad . \tag{5.16}$$

The full expression for radiation loss uses a similar approach to Phatak[8] as modified by Frankel[9] and is reproduced below:

$$\alpha_r(f) = \left(\frac{\pi}{2}\right)^5 \cdot \sqrt{\frac{\epsilon_r}{\epsilon_{re}(f)}} \cdot \left(1 - \frac{\epsilon_{re}(f)}{\epsilon_r}\right)^2 \cdot \frac{(S+2W)^2 \epsilon_r^{3/2}}{c^3 K'(k) K(k)} \cdot f^3 \tag{5.17}$$

The above expression is accurate to ± 3% provided that three conditions apply:

(i) $0.1 < S/W < 10$

This condition is met by the alumina line and both GaAs lines.

(ii) $\lambda > S+2W$

The wavelength constraint limits the validity to approximately 400 GHz for the alumina and large GaAs lines. (For the small GaAs line the range of validity with this condition extends into the terahertz regime).

(iii) $d > 3W$

This condition is only met by the small GaAs line. The large GaAs line has a central line width $W = 280\ \mu m$ and substrate thickness $d = 450\ \mu m$. The alumina line has $W = 380\ \mu m$ and $d = 635\ \mu m$. An additional error for the last two lines of ±2% is therefore included.

The uncertainties of each term in expression (5.17) have been discussed previously. The total uncertainty in $\alpha_r(f)$ is therefore estimated to be: ± 22% for the alumina line; ± 23% for the large GaAs line; and ± 29% for the small GaAs line.

5.2.5 Summary of terms in model

Using the terms discussed above, and ignoring the frequency dependence of the dielectric components in the equations, the functional dependence of the total loss can be summarised as

$$\alpha(f) \propto \frac{1}{W}\sqrt{\frac{f}{\sigma}} + f\tan\delta(f) + f^3(S+2W)^2 \quad . \tag{5.18}$$

The equations in the model are used to calculate the losses and phase changes for the three CPW lines. The results from the model in the frequency-domain are given in *section 5.3.4* and are compared to experimental frequency-domain results in *section 5.3.5*.

The results from this section are used in *Section 5.4.2* to model the pulse propagation along CPW lines. The results are compared to experimental time-domain results in *section 5.4.3*.

5.3 Frequency-domain measurements

This section starts by describing the basic operation of an automatic network analyser. The instrument is used to perform measurements in the frequency-domain of different lines under different configurations. Where possible, the results are compared to a model.

5.3.1 The automatic network analyser

The frequency-domain measurements described here are performed with a two-port automatic network analyser[1] (ANA).[10] Before use, the ANA requires calibration with known standards at the reference planes.

The ANA can be modelled as a pair of transmission interferometers. The two-port ANA usually consists of a single synthesised microwave source and a switch which can excite either of the two halves of the system in turn (see Figure 5.3). The excitation, after transmitting through or reflecting off the device under test (DUT), is coupled with directional couplers onto microwave receivers which give vector indications proportional to the complex voltage amplitudes a_1, a_2, b_1, and b_2. The frequency-dependent scattering parameters[11] S_{11} and S_{21} are determined with the switch positioned to excite port 1, and S_{12} and S_{22} are determined with the switch positioned to excite port 2.

Imperfections in the ANA hardware, such as connector mismatches, non-ideal directional couplers, incorrect characteristic impedances of cables and non-perfect receivers, give rise to spurious signals that beat with the signal from the system under test. In order to correct for the corrupted signal paths, the ANA is defined to be perfect, but two fictitious "error" networks, X and Y, are added to allow the imperfections to be modelled (Figure 5.3). The calibration process essentially consists of finding the transmission-matrix components a_x, a_y, b_x, and b_y for the networks X and Y.

---

[1] The measurements were all made with a Wiltron 360B 60 GHz ANA located in DES branch C of NPL, in Malvern, Worcs. The help of Simon Hall and David Bannister in making some of the measurements, under my project supervision, is gratefully acknowledged.

Assumptions are made to simplify the two error networks, resulting in fourteen complex error-coefficients for the complete system. These are solved by connecting calculable calibration standards to the ANA measurement ports and using the ANA firmware routines to solve the fourteen error (or calibration) coefficients.

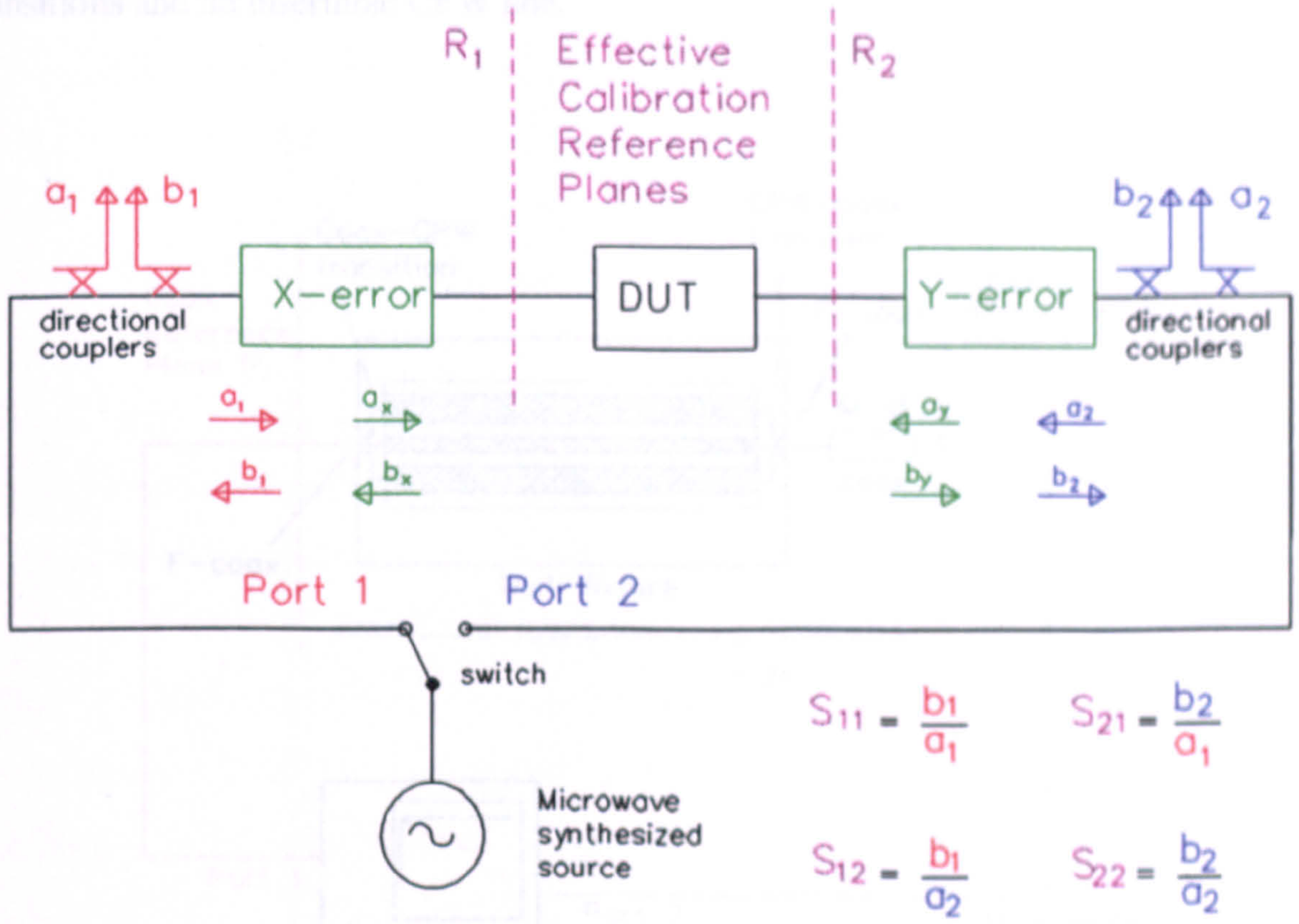

Figure 5.3 Schematic of ANA.

There are three main classifications of calibration routines, the first two of which are used in this thesis: the Open-Short-Load-Through (OSLT) procedure; the Through-Reflect-Line (TRL) procedure and the Through-Reflect-Match (TRM) procedure. Details are provided in a range of literature.[12,13] The fundamental requirement is for a minimum of three two-port standards which are sufficiently different from each other to provide three independent instrument states during calibration. One standard is needed to provide a reference characteristic impedance; the second is required to set the reference plane; and the third is needed to provide a relatively high mismatch reflection.

Once the ANA has been calibrated, a DUT can be inserted between the calibration

reference planes R_1 and R_2 and the full S-parameters measured.

5.3.2 Two transition measurements with an ANA

The aim of this section is to find the network parameters of a test-fixture containing two transitions and an insertable CPW line.

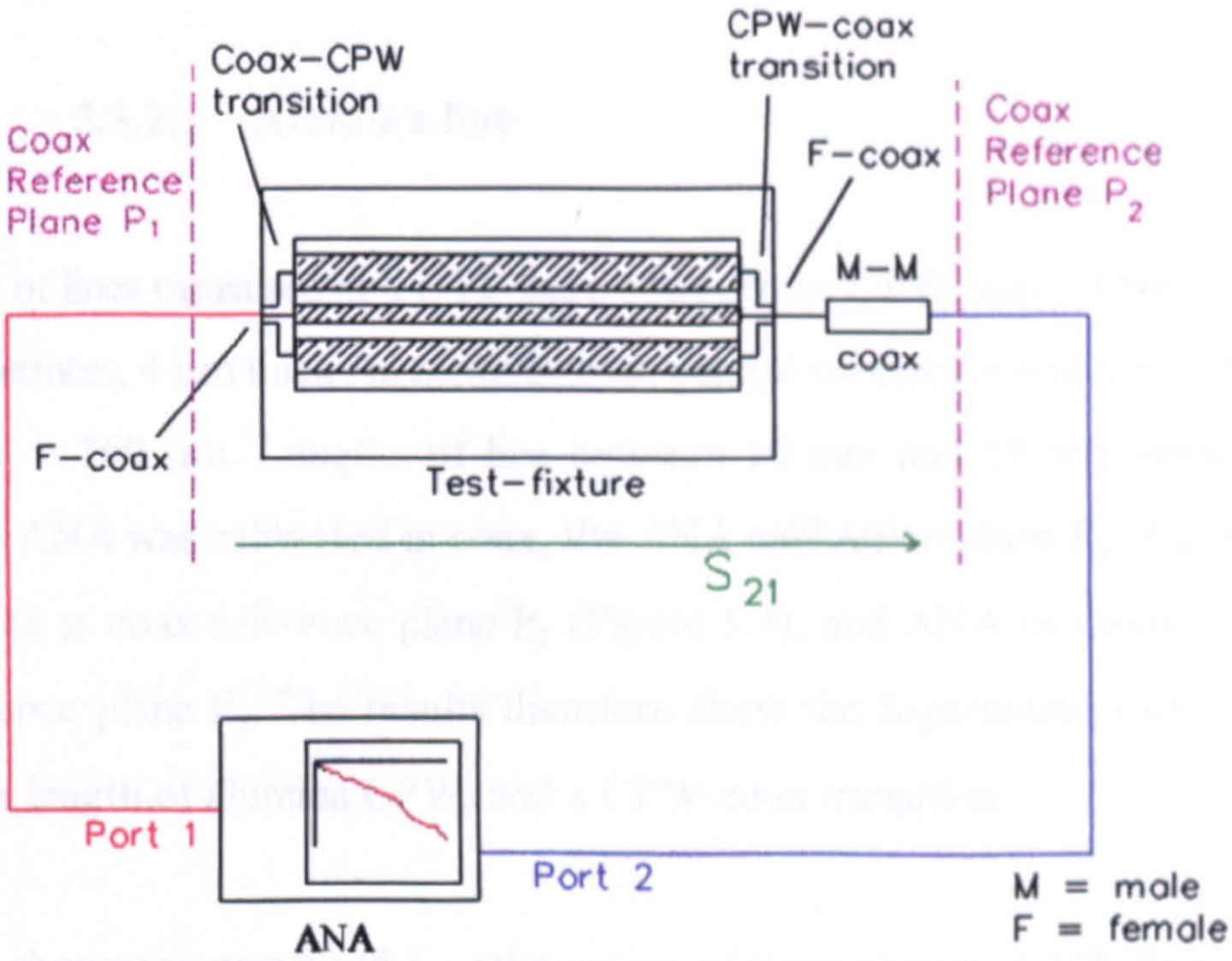

Figure 5.4 Reference planes of two transition ANA measurements.

A 60 GHz coaxial cable[2] was connected to each of the two ports of the ANA, and each end was calibrated with items from a calibration kit[3] by the OSLT procedure - used here for ease of use - defining two coaxial calibration reference planes. The coaxial connectors of a Universal Test Fixture (UTF) were then connected to the cables. The arrangement is described in Figure 5.4. (To complete the calibration procedure it was necessary for one cable to have a male connector and the other a female connector. Therefore an additional male-to-male adapter was attached to the UTF. The effect of the additional adapter was

---

2 Wiltron semi-rigid V-3670 cables.

3 Wiltron V-3564 connector calibration kit.

found to be small and hence the adapter was not itself de-embedded from the UTF results.)

Sets of CPW lines were inserted into one of two UTFs and the full S-parameters of each line and UTF were measured with the calibrated ANA between reference planes P_1 and P_2. Each measurement was performed over the 40 MHz to 60 GHz frequency range, corresponding to a frequency increment of 120 MHz for a 500 point S-parameter. Typically each data point was averaged between 32 and 128 times.

5.3.2.1 Alumina line

The first set of lines measured in a UTF were commercial CPW lines.[4] These had 650 μm alumina substrates, 4 μm thick Au metallisation, central conductor width S = 380 μm and slot gap W = 160 μm. Lengths of line between 10 mm and 19 mm were measured. Because the ANA was calibrated in coax, the ANA calibration plane R_1 (Figure 5.3) was defined to be at coax reference plane P_1 (Figure 5.4), and ANA calibration plane R_2 at coax reference plane P_2. The results therefore show the S-parameters of a coax-CPW transition, a length of alumina CPW, and a CPW-coax transition.

Figure 5.5 shows the measured S_{21} attenuation of three alumina CPW lines of different length, mounted in the first test-fixture, designated UTF1, to distinguish it from the second test-fixture UTF2 (with springs removed for GaAs devices). Up to about 40 GHz, the maximum difference between the attenuation of the 10 mm and 19 mm lines is about 1 dB. Above this frequency more structure is apparent in the measurements and the results from each line spread out more. The period of the rippled structure is found to be equal to the frequency of a standing wave, inversely proportional to the propagation distance defined by each length of line.

---

[4] Wiltron UTF Calibration/Verification kit model 36804-25C

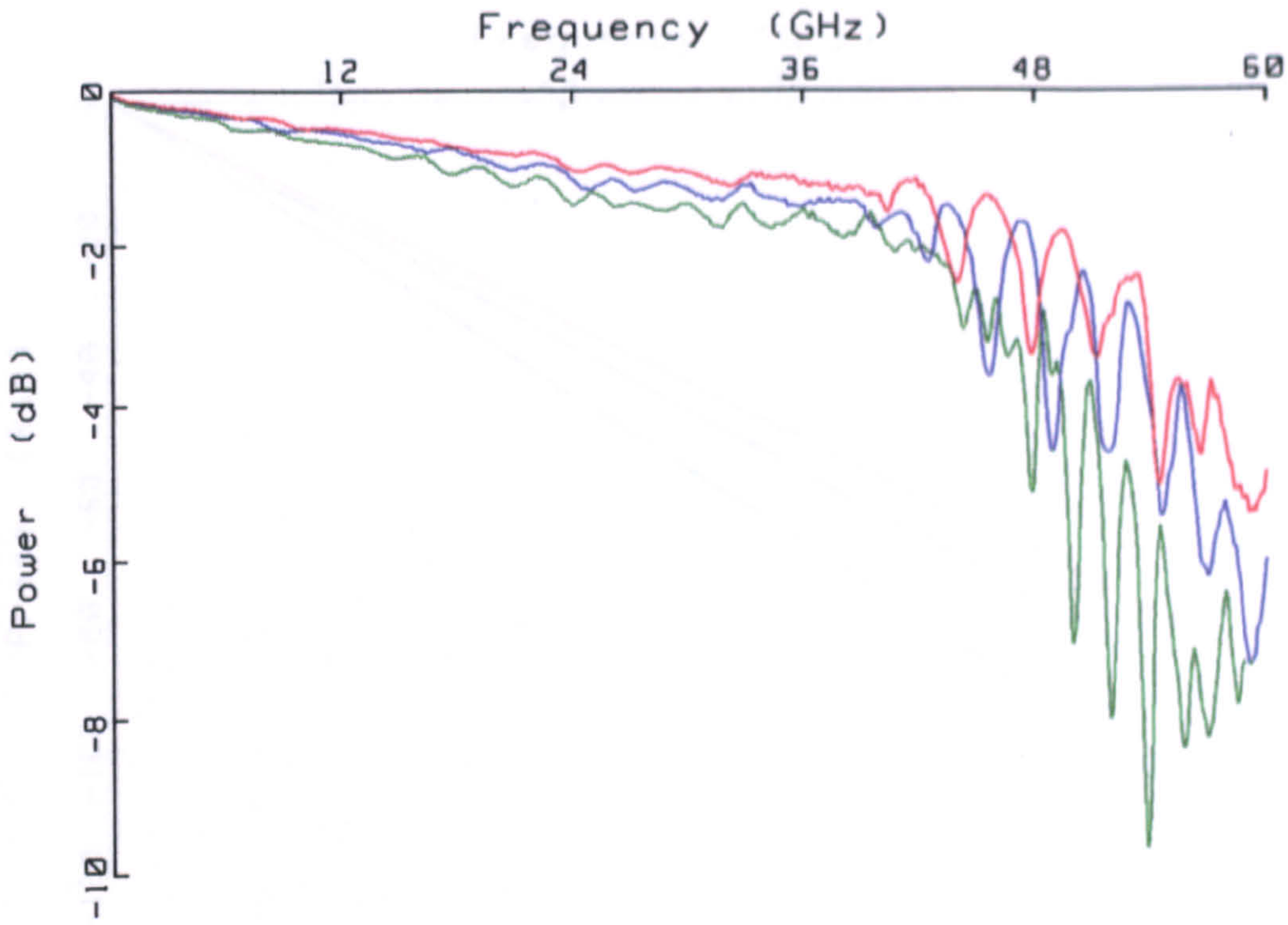

Figure 5.5 ANA S_{21} attenuation measurement of UTF1 and alumina CPW.
Line lengths: — 10 mm, — 13 mm, — 19 mm.

The phase of the same S_{21} measurements is displayed in Figure 5.6 Although the ANA displays phase results in a similar format, a more useful method is required to analyse the results. The linear changes in phase with frequency are a result of the electrical delay introduced by the insertion of the UTF between the ANA calibration reference planes. For example, at 48 GHz, the phase change of the 10 mm line is 68 rad or 10.8 periods (of 2π rad). The periods correspond to an electrical path length of 230 ps, consistent with a propagation velocity close to the speed of light for the two 7.9 mm transitions and adapter and a propagation velocity of $c/\sqrt{\epsilon_{re}}$ for the CPW line. Therefore, the linear changes are subtracted from the results, and the non-linear phase changes are plotted. The advantage is that effects such as dispersion are displayed more clearly. The disadvantage is some results may look noisier than measured.

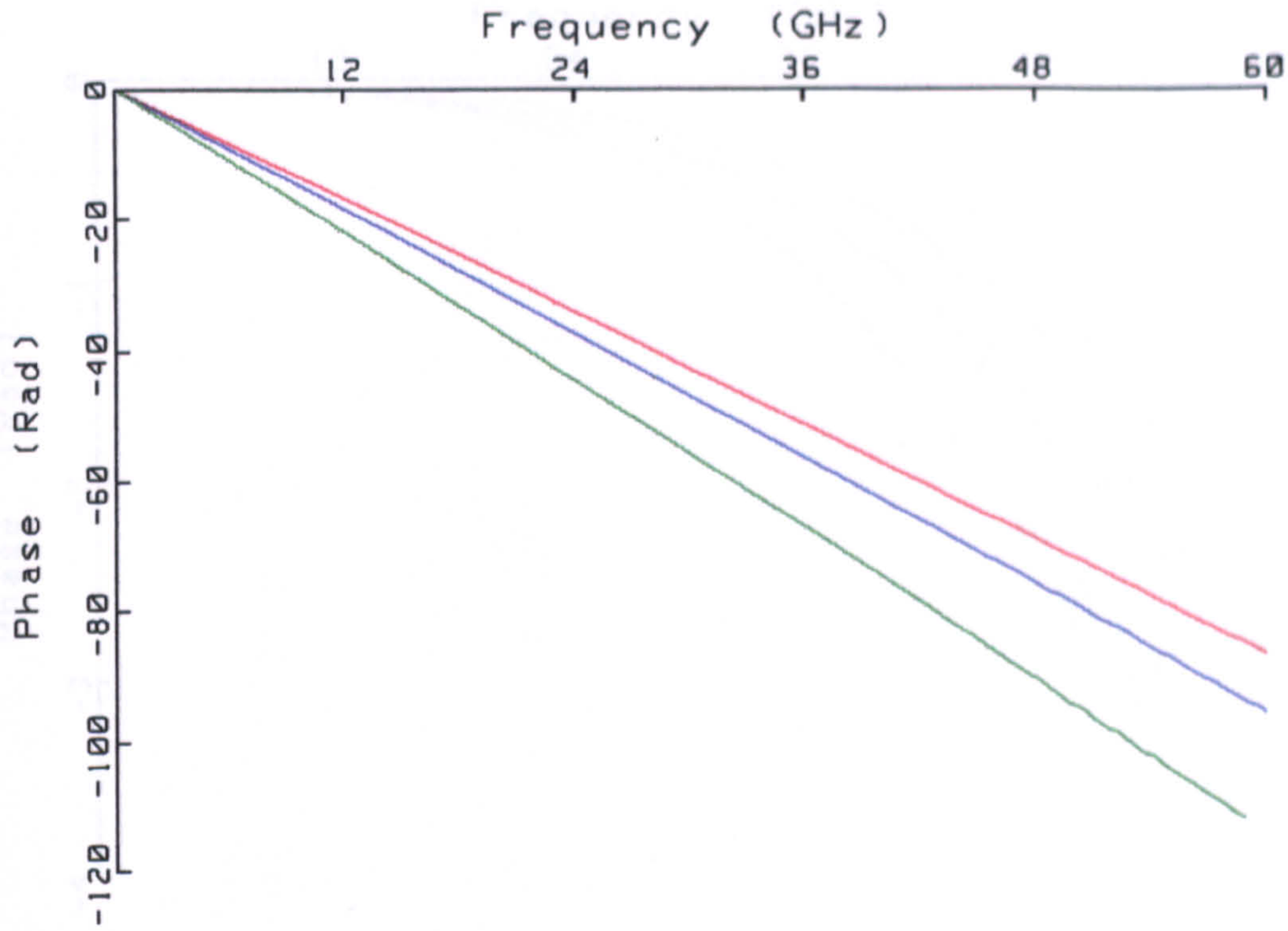

Figure 5.6 ANA S_{21} phase measurement of UTF1 and alumina CPW.
Line lengths: — 10 mm, — 13 mm, — 19 mm.

The phase in Figure 5.6 is re-plotted by subtracting from each CPW length a linear fit, defined over the first 5 GHz. The results are displayed in Figure 5.7 and show a dispersive component - the phase change increases with frequency and line length. Other phase results in this thesis are plotted using a similar method.

The second test-fixture, UTF2, was also measured with alumina lines, producing sets of results with similar structure to UTF1 (not shown). Up to about 50 GHz, each line measured in the two different test-fixtures agreed within 0.4 dB in power and within 0.2 radians in phase (non-linear). Although the results show the forward transmission coefficient S_{21}, the reverse parameter S_{12} was also measured. Typically both directions produced similar spectra, with the power agreeing within 0.1 dB and the non-linear phase agreeing within 0.04 radians.

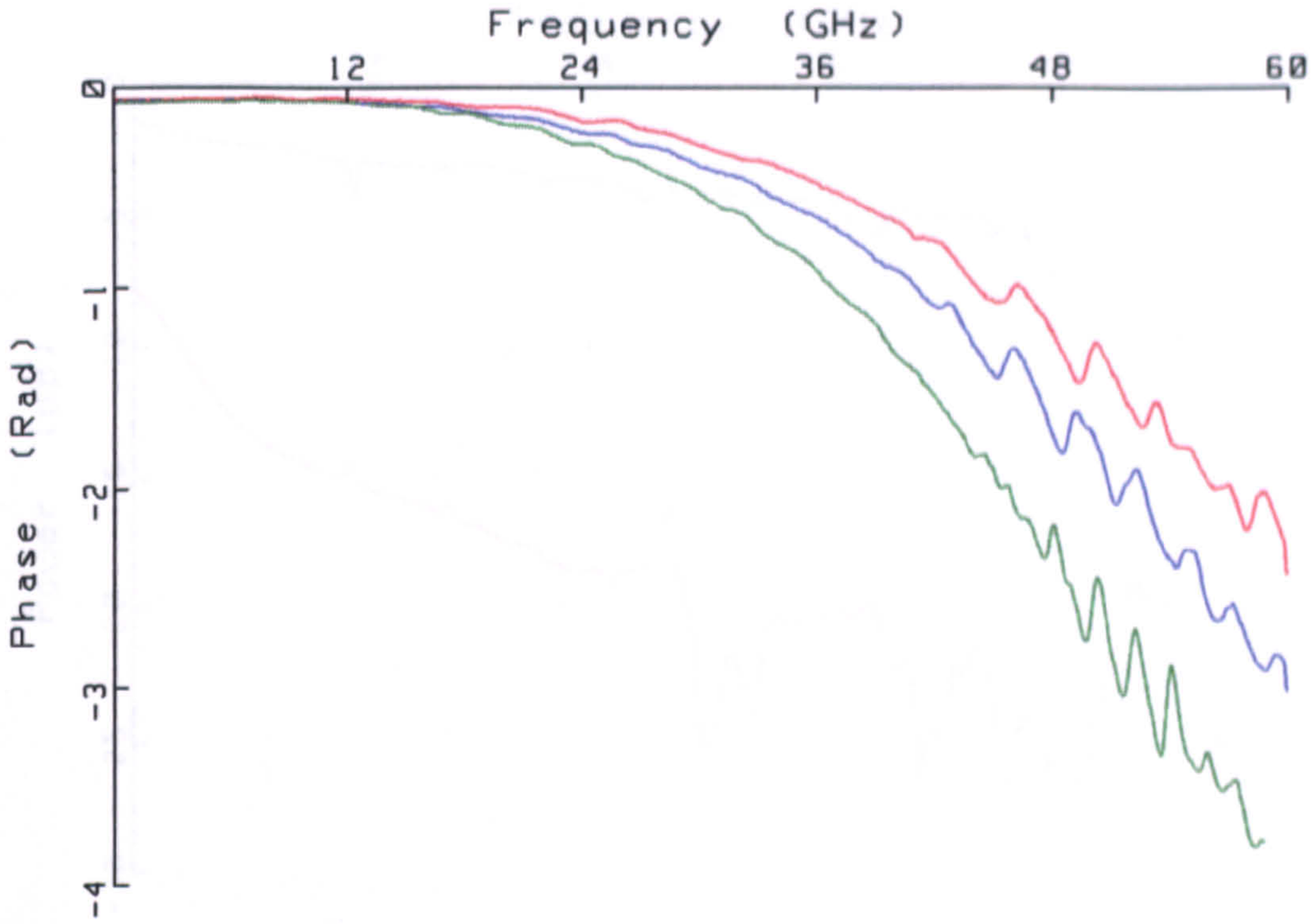

Figure 5.7 Re-plotted ANA S_{21} phase measurement of UTF1 and alumina CPW after subtracting linearities. Line lengths: — 10 mm, — 13 mm, — 19 mm.

5.3.2.2 GaAs line

In addition to measuring the alumina lines, the ANA was used to measure S_{21} of GaAs lines mounted in UTF2. Two examples are given in Figure 5.8. Unfortunately the ANA averaging was lower than before. Combining this with the resistance of the lines - device PG4 has a central line resistance of 14 Ω and device TL3 a resistance of 120 Ω - resulted in more structure and a lower S/N. The d.c. intercept of PG4 is -1.3 dB and of TL3 is -7.8dB. Figure 5.9 shows the phase of the same measurements (re-plotted for non-linearities). After subtracting the linear phase shift, the measurement of TL3 is very noisy.

It was hoped to use the ANA GaAs results to help derive the transfer-function of a single transition, but because the results are not very good, the time-domain approach, outlined later, is employed.

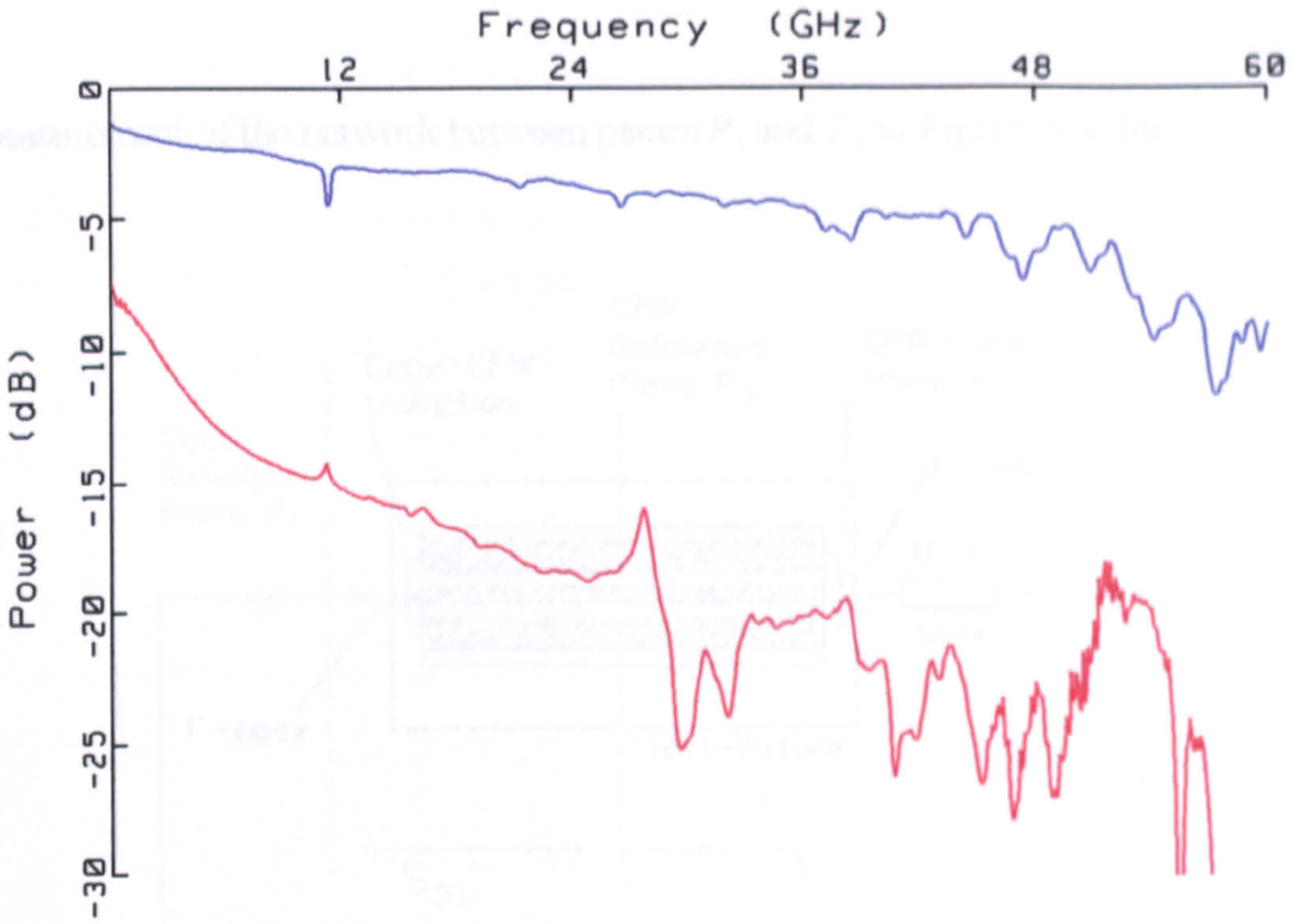

Figure 5.8 ANA S_{21} attenuation of GaAs lines: —— TL3, —— PG4.

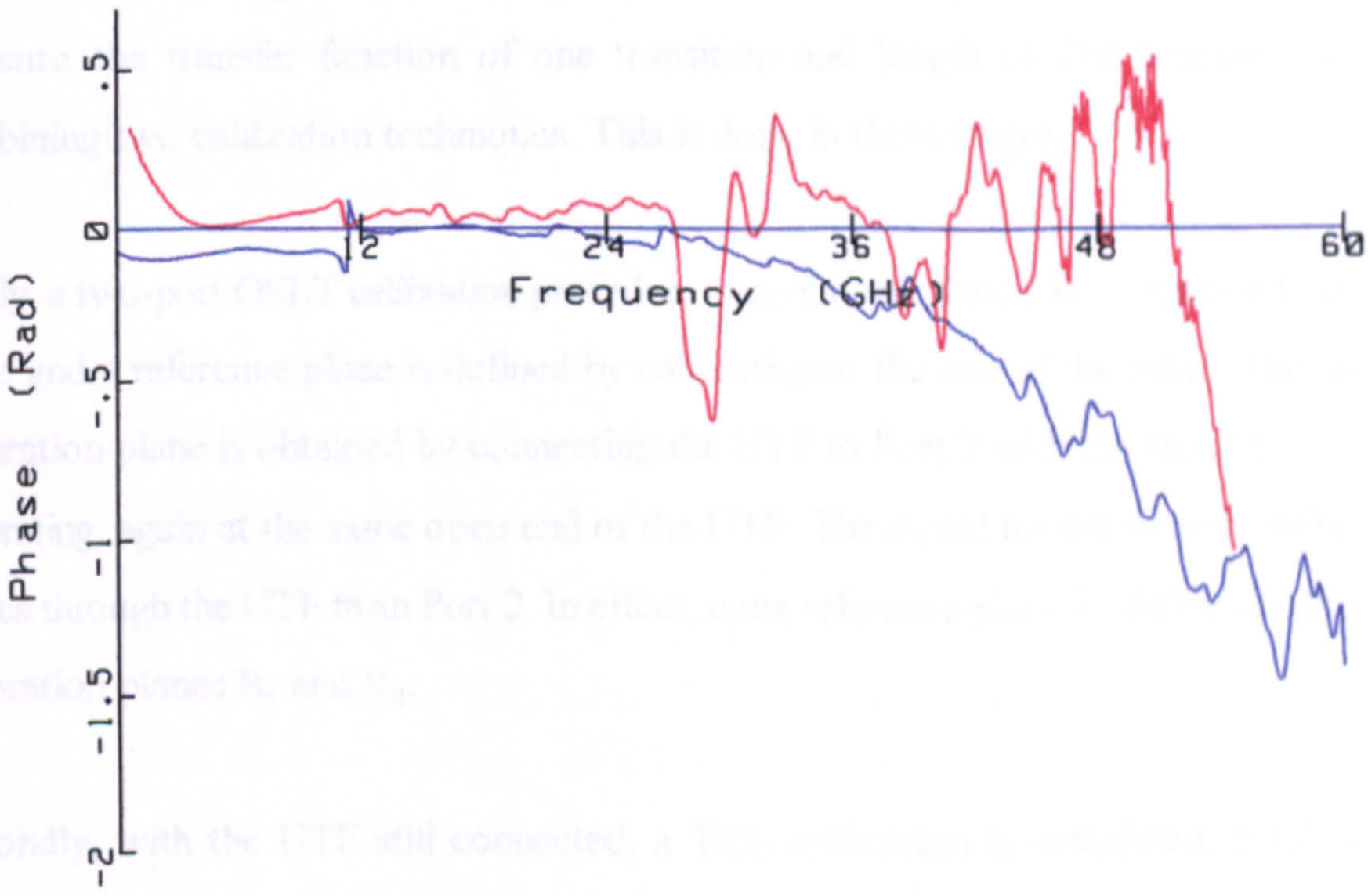

Figure 5.9 ANA S_{21} phase of GaAs lines: —— TL3, —— PG4.

5.3.3 Single transition measurements with an ANA

The measurement of the network between planes P_1 and P_2 in Figure 5.4 does not give the

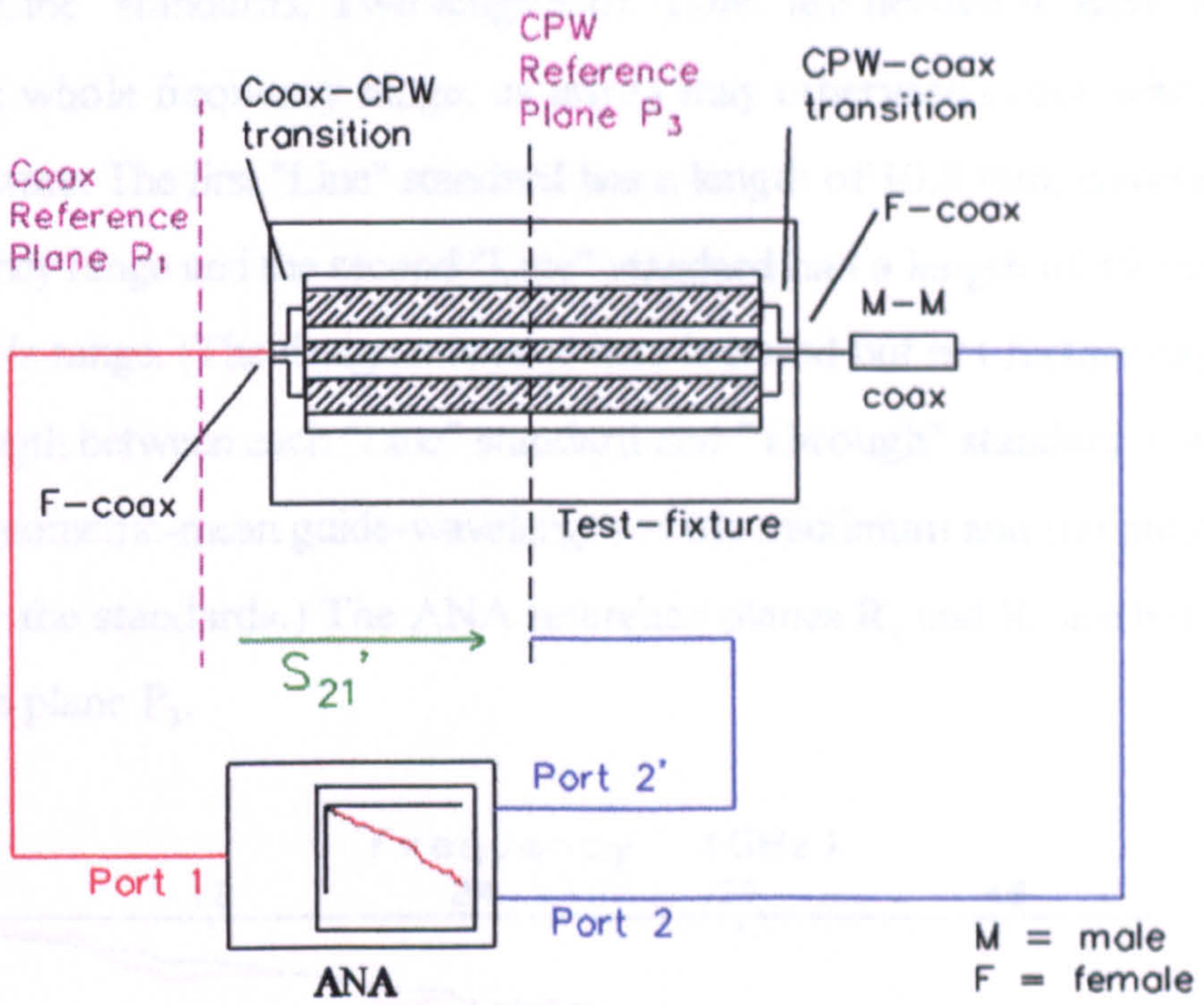

Figure 5.10 Reference planes of single transition ANA measurements.

S-parameters of a single transition and length of CPW directly. However, it is possible to measure the transfer function of one transition and length of line (Figure 5.10) by combining two calibration techniques. This is done in three stages:

Firstly, a two-port OSLT calibration procedure is performed. Port 1 is connected to a coax cable and a reference plane is defined by calibrating at the end of the cable. The second calibration plane is obtained by connecting the UTF to Port 2 with the second cable and calibrating, again at the same open end of the UTF. The signal for the second calibration passes through the UTF from Port 2. In effect, coax reference plane P_1 defines both ANA calibration planes R_1 and R_2.

Secondly, with the UTF still connected, a TRL calibration is completed in CPW. An OSLT procedure is not used here due to the lack of a "Load" standard defined sufficiently

well over the 60 GHz frequency range. (The coax calibration overcomes this limitation by measuring several positions of a variable (sliding) load - not available in CPW). The TRL calibration is achieved with items from the CPW calibration kit[4]. The 10 mm line is used as the "Through" standard; the offset short as the "Reflect" standard; and two lengths of CPW as the "Line" standards. Two lengths of "Line" are needed to have well-defined phase over the whole frequency range, as errors may otherwise occur within the ANA calibration software. The first "Line" standard has a length of 10.8 mm, covering the 5.5 - 60 GHz frequency range and the second "Line" standard had a length of 19 mm, covering the 0.5 - 5.5 GHz range. (The design rule used here is stated but not further explored - the difference in length between each "Line" standard and "Through" standard is equal to one quarter of the geometric-mean guide-wavelength of the maximum and minimum operating frequencies for the standards.) The ANA reference planes R_1 and R_2 are both defined at CPW reference plane P_3.

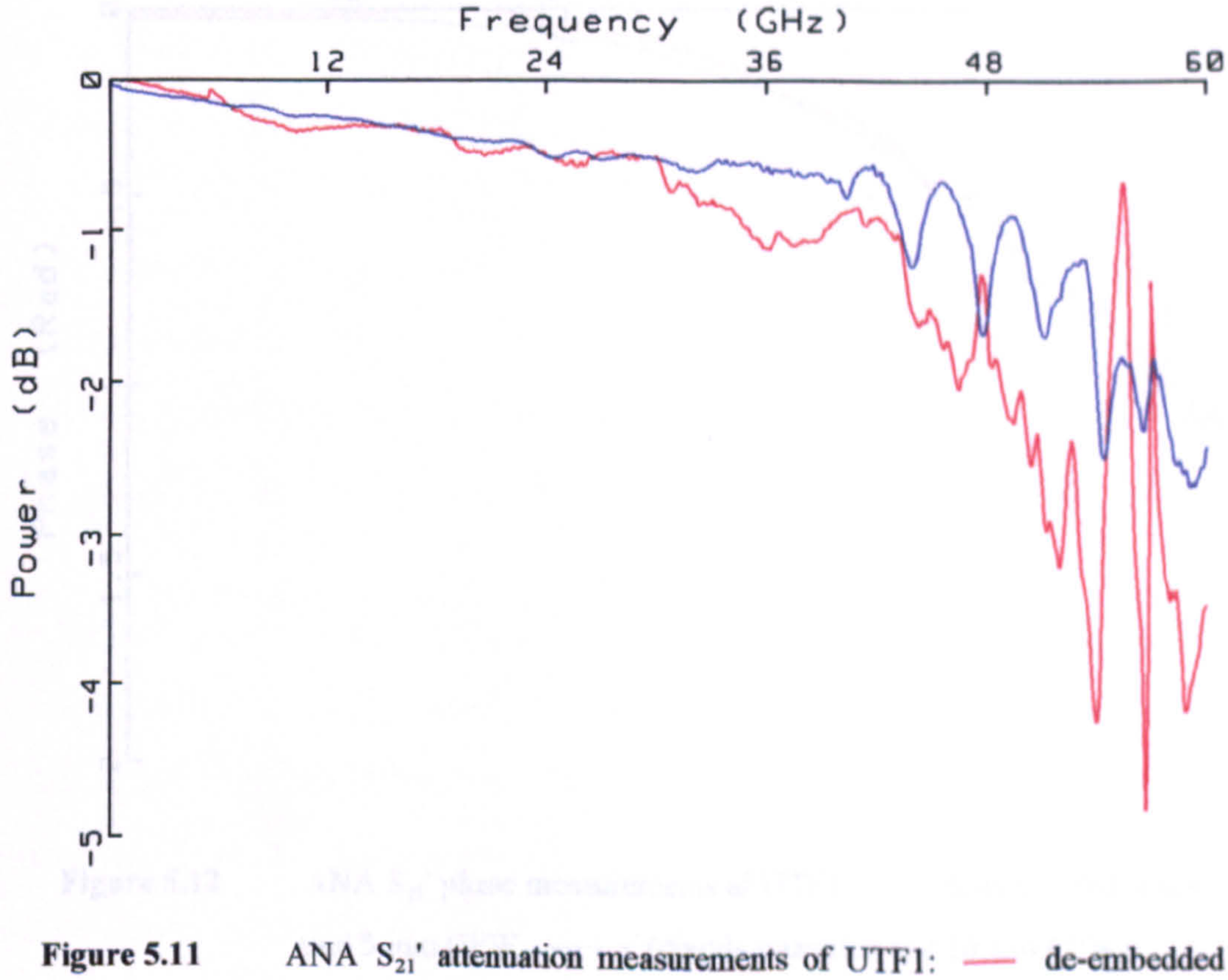

Figure 5.11 ANA S_{21}' attenuation measurements of UTF1: —— de-embedded single transition and 5 mm CPW; —— √(double transition and 10 mm CPW).

Finally, the above two calibrations are combined using adapter removal software,[14,15] designed to de-embed the effects of adapters on ANA measurements of devices. After the

combination, ANA calibration plane R_1 is still defined at coax reference plane P_1, but the second ANA calibration plane R_2 is now defined at the CPW reference plane P_3. The effective second port is labelled Port 2' in Figure 5.10.

By this indirect method, the S-parameters of a coax-CPW transition and a 5 mm length of alumina CPW were obtained. Figure 5.11 shows the attenuation and Figure 5.12 the phase plot for the forward transmission coefficient, S_{21}', of UTF1 de-embedded. From the structure of both the attenuation and phase it is observed that after about 48 GHz the measurement becomes noisier. Combining two calibrations is expected to degrade the S/N. In addition, there are frequency limits inherent in the TRL calibration of the CPW lines - for example, the fringing field capacitance information on the reference "Reflect" CPW standard is not defined above 40 GHz.

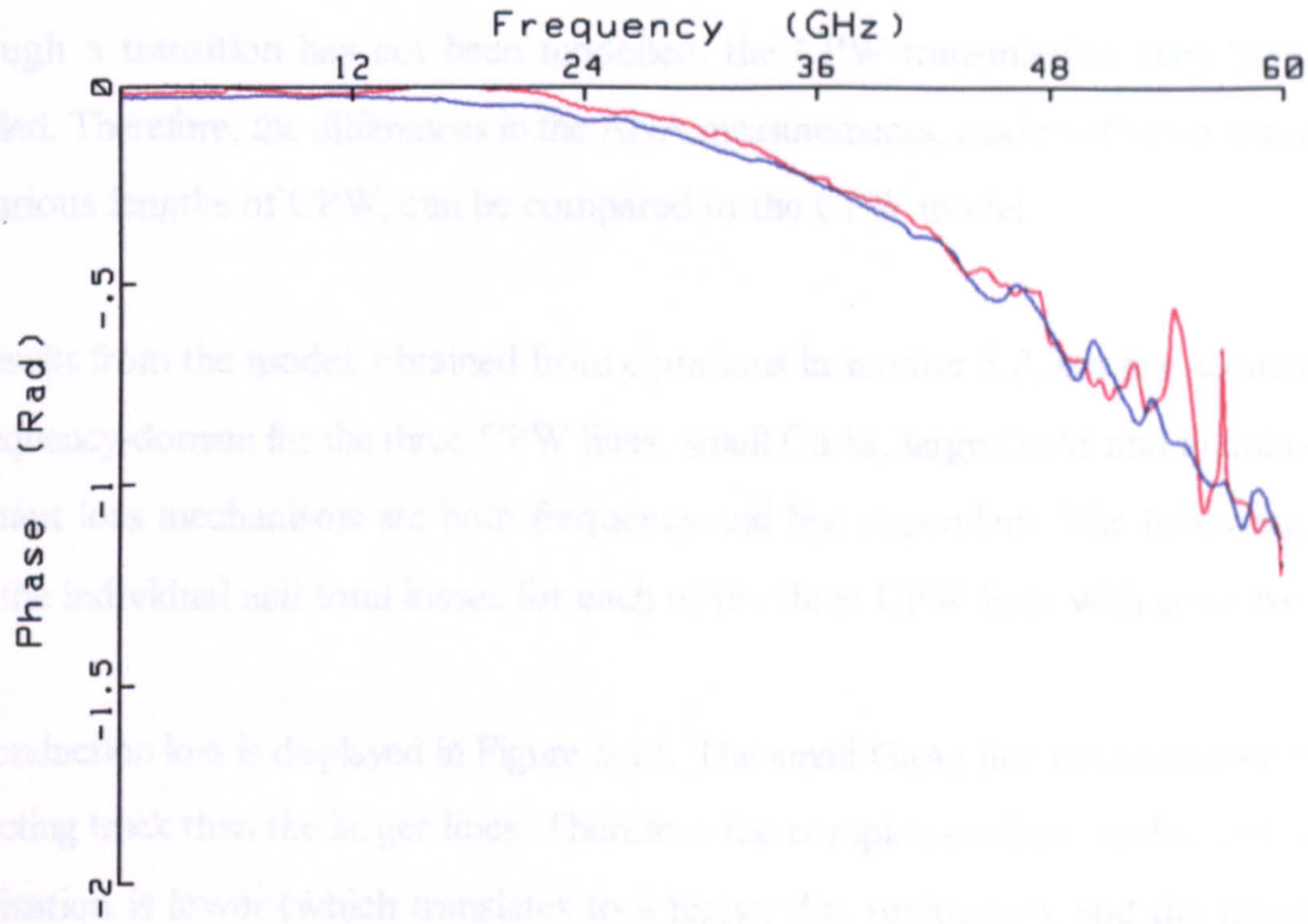

Figure 5.12 ANA S_{21}' phase measurements of UTF1: —— de-embedded single transition and 5 mm CPW; —— √ (double transition and 10 mm CPW).

For comparison purposes, the results of the two-transition UTF1 measurements are also considered. The two-transition results (comprising a coax-CPW transition, a 10 mm length of CPW and a CPW-coax transition) are in effect divided by two (which is equivalent to

a self or square-rooted deconvolution in the time-domain)[16] and are plotted on the same scale of Figure 5.11 and Figure 5.12. To achieve good agreement between the two, reciprocity for the system must hold,[17] and both transitions (coax-CPW and CPW-coax) and equal lengths of CPW must have approximately equal responses. Up to about 44 GHz, the agreement is reasonable, within ± 0.5 dB power and ± 0.1 rad phase ,suggesting the above statement holds.

A set of large CPW calibration items in GaAs has been fabricated, but a successful single transition de-embed has not been achieved. The complications of the small, large and tapered sections of the GaAs CPW have not been addressed.

5.3.4 Results of transmission line model in the frequency-domain

Although a transition has not been modelled, the CPW transmission lines have been modelled. Therefore, the differences in the ANA measurements, made with two transitions and various lengths of CPW, can be compared to the CPW model.

The results from the model, obtained from equations in *section 5.2*, are first examined in the frequency-domain for the three CPW lines: small GaAs, large GaAs and alumina. The dominant loss mechanisms are both frequency and line dependent. The following plots show the individual and total losses for each of the three CPW lines with error bars.

The conduction loss is displayed in Figure 5.13. The small GaAs line has narrower central conducting track than the larger lines. Therefore the complex surface conductivity of the metallisation is lower (which translates to a higher d.c. resistance), and the frequency-dependent loss is larger. The alumina line has thicker metallisation than the large GaAs (typically 4 μm compared to 0.6 μm) and hence lower losses.

Figure 5.14 shows the substrate dielectric loss which is small compared to the previous conduction loss. The larger error bars of the GaAs lines are mostly attributable to the uncertainty in the value and frequency-dependence of the loss tangent.

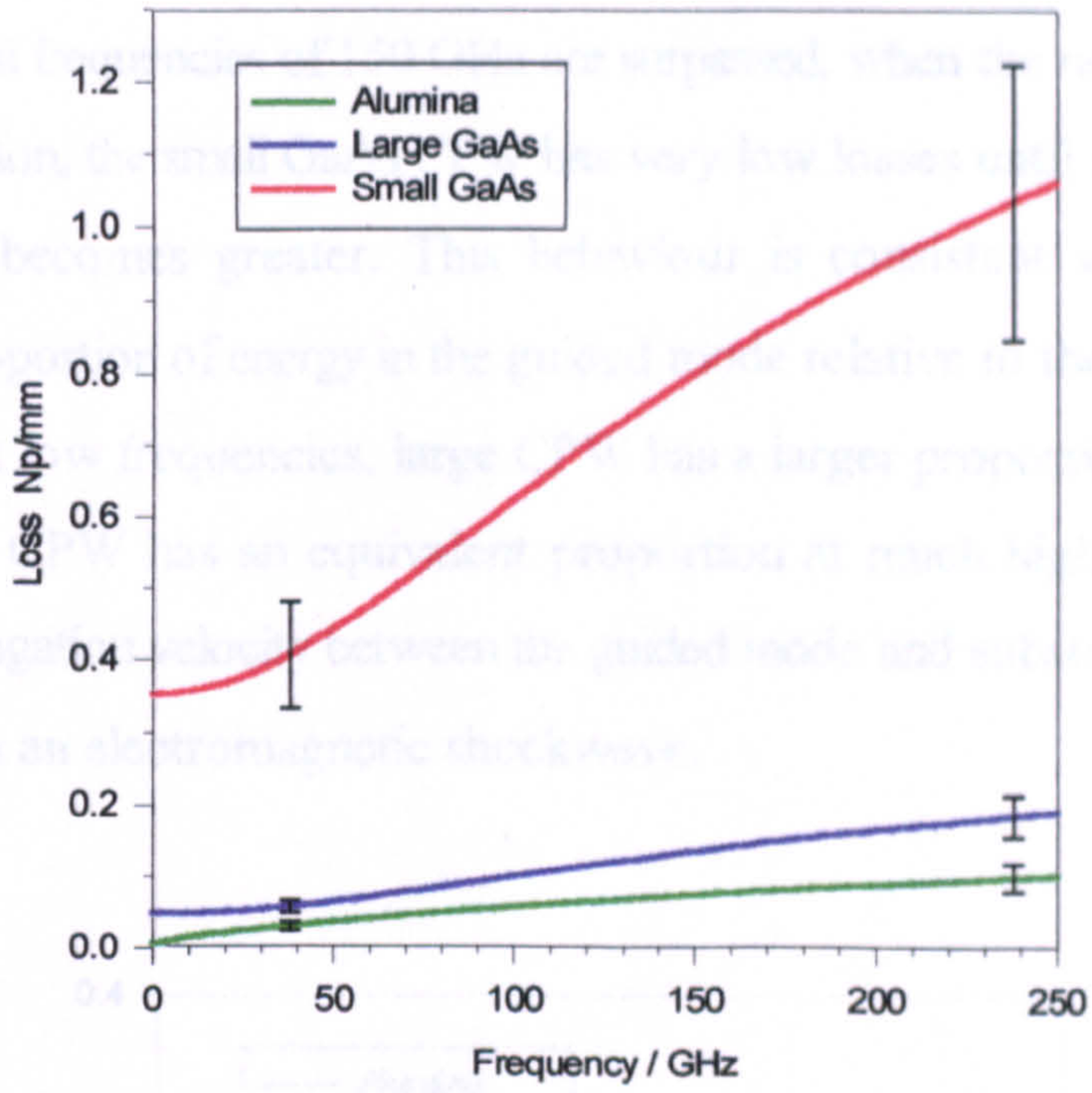

Figure 5.13 Modelled conduction loss α_c for CPW lines.

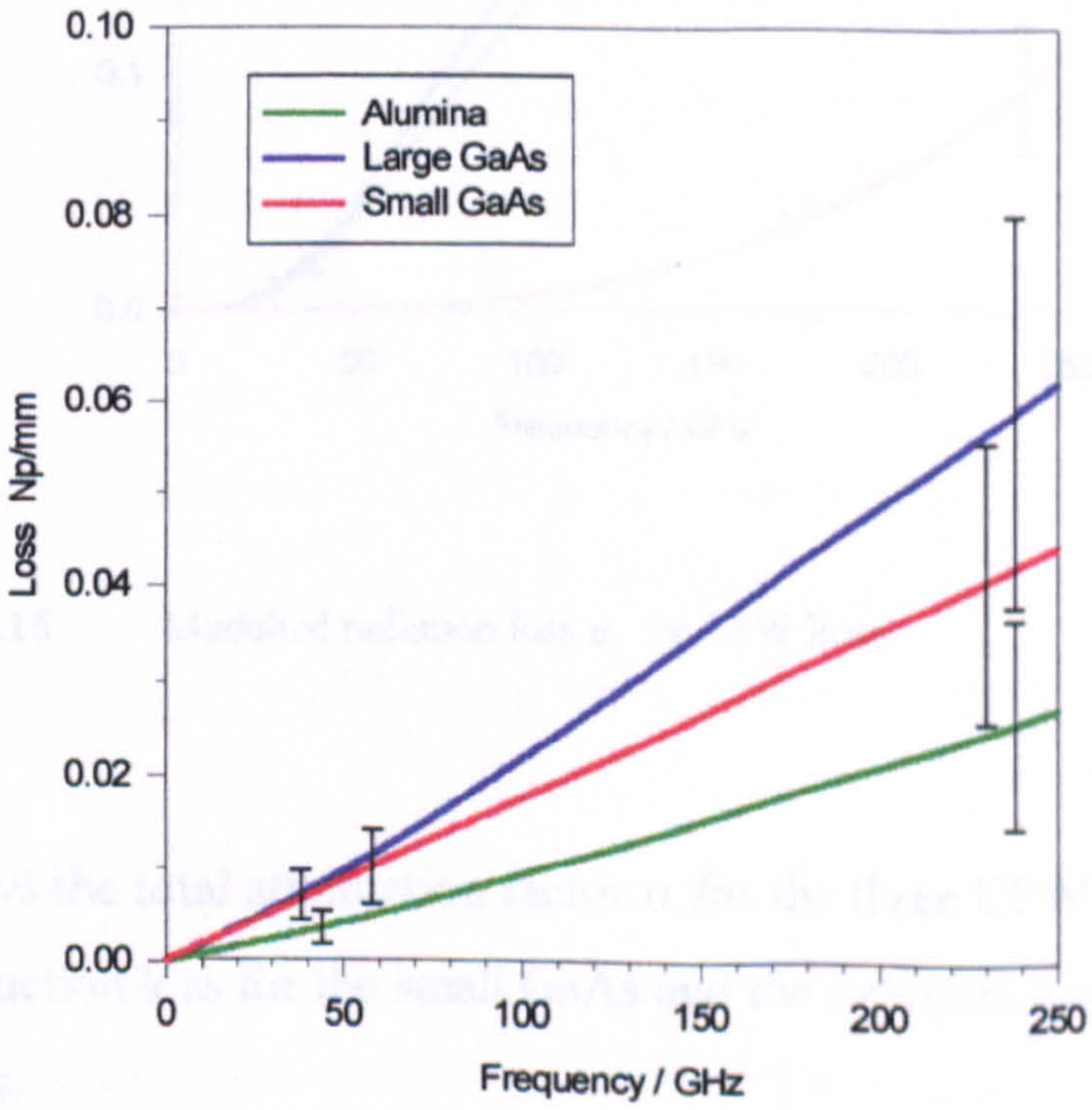

Figure 5.14 Modelled dielectric loss α_d for CPW lines.

The radiation loss is presented in Figure 5.15. Although small at low frequencies, the loss of the alumina and large GaAs lines can be seen to increase rapidly above frequencies of about 30 GHz until frequencies of 150 GHz are surpassed, when the rate of increase slows down. In comparison, the small GaAs CPW has very low losses until 150 GHz , when the rate of increase becomes greater. This behaviour is consistent with that previously described - the proportion of energy in the guided mode relative to the substrate increases with frequency. At low frequencies, large CPW has a larger proportion than small CPW. The small GaAs CPW has an equivalent proportion at much higher frequencies. The difference in propagation velocity between the guided mode and substrate causes radiation to be lost through an electromagnetic shockwave.

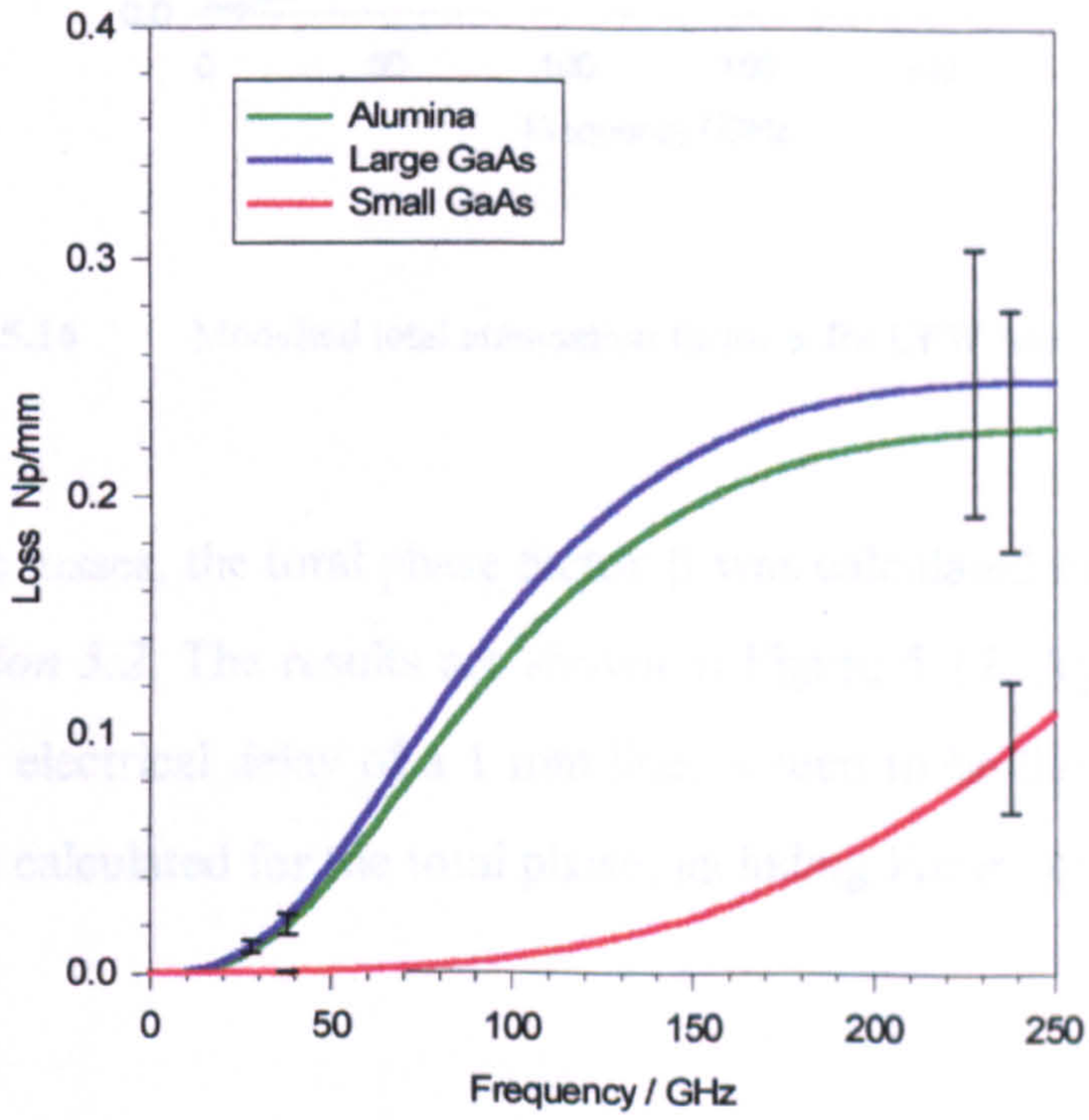

Figure 5.15 Modelled radiation loss α_r for CPW lines.

Figure 5.16 shows the total attenuation factor α for the three CPW lines. The dominant term is the conduction loss for the small GaAs and the radiation loss for the large GaAs and alumina lines.

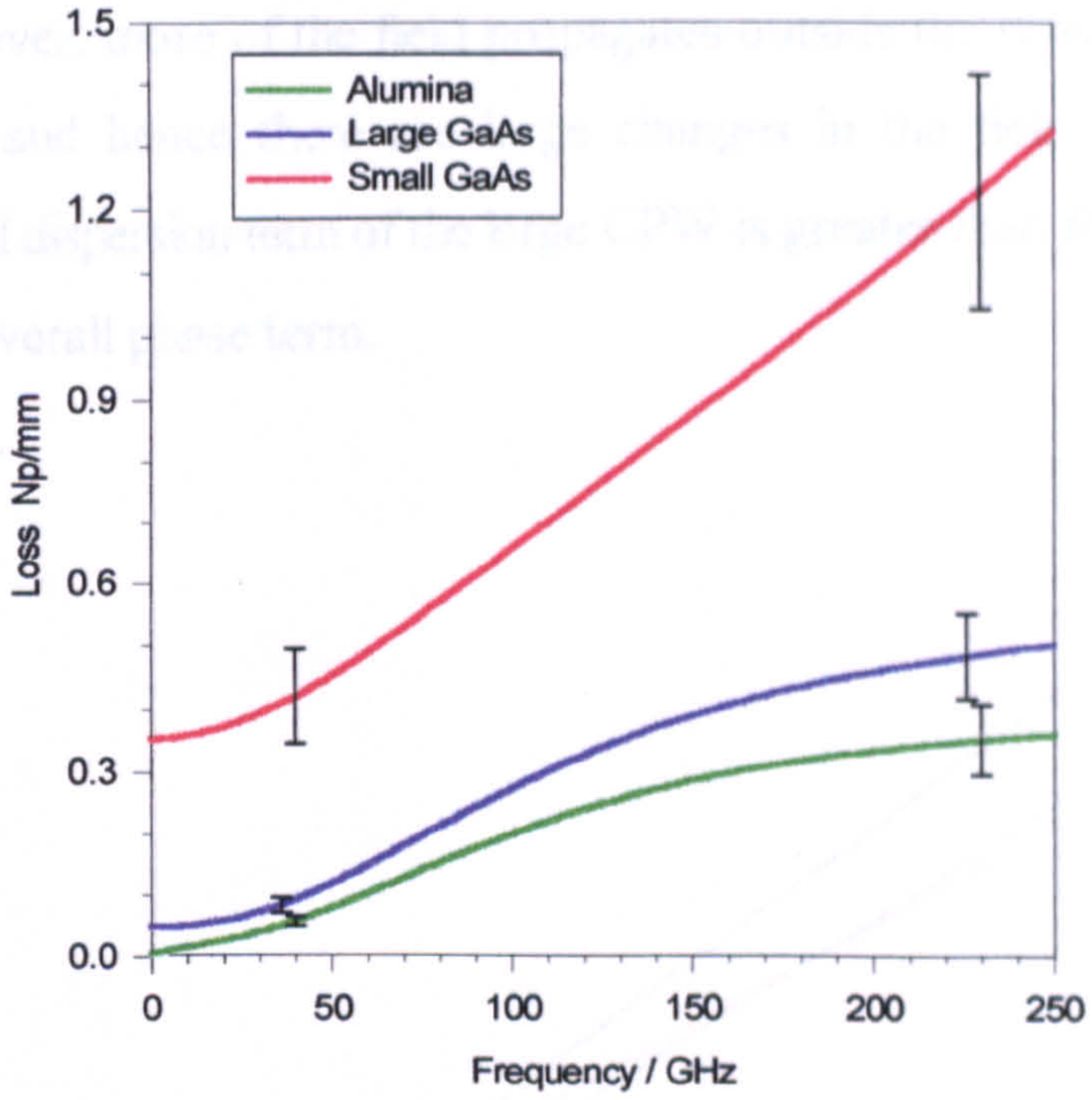

Figure 5.16 Modelled total attenuation factor α for CPW lines.

In addition to the losses, the total phase factor β was calculated for each line from the equations in *section 5.2*. The results are shown in Figure 5.17. Again the linear phase factor, due to an electrical delay of a 1 mm line, is seen to be the major contribution. Uncertainties were calculated for the total phase, including linear contribution, at around ± 8%.

Figure 5.18 plots the modelled phase change in radians after subtracting the linearities from each line. It is unclear how to derive the uncertainties in the non-linear terms - the same percentage as the total phase was assumed as an approximation.

Note the phase of the small GaAs CPW changes in the opposite direction to that of the large GaAs CPW. It has been noted that the small GaAs line has a relatively small complex conductivity term compared with the larger line. It follows that not only is the real part of the overall loss expression large (at d.c. the resistance), but the imaginary part - the change

in phase due to the conductivity loss - is also relatively large and dominates the overall phase term. For the large GaAs CPW (and also the alumina CPW) the conduction phase term is small. However, more of the field propagates outside the substrate than for the small GaAs CPW, and hence there are large changes in the field distribution with frequency. The modal dispersion term of the large CPW is greater than for the small CPW and dominates the overall phase term.

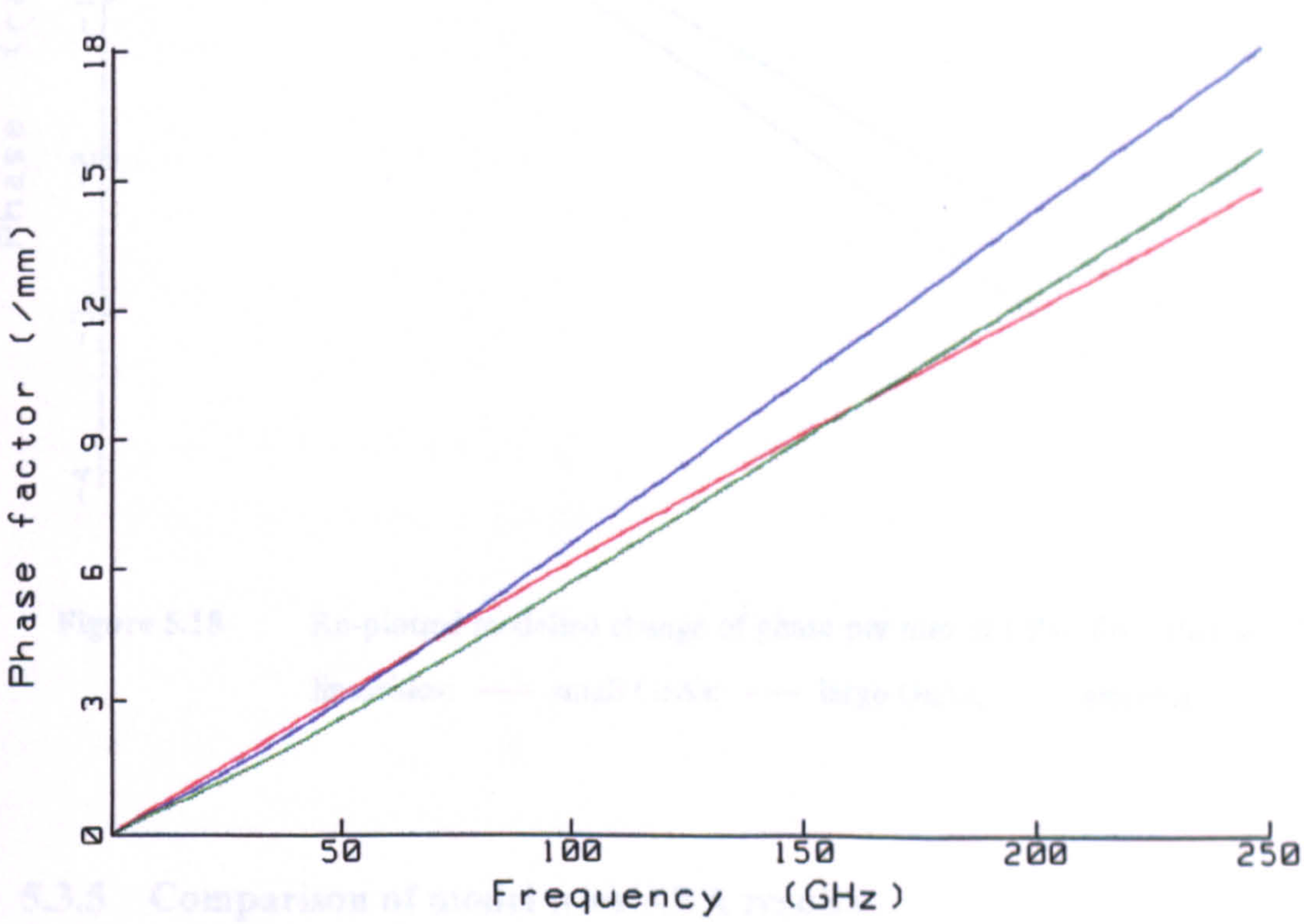

Figure 5.17 Modelled phase factor β of CPW lines: — small GaAs; — large GaAs; — alumina.

With modal dispersion, as the frequency increases, more energy is confined in the substrate and the effective dielectric constant increases, causing a subsequent decrease in the phase velocity. Therefore phase changes due to modal dispersion are negative going.

The phase change due to the conductors is positive going and in the opposite direction to modal dispersion. To explain this, one can imagine a device with thick metallisation. As the plane of the metallisation is higher than the plane of the substrate, then as the frequency increases (smaller wavelengths), the fields and hence energy are confined *away* from the substrate into the air. This has the effect of decreasing the effective dielectric

constant and increasing the phase velocity.

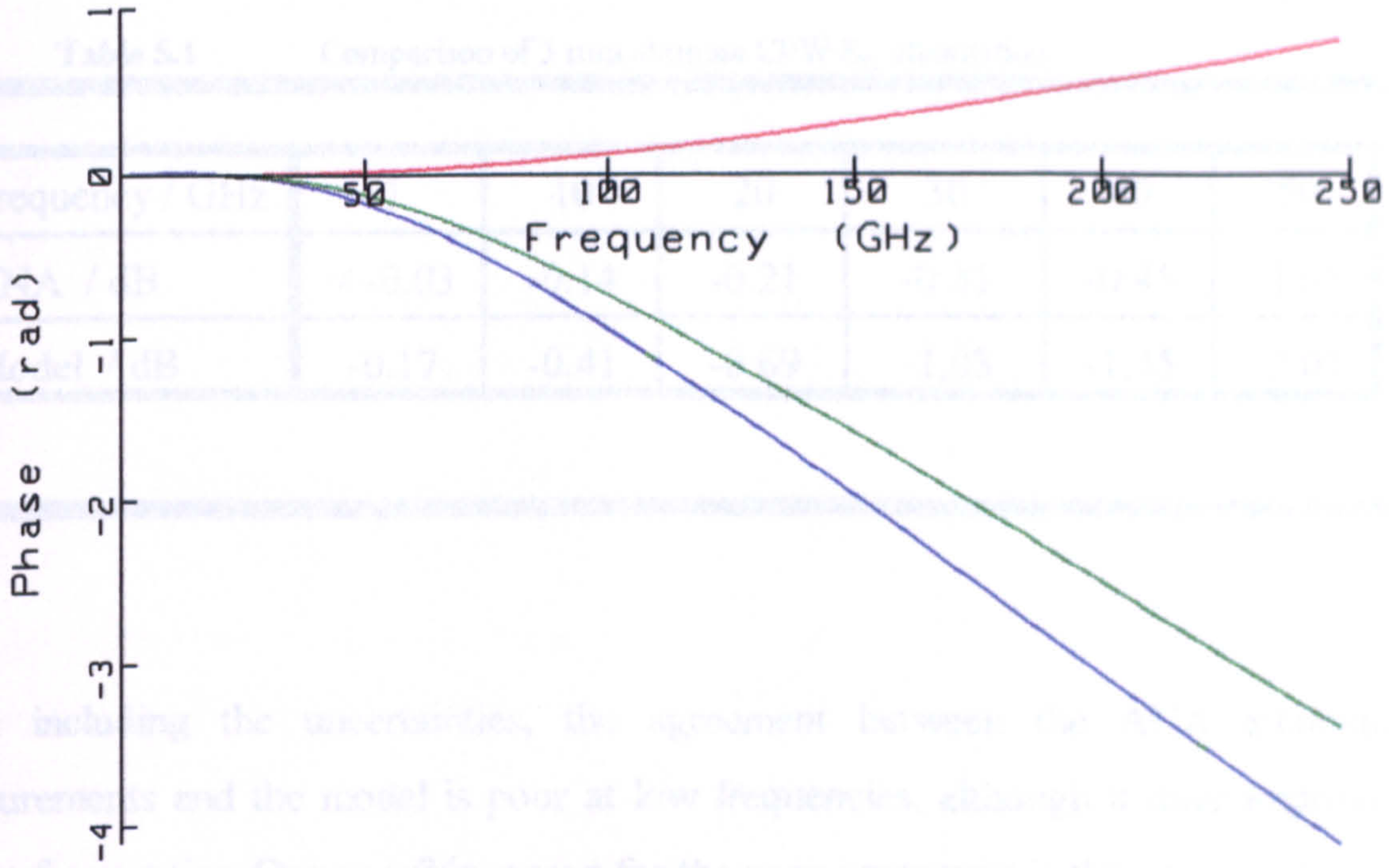

Figure 5.18 Re-plotted modelled change of phase per mm of CPW line, after subtracting linearities: — small GaAs; — large GaAs; — alumina.

5.3.5 Comparison of model with ANA results

The results from the model cannot be directly compared to the ANA S_{21} measurements, as the latter includes the effect of the CPW-coax transition. However, the model results can be compared to the difference between ANA measurements of two line lengths, as the effect of the transition is cancelled.

Because of the structure in the ANA power measurements (see Figure 5.5 on page 118) the difference between two lengths of alumina CPW, for example 10 mm and 13 mm, was not plotted. Lines were fitted through the centres of the structure and values for a difference in length of 3 mm were estimated from the fits at different frequencies. Table 5.1 compares these results with the attenuation of 3 mm derived from the model. The uncertainties in the model are those stated earlier, around 20%. A total uncertainty of 1 dB

is estimated for the ANA measurements at 50 GHz[18] - this is smaller at lower frequencies.

Table 5.1 Comparison of 3 mm alumina CPW S_{21} attenuation.

Frequency / GHz	1	10	20	30	40	50
ANA / dB	< -0.03	-0.14	-0.21	-0.31	-0.45	-1.05
Model / dB	-0.17	-0.41	-0.69	-1.03	-1.45	-2.07

Even including the uncertainties, the agreement between the ANA attenuation measurements and the model is poor at low frequencies, although it does improve at higher frequencies. One possible reason for the poor agreement is the uncertainty in the attenuation of the transition. Although in theory the transition effect is cancelled by the difference between the two line lengths, the attenuation of the transition dominates the ANA measurements. At 1 GHz, the model also predicts an offset (non-zero d.c. value), due to the finite resistance of the metallisation. Subtracting the d.c. value of - 0.17 dB from the model values, so that the frequency-dependence is compared - and not the absolute values - results in better agreement.

Table 5.2 Comparison of 3 mm alumina CPW S_{21} phase.

Frequency / GHz	10	20	30	40	50
ANA / rad	-0.02	-0.07	-0.24	-0.44	-0.76
Model / rad	-0.02	-0.06	-0.20	-0.36	-0.61

The difference in ANA phase measurements was also calculated and compared to the

model in a similar way (Table 5.2). It is seen that the agreement is better than for the attenuation. This may be because the transition does not dominate the phase term - in fact the phase change due to the transition appears to be very small and the phase is dominated by changes attributed to the CPW lines. The uncertainties in the model were previously calculated for the total phase (included linear term), and are approximately ± 8%. The uncertainty in the ANA phase is estimated to be ± 0.04 rad at 50 GHz.[118]

5.4 Time-domain measurements

The last section examines measurements and modelling in the frequency-domain. This section focuses on the time-domain.

5.4.1 Two transition measurements with a CRO

An alternative domain in which to measure the network transfer function of two transitions and a length of CPW is the time-domain. A system comprising a commercially available Time-Domain-Reflectometer (TDR), or an electrical pulse generator (such as the nominal 13 ps Tektronix 067-1338-01) and the SD32 sampling oscilloscope could be used. However, a high-speed photodiode[5] illuminated by femtosecond pulses from the Ti:sapphire laser and connected to the SD32 provides a better response than that achievable with either a commercial TDR or an electrical pulse generator and oscilloscope.

The FWHM of either of the two diodes listed below, as recorded by the oscilloscope, is approximately 12 ps. This measurement is the convolution of the following contributions: the optical pulse width; the response of the photodiode; the transfer function of the interconnecting transmission lines; the impulse response of the oscilloscope; and the jitter between the triggering and sampling circuits of the oscilloscope (including the contribution of trigger noise).

---

[5] GEC-Marconi *or* New-Focus Model-1002 50 GHz Schottky GaAs devices.

Adding an additional component between the photodiode and oscilloscope, such as a UTF with a CPW line (GaAs or alumina substrate), only changes the transfer function of the interconnecting transmission lines - all of the other listed contributions are constant. Hence, the effect of two coax-CPW transitions and a length of CPW on the propagation of 12 ps pulses can be investigated, by deconvolving the CRO measurement without the UTF from the CRO measurement with the UTF (and line).

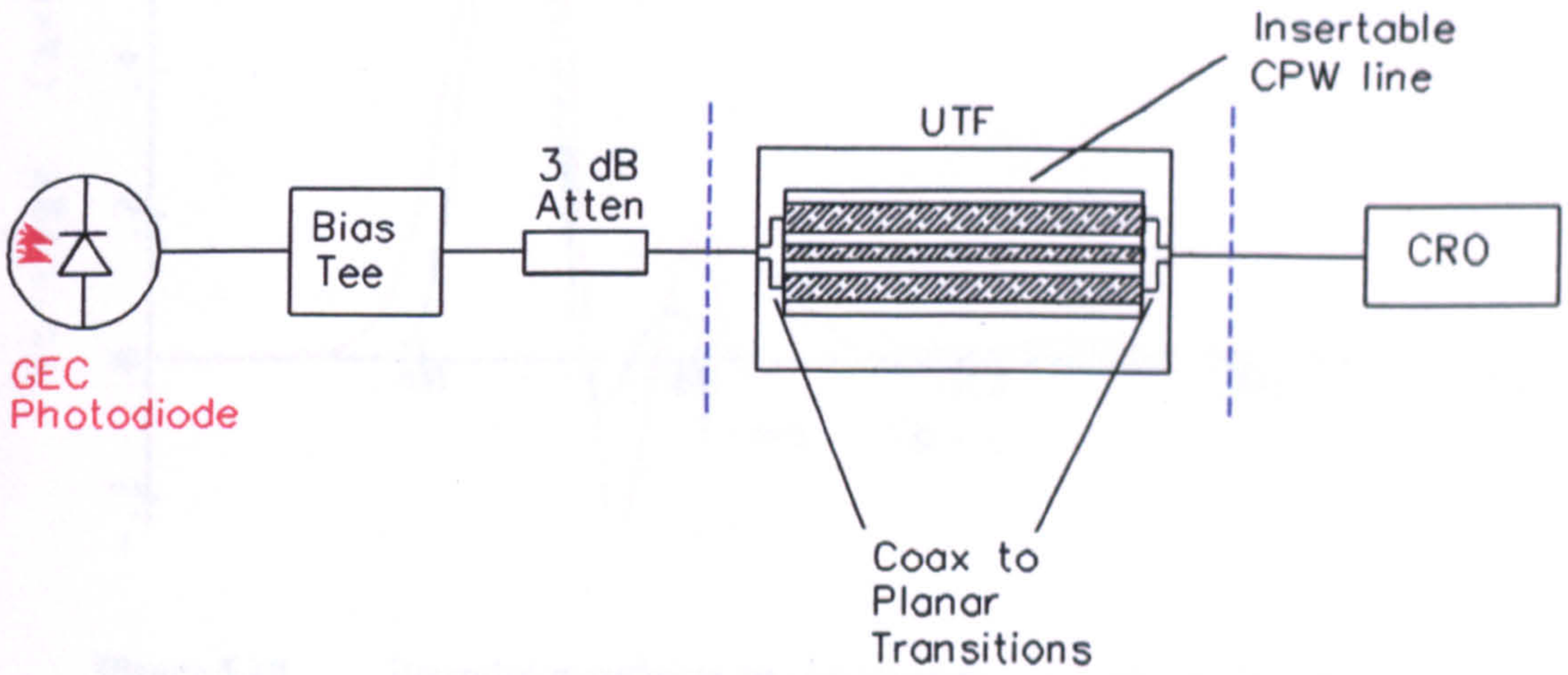

Figure 5.19 Schematic of photodiode transmission line measurement system.

A simplified block diagram of the photodiode transmission line measurement system is presented in Figure 5.19. In this instance the GEC diode, biased with a bias tee, provides the fast electrical pulses when illuminated by the Ti:sapphire laser. The attenuator serves to reduce reflections between the diode and oscilloscope.

Examples of results are shown in Figure 5.20 and Figure 5.21. Figure 5.20 contrasts the waveform obtained with the photodiode connected directly to the oscilloscope (no UTF connected between the dashed lines in Figure 5.19), with that obtained with test-fixture UTF2 inserted between the photodiode and oscilloscope. The additional effect of the test-fixture - consisting of two coax-CPW transitions and in this case 10 mm of alumina CPW - on the propagation of the pulse is apparent: the pulse is broadened and dispersed, with the FWHM increasing from 12.2 ps to 15.8 ps and the risetime from 10.0 ps to 15.1 ps. (Note the pulse amplitudes have been normalised to highlight the differences in structure).

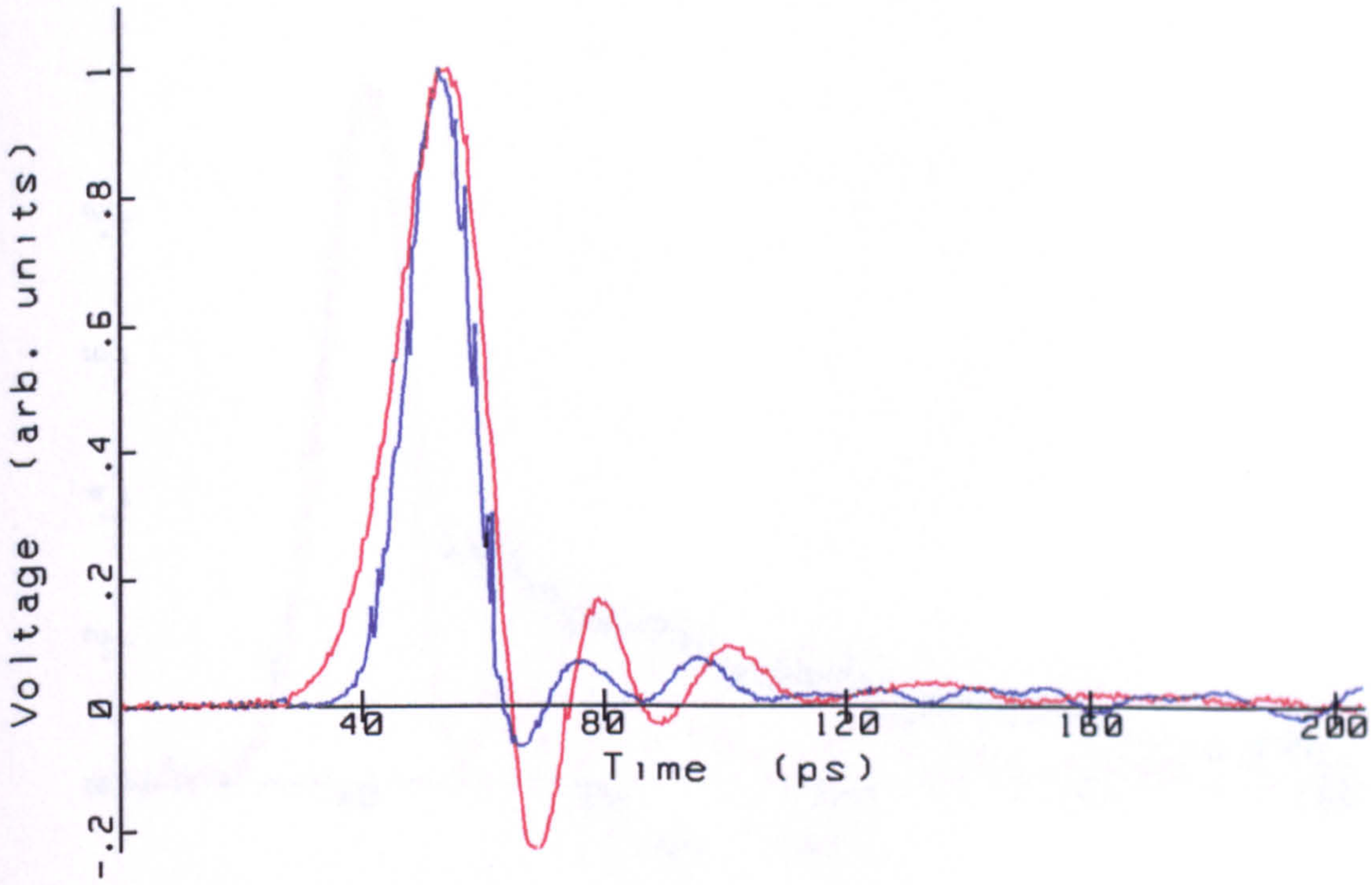

Figure 5.20 Recorded waveforms on oscilloscope: —— without UTF2; —— with UTF2 and 10 mm alumina CPW.

The reference alumina CPW was removed, and different GaAs circuits were inserted into the test-fixture and measured. The risetimes were found to be comparable with those attained with alumina lines in the UTF, but the structure was different. Figure 5.21 shows the transmission line measurements of two different GaAs circuits mounted in the UTF (plotted on the same time scale as Figure 5.20). The pulse recorded on the oscilloscope after propagating along annealed circuit TL3 (central line resistance = 120 Ω, FWHM = 17.5 ps, risetime = 13.2 ps) is compared to that recorded after propagating along unannealed circuit TL4 (resistance = 25 Ω, FWHM = 16.0 ps, risetime = 13.1 ps).

Note that although the structure is different on the two waveforms due to the emergence of long tails -"shoulders" - in the fall regions of the waveforms, the duration and risetime parameters do not vary much; this demonstrates the potential danger in relying on single parameters to describe complete waveforms. The extent of the shoulder formation appears to depend on the resistance of the lines. This supports the results of Paulter[19], who found

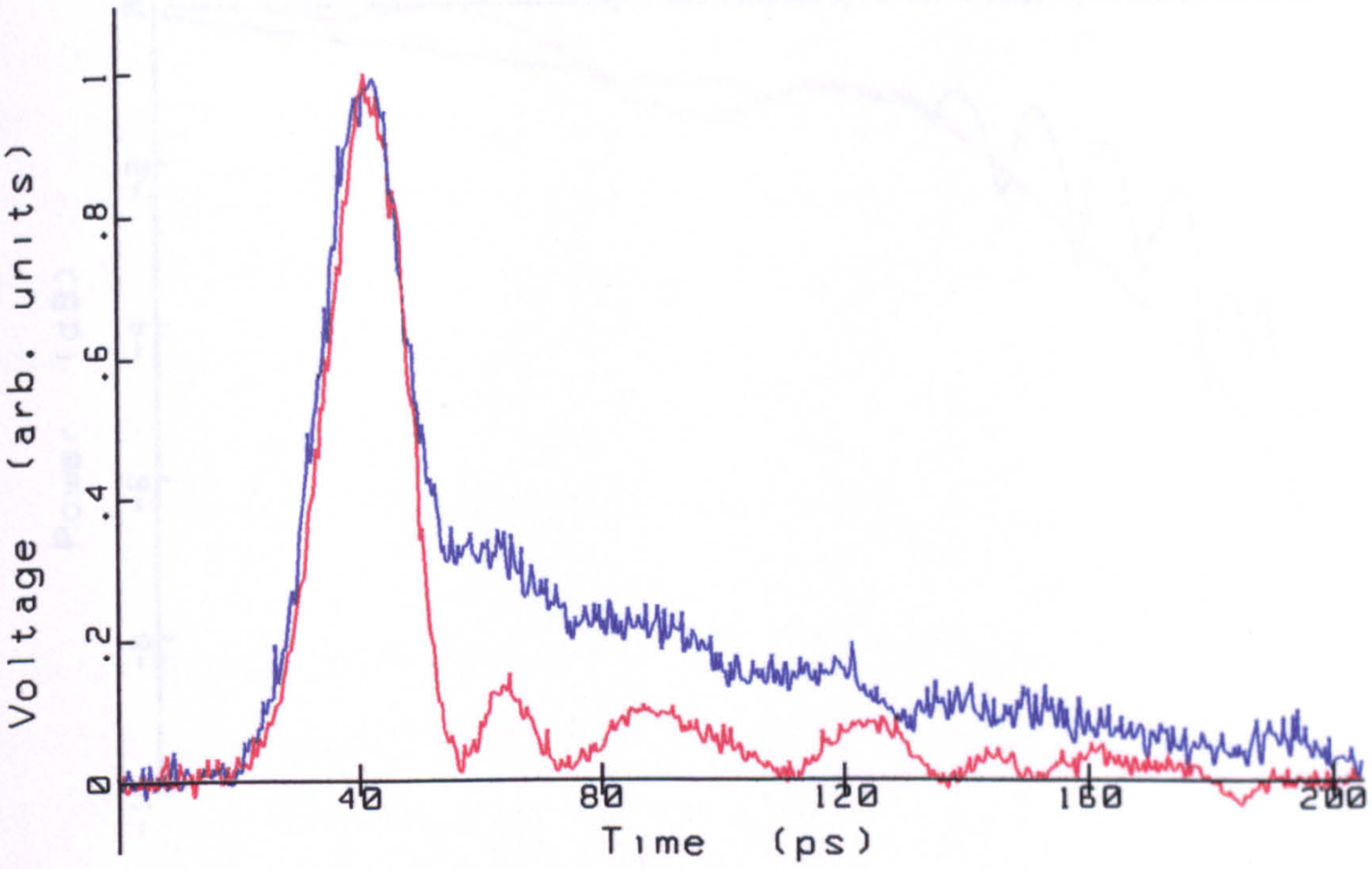

Figure 5.21 Recorded waveforms of GaAs circuits in UTF2: —— device TL4 (unannealed); —— device TL3 (annealed).

that low-frequency dispersion effects could be directly attributed to the ohmic resistance of the transmission lines.

The effect of the UTF and line can be quantified by deconvolving a measurement without the UTF from a measurement with the UTF. An example is shown here using the 10 mm alumina line. The filtering was optimised as discussed in *section 6.2* - the effective filter FWHM was approximately 8 ps, corresponding to a -3 dB bandwidth of around 70 GHz.

The deconvolved frequency-domain result for the alumina CPW in UTF2 is shown in Figure 5.22 (attenuation) and Figure 5.23 (phase). The two-transition ANA measurement is plotted for comparison. The structure of the attenuation, and to a lesser extent the phase, is different but the agreement is satisfactory, within 1.5 dB and 0.2 rad at 60 GHz. Deconvolution structure is discussed in *chapter 6*. Time-domain results are not compared as ANA measurements need extrapolation to over 100 GHz before Fourier transforming.

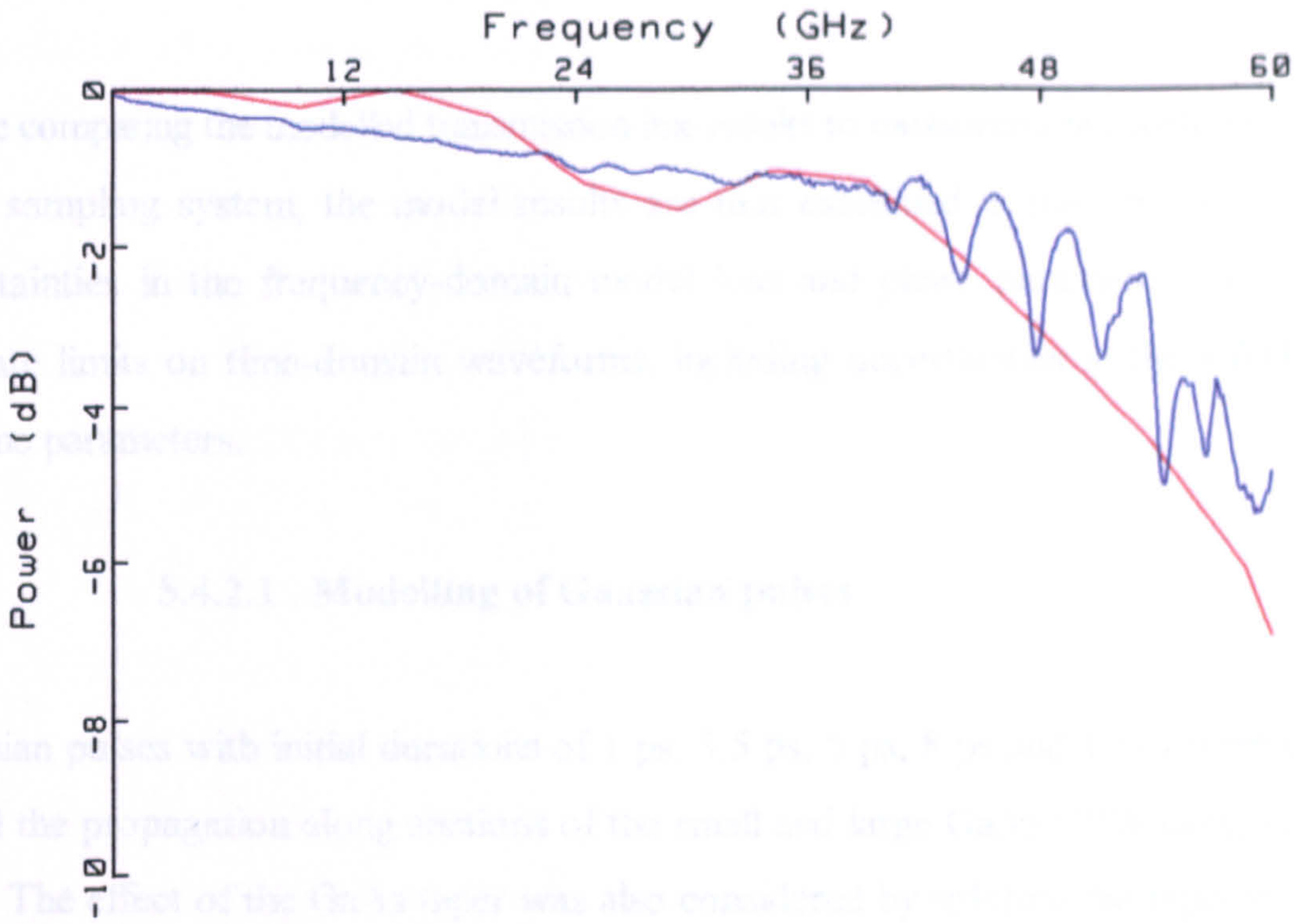

Figure 5.22 Attenuation result for UTF2 and 10 mm alumina line:
— deconvolved CRO; — ANA.

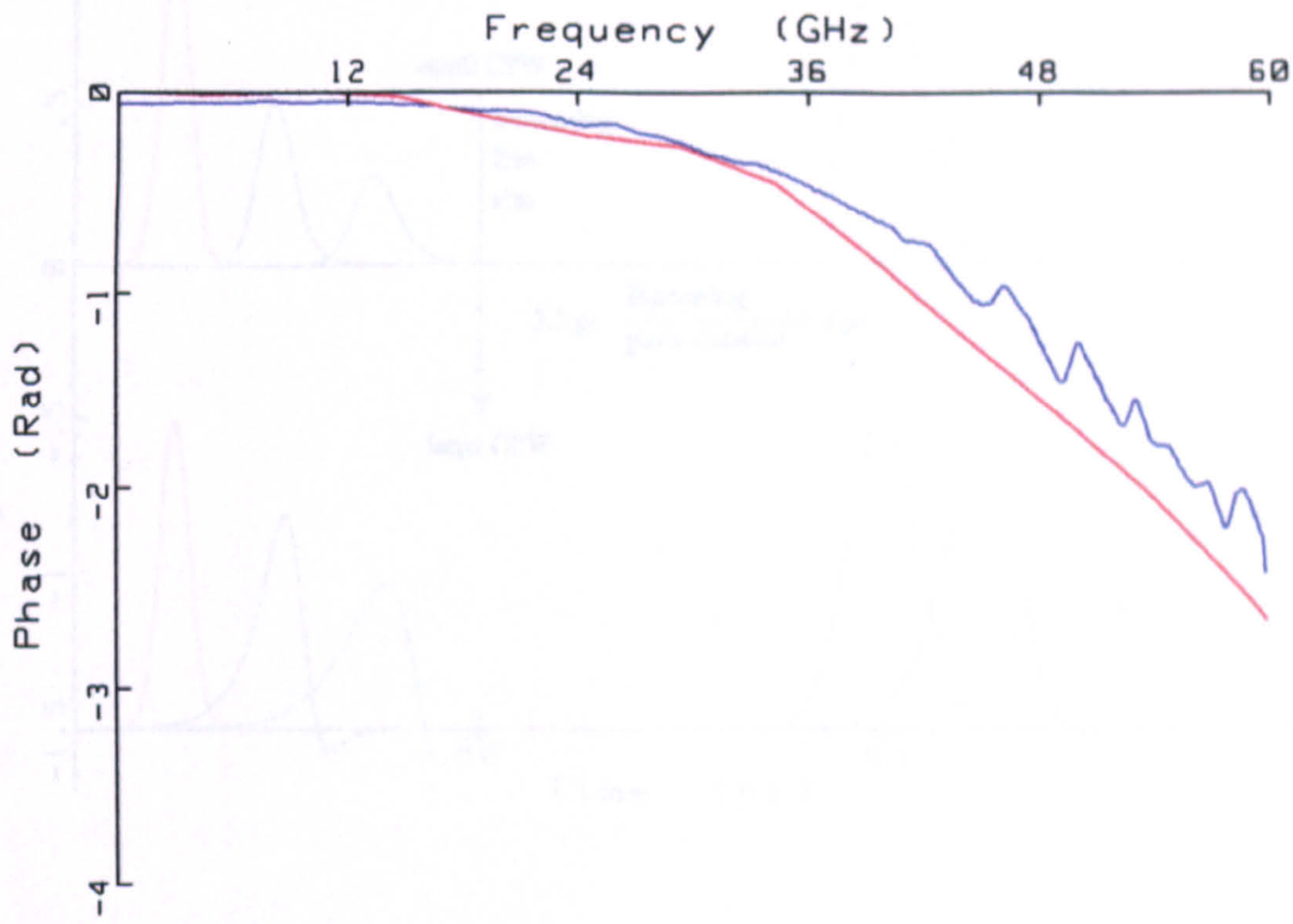

Figure 5.23 Phase result for UTF2 and 10 mm alumina line:
— deconvolved CRO; — ANA.

5.4.2 Results of transmission line model in the time-domain

Before comparing the modelled transmission line results to measurements with the electro-optic sampling system, the model results are first examined in the time-domain. The uncertainties in the frequency-domain model loss and phase parameters are used to estimate limits on time-domain waveforms, including uncertainties in the FWHM and risetime parameters.

5.4.2.1 Modelling of Gaussian pulses

Gaussian pulses with initial durations of 1 ps, 3.5 ps, 5 ps, 8 ps and 10 ps were used to model the propagation along sections of the small and large GaAs CPW using equation (5.3). The effect of the GaAs taper was also considered by splitting the tapered section into smaller sections (segmentation). Pulse durations of 7 ps, 8.5 ps, 10 ps and 12 ps were used to model the alumina CPW.

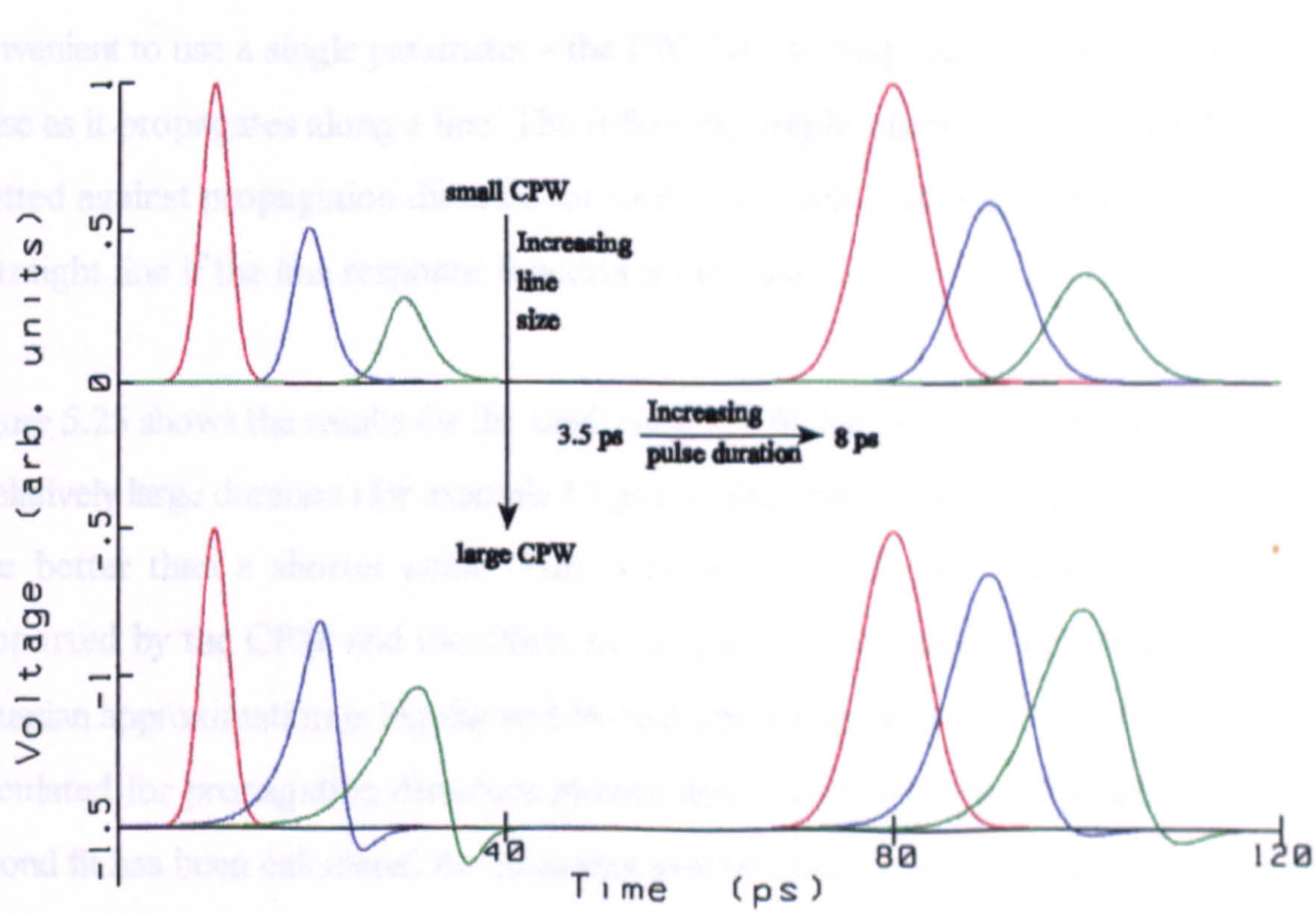

Figure 5.24 Results of model for initial Gaussian pulses along GaAs CPW lines after propagation distance: — 0 mm, — 1 mm, — 2 mm.

The waveforms in Figure 5.24 provide examples of the model with Gaussian input pulses. Propagation at two distances are shown for different size GaAs CPW (small and large) and different duration input pulses (3.5 ps and 8 ps FWHM). There are several conclusions to be drawn, which agree with previous statements made in discussions about the model parameters and frequency-domain results:

i) The large CPW displays overshoot and a degradation in the rising edge. Such overshoot confirms the presence of modal dispersion which is not present with the small CPW for the conditions shown.

ii) A shorter initial pulse displays more overshoot, as the higher frequencies are affected more by dispersion on the line.

iii) The initial pulses are broadened more by the large CPW - again the frequency-dependent losses and dispersion are greater.

iv) The pulse amplitude decreases more with the small CPW. This is due to the smaller d.c. line conductivity.

In order to compare the effect of each line on initial pulses of different duration it is convenient to use a single parameter - the FWHM - to map the modelled progress of the pulse as it propagates along a line. The following graphs show the square of the FWHM plotted against propagation distance for each line. Such graphs are expected to produce a straight line if the line response function is Gaussian.

Figure 5.25 shows the results for the small GaAs CPW line. It is observed that a pulse with a relatively large duration (for example 10 ps FWHM) follows the Gaussian approximation rule better than a shorter pulse. This is to be expected, as longer pulses are better supported by the CPW and therefore do not disperse as much. The deviation from the Gaussian approximation is highlighted by two linear regression fits. The first fit has been calculated for propagation distances greater than 1 mm with the 10 ps initial pulse. The second fit has been calculated for distances greater than 2 mm with the 5 ps initial pulse. (To highlight the differences between the fits and modelled data, the lines are displayed intercepting the y axis, although the range of the data for each fit is that stated.)

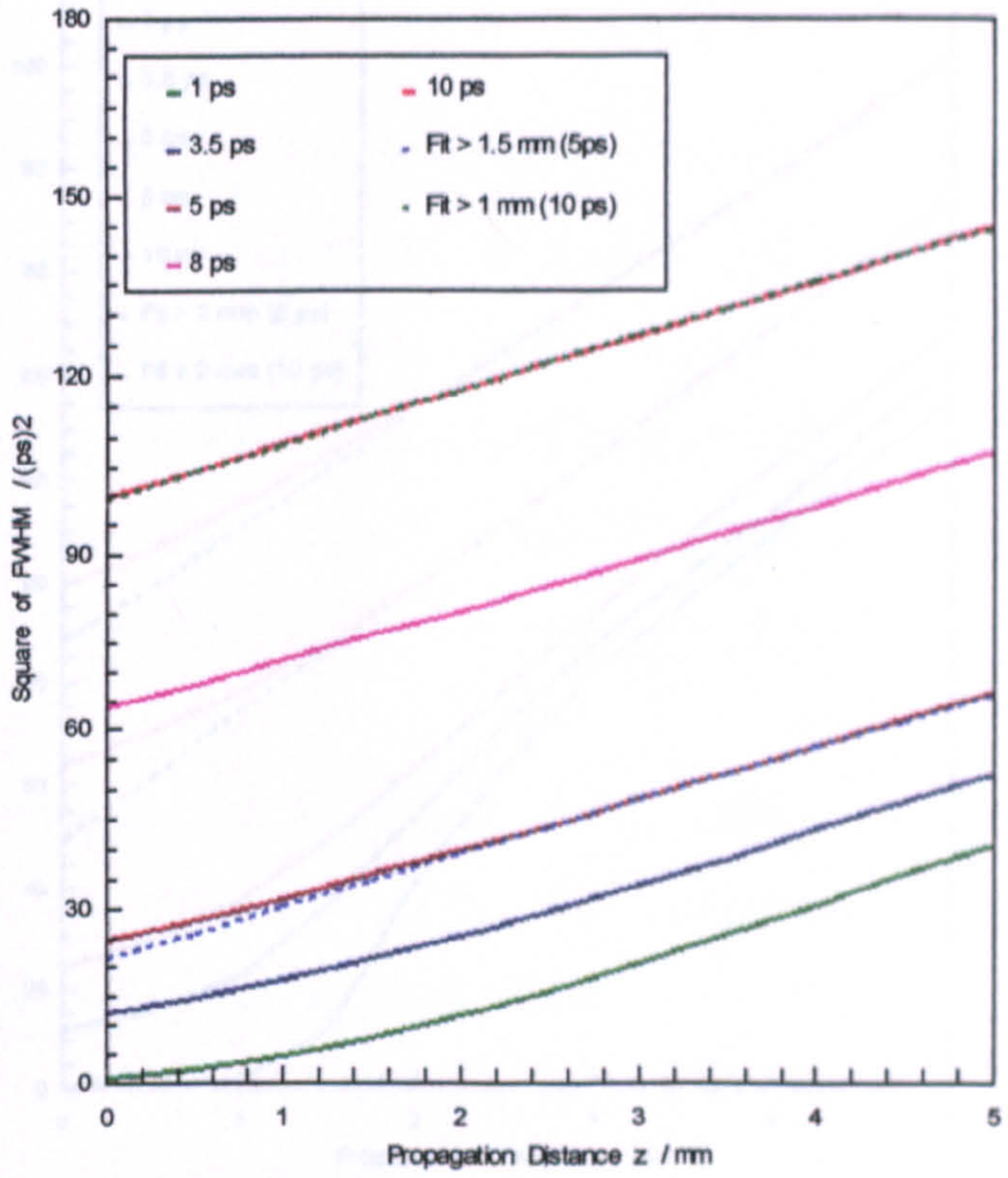

Figure 5.25 Results of propagation model for small GaAs CPW.

Figure 5.26 displays the results for the large GaAs CPW. Two fits are again shown, calculated for propagation distances greater than 2 mm with initial 8 ps and 10 ps FWHM Gaussian pulses. The same trend is apparent - longer duration pulses deviate less from the Gaussian rule than shorter pulses. The model also confirms that for a similar initial pulse, the large GaAs CPW is expected to cause more deviation from the Gaussian rule than the smaller CPW.

The results of the model for pulse propagation along the commercial alumina CPW are presented in Figure 5.27. Longer initial pulses have been modelled for this CPW as no shorter pulses are experimentally available for comparison - the CPW is not suitable for on-wafer pulse generation like the GaAs CPW. The dotted line is a fit for the 12 ps initial Gaussian for propagation distances beyond 1 mm.

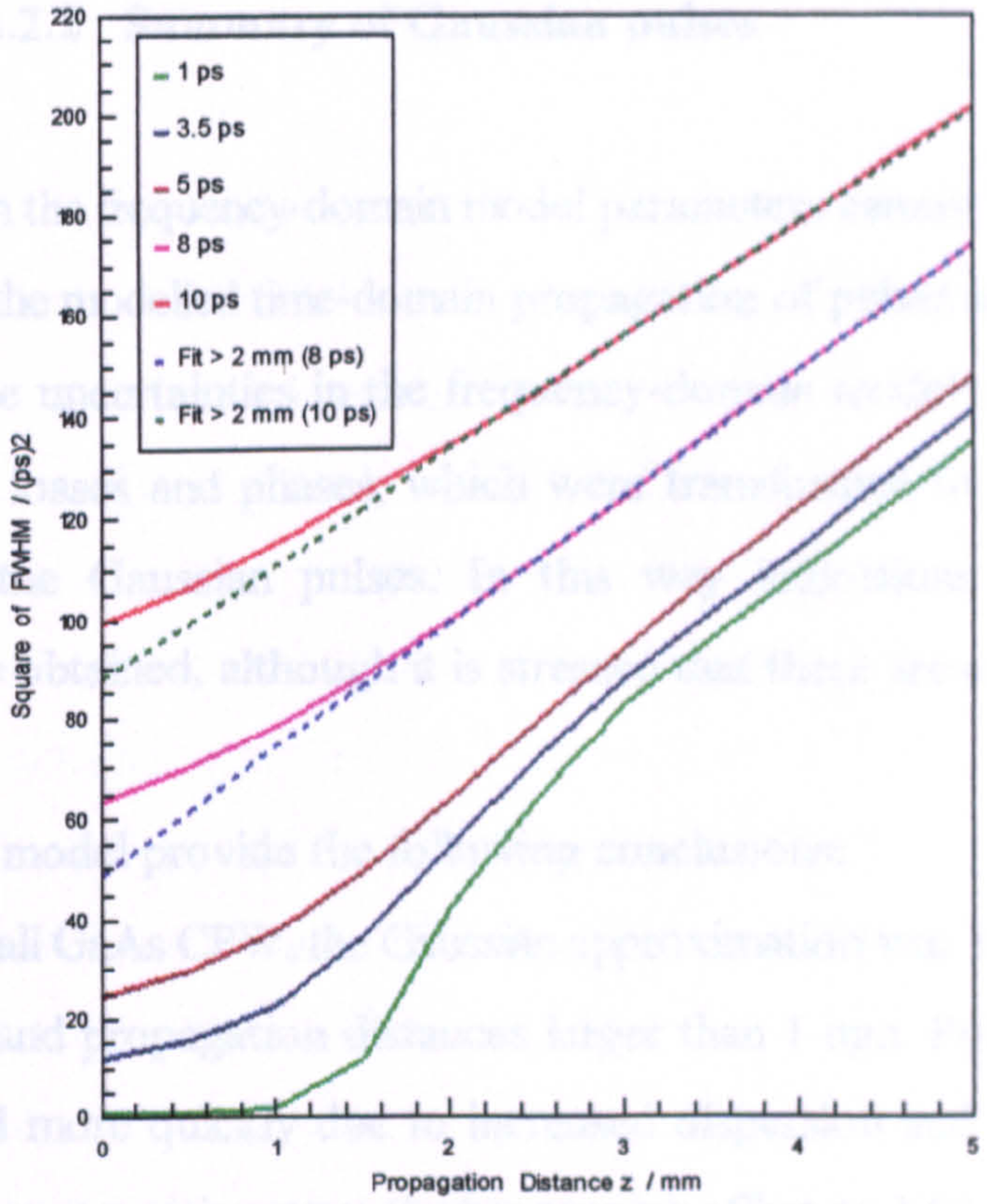

Figure 5.26 Results of propagation model for large GaAs CPW.

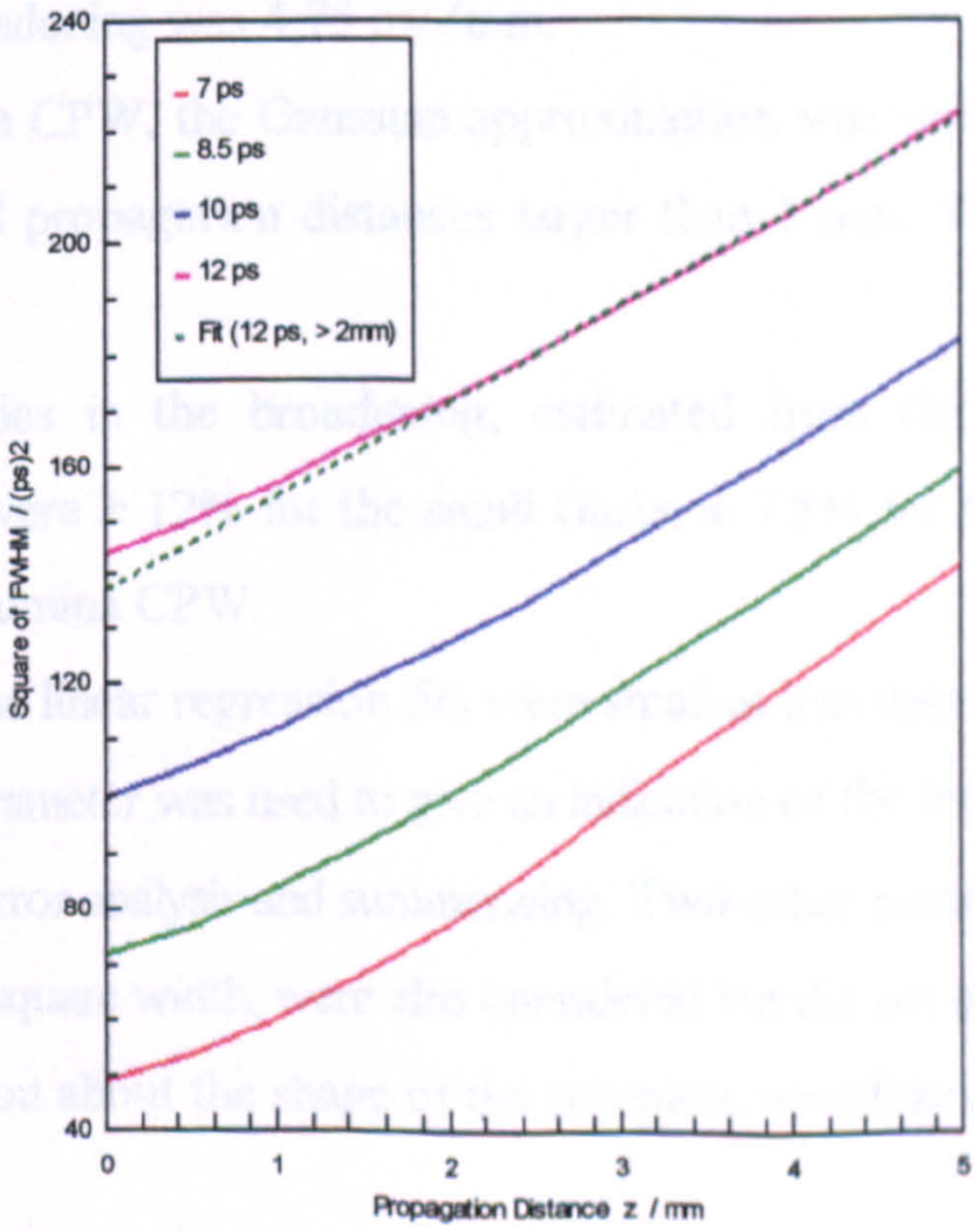

Figure 5.27 Results of propagation model for alumina CPW.

5.4.2.2 Summary of Gaussian pulses

The uncertainties in the frequency-domain model parameters cannot be easily transformed to uncertainties in the modelled time-domain propagation of pulses along the transmission line. However, the uncertainties in the frequency-domain model were used to define a range of possible losses and phases, which were transformed to the time-domain and convolved with the Gaussian pulses. In this way indications of the time-domain uncertainties were obtained, although it is stressed that these are estimates.

The results of the model provide the following conclusions:

(i) For the small GaAs CPW, the Gaussian approximation was valid for pulses longer than 5 ps and propagation distances larger than 1 mm. Pulses shorter than 5 ps broadened more quickly due to increased dispersion and losses. For the given range, linear regression gave the broadening effect as 3.00 ps/√mm.

(ii) With the large GaAs CPW, the dispersive and loss effects were greater than for the small CPW (given similar initial pulses). Therefore the Gaussian approximation was only valid for pulses longer than 10 ps and propagation distances larger than 2 mm. The broadening was 4.75 ps/√mm.

(iii) For the alumina CPW, the Gaussian approximation was valid for pulses longer than 12 ps and propagation distances larger than 1 mm. The broadening was 4.13 ps/√mm.

(iv) The uncertainties in the broadening, estimated from the frequency-domain uncertainties, were ± 12% for the small GaAs, ± 7.5% for the large GaAs and ± 8% for the alumina CPW.

(v) The errors in the linear regression fits were small at less than 1%.

(v) The FWHM parameter was used to give an indication of the broadening effect and was useful for error analysis and summarising. Two other parameters, the risetime and root-mean-square width, were also considered but did not provide significantly more information about the shape of the complete waveform.

5.4.2.3 Effect of taper

The effect of the taper, designed to maintain constant impedance between the large and small GaAs CPW (see Figure 3.3), was modelled by splitting it into segments. The segmentation was achieved by creating a stepped approach to the changes in the line dimensions, consisting of several small lengths of CPW with each section having different but constant central line and gap dimensions. To find the minimum number of segments required to provide reasonable accuracy, the 0.5 mm length taper was split into 1, 2, 5 and 10 segments (comprising sections of length 500 μm, 250 μm, 100 μm and 50 μm respectively). The model was applied to all the segments of each theoretical taper for three initial inputs: a Gaussian of 2.2 ps FWHM; a Gaussian of 3.5 ps FWHM; and an EOS waveform (measured just before the taper) of 2.2 ps FWHM. The durations of the resulting pulses are plotted against the reciprocal of the number of segments n (Figure 5.28). It is observed that splitting the taper into more than five segments did not significantly change the modelled results for any of the three input pulses.

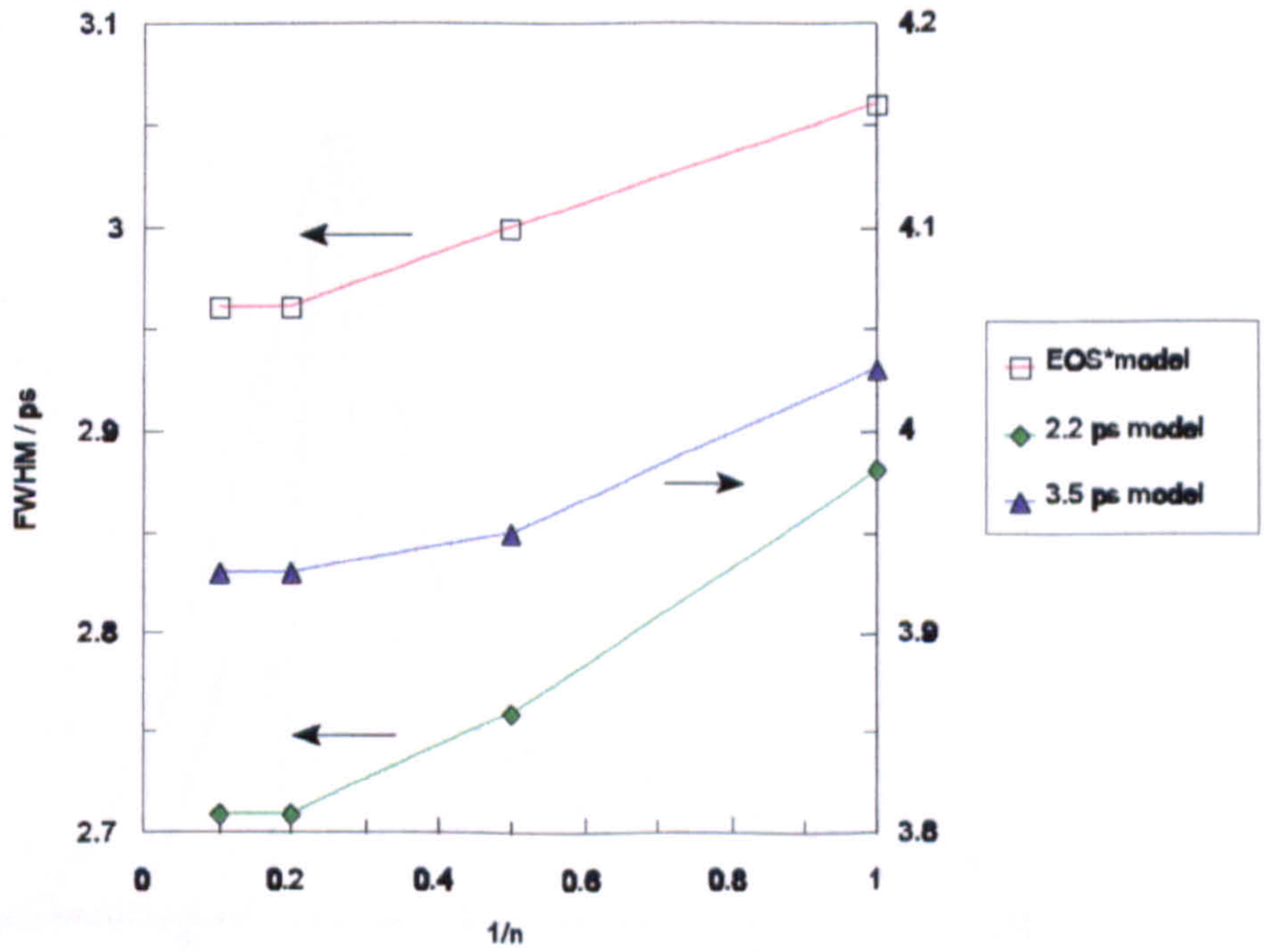

Figure 5.28 Modelled effect of splitting taper into segments.

The taper model broadened an initial 3.5 ps Gaussian pulse to 3.93 ps. This can be

compared to the broadening on the same pulse of the small GaAs line (to 3.87 ps) and the large GaAs line (to 4.00 ps). The equivalent broadening parameter of the taper was 3.19 ps/√mm.

5.4.3 Comparison of model with EOS results

5.4.3.1 GaAs line

Chapter 4 describes the Ti:sapphire laser electro-optic sampling measurement system and gives examples of some results. This section summarises EOS measurements made with Auston switch device PG6 with different separations between the generation and sampling reference planes, enabling comparison with the model results. Figure 5.29 shows the evolution of a pulse measured at different propagation distances from the generation point. It was found that the reproducibility of the EOS amplitudes after the voltage calibration was not good enough to compare the amplitude with that obtained from the model. To facilitate the comparison of pulse shapes each waveform was normalised.

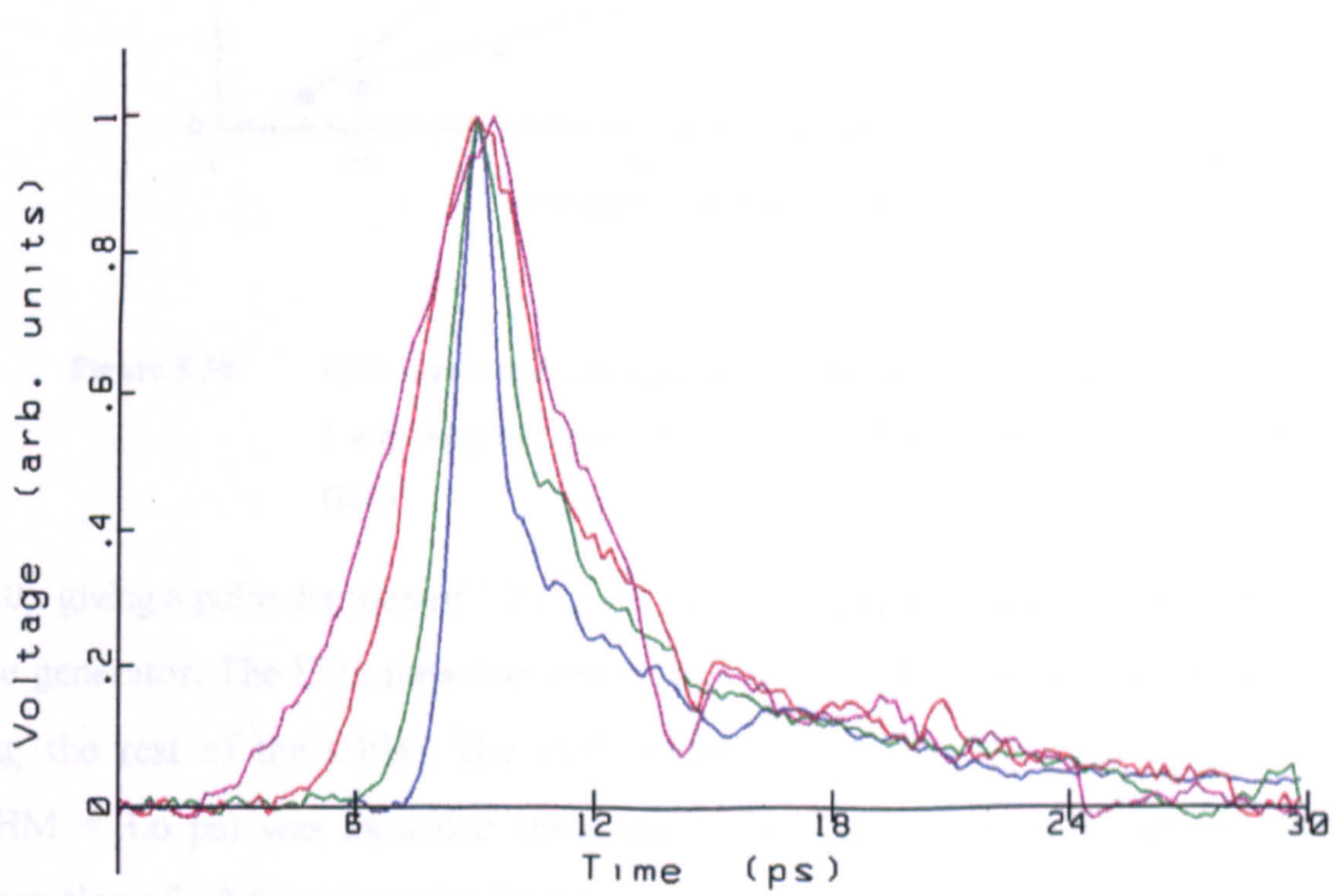

Figure 5.29 Example of EOS results showing pulse evolution along GaAs line at position z from the generation point: —— z = 0.3 mm, FWHM = 1.3 ps; —— z = 1 mm, FWHM = 2.2 ps; —— z = 1.5 mm, FWHM = 3.6 ps; —— z = 2 mm, FWHM = 4.8 ps.

Figure 5.30 plots the square of the EOS-measured FWHM along a GaAs pulse generator, and compares the effect of the model along different sections of the CPW with different initial pulses. The EOS pulse at z = 300 μm was extrapolated back to zero propagation

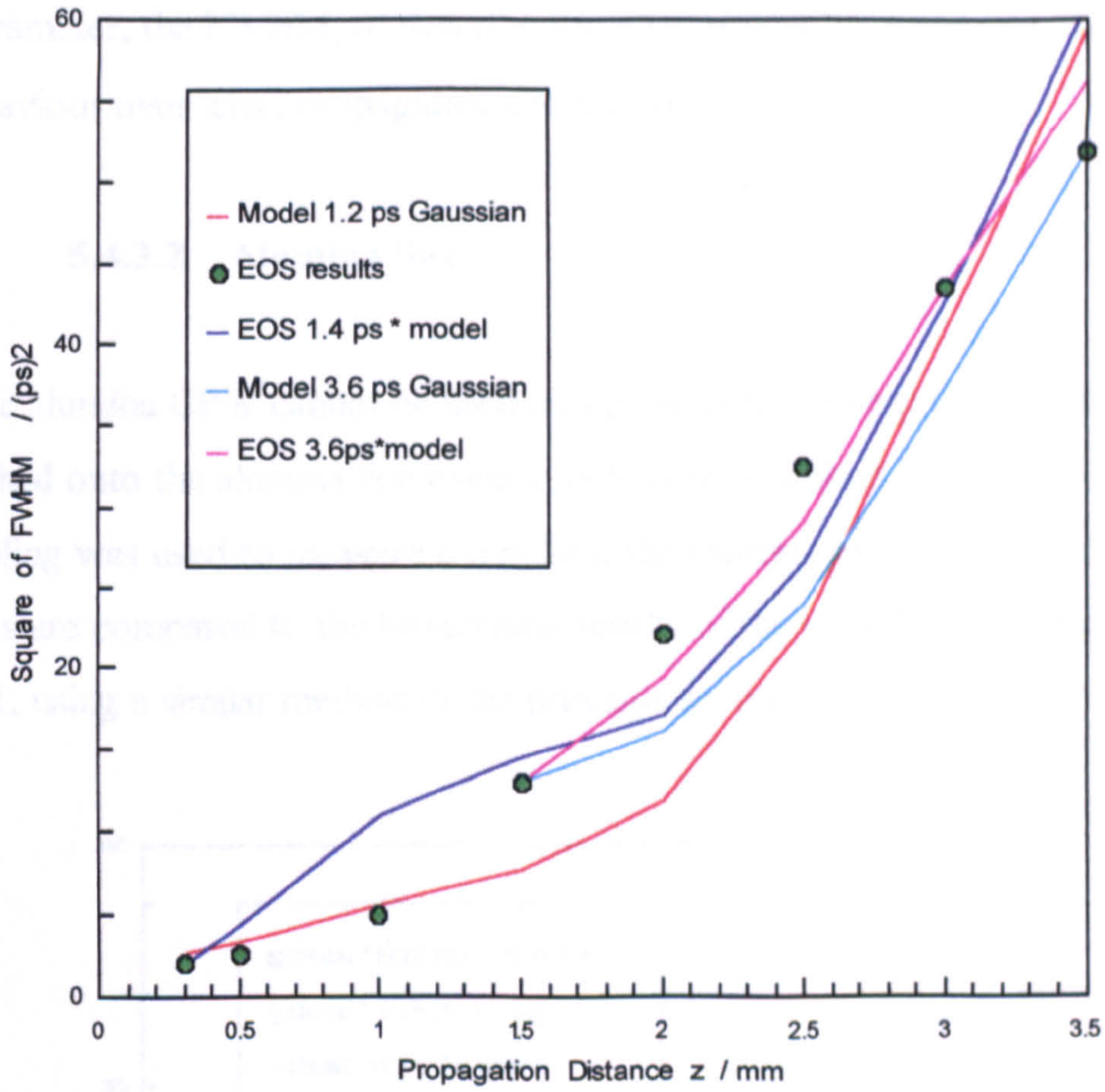

Figure 5.30 EOS results and propagation model along GaAs pulse generator, comprising a 1 mm length of small GaAs CPW, a 0.5 mm taper and a 2 mm length of large GaAs.

(z = 0), giving a pulse duration of 1.2 ps. A 1.2 ps Gaussian was modelled along the GaAs pulse generator. The EOS measurement at 300 μm (FWHM 1.4 ps) was also modelled along the rest of the CPW. The EOS measurement after the taper (z = 1.5 mm, FWHM = 3.6 ps) was modelled along the 2 mm large CPW, and compared to the propagation of a 3.6 ps Gaussian from the same position.

From the results it can be concluded that the model appears to overestimate the GaAs CPW broadening. Between z = 0.3 mm and z = 3.5 mm the model overestimates the

broadening by 8.5% relative to the EOS measurements, and by 5.5% between z = 1.5 mm and z = 3.5 mm. The discrepancy is within the uncertainties in the model (± 12% small GaAs and ± 8% large GaAs) and in the EOS measurements, caused by probe positional errors (estimated at ± 0.1 mm). A further uncertainty, likely to be significant, is the use of a single parameter, the FWHM, to describe waveforms which are not Gaussian in shape (nor in behaviour over small propagation distances).

5.4.3.2 Alumina line

Because the alumina CPW cannot be used as a photoconductive pulse generator, pulses were launched onto the alumina line using a technique described in *section 5.5*. Electro-optic sampling was used to measure the pulses, the shortest of which was 10 ps. These EOS results are compared to the broadening results of the model for the alumina line in Figure 5.31, using a similar method to the previous section.

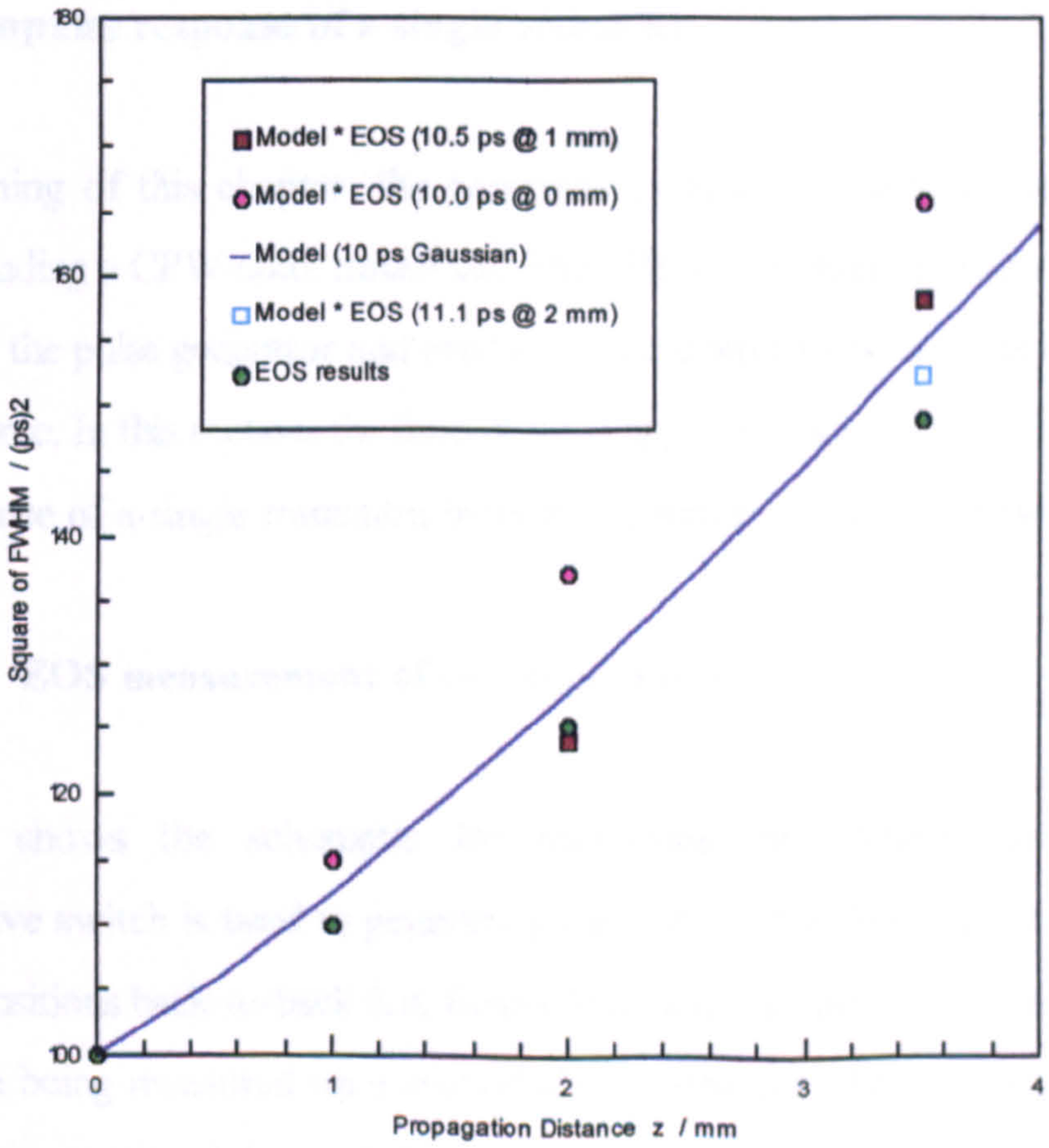

Figure 5.31 EOS results and propagation model along alumina line.

From the results, it is concluded that the alumina model overestimates the broadening, by 16% relative to the EOS measurements, between z = 0 mm and z = 3.5 mm. This difference is larger than the uncertainty in the alumina model broadening (± 8%), but including uncertainties in the EOS and use of FWHM parameter, the agreement is not too unsatisfactory.

Referring back to the frequency-domain measurements (*section5.3.5*), the model produced larger values of attenuation on the alumina CPW than measured with an ANA, mainly due to large predicted radiation losses. It is suggested that better overall agreement could be produced by assuming the radiation loss is smaller than currently modelled. Reasons for this could be the effect of the UTF transitions, metal UTF mount and alumina carrier, with other sources of error including the metallisation surface roughness. These are not further pursued here.

5.5 The impulse response of a single transition

At the beginning of this chapter, the components of a LT-GaAs pulse generator are described, including a CPW-coax transition. The effect of a single transition is important, to characterise the pulse generator and enable the generator to be used as an oscilloscope calibration source. In this section, the time-domain approach is employed to determine the impulse response of a single transition from measurements made with two transitions.

5.5.1 EOS measurement of two transitions

Figure 5.32 shows the schematic for measuring two transitions. A LT-GaAs photoconductive switch is used to generate pulses on a CPW line. The pulses propagate across two transitions back-to-back (i.e. from CPW to coax, and from coax back to CPW again), before being measured on a second CPW using the EOS system. By combining previous measurements and the modelling it is possible to extract the impulse response of a single transition.

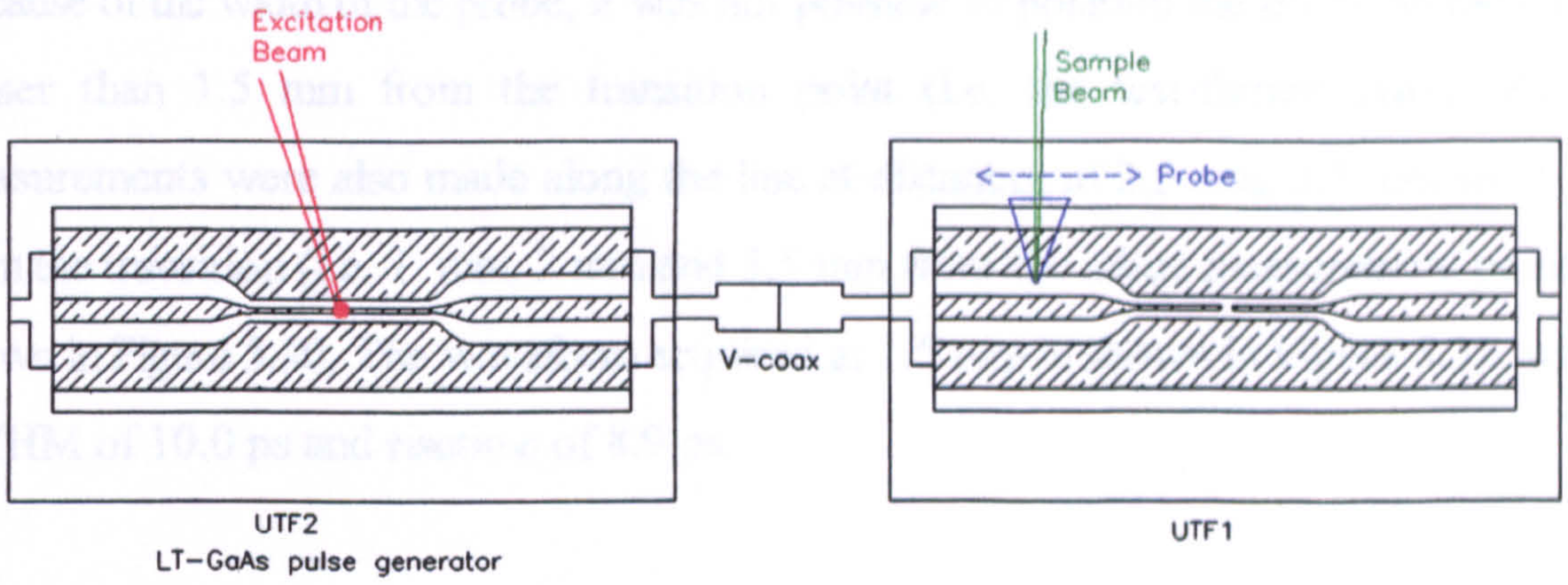

Figure 5.32 EOS two-transition measurement schematic.

Test-fixture UTF2 was used to hold pulse generator PG7 which was biased and illuminated as previously described. The resulting pulses were measured on the second CPW mounted in test-fixture UTF1. This CPW may be alumina or GaAs. Although the system would be more symmetrical if a second GaAs circuit were used, an alumina line was used as it is more sturdy in UTF1.

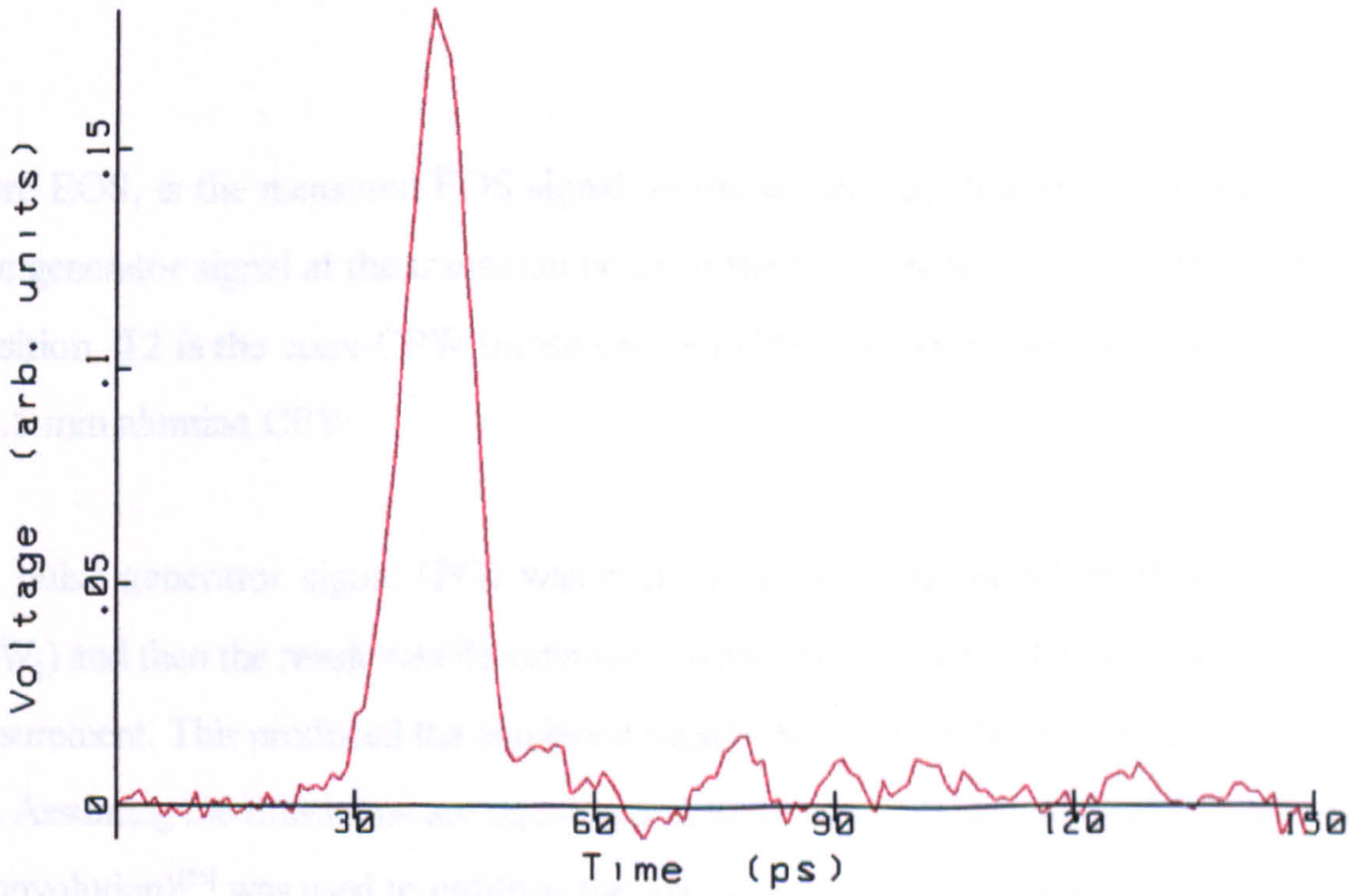

Figure 5.33 Two-transition EOS waveform.

A 19 mm alumina line provided more viewing space for positioning of the EOS probe. Because of the width of the probe, it was not possible to position the probe on the circuit closer than 1.5 mm from the transition point (i.e. the test-fixture jaws). Further measurements were also made along the line at distances of 2.5 mm, 3.5 mm and 5 mm from the transition (i.e. 1 mm, 2 mm and 3.5 mm from the initial measurement point) as shown in Figure 5.30. The waveform acquired at 1.5 mm is shown in Figure 5.33, with a FWHM of 10.0 ps and risetime of 8.9 ps.

5.5.2 Derivation of single-transition response

An EOS measurement of the GaAs pulse generator was also required for the calculation. A previous measurement was used at the initial position of the transition (i.e. where the UTF jaws would be, except that the measurement was performed on a longer line, before the transition, to provide space for the probe).

The derivation is explained with the following equation:

$$EOS_1 = PG \otimes T1 \otimes T2 \otimes CPW_1 \quad , \tag{5.19}$$

where EOS_1 is the measured EOS signal on the second test-fixture, PG is the measured pulse generator signal at the transition point of the first test-fixture, T1 is the CPW-coax transition, T2 is the coax-CPW transition, and CPW_1 is the transfer function of a length of 1.5 mm alumina CPW.

The pulse generator signal (PG) was convolved with the modelled effect of the line (CPW_1) and then the result was deconvolved, with filtering, from the two transition EOS_1 measurement. This produced the combined transfer function of the two transitions (T1 and T2). Assuming the transitions are equal and reciprocal, a self-deconvolution (square-root deconvolution)[16] was used to produce the impulse response of a single transition (Figure 5.34, FWHM = 6.0 ps).

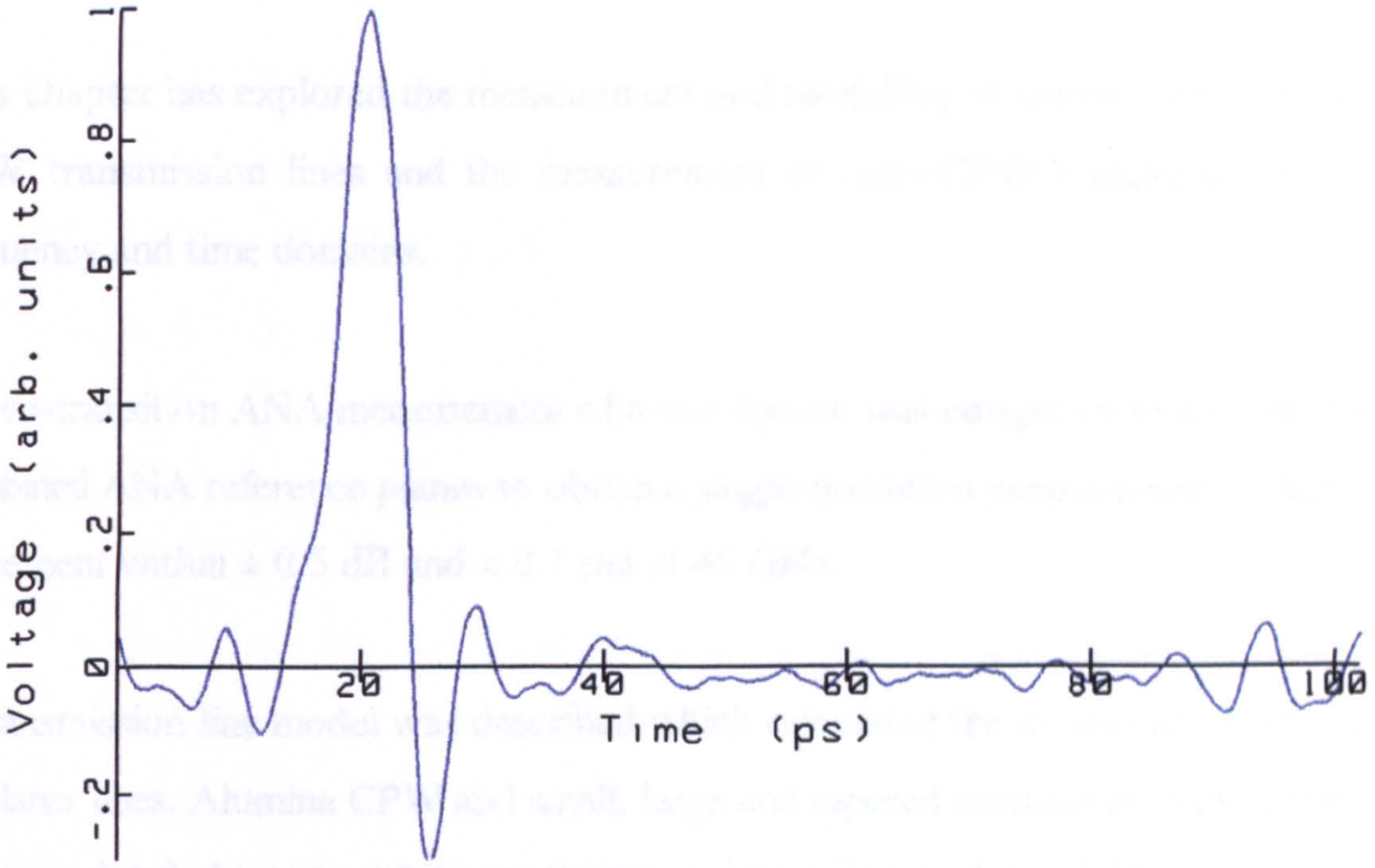

Figure 5.34 Derived single transition.

There are several contributions to the uncertainty in the derivation of the single transition, including EOS measurements, model of 1.5 mm alumina CPW, position of transition (stepper pin v ground plane) and deconvolution (filtering), including self-deconvolution. Most of these contributions are discussed elsewhere: the uncertainty due to the temporal resolution of the EOS system in *section 4.9*; due to the model in *section 5.4.2*; and due to deconvolution in *section 6.2*. The uncertainty due to positioning the probe within an accuracy of approximately ±0.1 mm must also be included. A range of ±0.2 mm is estimated in defining the position of the transition relative to the line, as the stepper pin and jaw clamps are not in the same position (see *section 5.1.2*).

The derivation of the transition uncertainty is not included here; an example of combining uncertainty contributions (for the derivation of the CRO response) is provided in *section 6.5*.

For the transition FWHM parameter, these uncertainties combine to give a transition impulse response of 6.0 -1.1 / +1.0 ps.

5.6 Conclusions

This chapter has explored the measurement and modelling of planar GaAs and alumina CPW transmission lines and the measurement of coax-CPW transitions in both the frequency and time domains.

A two-transition ANA measurement of a test-fixture was compared to a method which combined ANA reference planes to obtain a single-transition measurement, achieving an agreement within ± 0.5 dB and ± 0.1 rad at 45 GHz.

A transmission line model was described which calculated the losses and phase changes on planar lines. Alumina CPW and small, large and tapered sections of GaAs CPW were accommodated. Agreement between the transmission line model and ANA measurements was within the calculated uncertainties for phase, but the agreement in attenuation was not as good.

Deconvolved sampling oscilloscope measurements of the test-fixture were also compared to the ANA results, with agreement better than ± 1.5 dB and ± 0.2 rad at 60 GHz.

The model was used to calculate the broadening of pulses propagating along the transmission lines, with approximate uncertainties of 10%. The modelled broadening was compared to electro-optic sampling (EOS) measurements with satisfactory agreement within the uncertainties.

Using an EOS two-transition back-to-back technique and a combination of previous results from the chapter, the impulse response (time-domain transfer-function) of a single coax-coplanar transition was derived, producing a FWHM of 6.0 -1.1 / +1.0 ps.

5.7 References to Chapter 5

1 J.F.Whitaker, R.Sobolewski, D.R.Dykaar, T.Y.Hsiang and G.A.Mourou, "Propagation Model for Ultrafast Signals on Superconducting Dispersive Striplines", IEEE Trans MTT, Vol. 36 , No. 2, Feb 1988, pp 277-285 and references therein.

2 NIS3003, "The Expression of Uncertainty and Confidence in Measurement for Calibrations", edition 8, NAMAS guidelines, NPL, 1995.

3 See for example:
G.W.C.Kaye and T.H.Laby, "Table of Physical and Chemical Constants", Longman Scientific, edition 15, 1989.

4 A.D.Olver, "Microwave and Optical Transmission", John Wiley and Sons, chapter 8, 1992.

5 T.L.Simpson and B.Tseng, "Dielectric Loss in Microstrip Lines", IEEE Trans. MTT, Vol. 24, 1976, pp 106-108.

6 M.N.Afsar, "Millimeter-wave Dielectric Properties of Materials", Infrared & Millimetre Waves, Vol. 12, 1984, pp 32-.

7 Private communication with Bob Clark, Free-space microwave standards, NPL.

8 D.S.Phatak and A.P.Defonzo, "Dispersion Characteristics of Optically Excited Coplanar Striplines: Pulse Propagation", IEEE Trans. MTT, Vol. 38, No. 5, 1990, pp 654-661.

9 M.Y.Frankel, S.Gupta, J.A.Valdmanis and G.A.Mourou, "Terahertz Attenuation and Dispersion Characteristics of Coplanar Transmission Lines", IEEE Trans. MTT, Vol. 39, No. 6, 1991, pp 910-916.

10 G.H.Bryant, "Principles of Microwave Measurements", IEE Electrical Measurement Series 5, 1988, chapter 5.

11 A.L.Cullen, "Microwave Measurements", editor A.E.Bailey, IEE Electrical Measurement Series 3, 1985, chapter 3.

12 K.J.Silvonen, "A General Approach to Network Analyzer Calibration", IEEE Trans. MTT, Vol. 40, No. 4, April 1992, pp 754-759.

13 R.Pantoja, M.J.Howes, J.R.Richardson and R.D.Pollard, "Improved Calibration

and Measurement of the Scattering Parameters of Microwave Integrated Circuits", IEEE Trans MTT, Vol. 37 , 1989, pp 1675-1680.

14 D.Olney, "The Effects of Adapters on Vector Network Analyzer Calibrations", Microwave Journal, Nov 1994.

15 "Measuring Non-insertable Devices", Hewlett Packard Product Note 8510-13.

16 KRush, J.Kerley and S.Drawing, "Characterizing High-speed Oscilloscopes", IEEE Spectrum, 1990.

17 D.F.Williams and R.B.Marks, "Reciprocity Relations in Waveguide Junctions", NIST Industrial Consortium on MMIC technology", NIST (Software Manual), 1989.

18 Private communication with Dr David Bannister, Guided-wave microwave standards, NPL.

19 N.G.Paulter and D.N.Sinton, "Optoelectronic Measurement of Picosecond Electrical Pulse Propagation in Coplanar Waveguide Transmission Lines", IEEE Trans MTT, Vol. 37 , No. 10, Oct 1989, pp 1612-1619.

6 THE OSCILLOSCOPE RESPONSE

6.1 Introduction

This chapter explains the concept behind, and gives practical examples of, deconvolution and the measurement of jitter. It then uses various results in previous chapters, including the measurement of the LT-GaAs pulse generator and the de-embedding of a single transition, to derive the impulse response of a sampling oscilloscope, using the deconvolution and removal of jitter developed in this chapter.

6.2 Deconvolution

Section 1.4.4 defines convolution and states that deconvolution is the reverse process of convolution. Fourier and convolution theory states that a convolution is associative, commutative and distributive.[1] Furthermore, the product of two functions is the transform of the convolution of their individual transforms. Therefore, in the frequency domain, equation (1.6) may be expressed as:

$$H(\nu) = F(\nu).G(\nu) \quad , \tag{6.1}$$

where F(ν), G(ν), and H(ν) are the Fourier transforms of the time-domain waveforms f(t), g(t) and h(t).

6.2.1 Quadrature approximation

The product of two Gaussians is a third Gaussian, and the Fourier transform of a Gaussian is a Gaussian. It can be shown that the convolution of two Gaussian pulses, f1 and g1, results in a third Gaussian pulse, h1. The duration of h1 is given by the summation in quadrature of the durations of f1 and g1, i.e.

$$(\tau_{h1})^2 = (\tau_{f1})^2 + (\tau_{g1})^2 \quad , \tag{6.2}$$

where τ is the FWHM of each of the Gaussians.

It is therefore possible to deconvolve known system responses from recorded data, by approximating them to be Gaussian and subtracting the FWHMs in quadrature. Only the FWHM parameter is used, not the complete waveform. This approximation is known as quadrature deconvolution and can give a useful approximation to the width of the desired function.

6.2.2 Deconvolution and filtering

Gaussian quadrature deconvolution is only an approximation to full deconvolution. In the following example a known system response g(t) is deconvolved from the measured data h(t) to give the desired quantity f(t). Full deconvolution is performed in the frequency-domain (simplifying the mathematics of the deconvolution to a quotient) and is shown here with a filter term X(ν), such that:

$$F(\nu) = \frac{H(\nu)}{G(\nu)} . X(\nu) \quad . \tag{6.3}$$

The desired function f(t) is then obtained by Fourier transform of F(υ). (In the case of calibrating an oscilloscope, the system response g(t) is found by deconvolving a known pulse generator signal f(t) from the measured data h(t), so the terms F(ν)and G(ν) are transposed in equation (6.3). The rest of this section continues describing the first case.)

At first glance the reason for the additional filter term is not intuitively obvious. Sharp features in a time-domain waveform translate to high frequency components in the frequency-domain and conversely, power in components at higher frequencies in the frequency-domain can transform to unwanted structure, such as ringing, in the time-domain. For well-defined waveforms with excellent signal-to-noise, the filter term may not be required. If g(t) is significantly shorter than h(t), for example less than half the FWHM, then the advantage of using a filter is marginal. However, practical deconvolutions often

involve waveforms with noise. Without a filter, noise in the time-domain can be "blown-up" by the frequency-domain deconvolution process, particularly when the difference in the duration of both waveforms is small. For example, if G(ν) tends to zero at high frequencies and H(ν) has a finite value at such frequencies caused by noise, then without a filter F(ν) becomes very large and unwanted structure, usually in the form of ripple, is introduced into the deconvolution result f(t).

The choice of filter is critical to the deconvolution. The filter[2] used in this thesis has the form,

$$X(\nu) = \frac{|G(\nu)|^2}{|G(\nu)|^2 + \eta\nu^4} \quad , \tag{6.4}$$

where η determines the effective bandwidth of the filter. Such a filter discriminates against noisy data, particularly at higher frequencies. The ν^4 term is equivalent to minimising the second derivative of the signal in the time-domain, or smoothing the waveform.

The value of η requires careful choice. Too small a value may not filter sufficiently and the deconvolution could produce extreme noise in the result. Too large a value will over-filter, producing a result which, whilst smooth, more closely matches the time-domain response of the filter than the desired signal. Sometimes a low-pass filter, such as the aptly-named brick-wall filter, is also used to eliminate unwanted high-frequency components.

The quality of a deconvolution therefore depends not only on the shape and relative duration of the initial waveforms, but also on the type and bandwidth of the filter. There is no simple method, for example a single parameter, which can be used to define the quality of the result. This is best illustrated by the following empirical example.

6.2.3 Example of deconvolution

This section provides a typical example of a deconvolution.[1] It shows the parameters which give an indication of the quality of a deconvolution and illustrates the problem of choosing an optimum filter to obtain the "best" result.

However, there is one important difference between the deconvolution in this example and that used in deriving the oscilloscope response in *section 6.4*. Functions g(t) and h(t) are not measured but are represented by artificially generated data, to enable a comparison between the deconvolved results and the result that is expected, in addition to comparing the deconvolved results obtained with different filters.

Gaussian pulses were generated with widths of 12 ps and 16 ps, giving risetimes (equal to the falltime) of 8.60 ps and 11.46 ps. Across the epoch of both waveforms, noise was added to the amplitude at the 2% rms level. The first noised waveform (FWHM = 11.92 ps, risetime = 8.59 ps, and falltime = 9.08 ps) was used as the system response, g(t). The second noised waveform (FWHM = 16.24 ps, risetime = 11.94 ps, and falltime = 11.50 ps) was used as the data, h(t).

Six filters, numbered one to six and corresponding to six orders of magnitude of filter parameter η (but due to the ν^4 term equivalent to a factor of 30 in the overall filter), were used to deconvolve the system from the data. The effect of the different filters on various parameters, such as the FWHM and noise of the result, is summarised in Table 6.1. Figure 6.1 plots some of the parameters against the filter number.

---

[1] The program code for the deconvolution software is based on that written by Dr Alan G Roddie, whose help is gratefully acknowledged.

Table 6.1 Effect of filter on various parameters.

Filter No	Filter FWHM / ps	Filter Bdwth / GHz	Result RMS Noise %	Re-convolved data / ps	Result Bdwth / GHz	Result FWHM / ps	Result risetime /ps	Result falltime /ps
1	3	95	14.9	16.21	-	13.65	-	8.3
2	5	77	6.2	16.23	26.8	12.64	-	7.78
3	8	65	2.3	16.26	26.8	12.25	7.43	7.72
4	9	55	1.4	16.54	26.8	12.83	7.91	7.83
5	12	45	1.4	17.55	26.5	14.41	8.81	8.58
6	15	32	1.4	20.21	23.4	17.61	10.89	10.62

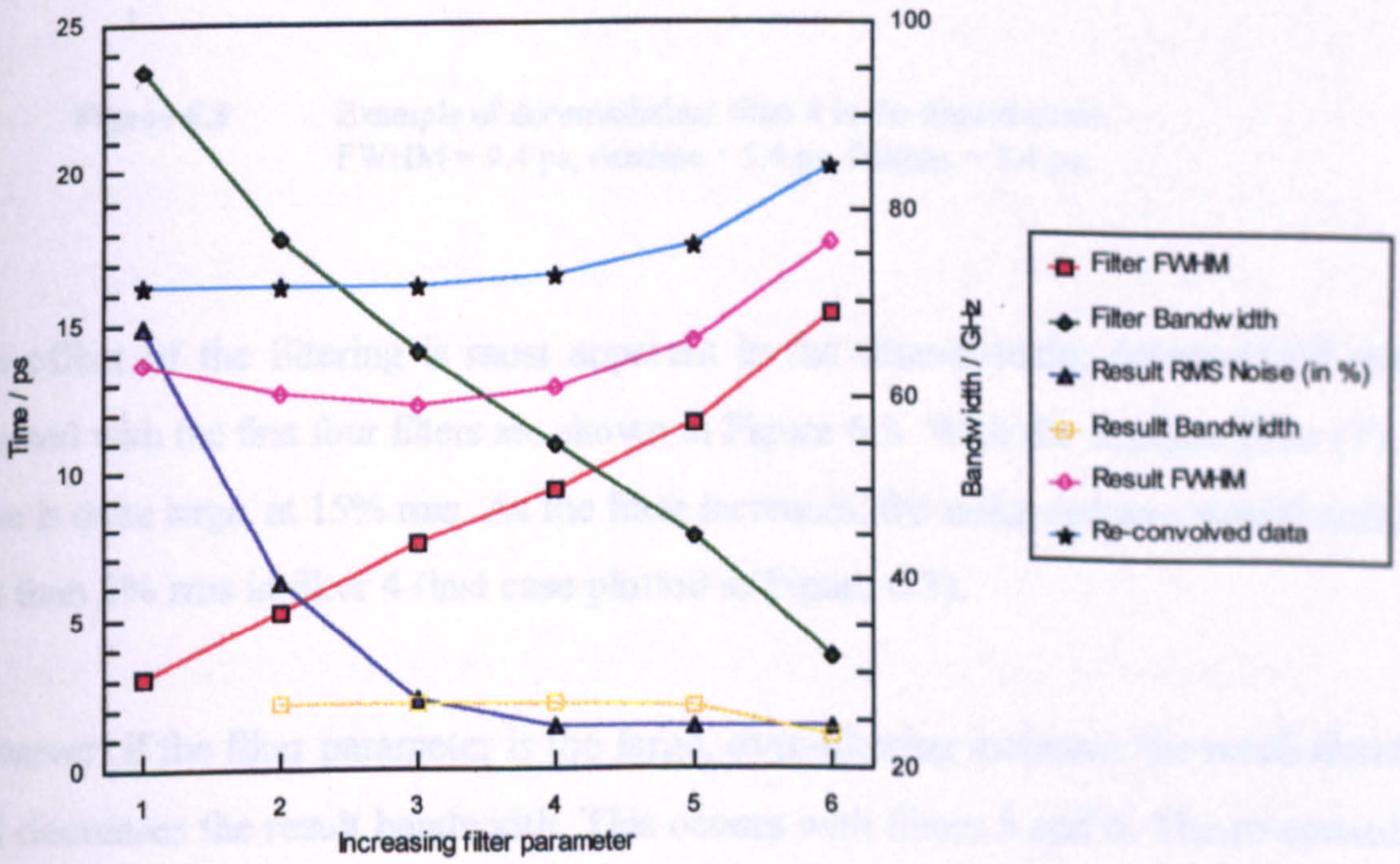

Figure 6.1 Example of deconvolution: effect of filter on various parameters of the deconvolved result.

As the filter parameter increases by each factor of ten, the calculated temporal filter width

increases by approximately 2 ps, and the filter bandwidth steadily decreases. An example of a filter (4) in the time-domain is shown in Figure 6.2. The filter does not affect the phase response - in the time-domain the filter is always symmetrical.

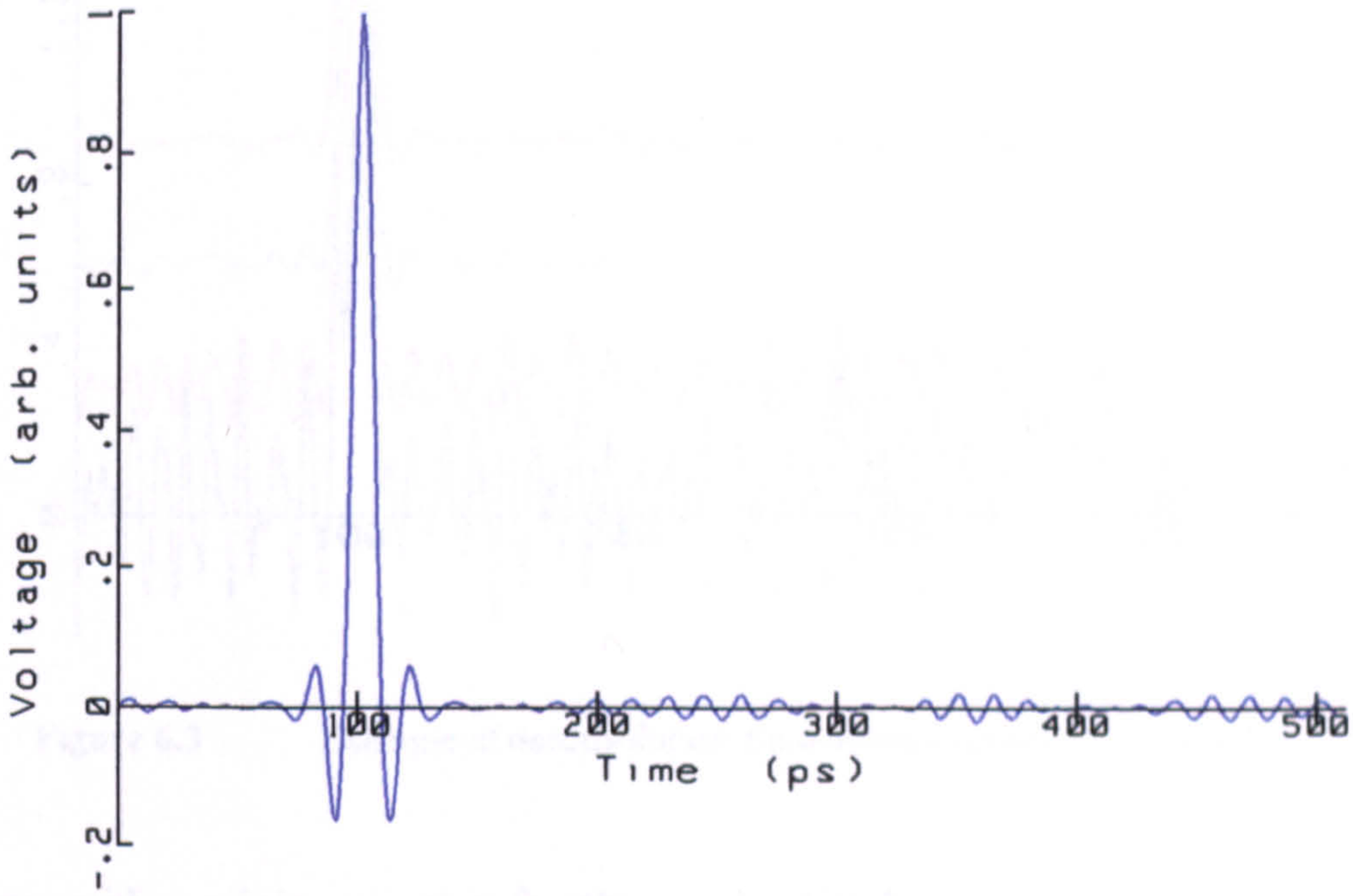

Figure 6.2 Example of deconvolution: filter 4 in the time-domain.
FWHM = 9.4 ps, risetime = 5.4 ps, falltime = 5.4 ps.

The effect of the filtering is most apparent in the time-domain; deconvolved results obtained with the first four filters are shown in Figure 6.3. With the smallest filter (1), the noise is quite large, at 15% rms. As the filter increases, the noise reduces significantly, to less than 2% rms in filter 4 (last case plotted in Figure 6.3).

However, if the filter parameter is too large, over-filtering increases the result duration and decreases the result bandwidth. This occurs with filters 5 and 6. The re-convolved data - defined as the original system convolved with the deconvolved result - gives a comparison with the original data and can be used to check that the deconvolved result is reasonable. The FWHM of the re-convolved data also increases with the filter parameter, significantly in the fifth and sixth cases.

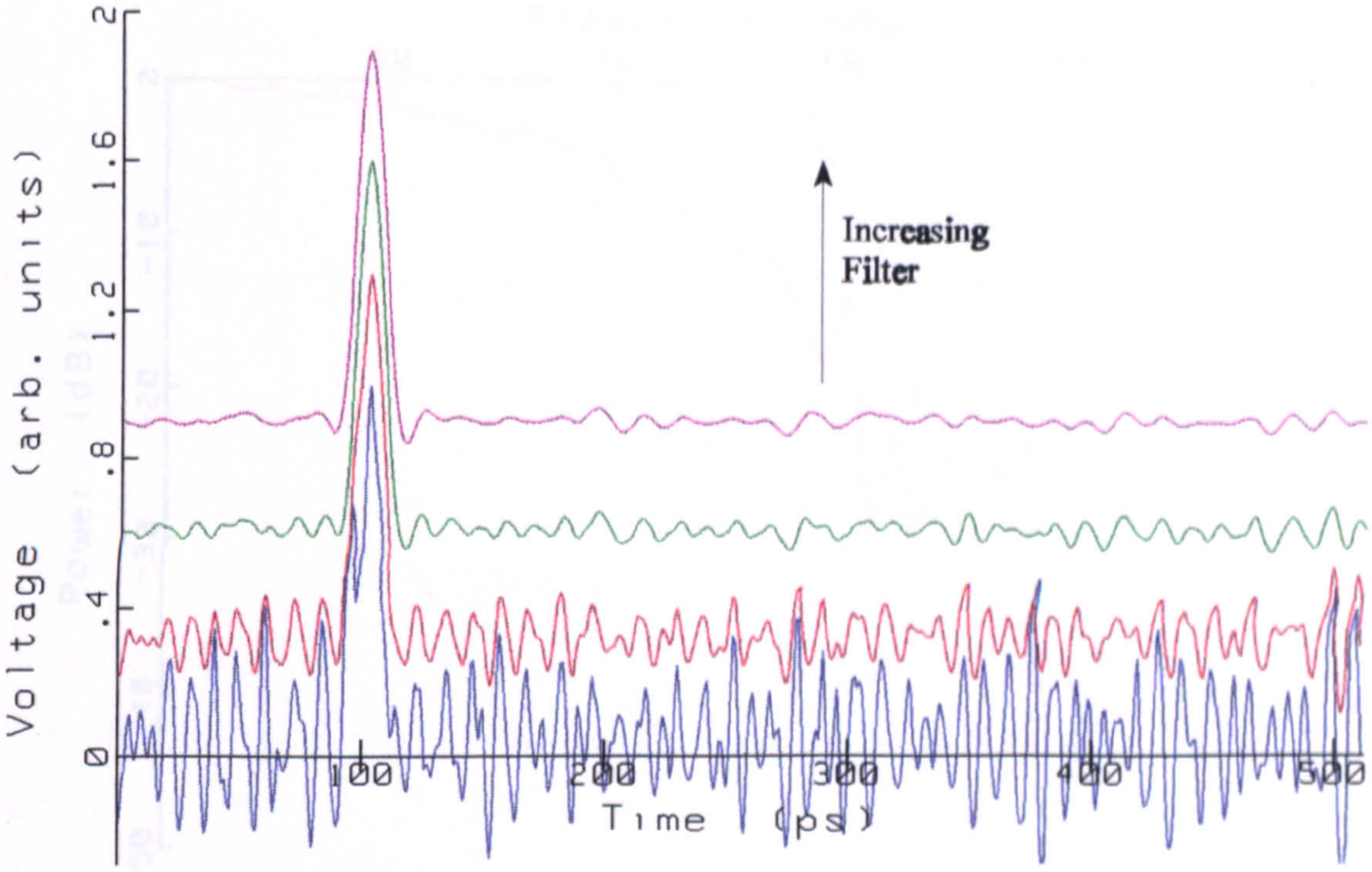

Figure 6.3 Example of deconvolution: time-domain results with filters 1-4.

A curve with a minimum value for the result FWHM (and in this case also the result risetime and falltime) is apparent with the different filter parameters (Figure 6.1). Providing that the deconvolution is not under-filtered - which can cause the measured FWHM and transition durations to vary widely due to the noisy structure - then the minimum gives a good indication of the optimum filter parameter.

In this example, the optimum result is obtained with filter 3 or possibly filter 4. The deconvolved frequency-domain result obtained with filter 4 is plotted in Figure 6.4 and compared with the filter. It is seen that at frequencies up to about 80 GHz the filter components are smaller than the result - this indicates over-filtering is unlikely. The smaller filters (1 to 3) do not coincide with their respective deconvolved result until frequencies higher than this, making over-filtering less likely still. Frequency components of the last filter (6) cross the result nearer to 50 GHz. There is still significant power (i.e. greater than -10 dB) in the result spectra at such a frequency, and therefore the result is over-filtered.

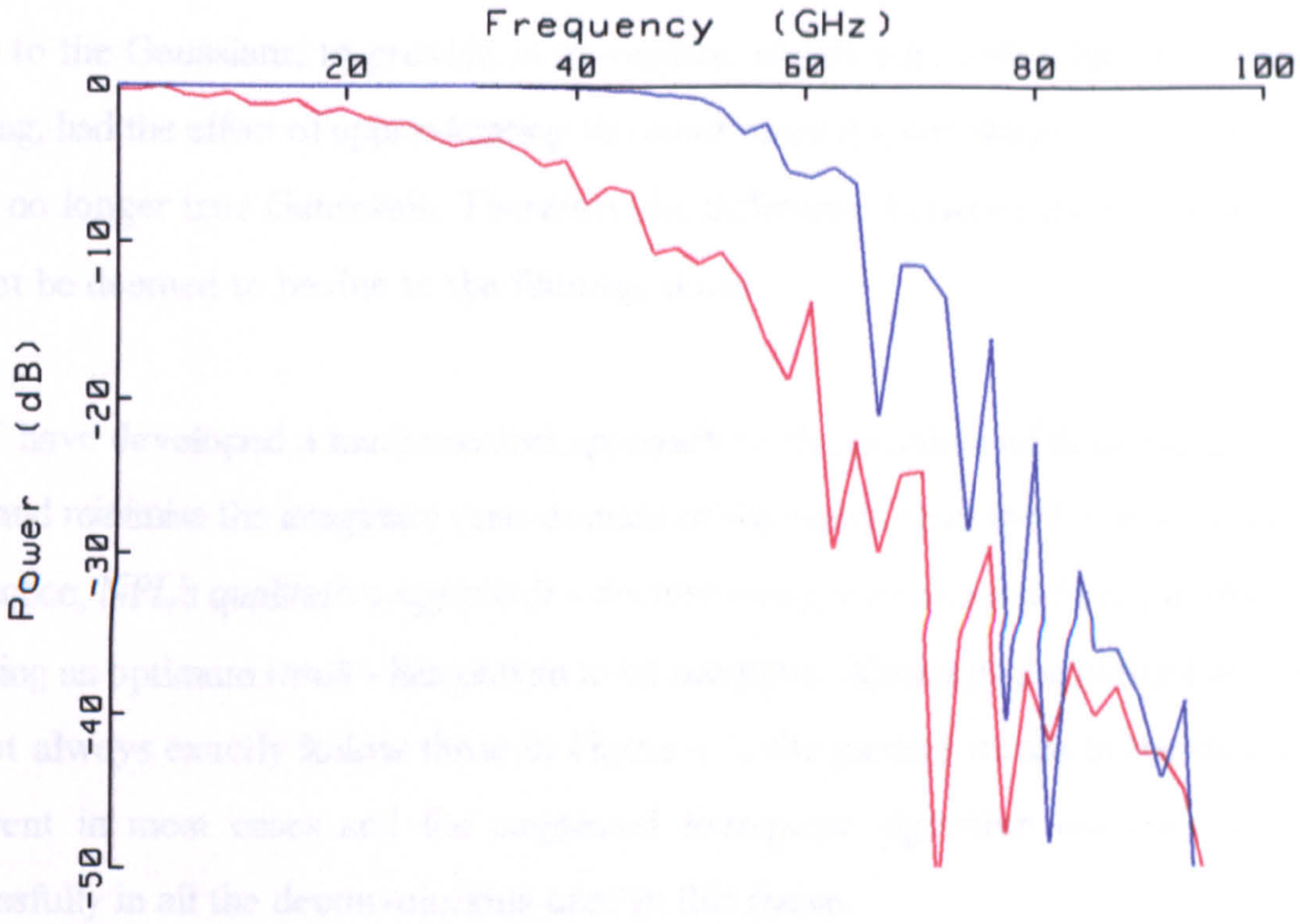

Figure 6.4 Example of deconvolution in the frequency-domain: —— deconvolved result, —— filter 4.

The suggested algorithm to select the optimum filtered result from those available, based on the above results, is to:

i) Check that the deconvolution returns acceptable noise in the result, smaller than less-filtered cases, and comparable to the noise in the system and data waveforms.

ii) Look for a result at, or near to, the FWHM minimum. Depending on the shape of the waveforms, a minimum in the risetime or falltime may provide a suitable alternative.

iii) Check that the bandwidth of the filter is larger than the bandwidth of such a result. A factor of at least two is desirable.

iv) Check that the shape of the re-convolved data does not differ significantly from the original data.

In the example, the third filter returned the following: FWHM = 12.25 ps, risetime = 7.43 ps, and falltime = 7.72 ps. The generated waveforms in the example were chosen to enable comparison with the quadrature deconvolution approximation method, which gave:

FWHM = 11.03 ps, risetime = 8.27 ps, and falltime = 7.06 ps. However, the addition of noise to the Gaussians, to provide more realistic waveforms with which to simulate the filtering, had the effect of approximating the quadrature deconvolution, as the waveforms were no longer true Gaussians. Therefore the difference between the above parameters cannot be deemed to be due to the filtering alone.

NIST have developed a mathematical approach to the problem of defining an optimum filter and minimise the imaginary time-domain of the result from the Hilbert Transform.[2] In practice, NPL's qualitative approach - deconvolving with several filter parameters and choosing an optimum result - has proven to be adequate. Although the plotted parameters do not always exactly follow those in Figure 6.1, the general *trends in the diagram are* apparent in most cases and the suggested four-point algorithm has been employed successfully in all the deconvolutions used in this thesis.

It should also be added that deconvolution is not simply a mathematical exercise to produce an "exact" result - uncertainties are also obtained. If the uncertainties are small enough for the application then the deconvolution is good enough, regardless of how "exact" it is.

6.2.4 Example of uncertainties in deconvolution

The results from the deconvolution example are used here to give indications of the size of uncertainty that may be obtained using a deconvolution and filter. There are two main uncertainties: the uncertainty in the choice of the "best" result, i.e. the optimal filter; and the uncertainty in the effect of the filter on the deconvolution result. The first uncertainty can be estimated by taking a range of results which give an acceptable result. In practice, the result either side of the chosen filter is used to provide limits, for example with optimum filter 3, the difference between that result and the FWHM of the result obtained with filters 2 and 4 defines the limits on the result. This is shown as "range due to choice" in Table 6.2.

The chosen optimal filter has a smoothing effect on the deconvolution result. The filter is not Gaussian and cannot be removed from the result. Estimating the uncertainty on the result due to this effect is not *trivial; the results of two methods* are shown in Table 6.2 for filters 2 to 5.

Method 1 de-convolves in quadrature the filter, τ_f, from the result, τ_r, and estimates the uncertainty, $\delta\tau_1$, to be the difference between this result and the original result:

$$\delta\tau_1 = \tau_r - \sqrt{\tau_r^2 - \tau_f^2} \quad . \tag{6.5}$$

Method 2 calculates the difference between a quadrature-calculated result using the system and original data, τ_d, and a quadrature-calculated result using the system and (full) re-convolved data:

$$\delta\tau_2 = \sqrt{\tau_d^2 - \tau_s^2} - \sqrt{(\tau_s \otimes \tau_r)^2 - \tau_s^2} \quad . \tag{6.6}$$

Table 6.2 Uncertainties due to filter.

Filter No	Filter FWHM τ_f / ps	Result FWHM τ_r / ps	Uncertainties / ps			
			Range due to choice	Filter method 1 $\delta\tau_1$	Filter method 2 $\delta\tau_2$	Total
2	5.19	12.64	+1.01 -0.39	-1.11	+0.03	+1.01 -0.69
3	7.53	12.25	+0.58 - 0	-2.58	-0.01	+0.58 -1.29
4	9.39	12.83	+1.58 - 0.58	-4.09	-0.42	+1.58 -2.33
5	11.71	14.41	+3.20 -1.58	-6.02	-1.83	+3.20 -4.23

A thorough examination of the relative merits of the two methods is not considered here, but it should be noted that the use of quadrature is an approximation. Method 1 is likely to over-state the uncertainty whilst method 3 is likely to under-estimate it. The mean of the two methods was used as a non-rigorous approximation; the mean was combined in quadrature with the uncertainty due to the choice of filter to give the total uncertainty column in Table 6.2.

For each filter, the deconvolved result and uncertainty can be compared to the quadrature-deconvolved result, FWHM= 11.03 ps. It is seen that the previous choice of filter 3, which produced the optimal result, is also the filter choice which provides the lowest positive and second lowest negative uncertainty.

Similar examinations of uncertainty, evaluated using different deconvolution examples and non-generated waveforms, produced similar results to those shown above. The uncertainties in the deconvolution to determine the single-transition in *section 5.5* and the oscilloscope response in *section 6.4* were calculated according to the above method.

6.3 Jitter

Jitter is the scatter in time measured between a trigger point and a sample point. Jitter in the time-domain is the equivalent of phase noise in the frequency-domain[4] and is also equivalent to the operation of a low-pass filter.[5]

An example of jitter, produced by a modelocked laser, is the variation in delay between successive pulses in the optical train of pulses. If the laser is passively mode-locked, then the jitter depends on the stability of the laser cavity. If the laser is actively mode-locked and driven by an r.f. synthesiser, then the jitter depends on the phase-noise of the source.

However, the jitter must be measured relative to something. The electro-optic sampling (EOS) system uses a modelocked laser which has variable pulse-to-pulse arrival times.

However, the system does not suffer jitter if an optoelectronic pulse generator is measured, as the same optical pulse is used both to illuminate the pulse generator (producing synchronous electrical pulses), and to sample the electrical pulses. An EOS system which measures an all-electrical pulse generator, for example driven by an r.f. source itself phase-locked to the laser, would suffer jitter, as there would be timing variations between the r.f. source and pulse generator, and also between the r.f. source and laser pulses.

In the case of a sampling oscilloscope measuring a pulse generator (electrical or optoelectronic), two main sources of jitter are present. Firstly, noise on the trigger signal alters the trigger point at which the sample is being made. The effect of the noise is dependent on the type and bandwidth of the trigger signal. Secondly, there is jitter between the trigger and sampling gate of the oscilloscope. This internal jitter is indistinguishable from that caused by trigger noise, but is intrinsic to the oscilloscope. In theory, only the first type of jitter should be removed from an oscilloscope measurement; in practice both contributions are treated together.

6.3.1 Measurement and removal of jitter

If the probability distribution of the jitter is known, then the effects of the jitter can be removed by deconvolution of a function describing the scatter. Modern sampling oscilloscopes, such as the Tektronix CSA803 and Hewlett-Packard HP54120-series, are able to measure the jitter in the triggering of the oscilloscope (and hence the system) with their firmware, using a histogram algorithm to return the standard deviation, σ, of the jitter.

It is important that the measurement time over which a jitter histogram is recorded is carefully chosen. Ideally this time should be the same as the acquisition time of the measured oscilloscope data waveform. In the case of the Tektronix oscilloscope, it takes about 10 s to average together 256 waveforms, each containing 512 sample points. If the times are not equal then the effect of other phenomena, such as drift in the oscilloscope

time-base, may dominate in one measurement.

The probability distribution of jitter is frequently assumed to be a Gaussian function. To investigate this assumption, a LT-GaAs optoelectronic pulse generator was measured using the SD32 plug-in. Figure 6.5 displays the obtained histogram using the firmware of the Tektronix CSA803 oscilloscope. The small red box outlines the time and voltage windows within which the histogram was defined.

The shape of the histogram distribution is represented below the jittered signal. In the diagram, the standard deviation of the distribution, denoted by RMSΔ, is equal to 1.9 ps and the peak-to-peak scatter is equal to 12.4 ps. The three parameters, $\mu \pm 1\sigma = 69.3\%$, $\mu \pm 2\sigma = 95.8\%$ and $\mu \pm 3\sigma = 99.7\%$, provide an indication of the probability distribution function of the jitter around the mean value, μ, for integer numbers of the standard deviation.

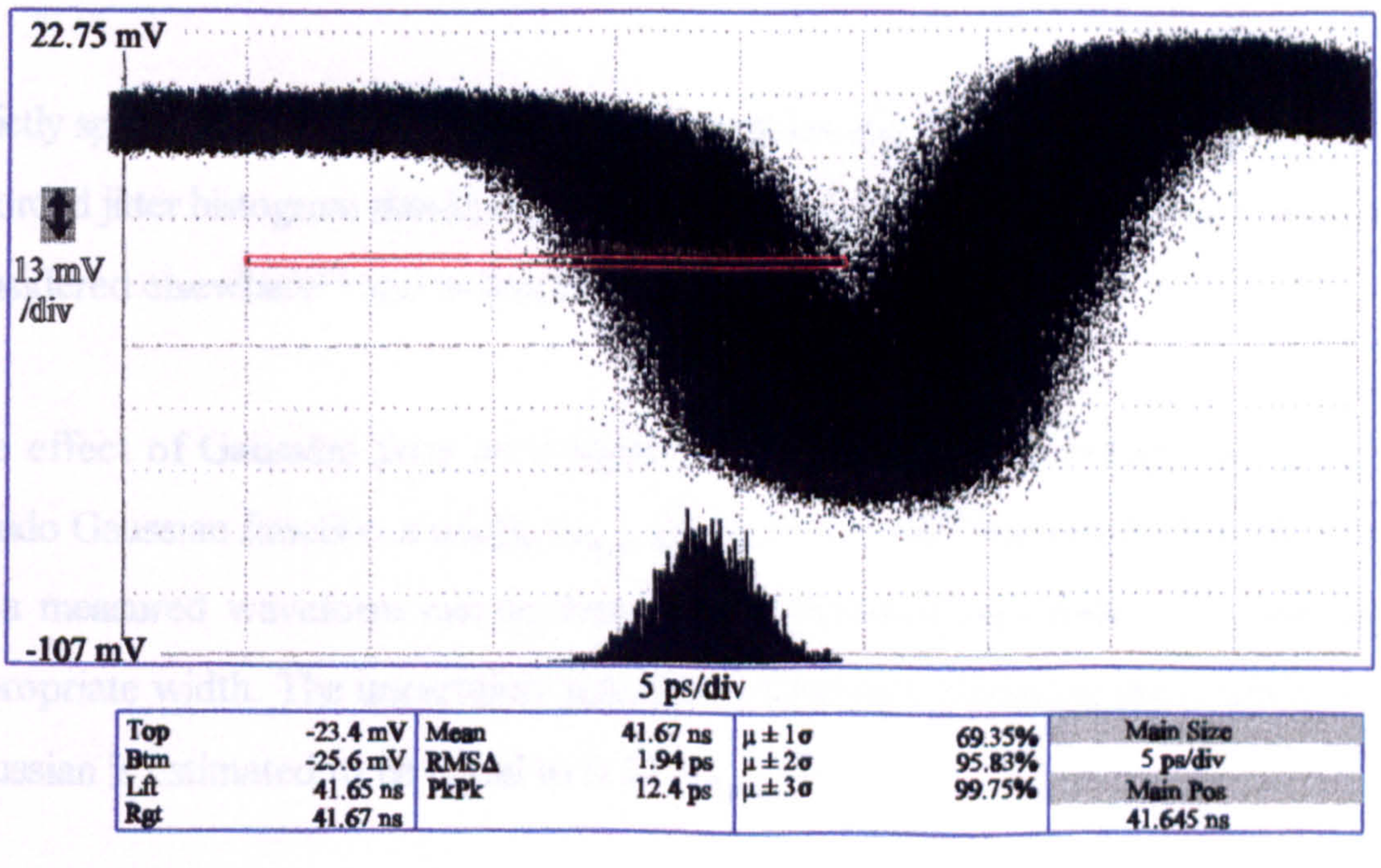

Figure 6.5 Measurement of jitter with oscilloscope histogram.

For a Gaussian, the "student's t test" or normal error integral,[6] is defined as:

$$erf(t) = \frac{1}{\sqrt{2\pi}} \int_{-t}^{t} e^{-\frac{z^2}{2}} . dz \qquad (6.7)$$

where erf(t) represents the probability that the function is within ± tσ of the mean value μ. From tables, the value of erf(t) for t = 1, 2 and 3 is 68.3%, 95.4% and 99.7% respectively. A comparison with the recorded oscilloscope values suggests that approximating the jitter to a Gaussian distribution is a reasonable estimate in this case.

Using such a histogram method with pulses requires the jitter to be small enough to eliminate the possibility of some of the histogram hits being defined on the falling edge rather than the rising edge of the pulse during the measurement. The jitter measurement of a step function does not suffer this problem. In this thesis, jitter is relatively small and hence a method to overcome such inaccuracies is not required. An alternative method of measuring jitter, designed to resolve such problems by spline-fitting several single-shot waveforms, is discussed elsewhere.[7]

Strictly speaking, the contribution of amplitude noise, e.g. from the laser, on the LT-GaAs recorded jitter histogram should be quantified and removed. Such contributions have been considered elsewhere[7] and in this case the effect is small.

The effect of Gaussian jitter on a signal is equivalent to convolving the signal with a pseudo Gaussian function a width, G_{jitter}, given by 2.35σ.[5] Therefore, the effect of jitter on a measured waveform can be removed by deconvolving from it a Gaussian with appropriate width. The uncertainty associated with approximating the distribution to be Gaussian is estimated to be equal to $0.12 \times G_{jitter}$.[8]

6.4 Deriving the oscilloscope response

The components needed to calibrate the oscilloscope response have now all been

described in the preceding sections and chapters. This section describes how the response is derived from these components.

The derivation of the CRO impulse response is described by:

$$CRO_{measure} = PG \otimes T1 \otimes G_{jitter} \otimes CRO_{response} \quad , \tag{6.8}$$

where PG is the EOS waveform of the pulse generator at the transition point (Auston switch PG6, 3.6 ps FWHM, *section* 5.4.3.1), T1 is the transfer function of a single CPW-coax transition (6.0 ps FWHM, *section* 5.5.2) and G_{jitter} is a 4.5 ps FWHM Gaussian representing the measured system jitter of 1.9 ps rms.

An equivalent jittered pulse generator at the input to the coax connector of the CRO was obtained by convolving PG with T1 and G_{jitter}. The resulting waveform, 8.8 ps FWHM, was then deconvolved from a CRO measurement of the pulse generator, $CRO_{measure}$ (10.9 ps FWHM), to obtain the impulse response of the oscilloscope, $CRO_{response}$.

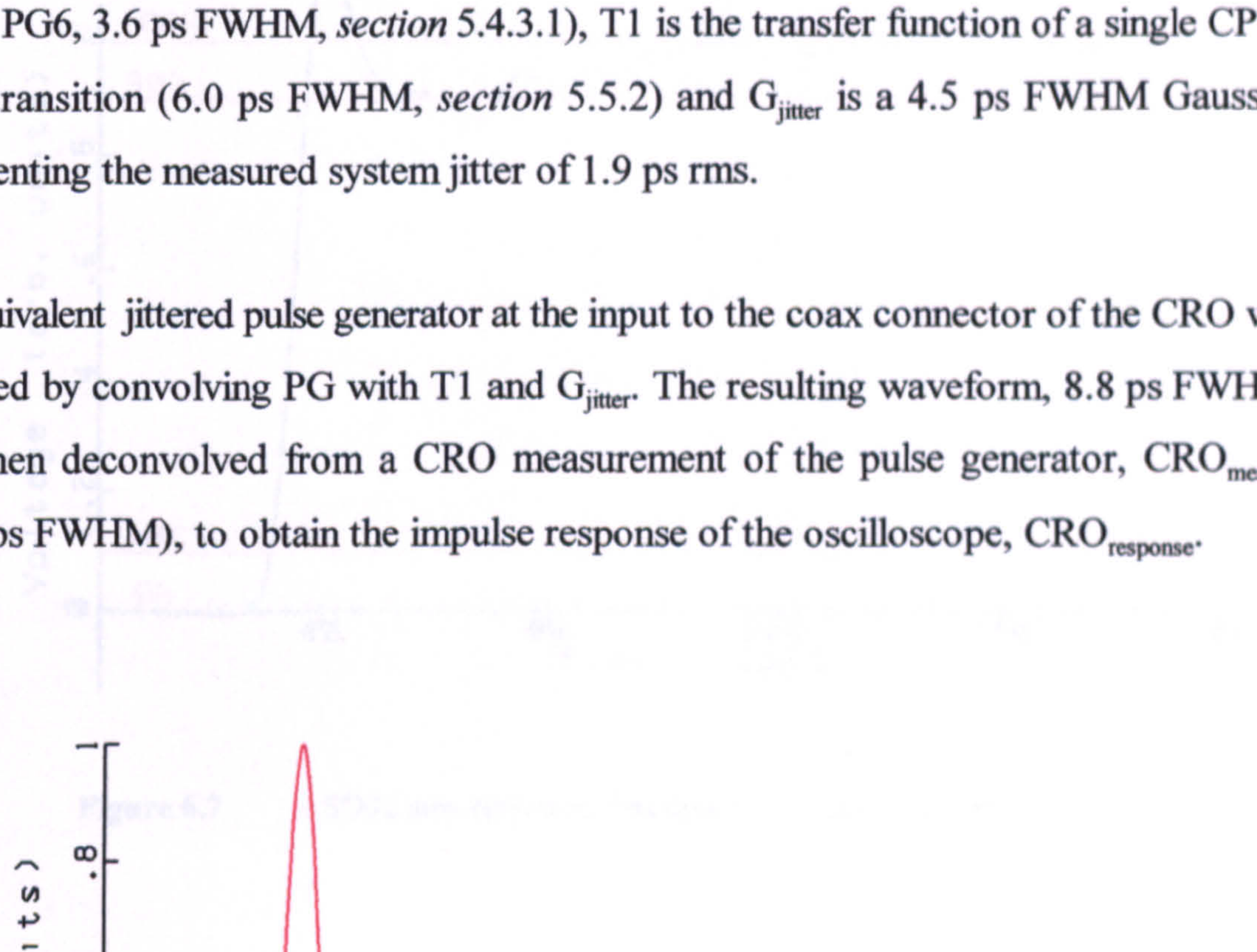

Figure 6.6 SD32 impulse response. FWHM = 7.7 -1.9 / +1.4 ps.

The derived impulse response of the NPL SD32 oscilloscope is shown in Figure 6.6 (FWHM=7.7 ps). The impulse response was integrated to produce the step response (Figure 6.7, risetime = 7.4 ps). It is noted that the step response is not equal to 1.09 times the FWHM, showing the response cannot be approximated to be Gaussian. The uncertainties quoted in the figures are derived in the next section.

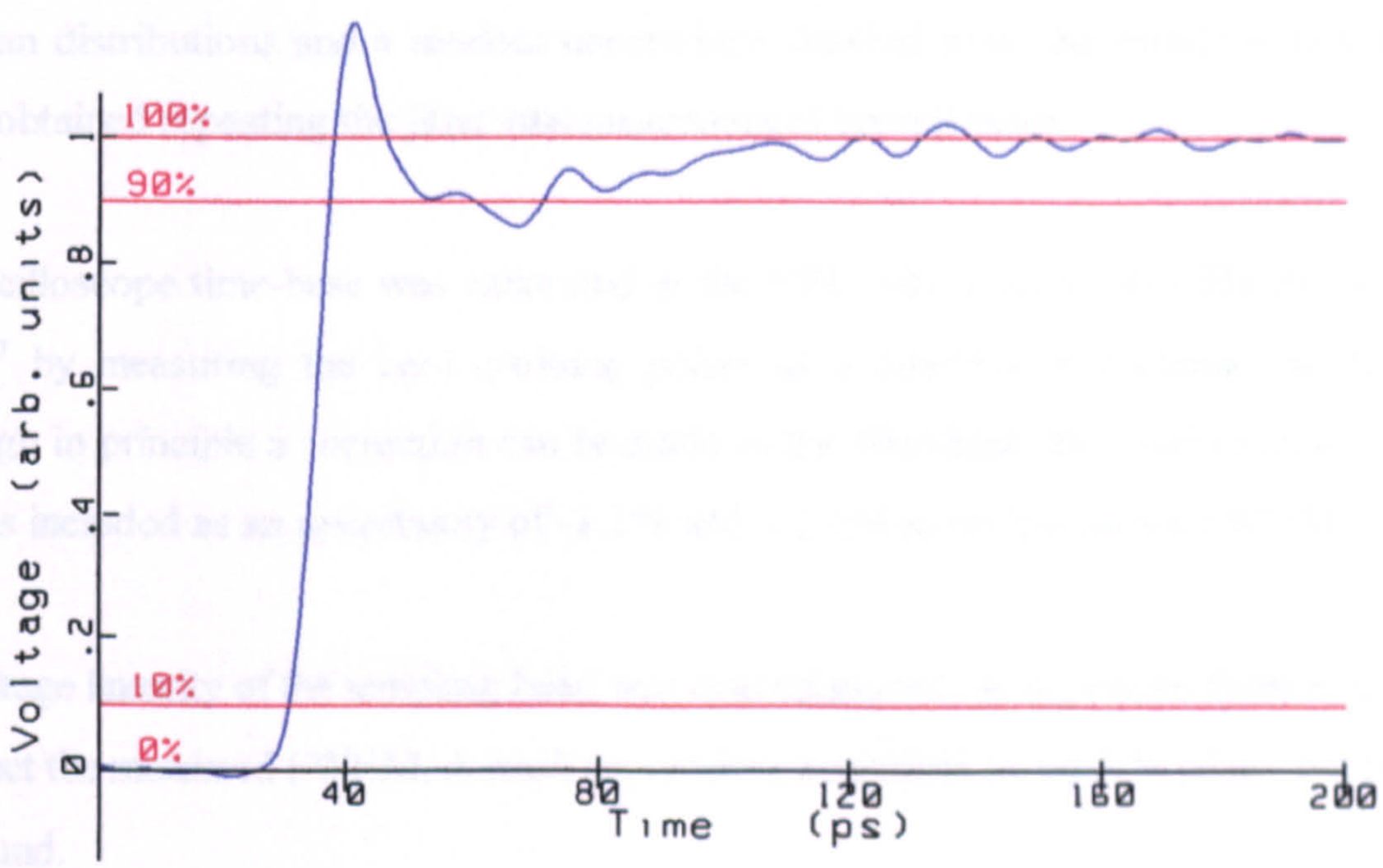

Figure 6.7 SD32 step response. Risetime = 7.4 -2.1 / +1.7 ps.

6.5 Uncertainties

There are several contributions to the uncertainty in deriving the oscilloscope impulse and step response, some of which have been described in previous sections of this thesis and references therein. Details and rationale behind some values of uncertainties are not necessary provided here,[8] but it should always be recognised that uncertainties are, by definition, arbitrary. A summary of contributions used in defining the uncertainty in the impulse response pulse duration, τ_{im} = 7.7 ps, is shown in Table 6.3.

The largest uncertainty was due to the deconvolution and filter (see example in *section 6.2.4*). The uncertainty in the pulse generator signal - in coaxial line the convolution of an EOS measurement and single CPW-planar transition - was calculated from the uncertainty in the single transition only (as in deriving the single transition an uncertainty in the EOS measurement was included).

Two contributions from jitter were included, a systematic uncertainty accounting for non-Gaussian distributions and a random uncertainty, derived from the standard deviation SD_{rms}, obtained repeating the jitter rms measurement several times.

The oscilloscope time-base was calibrated at the NPL with a stable 40 GHz frequency source[2] by measuring the zero crossing points as a function of oscilloscope delay. Although in principle a correction can be made to the time-base, the correction is small and was included as an uncertainty of -1.1% and + 2.1% in the measured FWHM.

The voltage linearity of the sampling head was also measured, as departure from nominal can affect the measured FWHM. A small uncertainty, equivalent to ±0.5 % of the FWHM, was found.

The uncertainty in calculating the step response first transition duration (risetime) was larger than calculating the pulse duration (FWHM), because of additional uncertainty in the definition of proximal and distal points after integration. The setting of these levels added an uncertainty of ± 1 ps[8] - due to structure from both the deconvolution (ripple) and the oscilloscope response (non-Gaussian shape), and due to the relatively narrow epoch. The risetime with the additional uncertainty was 7.4 -2.1 / +1.7 ps.

---

[2] Hewlett Packard 83597A sweeper.

Table 6.3 Contributions to uncertainty in oscilloscope FWHM.

Detail	Uncertainty Type A ps	Uncertainty Type B ps
Knowledge of Pulse Generator: FWHM τ_{pg} = 6.9 ps Uncertainty $\delta\tau_{pg}$ = -1.1 / +1.0 Systematic: $-\delta\tau_{pg}.\tau_{pg}/\tau_{jm}$	-	-0.90 / +0.99
Trigger jitter: 1.9. ps rms $G_j = 1.9 \times 2.35$ Non-Gaussian: 0.12 G_j Random: 2.35 $(SD_{rms})G_j/\tau_{jm}$	- ± 0.08	± 0.53 -
Deconvolution: Including range and filter	-	-1.20 / +0.25
Time-base correction:	-	-0.11 / +0.17
Voltage linearity:	-	± 0.04
Reproducibility: Spread in CRO FWHM	± 0.18	-
Sub-totals added in quadrature: σ Type A Semi-ranges -/+ Type B Type B/√3	± 0.20 - -	- -1.59 / +1.16 -0.92 / +0.67
TOTAL UNCERTAINTY (Type A and Type B added in quadrature and multiplied by 2 to give 95% confidence levels)	-1.88 / +1.39	

Table 6.4 show the improvements in the SD32 impulse FWHM and step risetime achieved with the work described in this thesis, compared to the previous NPL calibration of the same sampling head. For the previous measurement, the uncertainties were originally quoted to be smaller, but the uncertainties have been re-calculated using the method recommended by NAMAS[9] and draft ISO document.[10] (For comparison, the previous values are also shown.)

Table 6.4 Improvement in oscilloscope response.

	Previous value (pre-NIS3003 edition 8)	Previous value (re-calculated)	New value
Impulse response FWHM / ps	7.9 ± 2.1	7.9 ± 2.4	7.7 -1.9 / +1.4
Step response risetime / ps	8.5 -3.0 / +2.5	8.5 -3.5 / +2.9	7.4 -2.1 / +1.7

6.6 Conclusions

This chapter has explained the use of deconvolution and the measurement of jitter in the context of oscilloscope calibration. A qualitative approach to defining an optimum deconvolution filter was described with the aid of an example and uncertainties estimated. Various results in previous chapters, including the measurement of the LT-GaAs pulse generator and the de-embedding of a single transition, were combined to derive the impulse and step response of a 50 GHz sampling oscilloscope. A summary of the contributions to the measurement uncertainty was provided.

The impulse response FWHM and step response risetime for the oscilloscope - including the uncertainties - were significantly improved on previous calibrated values. The use of such optoelectronic techniques to provide electrical risetime calibration down to this level of accuracy is, to the best of the author's knowledge, unique.

6.7 References to chapter 6

1 R.N.Bracewell, "The Fourier Transform and Its Applications", McGraw-Hill Inc., 1986, pp 110-111.

2 N.S.Nahman and M.E.Guillaume, "Deconvolution of Time Domain Waveforms in the Presence of Noise", NBS Technical Note 1047, 1981.

3 Private communication with Bill Gans, Fast Waveform Metrology Group, NIST.

4 D.Henderson and A.G.Roddie, "A Comparison of Spectral and Temporal Techniques for the Measurement of Timing Jitter and their Application in a Modelocked Argon Ion and Dye Laser System", Optics Communications 100, 1993, pp 456-460.

5 W.L.Gans, "The Measurement and Deconvolution of Time Jitter in Equivalent-time Waveform Samplers", IEEE Tran. Instrum. Meas. IM-32, 1983, pp 126-133.

6 J.R.Taylor, "An Introduction to Error Analysis: the Study of Uncertainties in Physical Measurements", University Science Books, 1982.

7 D.A.Humphreys, "Measurement Techniques, Numeric Methods and Photodiode Risetime Transfer Standards for Picosecond Optoelectronic Device Metrology at 1 - 1.6 μm", Ph.D. Thesis, University College London, April 1990.

8 NPL internal reports.

9 NIS3003, "The Expression of Uncertainty and Confidence in Measurement for Calibrations", edition 8, NAMAS guidelines, NPL, 1995.

10 "Guide to the Expression of Uncertainty in Measurement", working draft, ISO, TAG 4/WG3, 1992.

7 CONCLUDING COMMENTS AND FUTURE WORK

7.1 Introduction

The aim of using a photoconductive switch to improve oscilloscope risetime calibration facilities has been addressed in this thesis, and work has been reported that achieves the calibration target of 8 ± 2 ps. *This chapter summarises* some of the achievements and highlights those areas where future opportunities have been revealed.

The demand for fast sampling oscilloscopes is growing, with 50 GHz instruments becoming more widely used in many applications. Characterising the response of such an instrument is essential - an oscilloscope user must have confidence in the accuracy and uncertainties associated with making measurements with an oscilloscope.

The ability of conventional electrical techniques to characterise a 50 GHz sampling oscilloscope is limited, due to the problem of using a test pulse with similar or lower bandwidth to that of the oscilloscope under test. This thesis has demonstrated that an optoelectronic approach to calibration is a viable alternative, and that the work described here significantly improves on that reported elsewhere.

This project was divided into four distinct sections: the development of an ultrafast optoelectronic pulse generator to act as an oscilloscope test source; the development of an electro-optic sampling system to measure the test pulses independently to, and with greater accuracy than, the oscilloscope under test; the de-embedding of transmission line and transition effects as measured at different calibration reference planes; and the calibration of the oscilloscope.

7.2 Concluding comments

7.2.1 Pulse generator

A photoconductive switch was chosen as a pulse generator, as semiconductor materials

with very fast carrier recombination time can produce pulses significantly shorter than those attainable with commercial photodiodes. Properties of semiconductor materials were considered and low-temperature grown (LT) GaAs was *identified as having the best* potential to fabricate reproducible, fast, high-amplitude photoconductive pulse generators. Wafers of LT-GaAs were procured and processed into pulse generator devices. Device fabrication concentrated on producing high conductivity CPW and CPS transmission lines and low semiconductor-metallisation contact resistances. The growth of further wafers will enable wafer growth reproducibility, as measured by x-ray diffraction and photoluminescence, to be related to device performance, an important long-term metrological aim for consistent device development.

The impulse response of LT-GaAs photodetectors was measured using electro-optic sampling. The speed of the fastest electrical pulse measured at the NPL was 650 fs FWHM, using a 10 μm CPS generator and a spacing of 50 μm between the generation and sampling points. The deconvolved response of the LT-GaAs was estimated to be less than 500 fs FWHM, short enough for the application.

7.2.2 Electro-optic sampling

The short pulses produced by the LT-GaAs switch were measured using a sampling system with an external electro-optic probe in close proximity to the switch. The electro-optic sampling (EOS) system was used to measure the electrical pulse shape at various positions along planar transmission lines.

Different configurations of photoconductive device were produced and measured: the CPW and CPS sliding contacts and the CPW Auston switch. The sliding contact was more flexible and device illumination was easier to achieve. For measurements with a sampling oscilloscope a bias tee was needed to isolate the dc bias from the sampler. An Auston switch configuration circumvented the need for additional knowledge of the effect of the bias tee between the pulse generator and oscilloscope.

It was found that the stripline mode of propagation could be excited along a CPW line by using the CPW sliding contact pulse generator. This was due to asymmetrical excitation of the CPW. Further measurements investigated the modal properties of both CPW and CPS lines using EOS, as this was relevant to optimise and characterise the photoconductive switch as a calibration test source.

Limitations of the two different laser systems were described. The Ti:sapphire EOS system had an estimated overall response of 500 fs FWHM, corresponding to a bandwidth of 630 GHz. This compared to a bandwidth of 120 GHz for the earlier dye laser EOS system.

A minimum detectable voltage of less than 0.5 mV/$\sqrt{\text{Hz}}$ and a dynamic range of over 60 dB were achieved with the Ti:sapphire EOS system. Both parameters were more than adequate for the application.

7.2.3 De-embedding

Attenuation and dispersion in transmission lines were very important in this application, as the short pulses were degraded by such phenomena. These properties were measured using frequency-domain vector network analysis, and were compared to time-domain techniques and predictions from theoretical models with good agreement.

The pulse generator produced sub-picosecond pulses near to the point of generation, but the pulses broadened to 7 ps after passing along a length of planar transmission line and a coplanar-coaxial transition. For a 50 GHz sampling oscilloscope with a coaxial input connector, this effect was significant. Frequency-domain measurements with a network analyser, further electro-optic sampling measurements, and the transmission line model were combined to derive an equivalent impulse response of 6 ps for a single transition, allowing the distorting effect of the transition to be de-embedded from an oscilloscope measurement of a planar pulse generator.

7.2.4 Oscilloscope calibration

Using the pulse generator, the electro-optic sampling system and the transition knowledge, a 50 GHz sampling oscilloscope was calibrated. The determination of the instrument step response (nominal risetime 7 ps) was improved from an earlier value of 8.5 -3.5 / +2.9 ps to a new value of 7.4 -2.1/ +1.7 ps. The use of the optoelectronic pulse generator and measurement system to provide electrical risetime calibration down to this level of accuracy is, to the best of the author's knowledge, unique. The lower uncertainty in the response provides greater confidence in the accuracy of the result and gives an oscilloscope user enhanced accuracy in making measurements with a calibrated oscilloscope.

7.3 Future work and opportunities

7.3.1 Oscilloscope calibration

As a result of the work described in this thesis, a calibration facility of at least 8 ± 2 ps was achieved, dependent on the shape of the response. However, to calibrate to specification an oscilloscope *with a risetime of <7 ps*, an improved facility is required, for example 6.5 ± 0.5 ps or 5 ± 2 ps. As developments in oscilloscope technology produce faster instruments, the need for better calibration facilities will also increase. Indeed, it would be unusual in the field of metrology if the need for yet better measurement were not insatiable. This section looks at future work which could be performed to extend the work reported in this project and elsewhere.

The use of a commercial test-fixture was ideal for testing switches, but the design of the CPW jaws and transition was not optimised for the application. An optimised coaxial pulse generator could be built which minimises the pulse distortion between the point of generation and coaxial connector. For example a small LT-GaAs chip could be directly connected into a coaxial connector with wire-bonds.

The effect of contact resistance on device performance was not fully resolved in this thesis. More work is required to investigate further the dependence of the contact resistance on device metallurgy, and to determine the effect that contact resistance has on device responsivity and pulse-evolution. An improved resistance may decrease the measurement time, but is unlikely to affect the risetime. Improvements could also be made to the S/N of the EOS system with similar consequence.

The temporal resolution of the NPL EOS system can be improved by replacing the acousto-optic modulator with a device with less temporal broadening. For example, a chopper and low-frequency detection scheme could be implemented, at the expense of slowing the data acquisition time due to more averaging. Use of thinner, less invasive probes and shorter optical pulses, from either pulse compression with existing lasers or using new laser sources (when available), would also decrease the EOS temporal resolution. However, the point was not reached in this project where such work would provide advantage to the application.

Future work could also investigate alternative measurement systems, such as photoconductive sampling, to improve uncertainties in measuring pulse generators. The mechanisms involved in pulse generation could be explored, for example, carrier dynamics of LT-GaAs could be measured using time-resolved reflectivity (pump-probe). Such techniques could be used to investigate alternative materials to LT-GaAs with shorter carrier recombination times.

Transmission lines were shown significantly to degrade pulse propagation, but the effect can be decreased, for example by using lift-off epitaxy.[1] By grafting a thin substrate onto a thin membrane, the effective dielectric of a transmission line can be made to approach that of air, lowering the losses and dispersion. The construction of a LT-GaAs pulse generator on such a planar transmission line would produce less pulse broadening, but a suitable method would need devising to launch the improved pulse onto the coaxial line. It is possible that superconducting technology could be implemented, not only to improved transmission lines, but also to improve pulse generation and sampling.[2] Work

would be required to implement a cryogenic system and oscilloscope together in such way that advantages bestowed by the superconducting technology were not lost.

Uncertainties in oscilloscope calibration can be reduced - relative to those used in this project - by improvements in system jitter and deconvolution techniques. An improved time-base is now available for the CSA803 oscilloscope which uses deskew averaging[3] and other refinements to decrease oscilloscope drift and jitter from typically 2 ps to < 1.5 ps rms. Theoretical work to improve deconvolution techniques using improved filters[4] and to reduce the uncertainties associated with the use of such techniques are also becoming available.

Other techniques to calibrate oscilloscopes have been used in the past and will doubtless be used in the future. A variety of techniques enables comparison of results and is especially important to improve uncertainties. Alternative techniques include swept frequency and nose-to-nose. The swept frequency method uses a sinusoidal frequency source stepped in frequency over the measurement range of the oscilloscope. Traceability of power response is to national power standards, but a phase response must be assumed if a time-domain response is required. The nose-to-nose[5] or kick-out method is presently only applicable to Hewlett Packard oscilloscopes. Here, a pulse is generated by a sampling oscilloscope at its input connector as a consequence of the sampling circuit's operation and is measured by a second, nominally identical, sampler. From this, the impulse response of the oscilloscope can be calculated. Both the above methods were compared to an EOS method in 1992,[6] but since then there have been improvements in national power standards and in the understanding of nose-to-nose techniques.[7]

7.3.2 Opportunities

Some of the technology described in this thesis has wider-ranging applications than oscilloscope metrology *per se*. For example, the development of techniques to generate and measure ultrafast electrical pulses provides opportunities to characterise time-resolved

properties of materials, interconnects and devices. Two of many applications for photoconductive switches and electro-optic probing are discussed below as examples.

Recently improved sophisticated quantum-well and novel device structures have produced high power pulsed or cw diode lasers[8] capable of optically driving millimetre-wave sources, operating up to terahertz frequencies. An efficient compact source, driven by such a laser, could be developed using photoconductive switching. The development of broadband diode-laser-pumped sources will facilitate more applications in this part of the electromagnetic spectrum, including ultrafast electronic devices, communications and imaging.

Time-domain network analysers can be built from systems with a fast pulse generator or microwave source and an optoelectronic measuring system. Broadband pulses generated with LT-GaAs photoconductors and measured with electro-optic sampling can extend the maximum frequency of a system beyond frequencies attainable with conventional network analysers, thus improving on their bandwidth limitations. An electro-optic system also offers the advantage of probing circuits such as MMICs with non-contacting, less invasive probes and also measuring circuits at locations within the circuit inaccessible to conventional probes.

7.4 References to Chapter 7

1 W.K.Chan, A.Yi-Yan and T.J.Gmitter, "Grafted Semiconductor Optoelectronics", IEEE Journ. Quant. El., Vol. QE-27, No. 3, March 1991, pp 717-725.

2 For example: R.Sobolewski, W.N.Maung, D.P.Butler, W.Xiang and W.Kula, IEEE Microwave Guid. Lett., Vol. 4, 1994, pp 132.

3 L.Dobos and J.Rettig, "Characterization of Accuracy for Time Interval Measurements performed on the 11800 Family of Oscilloscopes", Tektronix Users Group Meeting at SEMICON/West, 19 July, 1993.

4 A.Bennia and N.S.Nahman, "Deconvolution of Causal Pulse and Transient Data" IEEE Trans. Instrum. & Meas., Vol. 42, No. 6, Dec 1990, pp 933-939.

5 K.Rush, J.Kerley and S.Drawing, "Characterizing High-speed Oscilloscopes", IEEE Spectrum, 1990.

6 D.Henderson, A.G.Roddie and A.J.A.Smith, "Recent Developments in the Calibration of Fast Sampling Oscilloscopes", IEE Proc. A, Vol. 139, No.5, Sept 1992, pp 254-260.

7 J.Verspecht, "Calibration of a Measurement System for High Frequency Non-Linear Devices", Ph.D. Thesis, Free University of Brussels, submitted Sept 1995.

8 P.P.Vasil'ev, I.H.White, D.Burns and W.Sibbett, Technical Digest CLEO, Paper CThC8, 1993, pp 390.

APPENDICES

A Measurement of bias tees and attenuators

A.1 Introduction

Coaxial bias tees and attenuators are in general use with electrical and optoelectronic measurement systems. During the course of this thesis, the effect of such components on systems was measured in the time and frequency-domains and it is noteworthy to summarise some results.

A.2 Measurements

A Ti:sapphire-illuminated LT-GaAs photoconductive switch (Auston device PG7 mounted in UTF2) was measured with a 50 GHz sampling oscilloscope in the time-domain. With only a male-to-male "V" adapter between the UTF coaxial connector and oscilloscope, a FWHM of 11.0 ps was obtained. Each of the components shown in Table A.1: a "K" and "V" 3 dB attenuator[1], "K" bias tee[2] and "2.4" bias tee[3], was inserted between the switch and oscilloscope using "V-to-K" adapters where appropriate, and the broadened pulse measured on the oscilloscope. A random uncertainty (reproducibility) in the FWHM of ± 0.2 ps was achieved. The waveforms were approximated to be Gaussian and quadrature deconvolution was performed to provide an indication of the component broadening. The equivalent frequency-domain bandwidth was approximated from equation (1.4) in *chapter* 1.

The components were also measured with an ANA in the frequency-domain, using the two-port OSLT "V" calibration performed in *section* 5.3.2 (except for the "K" bias tee, which was measured using a "K"calibration defined up to 46 GHz). The -3 dB ANA-measured bandwidths are shown in Table A.1. However, for the two attenuators, the

---

1 Wiltron 41KC-3 and 41V-3

2 Wiltron K250

3 Hewlett Packard 11612B

bandwidth is beyond the ANA measurement capability and so the frequency at which the power spectra has changed by 1 dB is also shown in Table A.1 (where * indicates a 1 dB change from the dc value of 3 dB).

Table A.1 Broadening and bandwidth of bias tees and attenuators.

Component	CRO measured FWHM ps	Quadrature deconvolved FWHM ps	Equivalent 3 dB bandwidth GHz	ANA 1 dB frequency GHz	ANA 3 dB bandwidth GHz
"K" 3 dB attenuator	12.1	5.0	62	44 *	> 60
"V" 3 dB attenuator	11.9	4.5	69	58 *	> 60
"K" Bias Tee	12.6	6.2	50	40	> 46
"2.4" Bias *Tee*	14.3	9.1	34	26	50

A.3 Conclusions

There is good agreement between the trends shown in the time and frequency-domain measurement of the components. Although approximating the components as Gaussian does not produce good agreement in the bandwidth values, the uncertainties in the measurements and in the use of single parameter comparisons provides reasonable grounds for the level of disagreement shown. The purpose of this appendix was to highlight the typical effect commonly-used components such as bias tees and attenuators can make on measurement systems.

B List of publications during project

D.Henderson, A.G.Roddie and A.J.A.Smith, "Recent Developments in the Calibration of Fast Sampling Oscilloscopes", IEE Proceedings-A (Science, Measurement and Technology), Vol. 139, No. 5, Sept 1992.

S.R.G.Hall, D.Henderson, A.G.Roddie and A.J.A.Smith,"Applications of Time and Frequency Domain De-embedding Techniques to Picosecond Optoelectronics, Sixth British Electromagnetic Measurements Conference, Teddington, UK, Nov 1993.

A.G.Roddie, A.J.A.Smith and D.Henderson, "Application of Femtosecond Pulses to Electrical Metrology", International Workshop on Femtosecond Technology, Tsukuba, Japan, Feb 1995.

A.G.Roddie, A.J.A.Smith, A.D.Gifford and D.Henderson, "Application of Femtosecond Pulses to Electrical Metrology", Seventh British Electromagnetic Measurements Conference, Malvern, *UK, Nov 1995.*

A.J.A.Smith, A.G.Roddie and D.Henderson, "Electro-optic Sampling of Low Temperature GaAs Pulse Generators for Oscilloscope Calibration", submitted to Optical and Quantum Electronics - special issue on optical probing of ultrafast devices and integrated circuits.

A.G.Roddie, A.J.A.Smith, A.D.Gifford and D.Henderson, "Realisation of Improved Calibration of Sampling Oscilloscopes using Photoconductive Switches", submitted to IEE Proceedings-A (Science, Measurement and Technology).

ACKNOWLEDGEMENTS

I wish gratefully to thank Professor Gareth Parry for his advice, his encouragement and his time - despite a bewilderingly hectic schedule - during the period of this thesis.

I wholeheartedly acknowledge the advice, support and friendship of all my colleagues at the NPL, with particularly special thanks to Dr Alan Roddie and Dr Dale Henderson for their supervision. I also acknowledge the useful discussions with Simon Hall, Dr David Bannister, Alan Gifford, Dr David Humphreys and David Ives.

I thank the clean room staff at *UCL: Tony Rivers* for initial input; Dave Prescott and Fred Strides for their contributions to device fabrication. I also thank Martin Wicks for advice and help with clean room facilities at the NPL.

I thank Mark Hopkinson at Sheffield for the growth of LT-GaAs and his encouragement of the work.

I acknowledge the support of the Chief Executive and Managing Director at the NPL. I also acknowledge the National Measurement System Policy Unit for funding the work.

Lastly, but by rights first, I thank my wife Mary and my family for their patience, encouragement and love throughout the period of this thesis.

Paginated

blank pages are scanned as found in original thesis

No information is missing